Dynamical behavior of trampoline membranes

de Jong, M.H.J.

DOI
10.4233/uuid:4f4196f3-fadb-4170-b6d2-c0923dbd325a

Publication date
2022

Document Version
Final published version

Citation (APA)
de Jong, M. H. J. (2022). *Dynamical behavior of trampoline membranes*. [Dissertation (TU Delft), Delft University of Technology]. https://doi.org/10.4233/uuid:4f4196f3-fadb-4170-b6d2-c0923dbd325a

Important note
To cite this publication, please use the final published version (if applicable).
Please check the document version above.

Dynamical behavior of trampoline membranes

Dynamical behavior of trampoline membranes

Proefschrift

ter verkrijging van de graad van doctor
aan de Technische Universiteit Delft,
op gezag van de Rector Magnificus prof. dr. ir. T.H.J.J. van der Hagen,
voorzitter van het College voor Promoties,
in het openbaar te verdedigen op
donderdag 15 december 2022 om 15:00 uur

door

Matthijs Hendrik Jan DE JONG

Ingenieur in de Technische Natuurkunde,
Technische Universiteit Delft, Nederland
geboren te Gouda, Nederland.

Dit proefschrift is goedgekeurd door de

promotor: Prof. dr. S. Gröblacher
copromotor: Dr. R.A. Norte

Samenstelling promotiecommissie:

Rector Magnificus,	voorzitter
Prof. dr. S. Gröblacher,	Technische Universiteit Delft
Dr. R.A. Norte,	Technische Universiteit Delft
Onafhankelijke leden:	
Prof. dr. P. G. Steeneken,	Technische Universiteit Delft
Prof. dr. G. A. Steele,	Technische Universiteit Delft
Dr. W. Löffler,	Universiteit Leiden
Prof. dr. A. Schliesser,	University of Copenhagen, Denmark
Prof. dr. S. Schmid,	Technical University of Vienna, Austria

Nederlandse Organisatie voor Wetenschappelijk Onderzoek

Keywords: Silicon nitride microresonators, nanomechanics, optomechanics, mode coupling, frequency combs, noise cancellation

Printed by: Gildeprint

Cover: Laser light incident on Si_3N_4 trampoline membrane

Casimir PhD Series, Delft-Leiden 2022-34

ISBN 978-90-8593-543-8

An electronic version of this dissertation is available at
http://repository.tudelft.nl/.

To family

Contents

Summary

This thesis comprises several experiments involving silicon nitride trampoline membranes. These membranes are excellent mechanical resonators and can be fabricated with desirable optical properties. Their dynamical behavior, particularly the interaction of their mechanical motion with light, is of interest for optomechanics and sensing applications.

In the first experiment, I study the dissipation of trampoline membranes due to coupling to the substrate modes. It is known that the clamping of the substrate can affect the dissipation of its resonators, and this experiment provides a systematic investigation into this effect. The results show a clear reduction of mechanical Q-factor (increase of dissipation) when a resonator is resonant with a substrate mode. This highlights the design of the substrate modes for high-Q mechanical resonators.

In the second experiment, I study the appearance of mechanical frequency combs in trampoline membranes. The interaction of a standing wave light field with the silicon nitride membrane through the dielectrophoretic force is similar to an optical trap. If the mechanical motion is sufficiently large, the periodicity of that force creates perfect integer multiple copies of the original motion frequency, which form a frequency comb. This makes it possible to generate mechanical frequency combs using a simple setup with little technical requirements.

In the third experiment, I study the behavior of ringdown measurements involving near-degenerate modes. When both modes are within the detection bandwidth of the setup, their signal interferes and the ringdown displays 'ringing'. It is possible to extract the linear and non-linear parameters of both near-degenerate modes, and extract their relative coherence in the Brownian motion regime. This provides a characterization method for systems with near-degenerate mechanical modes.

In the fourth experiment, I study the interaction of two trampoline membranes with a single optical cavity mode. The optical field couples the mechanical motion of the two membranes, but with a time delay based on the cavity lifetime. The associated phase-shift of the mechanical responses causes destructive interference, which leads to mechanical noise cancellation. This could be used to improve sensors suffering from mechanical thermal noise, and is important when studying optomechanical multi-resonator interactions.

Samenvatting

Dit proefschrift omvat meerdere experimenten met trampoline membranen van siliciumnitride. Deze membranen zijn bijzonder goede mechanische resonatoren, en ze kunnen gemaakt worden met wenselijke optische eigenschappen. De dynamica van deze membranen, specifiek de interactie tussen hun beweging en licht, is interessant voor de optomechanica en voor toepassingen als sensor.

In het eerste experiment bestudeer ik de mechanische dissipatie van trampoline membranen door de koppeling met de beweging van het substraat. Het is welbekend dat het vastklemmen van het substraat van invloed is op de dissipatie van membranen, en dit experiment is een systematische studie van dit effect. De resultaten laten een duidelijke reductie in mechanische Q-factor zien (toename in dissipatie) wanneer het membraan resonant is met een resonantie van het substraat. Dit benadrukt het belang van de substraat resonanties voor mechanische resonatoren met een hoge Q-factor.

In het tweede experiment bestudeer ik mechanische frequentiekammen in trampoline membranen. De interactie tussen een staande lichtgolf en het silicium nitride membraan door de diëlektroforetische kracht is bekend van een optisch pincet. Als de mechanische verplaatsing groot genoeg is, zorgt de periodiciteit van de kracht voor heeltallige kopieën van de mechanische frequentie, die samen een frequentiekam vormen. Dit maakt het mogelijk om dit soort frequentiekammen te genereren met een simpele setup zonder veel technische vereisten.

In het derde experiment bestudeer ik aftrilmetingen van bijna-resonante trillingen. Als de frequenties van beide trillingen binnen de bandbreedte van het meetinstrument vallen, ontstaat er interferentie tussen de signalen en vormt er een specifiek patroon in de aftrilmeting, genaamd 'ringing'. Het is mogelijk om de lineaire en niet-lineaire eigenschappen van de individuele trillingen uit dit patroon te halen, evenals de relatieve coherentie van de trillingen in het regime van Brownse beweging. Dit effect creëert dus een manier om de eigenschappen van een systeem met bijna-resonante trillingen te karakteriseren.

In het vierde experiment bestudeer ik de interactie van twee trampoline membranen met een enkel optisch veld. Dit veld koppelt de mechanische bewegingen van de membranen, maar met een tijdsvertraging proportioneel aan de vervaltijd van de optische trilholte. De bijbeoherende fasevertraging tussen mechanische resonatoren zorgt voor destructieve interferentie, wat leidt uitdoving van de mechanische ruis. Dit effect kan potentiëel gebruikt worden in sensoren waar mechanische ruis een probleem is, en het is belangrijk voor verdere studie van systemen met meerdere optomechanische resonatoren.

1

Introduction

Physics is commonly divided by subject (e.g. classical mechanics, optics, thermodynamics, etc.), where a shared body of concepts and (theoretical) descriptions exists. This is convenient for investigating new parts of physics and improving on existing parts, but most importantly for communicating the results. It is the author's task to provide a clear terminology and explain conventions when necessary. This is easiest if there is a clear red thread for the reader to follow. In this work, the red thread is silicon nitride (Si_3N_4) trampoline membranes, which look like this:

→ ▫ ←

That small square is the actual trampoline design, printed to scale. It is approximately 800 µm by 800 µm, but the layer of ink on the page (2-3 µm [1]) is much thicker than the real thing (0.05-0.2 µm, typically). Since it is difficult to resolve the structure by the naked eye, there are some images taken with optical microscopes and scanning electron microscopes (SEMs) in Fig. 1.1. The trampoline membranes are suspended from the substrate, which makes them mechanical resonators with their first mode frequency around 100 kHz[1] and they are good resonators: They have a high quality factor (Q-factor). The Q-factor corresponds to the rate a resonator loses (dissipates) energy, and how long it will vibrate once struck. For comparison, most musical instruments are also good resonators and reach Q-factors of $10^3 - 10^4$, but trampoline membranes can reach 10^8 at room temperature.

The development of these membranes came from the desire to have lightweight, mechanically compliant mirrors from the field of optomechanics. At that time (around 2010), cavity optomechanics [2] was a fast growing field studying the interaction of mechanical motion with light. To see the effect of light on the motion of a mechanical element, that element must be 1) lightweight, 2) a good mechanical resonator, and 3) a good optical reflector. However, lightweight objects that

[1] In perspective: This frequency is 5 times higher than the upper bound of human hearing.

are good mechanical resonators are often bad reflectors, and vice versa. A potential way around this issue is to combine a good optical reflector made out of one material with a good mechanical resonator made out of another. For example, a micrometer-sized Bragg mirror resting on top of a doubly clamped Si_3N_4 beam [3] will have a high reflectivity while the mechanical Q-factor can still be significant. This system can have strong coupling between the optical (cavity) resonator and the mechanical motion [4]. An alternative route is to use two mechanically rigid mirrors to form a good optical cavity and insert a mechanically compliant element between them. This 'membrane-in-the-middle' approach separates the optical and mechanical parts, and can also realize strong coupling between light and motion [5].

While the integration of Bragg mirrors with mechanical elements saw some improvements in performance [6], the membrane-in-the-middle approach advanced quickly. Square silicon nitride membranes were already commercially available[2], mainly as x-ray diffraction windows or substrates for transmission electron microscopy. The mechanical properties of these membranes make them excellent mechanical resonators, particularly if they are made from stoichiometric Si_3N_4 with a high tensile stress [7, 8]. This stress effectively dilutes the dissipation (damping) and thus increases the mechanical Q-factor. While Si_3N_4 natively has beneficial optical properties for telecom wavelengths (low absorption at 1550 nm), it is possible to improve the reflectivity of these membranes by creating a (subwavelength-size) pattern in the Si_3N_4 [9–12], which forms a diffraction grating or photonic crystal. This ability to simultaneously and independently engineer the mechanical and optical properties culminated in the trampoline design of the Si_3N_4 membranes [13, 14], on which this thesis is based.

These membranes, and their combination of optical and mechanical properties, were a resource for many tantalizing proposals within optomechanics. Three examples: Firstly, to transport a quantum state from one microwave qubit in one dilution refrigerator to another, thus forming a quantum internet, requires suitable transduction from microwave to optics [15]. Si_3N_4 membranes could serve as a mechanical intermediary to reliably transduce these quantum states, and this has been an major direction of the field [16–20]. Secondly, these membranes can be used as force or acceleration sensors that are limited only by quantum noise [21–23]. This could allow detection of single spins, but could also be used for sensing of dark matter [24–26]. Thirdly, membrane resonators are among the heaviest objects to reach the quantum regime of motion [27–29]. Together with their long coherence times, this makes them a viable candidate to search for signals of gravitational decoherence [30–32].

Two different proposals were part of the rationale behind this thesis. It was theorized that arrays of trampolines could have enhanced optomechanical coupling for the breathing modes of the mechanical resonators [33]. The optomechanical coupling rate g_0 (units of Hz) governs and restricts many interesting optomechanical effects, and the search for this enhanced coupling was the basis of works done by colleagues [34–36] and others [37]. Additionally, the high mechanical Q-factor, isolation from the environment, and optomechanical cooling capabilities [38] could

[2] E.g. from Norcada, Silson, Labtech and others.

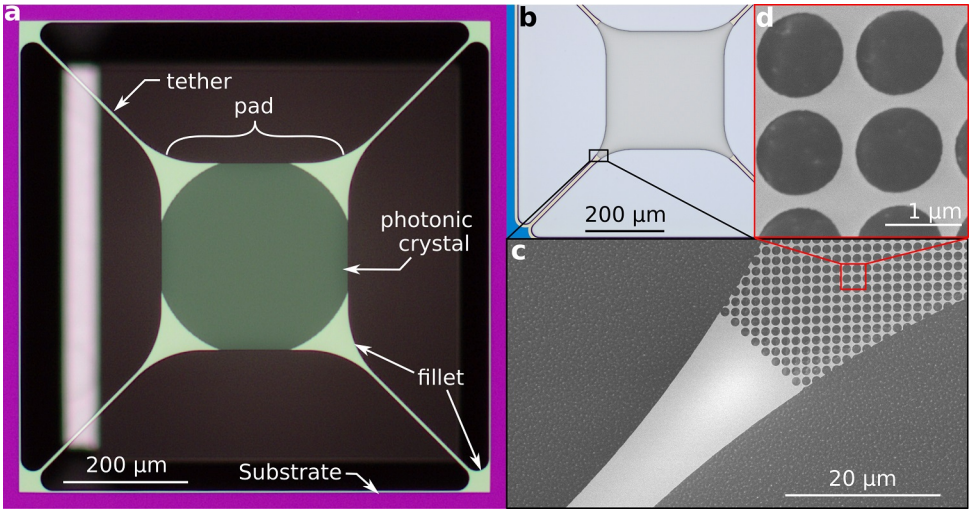

Figure 1.1: **a**: Microscope image of Si_3N_4 trampoline membrane suspended over a hole through the chip. The magenta frame color is due to thin-film interference effects. The center of the membrane is patterned with a photonic crystal, forming a differently-colored circle. **b**: Microscope image of slightly different design trampoline membrane, suspended over a shallow (~ 20 µm) hole. Different Si_3N_4 film thickness causes the blue color of the outside frame. **c**: Electron microscope image of membrane corner, where the tether meets the membrane pad. The periodic pattern of holes is the photonic crystal. **d**: Electron microscope image of the photonic crystal. The holes and their spacing are similar in size to the wavelength, which causes interactions with light that let us control the reflection and transmission of the membrane.

allow room-temperature quantum operation of the mechanical resonators. This would avoid costly and complicated cryogenics, at a cost of stringent mechanical requirements [13, 39, 40]. Others have been working towards this goal in different systems or using different mechanisms, see e.g. [41].

The dynamical behavior of our trampoline membranes proved to be different than expected, particularly in arrays or when interacting with light. Along the way of our original goals, other effects were found that were interesting in their own right, and those form the majority of the content of this thesis. As of writing, the investigation into enhanced coupling is still in progress, as is the research into room-temperature ground-state optomechanics.

Trampoline membranes

The Si_3N_4 trampoline membranes used throughout this work are not all precisely the same, but their designs are similar enough that they should be introduced here. Much of the design and fabrication processes were developed in earlier works [13, 34–36].

In general, the membranes are made out of a thin Si_3N_4 layer ($20 - 350$ nm) deposited on a much thicker silicon substrate ($100 - 1000$ µm). The Si_3N_4 can be grown in such a way that it has a high tensile stress, typically 1 GPa. We can pattern

the Si_3N_4 like a trampoline, consisting of a large central pad connected to a rigid frame by thin tethers, Fig. 1.1**a**. By etching away the silicon substrate underneath, we can then suspend the trampoline. Depending on the precise fabrication process used, this under-etch either goes all the way through the substrate (Fig. 1.1**a**) or only about $\sim 20\,\mu m$ (Fig. 1.1**b**).

To facilitate the under-etching, there is a periodic array of holes patterned into the pad. If we design the size and spacing of these holes correctly, they can interact with light of specific wavelengths and form a photonic crystal Fig. 1.1**c,d**. This gives us control over the reflectivity of our membrane to light of specific wavelength, so we can engineer the optical characteristics of the membrane. Since the holes are so small compared to the membrane motion of interest, they do not significantly impact the mechanical dissipation. For the dissipation, the interfaces between central pad, tether and substrate are more important. To control the distribution of the bending and the stress, we pattern fillets at both ends of the tether. This completes the general features of the trampoline membrane design.

Thesis outline

In chapter 2, there will be a brief introduction of relevant concepts, models and the experimental setup. We will start with the harmonic oscillator and the relation between decay rate and Q-factor. Then we will see how to model Si_3N_4 membranes using the finite element method and how to simulate their Q-factor. After that, we will describe the setup used for double-membrane experiments and introduce the frequency stabilization scheme. The chapter closes with a brief introduction of optomechanics for one and two membranes.

Chapters 3-6 are the main scientific content of this thesis, and are published works or in preparation. In chapter 3, we explore the interaction between the mechanical modes of the membrane and the substrate, and show that this interaction can reduce the Q-factor of the mechanical mode. Then, in chapter 4 we discover a new mechanism to generate a mechanical frequency comb based on the interaction between a membrane mode and its optical environment. Afterwards, in chapter 5 we report on an interference mechanism in the (optical) detection of near-degenerate mechanical modes. Finally, in chapter 6 we find that the cavity induces a time-delay in the effective interaction between two mechanical resonators. This causes interference that leads to cancellation of the mechanical noise.

There will be a short conclusion, with some outlook towards future and further work. This is followed by the final and most important part, the acknowledgments.

2

Background

2.1. Theoretical description

There are some useful relations and concepts that are worthwhile to highlight here. These include the harmonic oscillator, its frequency and decay rate and the link to the frequency spectrum and Q-factor. The harmonic oscillator is commonly treated in introductory textbooks (e.g. chapter 13 of [42]), but I found it helpful to revise them during this project.

2.1.1. Harmonic oscillator

Let us start by posing the equation of motion for a damped and driven harmonic oscillator,

$$\ddot{x} + \gamma\dot{x} + \omega_0^2 x = F_\mathrm{d}(t)/m_\mathrm{eff}. \tag{2.1}$$

This equation describes the position of a mechanical resonator as a function of time, $x(t)$, and its two derivatives with respect to time, velocity ($\dot{x}$) and acceleration ($\ddot{x}$). It contains two properties of our resonator, the decay rate γ and angular frequency ω_0, and a way for us to drive the resonator through force $F_\mathrm{d}(t)$. Note that we have divided out the effective mass m_eff of our resonator, which relates the spring constant k via $\omega_0 = \sqrt{k/m_\mathrm{eff}}$ if one considers a mass-on-a-spring model of a harmonic oscillator.

For practical reasons, we are often interested in the spectrum (i.e. the frequency components) of a resonator's motion more than in its position at every time $x(t)$. We typically have experimental access to the power spectrum $|x(\omega)|^2$ (power spectral density, units [W/Hz]). An example is shown in Fig. 2.1**a**, where we simulate the power spectrum.

To obtain the power spectrum analytically from Eq. (2.1), we use a Fourier transform to get

$$(\omega_0^2 + i\gamma\omega - \omega^2)x(\omega) = F_\mathrm{d}(\omega)/m_\mathrm{eff}, \tag{2.2}$$

where $x(\omega)$ and $F_\mathrm{d}(\omega)$ are the Fourier transforms of $x(t)$ and $F_\mathrm{d}(t)$ respectively. Since power is amplitude squared, we can obtain the power spectrum of $x(\omega)$ in

terms of our driving force and oscillator properties,

$$|x(\omega)|^2 = \frac{|F_\mathrm{d}(\omega)|^2/m_\mathrm{eff}^2}{(\omega_0^2-\omega^2)^2+\gamma^2\omega^2}. \tag{2.3}$$

In the regime $\gamma \ll \omega_0$, the power spectral density has a sharp peak around $\omega = \sqrt{\omega_0^2-(\gamma/2)^2}$. A common approximation is to consider the spectrum around the peak as a Lorentzian (orange line in Fig. 2.1)[1]. In Fig. 2.1, we take $\omega_0 = 2\pi \times 12410$ Hz, $\gamma = 2\pi \times 1$ Hz so we are well within this limit, and the Lorentzian closely approximates the power spectrum around the peak at ω_0. Formally, this gives us

$$|x(\omega)|^2 = \frac{|F_\mathrm{d}(\omega)|^2}{(2m_\mathrm{eff}\omega_0)^2}\frac{1}{(\omega-\omega_0)^2+(\gamma/2)^2}. \tag{2.4}$$

The center frequency ω_0 and full-width at half maximum (FWHM) γ of the Lorentzian peak are useful and quick measures of the oscillator properties. These are marked in the inset of Fig. 2.1**a**, with the half-maximum in logarithmic scale being at -3 dB.

2.1.2. Q-factor

For resonators with small decay rates compared to their resonance frequency, it is common to refer to the quality factor (Q-factor, [44]) rather than the decay rate. There are several definitions for the Q-factor, and it is useful to link them to the harmonic oscillator properties. One can define the Q-factor based on the bandwidth of the peak,

$$Q = \frac{\omega}{\gamma}, \tag{2.5}$$

which links the peak width in the power spectrum of Fig. 2.1 to the decay rate of the harmonic oscillator in Eq. (2.1). For the values of the harmonic oscillator above, $Q = 12410$. Equivalently, the Q-factor can be defined as the ratio of stored and dissipated energy per cycle of the oscillator,

$$Q = 2\pi \times \frac{\text{Stored energy}}{\text{Dissipated energy per cycle}}. \tag{2.6}$$

For resonators with sufficiently high Q-factor, the spectral peak can become difficult to resolve and the dissipated energy per cycle provides an easier measure. This can be probed by performing a ringdown measurement, whereby an oscillator is driven at its resonance frequency until it has reached steady state, and then left to decay naturally.

A simulated example of a ringdown measurement is shown in Fig. 2.1**b,c**. We start from an initial position $x(t=0)=1$, $v(t=0)=0$ with the drive off, $F_\mathrm{d}=0$. The displacement over time is plotted in Fig. 2.1**b**, which shows an exponential decay. The amplitude of the displacement envelope is fitted with $e^{-\gamma t/2}$ (orange).

[1] Consider the small frequency range ε around ω_0: $\omega = \omega_0+\varepsilon \to \varepsilon = \omega-\omega_0$. Then $(\omega^2-\omega_0^2) = (\omega+\omega_0)(\omega-\omega_0) \simeq 2\omega_0\varepsilon = 2\omega_0(\omega-\omega_0)$ and $i\omega\gamma \simeq i\omega_0\gamma$. Per §26 of Ref. [43].

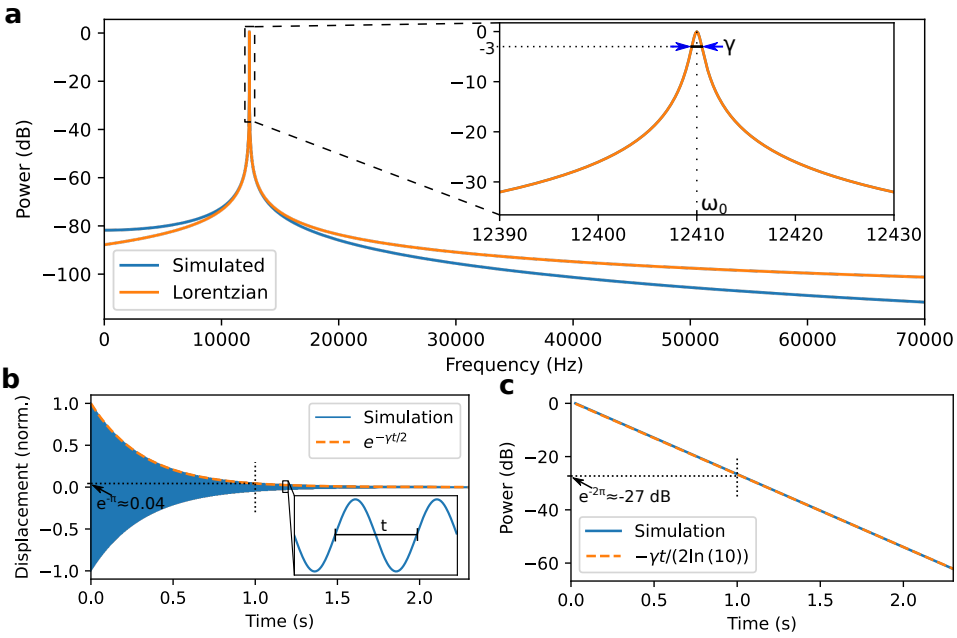

Figure 2.1: **a**: Power spectrum of a harmonic oscillator, simulated (blue) and with a Lorentzian approximation (orange). Inset shows the peak at ω_0, with linewidth γ, the full-width half maximum indicated at the -3 dB point. **b**: Displacement of the oscillator from initial conditions, and Fourier-transform of the spectrum shown in **a**. Inset shows the periodicity of the signal, with period $t = 2\pi/\omega_0$. Dotted lines indicate time where the displacement amplitude has decayed to $e^{-\pi}$ times the original value. **c**: Decay of displacement power, from the same simulation as **a,b**. Dotted lines indicate the time where the power has decayed to $e^{-2\pi}$ times the original value (-27 dB).

After $\gamma/2\pi$ seconds, the amplitude has decayed to $e^{-\pi} \simeq 0.04$ times the original value. Equivalently, this amplitude is reached after Q oscillations.

Since we are interested only in the power of the resonator, we do not need to resolve each oscillation and can detect resonantly: Monitoring the power via e.g. a spectrum analyzer or lock-in amplifier. When plotting the power in logarithmic scale, the exponential ringdown of Fig. 2.1**b** becomes the linear signal of Fig. 2.1**c**. We can relate the slope a of the linear fit ($y = at + b$ for time t, plotted in orange) to the exponential decay and to the Q-factor. In other words,

$$Q = \frac{\omega}{-2a\ln(10)} \tag{2.7}$$

where the factor $\ln(10)$ comes from the conversion between exponential decay (base e) and the logarithmic scale (base 10). After $\gamma/2\pi$ seconds, the power has decayed to $e^{-2\pi} \simeq 0.0019$, or -27 dB.

2.1.3. Thermal driving

The power spectrum we have shown so far has been given in relative units, dB. In most commonly used measurement setups, there is no direct access to the actual

mechanical displacement. Instead, light is used such that the mechanical displacement introduces phase fluctuations of the reflected light, which are then converted into amplitude changes via an interferometer. These can be detected via a photodetector, and be read out via e.g. an oscilloscope or a spectrum analyzer. All these steps in the detection path mean that, e.g. 0 dB measured power does not necessarily correspond to 1 µm displacement, and needs to be calibrated instead. One way to do this is to use the thermal Brownian motion of a mechanical resonator [45].

The thermal motion of a resonator (motion due to thermomechanical noise) has a specific spectral form (flat i.e. white spectrum) and a well-defined amplitude if the temperature is known. Using this noise to calibrate the amplitude of motion of a resonator thus makes the assumption that the mode of interest is well-thermalized to the environment. In a room-temperature setup where there is negligible optical absorption and no other noise sources close to the frequency of interest, this is a good assumption. By using the equipartition theorem, we can link the well-defined thermal energy $\frac{1}{2}k_{\mathrm{B}}T$ to the displacement power integrated over all frequencies,

$$\frac{1}{2}k_{\mathrm{B}}T = \frac{1}{2}m_{\mathrm{eff}}\omega_0^2\frac{1}{2\pi}\int |x(\omega)|^2\mathrm{d}\omega. \tag{2.8}$$

Since thermal noise is spectrally flat, it does not depend on frequency, $|F_{\mathrm{d}}^{\mathrm{th}}(\omega)|^2 = |F_{\mathrm{d}}^{\mathrm{th}}|^2$ and [45]

$$\frac{1}{2}k_{\mathrm{B}}T = \frac{\left|F_{\mathrm{d}}^{\mathrm{th}}\right|^2\omega_0^2}{2\pi m_{\mathrm{eff}}}\int \frac{\mathrm{d}\omega}{(\omega^2-\omega_0^2)^2+\gamma^2\omega^2}. \tag{2.9}$$

By integrating [45, 46], we get an expression for $\left|F_{\mathrm{d}}^{\mathrm{th}}\right|^2$, which reads

$$\left|F_{\mathrm{d}}^{\mathrm{th}}\right|^2 = 4k_{\mathrm{B}}Tm_{\mathrm{eff}}\gamma. \tag{2.10}$$

This expression thus allows us to relate the integral over $|x(\omega)|^2$ to parameters of the environment and resonator itself, thereby allowing calibration of our system.

The only parameter in Eq. (2.10) that we cannot measure (easily) is the effective mass m_{eff}. In principle, the definition of the effective mass is arbitrary, however our use of the equipartition theorem implies a particular definition already [45]. This follows from the total potential energy of any mechanical mode,

$$U = \frac{1}{2}\omega_0^2 m_{\mathrm{eff}}|x(t)|^2. \tag{2.11}$$

which we use in Eq. (2.8). For a mechanical mode with normalized mode shape $\vec{r}(\vec{x})$ with mass distribution $\rho(\vec{x})$, the effective mass is given by

$$m_{\mathrm{eff}} = \int \rho(\vec{x})|\vec{r}(\vec{x})|^2)\mathrm{d}V. \tag{2.12}$$

This requires knowledge of the normalized mode shape $\vec{r}(\vec{x})$ across the domain V, which generally requires finite element method simulations (see Sec. 2.2.1). Nonetheless, it is possible to calibrate the mechanical displacement in the thermal motion limit.

2.2. Silicon nitride membranes

Si_3N_4 membranes are versatile structures useful for x-ray windows [47], transmission electron microscopy substrates [48], nano-calorimeters [49] and as high-Q mechanical resonators [7]. In this thesis, we focus on the latter. First, we introduce the mechanical models used throughout this work, and then we briefly cover some dissipation mechanisms.

2.2.1. Membrane models

To understand the dynamical behavior of trampoline membranes, we build a model in the commercial finite-element package COMSOL. The chapters 3, 4, 5, and 6 all use variations or results of this model, and the relevant parts and specifics are reported there. In this section, we first treat the basics of the model, and then discuss some variations and results that did not make it into any of the other chapters.

We show the model in Fig. 2.2. It consists of a 3D part representing the Si chip, and a 2D part that forms the top Si_3N_4 boundary and the suspended trampoline membrane. Others [14, 50, 51] typically only consider the 2D suspended trampoline part. Treating the trampoline boundaries as fixed gives correct mode shapes and frequencies, but it does not take into account any interactions with substrate modes (see chapter 3). This is particularly relevant when high mechanical Q-factors are desired and the interaction with the substrate can be affected by the shape and size of the membrane tethers [13, 52–54]. Because Si_3N_4 chemically bonds to the Si chip during fabrication, their interface can be modeled as parallel boundaries. There is little risk of delamination, and negligible friction from relative shifting of the layers.

In Fig. 2.2**b**, we show a zoom of the suspended trampoline membrane. The center part of the membrane has a photonic crystal, a periodic array of holes. They can be taken into account by locally reducing the effective density of the material ('PhC-Si_3N_4'), while keeping the other material properties constant. This significantly simplifies the model. Furthermore, the trampolines typically are symmetric along two axes (dashed lines in Fig. 2.2**b**), which can be used to reduce the simulation domain further. Finally, the mesh must be fine where the mechanical modes sharply change near the tether foot (Fig. 2.2**c**), but can be coarse everywhere else. These simplifications allow the model to be run on a decent laptop in less than 5 min rather than requiring time on a computing cluster.

We can simulate a small part of the membrane fully 3D, Fig. 2.2**d**, by fixing the number of elements along the thickness of the Si_3N_4 to 5. We effectively simulate a pre-stressed string by applying a symmetry condition on the bottom right interface. Interestingly, the model predicts a static out-of-plane displacement of $\lesssim 15\,\mathrm{nm}$ (exaggerated in Fig. 2.2**d**). In general, an out-of-plane gradient of the tensile prestress is considered to be responsible for curving of cantilevers [52]. However, no such gradient is present for the model of Fig. 2.2**d**. The displacement could originate from the asymmetry of the Si_3N_4, as the bottom face is connected to the substrate while the top face is free. It is experimentally challenging to verify such a small, static displacement over such a large distance, due to the requirements of parallelism and flatness of the sample and measurement setup.

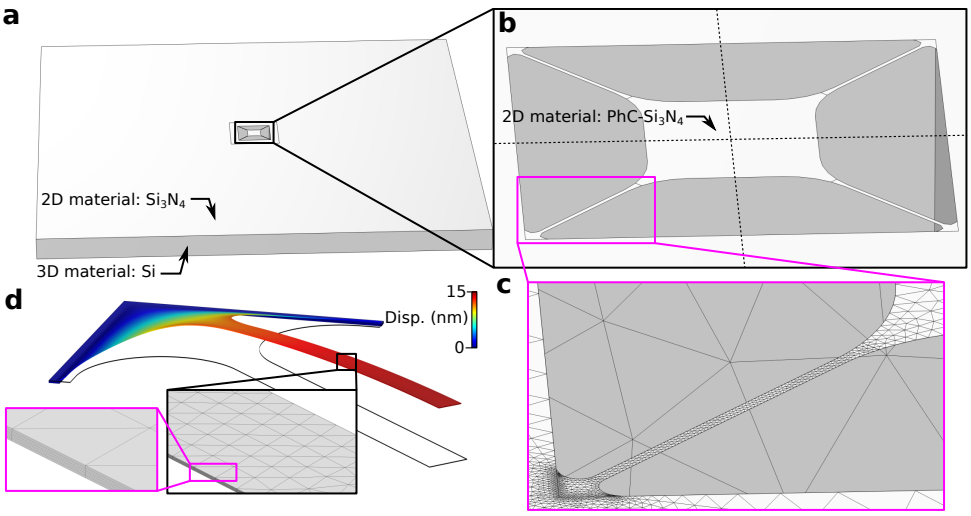

Figure 2.2: **a**: Overview of simulated domain of a Si_3N_4 trampoline membrane on a Si chip. The top layer is treated as a 2D material, Si_3N_4. **b**: Zoom of the 2D membrane. The center area has a different 2D material, with reduced mass due to the photonic crystal holes. Dashes lines indicate symmetry axis that can be used to reduce the simulation domain and time. **c**: Mesh of the photonic crystal membrane tether, showing at least three elements across the width of the tether, with more at the tether foot and less further away from the tether. **d**: Static displacement simulated for 3D Si_3N_4, showing a slight ($\lesssim$15 nm) out-of-plane displacement. This simulation uses 5 elements across the thickness (inset), treated as separate layers with identical pre-stress.

2.2.2. Membrane Q-factor

The property of trampoline resonators that garnered the most interest has been their Q-factor. There have been many studies involving different resonator and substrate geometries, materials and probing different loss mechanisms. The full scope of the question of how to build the mechanical resonator with the highest Q-factor is well beyond the scope of this thesis; This would require considerations of different materials, studies of all the loss mechanisms and optimized design strategies. However, for Si_3N_4 trampoline resonators, we can contribute a small piece of the puzzle.

Dissipation dilution

Si_3N_4 is unique among the amorphous materials (glasses) because it was the first to reach dissipation as low as in crystalline solids. Previously, all amorphous solids reached a plateau in dissipation at low temperature ($\sim$ 10 K), where their Q-factor would be between 10^3 and 10^4 [55, 56]. Their poor performance compared to similar resonators made from crystalline materials (reaching Q-factors of $10^7 - 10^8$) was quantitatively explained by atoms tunneling between different positions in the material [55]. This gave rise to the universality of the dissipation plateau, regardless of amorphous material composition or resonator geometry.

Thin-film Si_3N_4 can be manufactured to have a large tensile pre-stress (see e.g. [57]), which led to doubly-clamped beams with Q-factors of 10^5 [58]. The

tensile stress is key, as it leads to dissipation dilution [59], which can be seen as follows: Imagine a (guitar) string clamped on both sides, which we excite to have a certain amplitude and energy. The dissipation (energy loss) due to bending is proportional to the amplitude (energy). By adding tensile stress, the same energy will have less amplitude (it is more difficult to bend a tight guitar string out of plane than a loose one), leading to less dissipation. More detailed explanations can be found from other sources, e.g. [60].

Loss mechanisms

There are many different dissipation mechanisms known to affect the Q-factor in Si_3N_4 trampoline resonators, but some are more relevant than others: Gas damping can be largely excluded by operating in a good vacuum as long as $Q < 10^9$ [61] (practical limit, 10^{-9} mbar vacuum for ~ 100 kHz resonators). Thermoelastic damping is reduced in high-stress membranes by dissipation dilution[2]. The remaining, relevant, damping mechanisms can be divided in two categories: damping that happens within the Si_3N_4 (bending loss [59, 62–64]), and damping that happens within the substrate. Energy from the resonator can travel to the substrate via e.g. acoustic loss [65] or phonon tunneling [54, 66]. The leaking of energy from resonator to substrate is motivated due acoustic wavelength being larger than the resonator itself (typically). However, this this wavelength ($\simeq$40 mm for 150 kHz in Si) is also larger than the substrate in many cases (10×10 mm^2), so why only consider the substrate? The connection of the substrate to e.g. a sample holder is known to have have an effect on the Q-factor [54, 62, 67–70], so it makes sense to include it as a possible loss vector.

Modeling the interface between a Si substrate and a (typical) stainless steel sample holder is difficult. Tape, glue or other bonding materials typically have high losses, so the chip is clamped by gravity alone. This makes the interface highly nonlinear, since motion of the chip is restricted one way (down) but not the other (up). We can assume a spring foundation, with the material parameters of stainless steel (Young's Modulus $E = 295$ GPa, Poisson's ratio $\nu = 0.29$), a thickness of 10 mm and viscous damping with some (fit) constant. This is a simple model, but it suffices for a quick comparison with simple models for isotropic loss in Si_3N_4, $\eta_{\mathrm{SiN}} = 10^{-7}$ [71] or in the Si, $\eta_{\mathrm{Si}} = 10^{-4}$ [62, 68].

We can compare the different models against experimental data from [13], as we show in Fig. 2.3. The thicknesses of Si chip and Si_3N_4 layer are varied in Fig. 2.3**a**. Two loss models, isotropic Si loss and acoustic loss, share the same trend as the data, while isotropic Si_3N_4 loss does not. However, the chosen isotropic loss parameter is high, considering single-crystalline Si typically has exceedingly good mechanical properties [72]. Additionally, the simulated Q-factors for this loss parameter are two order of magnitude higher than the observed Q-factors (all simulated curves in Fig. 2.3 are rescaled to fit the data). The simulation considering only acoustic loss from substrate to sample holder has the same trend, realistic properties of that sample holder and only a small (0.2) scaling factor. This suggests that

[2]There is an unpublished, formal derivation by Prof. D.E. Chang available upon request.

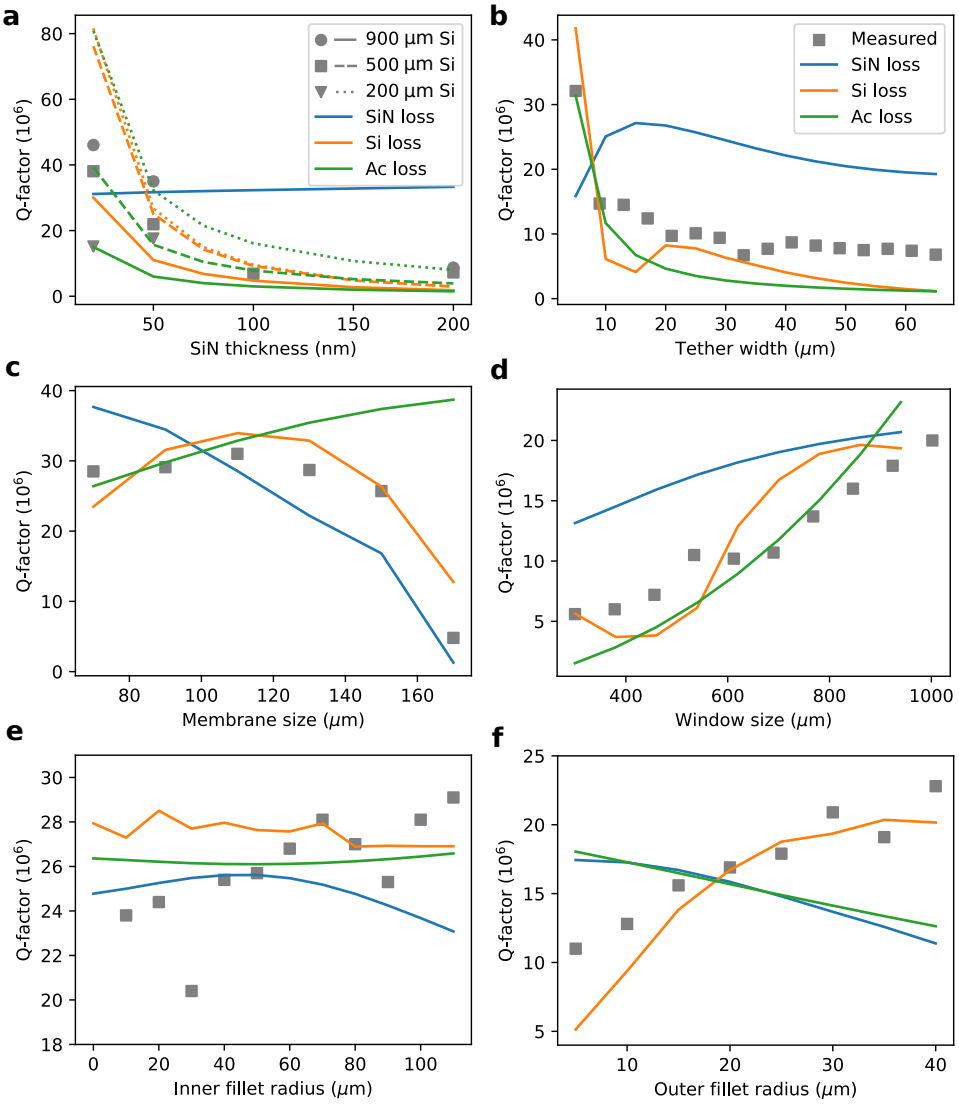

Figure 2.3: Measured and simulation Q-factor of membrane for different loss mechanisms and design parameters. Experimental data taken from [13]. Colors indicate loss mechanism (in Si_3N_4, in Si, and acoustic). **a**: Q-factor depending on thickness of the Si_3N_4 layer and the Si chip (solid: 900 µm, dashed: 500 µm, dotted: 200 µm). Q-factor depending on **b**: tether width, **c**: membrane size, **d**: window size, **e**: inner fillet radius, **f**: outer fillet radius.

acoustic loss through the chip to the outside world can be as important as loss of the Si substrate itself.

By changing the design parameters of the membrane, we can further compare the loss mechanisms. While the same pair of Si loss and acoustic loss fit well to the results of the tether width sweep (Fig. 2.3**b**), this is not true for the other sweeps. For the membrane size (Fig. 2.3**c**), both Si_3N_4 and Si loss fit decently, for the window size (Fig. 2.3**d**), all three show a similar trend, for the inner fillet radius (Fig. 2.3**e**) neither matches while for the outer fillet radius (Fig. 2.3**f**) only the Si loss shows some agreement to the data. This thus only shows that there is probably not one single loss mechanism that is dominant in all cases, or is affected by all design parameters. By systematically investigating different structures, in different parameter regimes, it should be possible to build a better understanding and consistent model of the losses and Q-factor in these trampoline membranes or mechanical resonators in general.

2.3. Optomechanical setup

One of the main goals of this thesis was to develop a setup that could be used to study multi-membrane optomechanics. This followed the development of a fabrication procedure [36] and systematic investigation into the mechanical [13] and optical [34, 35] properties of multi-membrane devices. At that time, other groups had performed similar studies [73, 74], and even achieved first experimental results of increased coupling [37] and state transfer [75]. The main experimental challenge was to operate the setup such that the laser and cavity frequencies are stabilized ('locked') together. Our results towards this goal are described in this section, and in chapter 6.

Since then, other groups have achieved similar progress, and shown important experimental results. These include the nonlinear dynamical behavior of the membranes, e.g. synchronization [76, 77] and phononic low-pass filters [78], cavity-controllable thermal transport [79] that can be used as a heat engine [80] and non-Hermitian dynamics [81].

2.3.1. Fabry-Pérot cavity

The setup is based on a free-space Fabry-Pérot cavity. This is a common type of optical cavity consisting of two mirrors facing each-other, first developed over a century ago [82]. The optical field strength between the two mirrors is enhanced compared to the input optical field from a laser, which is a common method of enhancing the optomechanical interaction (see [2] and references therein). The membranes or other structures we want to investigate are then inserted between the two mirrors such that they interact with the light.

We show a render of the setup design in Fig. 2.4**a**. The left panel shows a cut-through of the structure, with the laser path highlighted in green. Between the two mirrors (blue) the cavity field is enhanced. The mirrors are fixed to a single steel part, the cavity monolith, to reduce their relative motion [83]. This means the optical access to the cavity is through a threaded hole drilled all the way through

the monolith. Each mirror is encapsulated in a stack of threaded metal rings and Viton gaskets, to coarsely position them along the optical axis of the threaded hole. The bottom mirror also rests on a cylindrical piezo stack (Noliac NAC2123-H06, with through-hole) to more finely tune its position. Further along the beam axis, there are two lenses to aid in matching the incident beam to the cavity mode.

The precise placement of the membranes within the optical cavity is crucial [35, 67]. But especially for multi-membrane structures, the tip and tilt positioning of the device are more important than its position along the optical axis. Our setup features 5-axis control (x, y, z, tip, and tilt, see Fig. 2.4**a**) by combining three stages. Below the sample holder, there is an x-y stage (Optosigma TSDS-402SFP) with two open-loop motors (Newport Picomotor UHV). These give us 12.7 mm travel range, enough to scan across the whole chip. Directly below the chip, there is a piezo (another Noliac NAC2123-H06) that can move 6 µm along the z-axis. There is a mirror mount that functions as a tip-tilt alignment stage (Siskiyou IXF2.0tss). The mass resting on this stage is significant, and to avoid problems with long-term stability of the tip-tilt stage (sliding), a counterweight was added. This ensured the center of mass of the assembly was close to the middle of the tip-tilt stage. Finally, the tip-tilt state rests on the bottom part of the cavity monolith, which is fixed to the flange of the vacuum chamber.

The chip is mounted to the sample holder by gravity, as clamps can reduce the mechanical Q-factor (see chapter 3). In this setup, we empirically found that the clamp reduces low-frequency noise (<1 kHz), but drastically increases noise at higher frequencies. In particular noise at 30 kHz and multiples is dominant when the sample is clamped, likely due to more efficient coupling of a piezo resonance mode (which is at that frequency). To achieve some damping of low-frequency modes without overly increasing the noise around the piezo modes, a clamp was left resting on the chip with a Viton ring but not screwed into the sample holder (Fig. 2.4**b**); the additional mass fixes the sample such that it does not move when aligning the chip in the cavity, but the connection is not so rigid that the 30 kHz tones dominate.

The chips used in this work are 10×10 mm^2 silicon chips covered on both sides with a thin (50-200 nm) Si_3N_4 layer. Their fabrication process is described in much more detail elsewhere [36]. An example chip is shown in Fig. 2.4b), which was measured extensively in chapter 6. It contains 9 750×750 µm^2 holes, one of which is empty (through-hole) and used for alignment of the beam and empty cavity measurements. Two spots contain only a single membrane and the remaining six have membranes on both sides of the chip. In the figure, three of the six double-membrane stacks have collapsed, which typically happens due to dirt in the fabrication process.

We have optical access through the bottom of the cavity, via an optical window in the vacuum flange. To couple to the longitudinal modes of the cavity (and avoid coupling to the transversal modes), we matched the beam size and shape to the cavity mode. For that, we used two mode-matching lenses and two alignment mirrors (Fig. 2.4**c**). The positioning and focal distance of the lenses required to achieve good mode-matching to the cavity can be calculated using commercial

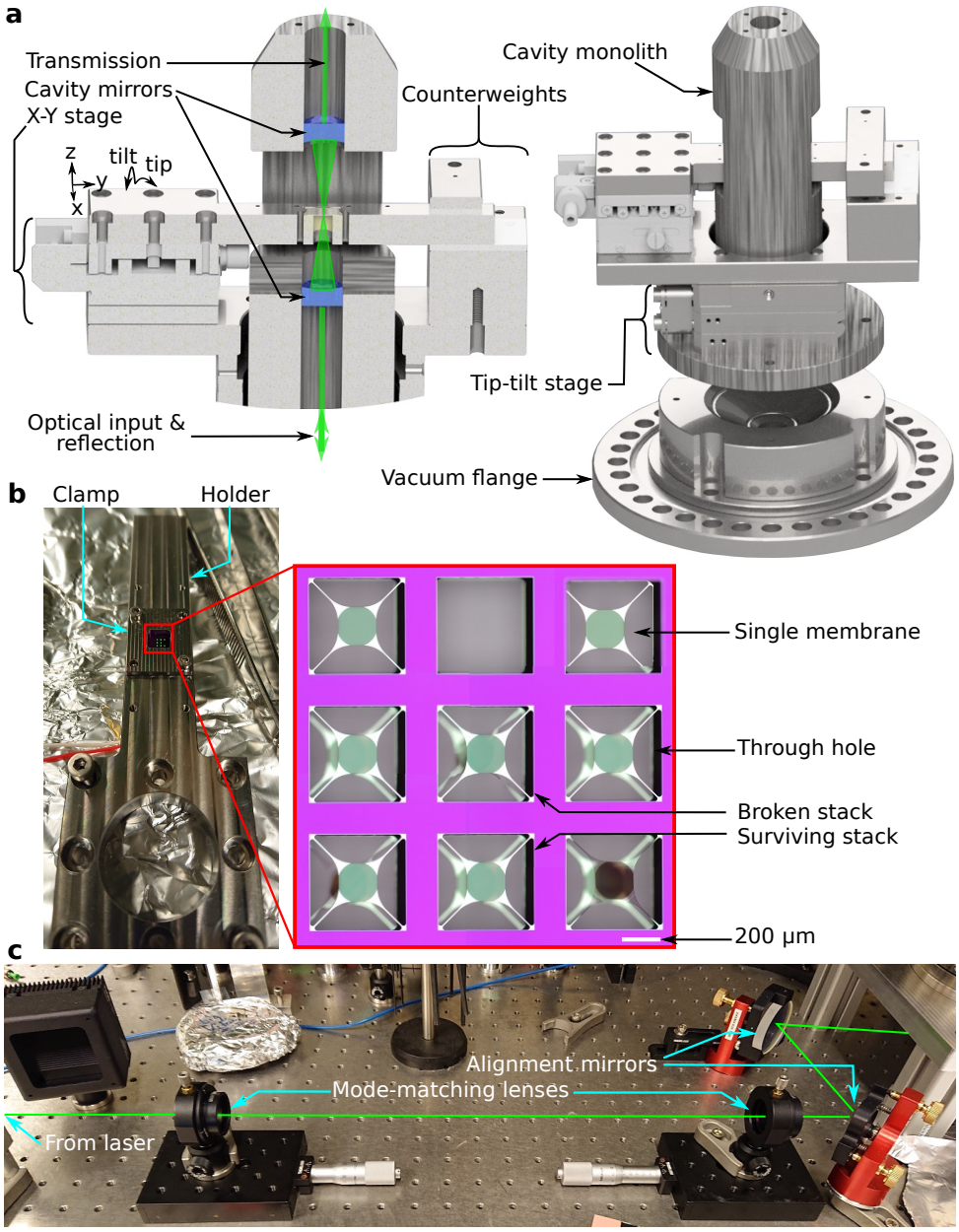

Figure 2.4: **a**: Renders of monolithic Fabry-Pérot cavity showing mirrors and optical path in cut-through (left) and full structure as mounted in the vacuum chamber (right). **b**: Sample holder with double-membrane sample mounted. Shown is a stitched microscope image of a double-membrane chip with three surviving double-stacks. **c**: Optical (free-space) path for beam aligning and mode-matching to the cavity.

software, e.g. JAMMT[3].

2.3.2. Locking the cavity

The main experimental difficulty of a free-space optical cavity with multiple membranes is operating it at the resonance frequency ('locking'). Thermal noise, electrical noise and other perturbations can shift the position of the cavity mirrors, which shifts the cavity resonance frequency. To use the optical field enhancement by the cavity, and study the optomechanical response of the membranes, we must be close to the resonance frequency. The detuning Δ, which is the difference between the laser and cavity frequencies, impacts many optomechanical effects (e.g. cooling, heating). There are two main avenues to facilitate frequency locking between cavity and resonator. The first is to passively reduce effects that can shift either cavity or laser frequency, while the second is to actively control either of the two frequencies to match the other.

Passively reducing the frequency shifts mainly relates to the cavity, as the laser (NKT Adjustik C15) already has good stability. To estimate the stability of the cavity, consider a 50 mm Fabry-Pérot cavity with a target linewidth $\kappa = 2\pi \times 150$ kHz. For this system, a position shift of only 38 pm (picometer!) of one of the mirrors corresponds to a shift in resonance frequency by a full linewidth κ. Only the relative motion between the mirrors is of importance, so the frequency stability can already be improved by integrating the mirrors in a single steel piece [83]. This means dominant contribution of noise in our setup comes from the piezo stacks used to fine-tune the mirror positioning.

We can calculate an example to show the limits of the passive frequency stability of the cavity. The piezo stack below the mirror has a stroke of about 6 µm for 150 V input, so 38 pm corresponds to 0.95 mV. But the constraint on voltage noise is tighter than this: to successfully lock the frequencies for longer times, the maximum tolerable shift should be much smaller than κ. If we can allow for $\kappa/10$ shifts due to noise, the constraint becomes 95 µV. This is close to the performance of our low-noise amplifier (Falco WMA200, 50 μV_{RMS}) or our programmable voltage source. Thus even good (commercially available) electronics already limit the passive frequency stability of our cavity.

Active stabilization of the cavity frequency to a laser (or vice versa) is typically done with Pound-Drever-Hall locking [84, 85]. A thorough introduction can be found in Ref. [86], and we will only briefly review it here. Suppose we send light from a laser to a cavity, and detect the reflected signal (Fig. 2.5**a**, top panel). If we sweep the laser frequency, there will be a dip in the reflected signal at the frequency of our cavity (ω_c), plotted in blue in Fig. 2.5**a**, bottom panel. We want to lock to the center of this dip, where the frequencies of our laser (ω_ℓ) and cavity are matched. Any perturbation of the frequency will change the reflected signal, which tells us that we need to change the frequency. However, the reflected signal does not tell us in which direction we need to shift, because it is symmetric around ω_c. Ideally, one would use another property of the laser light, its phase, to determine

[3] We used JAMMT, Just Another Mode Matching Tool. As the name implies, there are other tools that can achieve the same.

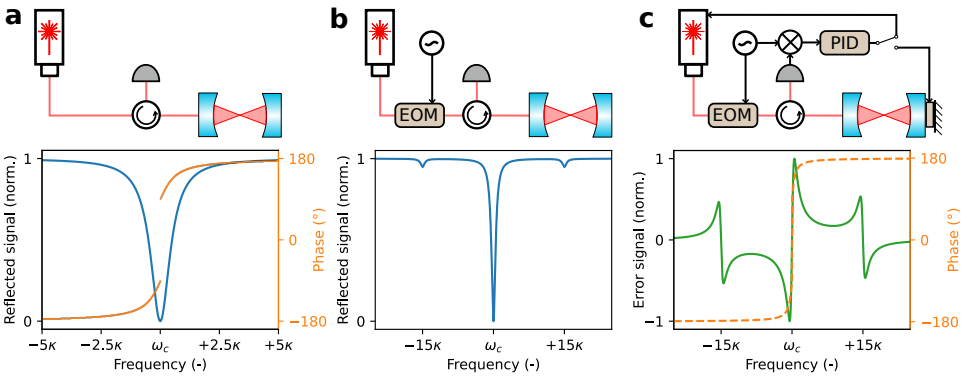

Figure 2.5: **a**: Schematic of laser, cavity and detector (top panel). Scanning either the laser frequency or the cavity resonance frequency shows a dip in the reflected signal (bottom panel). The light also gains a phase shift. Since the reflected signal is symmetric, it does not tell us in which direction to move to stabilize the frequency. For a lossless cavity, the reflection vanishes and the phase is undefined. **b**: Adding an EOM with a weak sinusoidal signal at 15κ creates sidebands in the reflection signal. These form a convenient frequency ruler to calibrate the cavity linewidth. **c**: By mixing the output of the photodiode with a copy of the signal applied to the EOM, we obtain the characteristic Pound-Drever-Hall error signal. This is antisymmetric around the resonance frequency, so it does tell us in which direction to move to stabilize the frequency. We send to this signal to a controller (Proportional, Integral and Derivative, PID), and then towards the laser or the mirror piezo to shift the frequency.

this. The phase of the reflected light would tell us the direction to shift, since it is antisymmetric around ω_c (orange in 2.5**a**). However, no direct detector for optical phase exists.

The Pound-Drever-Hall method creates a signal that is antisymmetric around ω_c. We do this by adding a sinusoidal perturbation to our laser light, using an EOM (Electro-Optic Modulator). This creates sidebands around our laser frequency, which are visible as small dips symmetrically around the cavity resonance frequency. The applied sine wave should have a frequency much larger than κ, such that the peaks are well-separated. We typically use 30 MHz. This has the added benefit that the distance between the peaks is known, and can be used to calibrate κ.

If we are close to resonance ($|\omega_c - \omega_\ell| \lesssim \kappa$), the two sidebands are reflected and show up in the detector signal. They interfere with the reflected carrier beam, so they create a beating pattern at the modulation frequency. The phase of this beating pattern corresponds to the phase shift due to the cavity. If we mix (multiply) the detector signal with a copy of the original modulation (Fig. 2.5**c**), we get a component at zero frequency: the amplitude corresponds to the cavity phase. The shape of this signal (green in Fig. 2.5**c**) is characteristic of the Pound-Drever-Hall method, and it is referred to as the 'error signal': It gives us the magnitude and direction of the shift we need to apply to return to resonance.

In practice, the error signal is fed to a PID (Proportional-Integral-Derivative) controller and we can apply it either to the laser or to a piezo to control the cavity length. Due to the sensitivity of the cavity length to electrical noise, we feed it back to the laser.

2.4. Optomechanics with one and two membranes

Optomechanics describes the interaction of light and mechanical motion; between photons and phonons [2]. It is typically described in the language of quantum mechanics, using a Hamiltonian $\hat{H}$, operators ($\hat{x}$, $\hat{p}$, $\hat{a}$, $\hat{b}$, etc.) and wavefunction ψ. Introductions to these concepts can be found in [87], [88] and [89], in that order. For now, we focus on the parts which are necessary to understand the rest of this thesis, based on Ref. [2].

A Hamiltonian describes a system in terms of its energy. For a system of uncoupled harmonic oscillators such as optical or mechanical modes, it has the form

$$\hat{H} = \hbar\omega_{\mathrm{c}}\hat{a}^{\dagger}\hat{a} + \hbar\omega_{\mathrm{m}}\hat{b}^{\dagger}\hat{b}. \tag{2.13}$$

Here, $\hbar$ is Planck's reduced constant $h/2\pi \simeq 1.055 \times 10^{-34}$ J Hz^{-1}, ω_{c} is the frequency of the optical cavity light (typically 193 THz) and ω_{m} is the frequency of the mechanical resonators (typically 150 kHz). The operators $\hat{a}$, $\hat{b}$ represent photons in the optical cavity and phonons in the mechanical resonator. If we let these operators operate on a wavefunction, $\hat{a}$ will return the wavefunction with one photon removed (annihilated), while $\hat{a}^{\dagger}$ will return it with one photon added (created), and $\hat{b}$, $\hat{b}^{\dagger}$ will do the same for phonons. The pair $\hat{a}^{\dagger}\hat{a}$ (idem for $\hat{b}$) is known as the number operator, as it returns the number of photons (or phonons) present in the wavefunction. Thus our Hamiltonian simply counts the number of photons and phonons present in a wavefunction, and multiplies each by their relevant energy ($\hbar\omega$): it returns the energy present in the system.

Optomechanics describes the coupling of the optical and mechanical resonators. Usually, we take a dispersive coupling, where the frequency of the optical cavity depends on the position of the mechanical resonator, $\omega_{\mathrm{c}} = \omega_{\mathrm{c}}(x)$. For small position shifts, we expand and retain only the linear term, $\omega_{\mathrm{c}}(x) \simeq \omega_{\mathrm{c}} + x\partial\omega_{\mathrm{c}}/\partial x$. This means Eq. (2.13) becomes

$$\hat{H} = \hbar\omega_{\mathrm{c}}\hat{a}^{\dagger}\hat{a} - \hbar G\hat{x}\hat{a}^{\dagger}\hat{a} + \hbar\omega_{\mathrm{m}}\hat{b}^{\dagger}\hat{b}. \tag{2.14}$$

We have written the shift of cavity frequency due to resonator motion as $G = -\partial\omega_{\mathrm{c}}/\partial x$, and replaced the classical position x by its operator equivalent $\hat{x}$. The description of the classical harmonic oscillator in terms of its position x and momentum $p(= mv)$ is linked to the quantum mechanical description involving the position $\hat{x}$ and momentum $\hat{p}$ operators. Similarly, we can define a link between the position operator $\hat{x}$ and the phonon creation and annihilation operators: $\hat{x} = x_{\mathrm{ZPF}}(\hat{b} + \hat{b}^{\dagger})$. The zero point fluctuation amplitude $x_{\mathrm{ZPF}} = \sqrt{\hbar/2m_{\mathrm{eff}}\omega_{\mathrm{m}}}$ provides a scale factor between the position and number of phonons, in terms of the frequency and effective mass m_{eff} of the mechanical resonator. This means that our Hamiltonian becomes

$$\hat{H} = \hbar\omega_{\mathrm{c}}\hat{a}^{\dagger}\hat{a} + \hbar\omega_{\mathrm{m}}\hat{b}^{\dagger}\hat{b} - \hbar g_0\hat{a}^{\dagger}\hat{a}(\hat{b} + \hat{b}^{\dagger}) + i\hbar E\left(\hat{a}^{\dagger}e^{-i\omega_{\ell}t} - \hat{a}e^{i\omega_{\ell}t}\right). \tag{2.15}$$

We have written the interaction rate between a single photon and a single phonon $g_0 = Gx_{\mathrm{ZPF}}$, instead of the cavity frequency shift G. Arguably, G is easier to measure

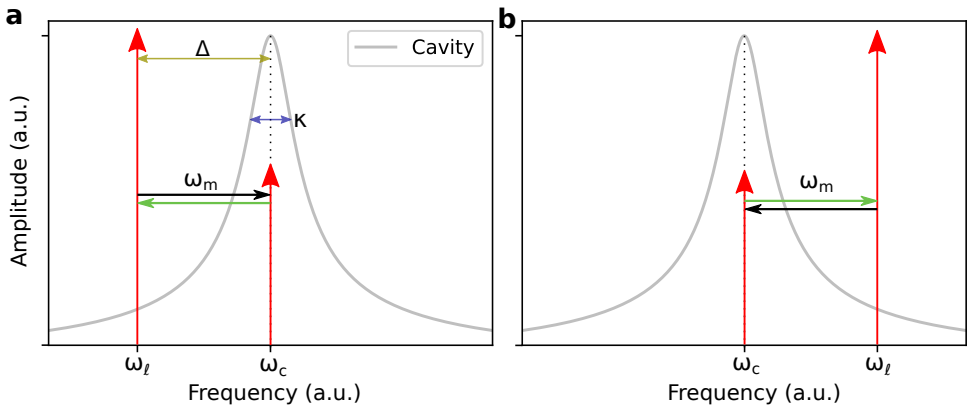

Figure 2.6: **a**: Schematic of optomechanical interaction between red-detuned laser and cavity with one membrane. The membrane scatters laser photons (ω_ℓ) to the cavity (ω_c) by absorbing a phonon (ω_m). The Hermitian conjugate of this process is in green. **b**: Same as **a**, but for blue-detuned laser.

but g_0 is more fundamental. We have also introduced a laser operating at frequency ω_ℓ that is incident on the cavity and couples to the optical field. The coefficient $E = \sqrt{P_\ell \kappa_e / \hbar\omega_\ell}$ relates it to the laser power P_ℓ (in Watt) and external (empty) cavity linewidth κ_e.

We focus only on the interaction term, and expand the cavity operators in an average $\bar{a}$ and fluctuating term $\delta\hat{a}$. The average $\bar{a}^*\bar{a} = n_c$, or the number of photons in our cavity. It is convenient to omit the laser driving term and define the detuning between the cavity and laser frequencies as $\Delta = \omega_\ell - \omega_c$. We can then expand and linearize the Hamiltonian to get

$$\hat{H} \simeq -\hbar\Delta\delta\hat{a}^\dagger\delta\hat{a} + \hbar\omega_m\hat{b}^\dagger\hat{b} - \hbar g_0\sqrt{n_c}\left(\delta\hat{a}^\dagger + \delta\hat{a}\right)\left(\hat{b} + \hat{b}^\dagger\right). \tag{2.16}$$

We have skipped some of the math, which can be found in Ref. [2]. A lot of the works in literature simply use $\hat{a}$ to refer to $\delta\hat{a}$, as the meaning is the same: $\delta\hat{a}$ annihilates a cavity photon while $\delta\hat{a}^\dagger$ creates one.

Now, we can study the different interactions that are resonant (i.e. very likely to happen) in our system depending on the detuning Δ. This is qualitative, for a quantitative description of the number of photons and phonons it is better to use the equations of motion (see chapter 6). That way, we can take care of dissipation, noise and driving. Based on the Hamiltonian description, we can consider different interactions when they are resonant (conserve energy).

One membrane, laser red detuned

Suppose we have a laser red-detuned (lower frequency) from the cavity, and a single mechanical resonator. The interaction term in Eq. (2.16) will become a beam-splitter interaction between mechanical phonons and cavity photons. The term is $\propto g_0\sqrt{n_c}\left(\hat{a}^\dagger\hat{b} + \hat{a}\hat{b}^\dagger\right)$; this exchanges mechanics with cavity (→) and cavity with mechanics (←).

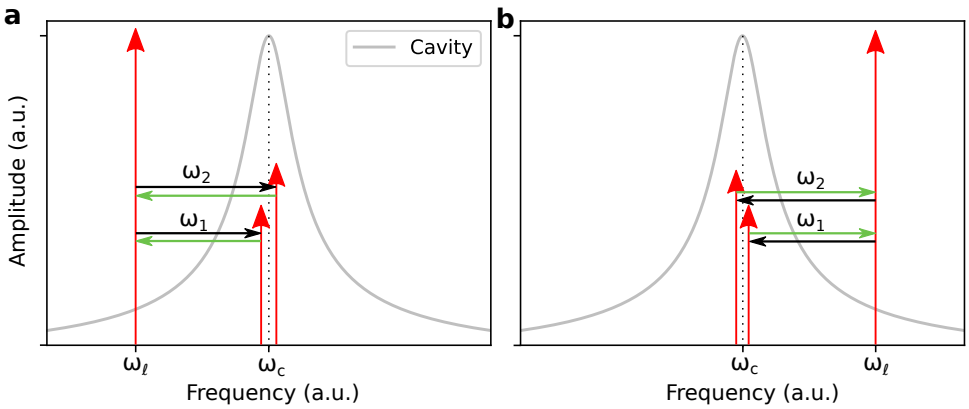

Figure 2.7: **a**: Schematic of optomechanical interaction between red-detuned laser and a cavity with two membranes. Laser photons can scatter from either membrane (ω_1, ω_2), absorbing a phonon from either (but not both) membranes. **b**: Same as **a**, but for a blue-detuned laser.

If our laser is at the right frequency ($\omega_\ell = \omega_c - \omega_m$) and we are sideband resolved ($\omega_m \gtrsim \kappa$), the mechanics to cavity (→) process is strong, because there are many laser photons. This process corresponds to anti-Stokes scattering of a laser photon into the cavity. Simultaneously, the cavity to mechanics (←) process is weak, because there are few cavity photons (without driving the cavity). This process corresponds to Stokes scattering of cavity photons into the laser line. The relative strengths of these processes mean that the light is more likely to annihilate mechanical phonons rather than create them, which effectively cools the mechanical mode.

One membrane, laser blue detuned

Now suppose our laser is blue-detuned (higher frequency) with respect to our cavity. The interaction term in our Hamiltonian now takes the form to a two-mode squeezing interaction, $\propto g_0\sqrt{n_c}\left(\hat{a}^\dagger\hat{b}^\dagger + \hat{a}\hat{b}\right)$. This way, we can create (←) simultaneous excitations of our cavity and mechanics, or annihilate (→) them. Here, the annihilation (→) process is weak, because there are few cavity photons. In this case, the light is more likely to create mechanical phonons than to annihilate them, which effectively heats (drives) the mechanical mode.

Two membranes, laser red detuned

What happens if we have two membranes instead? We consider two mechanical frequencies ω_1, ω_2, where each of the two resonators results in the same beamsplitter interaction as before. That means our Hamiltonian is

$$\propto g_{0,1}\sqrt{n_c}\left(\hat{a}^\dagger\hat{b}_1 + \hat{a}\hat{b}_1^\dagger\right) + g_{0,2}\sqrt{n_c}\left(\hat{a}^\dagger\hat{b}_2 + \hat{a}\hat{b}_2^\dagger\right). \tag{2.17}$$

However, if $\omega_1 \simeq \omega_2$, there are other combinations of operators that are resonant,

$$\propto g_{0,1}g_{0,2}n_c\left(\hat{a}^\dagger\hat{b}_1\hat{a}\hat{b}_2^\dagger + \hat{a}\hat{b}_1^\dagger\hat{a}^\dagger\hat{b}_2\right) \tag{2.18}$$

By tracing out the cavity operators, we are left with

$$\propto g_{0,1} g_{0,2} n_c \left(\hat{b}_1 \hat{b}_2^\dagger + \hat{b}_1^\dagger \hat{b}_2 \right). \tag{2.19}$$

This process is resonant and linear in the mechanical operators. It was quadratic in the optical resonators, but by tracing out the cavity field we obtain this effective linear mechanical process. This is thus the effective mechanics-mechanics beam-splitter interaction: it exchanges the states of the mechanical resonators. If we consider the actions of the photons we traced out, we have both Stokes and anti-Stokes scattering, which can be simultaneous [75] or subsequent, depending on the cavity. For the latter, we found that the presence of a cavity introduces a time delay in this interaction, which is the subject of chapter 6.

Two membranes, laser blue detuned

Now consider the case where we have two membranes with a blue detuned laser. We get the same two-mode squeezing interaction in our Hamiltonian,

$$\propto g_{0,1} \sqrt{n_c} \left(\hat{a}^\dagger \hat{b}_1^\dagger + \hat{a} \hat{b}_1 \right) + g_{0,2} \sqrt{n_c} \left(\hat{a}^\dagger \hat{b}_2^\dagger + \hat{a} \hat{b}_2 \right). \tag{2.20}$$

But if $\omega_1 \simeq \omega_2$, there are again other combinations of operators that are resonant,

$$\propto g_{0,1} g_{0,2} n_c \left(\hat{a}^\dagger \hat{b}_1^\dagger \hat{a} \hat{b}_2 + \hat{a} \hat{b}_1 \hat{a}^\dagger \hat{b}_2^\dagger \right). \tag{2.21}$$

By tracing out the cavity operators, we get

$$\propto g_{0,1} g_{0,2} n_c \left(\hat{b}_1^\dagger \hat{b}_2 + \hat{b}_1 \hat{b}_2^\dagger \right). \tag{2.22}$$

But this is exactly the same as Eq. (2.19)! This means that if $\omega_1 \simeq \omega_2$, both a laser detuning of $\omega_\ell = \omega_c + \omega_1$ and $\omega_\ell = \omega_c - \omega_1$ will result in an effective mechanics-mechanics beam-splitter interaction. The difference is in the effect of the optics on each membrane individually: similar to the case of one membrane, the red-detuned laser will cool the mechanical mode while the blue-detuned laser will heat/drive the mechanical mode.

2.4.1. Enhanced coupling

It was proposed that placing arrays of membranes in an optical cavity enhances the coupling of their motion to the optical field with respect to single membranes [33]. The dispersive shift $\partial \omega c / \partial x$ for a system with two cavities can be defined in terms of the separate membrane positions, x_1, x_2 [37], but can also be defined in terms of the collective motion of an optical 'superelement' consisting of multiple scatterers [33]. These two descriptions make sense in different regimes of cavity operation (low power and high power, respectively), but they predict similar results for the optomechanical coupling strength.

The positioning of two dielectric membranes inside the a Fabry-Pérot cavity affects the optical modes of that cavity. If the membranes are spaced by an integer

multiple of the wavelength λ, the optical mode is enhanced between the two membranes. Effectively, they form a cavity within a cavity. If the two membranes move in the same direction (center-of-mass motion), the optical field intensity between the two membranes changes little. However, when the two membranes move in the opposite direction (breathing motion), the optical field intensity between the membranes is affected strongly. The optomechanical coupling G introduced in the previous section is due to the optical radiation pressure, which thus couples the optical intensity to the mechanical motion. The field focusing from the two membranes increases the coupling strength without actually increasing the number of photons. This leads to the predicted enhancement of the optomechanical coupling g_0 of the breathing motion of two membranes in a cavity.

In the regime of the individual membrane reflectivity approaching 1, the optomechanical coupling is enhanced by a factor $L/2d$, where L is the length of the total Fabry-Pérot cavity and d is the distance between the membranes [90]. For our 50 mm cavity with 100 µm distance between the membranes, the enhancement is a factor 150. Such an enhancement would be an asset nearly all optomechanical effects, from cooling [38, 91] to transduction [17], as they commonly scale with g_0 in some way.

3

Mechanical dissipation by substrate-mode coupling in SiN resonators

State-of-the-art nanomechanical resonators are heralded as a central component for next-generation clocks, filters, resonant sensors, and quantum technologies. To practically build these technologies will require monolithic integration of microchips, resonators, and readout systems. While it is widely seen that mounting microchip substrates into a system can greatly impact the performance of high-Q resonators, a systematic study has remained elusive, owing to the variety of physical processes and factors that influence the dissipation. Here, we analytically analyze a mechanism by which substrates couple to resonators manufactured on them, and experimentally demonstrate that this coupling can increase the mechanical dissipation of nanomechanical resonators when resonance frequencies of resonator and substrate coincide. More generally, we then show that a similar coupling mechanism can exist between two adjacent resonators. Since the substrate-mode coupling mechanism strongly depends on both the resonator position on the substrate and the mounting of the substrate, this work provides key design guidelines for high-precision nanomechanical technologies.

A trampoline and a chip
talk
but the sound gets lost

This chapter has been published together with M.A. ten Wolde, A. Cupertino, S. Gröblacher, P.G. Steeneken and R.A. Norte in Applied Physics Letters **121**, 032201 (2022). All data, measurements and analysis scripts in this work are available at 10.4121/19209333.v2.

3.1. Introduction

Optomechanics [2] represents one of the core research directions for improving the precision and accuracy of sensors, by combining the low loss of mechanical sensors [18, 23, 92–94] with the accuracy of optical readout and control [95–97]. An important figure of merit for maximizing performance is the mechanical Q-factor, which greatly reduces the effect of thermomechanical noise that limits sensors, but when considering future applications of these resonators, their footprint, fabrication complexity, and integration with other sensor components, such as the substrate, are also crucial properties. High-stress silicon nitride resonators (Si_3N_4) exhibiting state-of-the-art mechanical quality factors can be negatively impacted by interactions with their substrates. Phononic shields [39, 72, 98–100] have been used to reduce these interactions and reach exceptionally high Q-factors (10^9), but their size, complexity, and thermal performance limits many real-world applications. It is well-known that thin and clamped-down substrates can produce significant losses in high-Q Si_3N_4 resonators [13, 67], but to date, little is known about their precise interaction. Several works have focused on acoustical impedance mismatching or phonon tunneling [65, 66, 101] to study and minimize dissipation channels of mechanical resonators to their environment by treating the substrate as a semi-infinite structure, and some works have studied the interaction between resonator modes and the substrate [54, 68, 69, 102]. In this chapter, we build on this latter direction by linking it to the well-known effect of dissipation in resonant coupled resonators [103], and show that coupling between resonator and substrate modes can negatively affect the Q-factor of trampoline resonators [13] despite their difference in size. We deliberately fabricate resonators with resonance frequencies near those of a substrate mode, and show that their dissipation is increased by the coupling to this low-Q substrate mode. Furthermore, we show that the substrate can even mediate resonant coupling between two resonators separated by 1.5 mm, which can provide an additional loss path when the density of resonators on a microchip is increased. With this study, we show the mechanism by which resonators and substrate couple and highlight the largely unexplored effect of substrate design, which can prove to be important for future optomechanical microchip designs, particularly when considering arrays of high-Q mechanical resonators [104, 105].

3.2. Results

3.2.1. Analytical model

The substrate, to which high-tension Si_3N_4 membranes are anchored, is often treated as a fixed boundary (i.e. a simple spring model) [13, 50, 51]. This simplification results in a negligible error when considering the mode shapes and frequencies of the resonators, since the stiffness and mass of the (typically ~500 µm) thick substrate are much bigger than that of the thin membrane. Through the mode shape and frequencies, the fixed-boundary method correctly takes into account bending (and intrinsic) losses [61, 62], and by adding a lossy spring model, one can take into account radiative losses to traveling waves in the substrate [50, 66, 70] (phonon tunneling, cf. Fig. 3.1**a**, top) as well. However, this method does not treat losses

due to coupling to a specific substrate *resonance mode* (Fig. 3.1**a**, bottom), which might reduce the Q-factor when particular modes of the resonator and substrate coincide, an effect well-known from classical mechanics [103].

To gain insight, we consider a simple analytical model of two stacked and coupled masses $m_1,\ m_2$ with springs $k_1,\ k_2$ and dampers $c_1,\ c_2$ (see inset of Fig. 3.1**b**), representing a light resonator coupled to a heavy substrate ($m_2 \ll m_1$). Without driving, the equation of motion describing the positions of the masses $x_1,\ x_2$ for this system is

$$\begin{bmatrix} (k_1 - \omega^2 m_1) + i\omega c_1 & -m_2\omega^2 \\ -(k_2 + i\omega c_2) & (k_2 - \omega^2 m_2) + i\omega c_2 \end{bmatrix} \begin{bmatrix} x_1 \\ x_2 \end{bmatrix} = 0, \tag{3.1}$$

which we can straightforwardly solve for complex eigenfrequencies ω_i $(i = 1, 2)$ from which we can extract the Q-factor via

$$Q_i = \frac{\mathrm{Re}(\omega_i)}{2\mathrm{Im}(\omega_i)}. \tag{3.2}$$

We use realistic parameters $m_1 = 1.47\,\mathrm{mg}$ and $m_2 = 11.8\,\mathrm{ng}$ for the effective masses [45] of substrate and resonator mode, choose $\omega_1 = \sqrt{k_1/m_1} = 2\pi{\times}100\,\mathrm{kHz}$, and choose $c_1,\ c_2$ such that our resonator is intrinsically limited to $Q_2 = 10^6$ but our substrate Q_1 is substantially lower. Then, we vary ω_2 by adjusting k_2. When the (real part of the) eigenfrequencies of the two modes is very different ($\omega_2 \neq \omega_1$), the two resonances are essentially independent; thus, there is little energy transfer between the modes. However, when their eigenfrequencies are closer together ($\omega_2 \approx \omega_1$), the modes hybridize and energy transfer from one mode to the other can occur [103, 106]. If the damping of the substrate mode is higher than that of the resonator mode, the substrate mode essentially functions as an additional loss mechanism for the resonator mode as shown in Fig. 3.1**b**. The frequency range over which the energy transfer is significant is determined both by the Q-factor of the low-Q mode and by the difference in mass/stiffness of the two resonators. From this basic model, it is expected that low-Q substrate modes might have significant impact on the Q-factor of high-Q resonators under certain conditions. We will numerically and experimentally explore this loss mechanism in more detail for Si_3N_4 trampoline resonators.

3.2.2. FEM model

We use a finite-element model of our resonator and substrate to numerically analyze the loss mechanism by substrate-resonator mode-coupling (see Sec. 3.4.1 for details). We take a viscoelastic material loss model for both the substrate [62, 68] (loss factor $\eta_{\mathrm{Si}} = 10^{-4}$) and membrane [71] ($\eta_{\mathrm{SiN}} = 10^{-7}$), where we choose the values such that $Q = \eta^{-1}$ matches with experimental observations of the substrate modes (Sec. 3.4.2) and resonator modes, respectively. To distinguish these Q-factors, we will refer to the viscoelastically limited (intrinsic) Q-factors as Q^i, and the hybridized Q-factors with Q^h.

In Fig. 3.2, we plot the Q-factor of the simulated membrane mode as a function of resonator mass, such that its resonance frequency crosses two substrate modes.

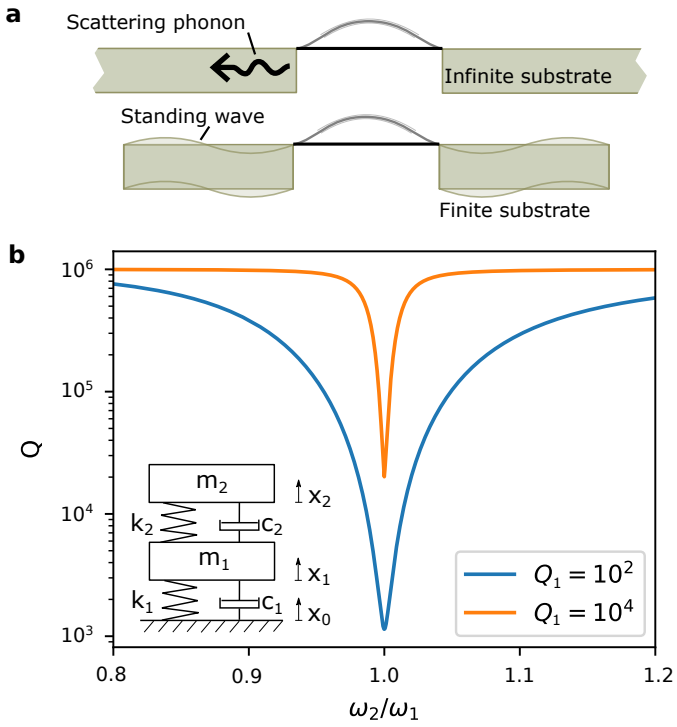

Figure 3.1: **a**: Schematic of (incoherent) phonon scattering into an infinite substrate (top), and (coherent) phonon transfer into a discrete mode of a finite substrate that is the focus of this chapter (bottom). **b**: Mode coupling between a high-Q resonator (m_2) and a low-Q substrate mode (m_1, inset) reduces the effective resonator Q-factor (y-axis) if their frequencies ω_1 and ω_2 are identical. The reduction of resonator Q-factor depends on the intrinsic substrate Q_1 as indicated by the difference between the orange ($Q_1 = 10^4$) and blue ($Q_1 = 10^2$) curves.

When the resonator frequencies are very different, the resonator's Q-factor is limited by the Si_3N_4 material loss, $1/\eta_{\mathrm{SiN}} \simeq 10^7$ so $Q_2^h = Q_2^i$, as expected from uncoupled modes. Close to a substrate mode (dashed line), the Q-factors of the modes hybridize similarly to the analytical model; Q_2^h decreases to $Q_1^h \simeq 1/\eta_{\mathrm{Si}} \simeq 10^4$ limited by the substrate material loss. Here, energy-loss via coupling to the lossy substrate mode is the dominant loss mechanism. Not all substrate modes decrease the resonator Q_2^h equally, e.g. the mode of Fig. 3.2**a** with frequency $\omega_1 = \omega_{\mathrm{n}}$ shows no decrease, while the mode of Fig. 3.2**b** with frequency $\omega_1 = \omega_{\mathrm{an}}$ shows a pronounced decrease. If the resonator is located at a node of the substrate mode (mode shape shown in Fig. 3.2 insets), there is no motion to couple to, so there is almost no energy transfer between the modes. Trends visible in the resonator Q-factor in Fig. 3.2**a** are attributed to nearby substrate modes (not shown) that do couple to the resonator mode.

Aside from the mode shape, the substrate thickness also affects the mode coupling, as can be seen from the different colored curves of Fig. 3.2. While Q_2^h goes to the same level when the resonance frequencies are equal (if $\omega_2 = \omega_1$,

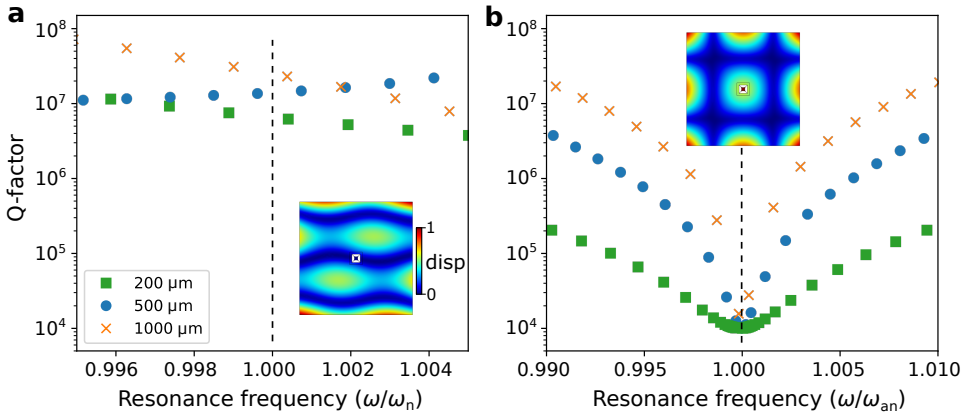

Figure 3.2: Simulated Q-factor Q_2^h of resonator mode at ω_2, at different values of $\omega_2 \approx \omega_1$ coupling to two different substrate modes, with **a** a node at the resonator position ($\omega_1 = \omega_n$), and **b** an anti-node at the resonator position ($\omega_1 = \omega_{an}$). Insets show the normalized out-of-plane displacement of the substrate mode, with the resonator located in the center. The lossy substrate mode significantly reduces the Q-factor of the resonator mode over a large frequency range when located at an anti-node (**b**), but has little effect when located at a node (**a**). Different curves show the effect for different substrate thicknesses.

$Q_2^h \to Q_1^h \simeq Q_1^i \simeq 1/\eta_{\mathrm{Si}} \simeq 1 \times 10^4$), the frequency range over which this happens is much more narrow for a thick substrate. The reason is that the mass difference between resonator and substrate is bigger for a thicker substrate, which reduces the effective coupling between the masses (top-right term in Eq. (3.1) after normalization). While the shape and size of a substrate are important parameters for the frequency distribution of substrate modes, Eq. (3.1) and the results of Fig. 3.2 suggest that the substrate mass governs the coupling strength between resonator and substrate modes at resonance. This points to thicker substrates being better (less coupled) in general, but for a given substrate thickness and resonator frequency, the optimal substrate shape and size must be carefully designed.

3.2.3. Q-reduction by resonator-substrate coupling

To investigate the effect of coupling to the substrate mode on the resonator's Q-factor Q_2^h, we fabricate (see Sec. 3.4.3) resonators with slightly different resonance frequencies, by varying the membrane's mass-per-area by perforating it using small holes of controlled radius. This square lattice of holes also functions as a photonic crystal to increase the membrane's reflectivity [34] and causes the membrane to release evenly during the fabrication process. Since this method ensures that the geometry of the resonator is almost constant, this allows varying the resonance frequency with minimal effect on the Q-factor [13, 52, 53]. We change lattice constant a and hole radius r (Fig. 3.3**a-c**). The mass ratio $r_{\mathrm{m}} = 1 - \pi r^2/a^2$ relates the mass of the patterned photonic crystal to the mass of unpatterned Si_3N_4. The range over which r_{m} can be varied is limited, due to stress focusing (see Sec. 3.4.4 for details) and fabrication constraints. The effect of r_{m} on Q_2^i is negligible; simulations

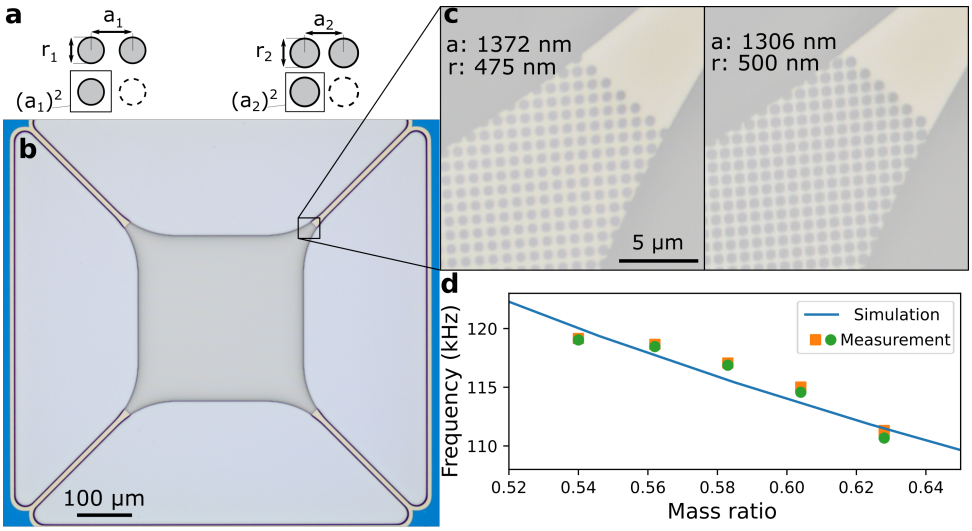

Figure 3.3: **a**: Schematic of variation of photonic crystal parameters used to change the mass ratio. **b**: Optical microscope image of suspended membrane, the blue color is from thin-film interference effects of the Si_3N_4. **c**: Zoom-in of photonic crystal edge to show change in hole size and spacing. **d**: Simulated and measured resonator frequencies as function of designed r_m for two nominally identical chips. Standard deviation of frequencies is approximately equal to the size of the data points.

predict at most 20% change over the parameter range (Sec. 3.4.4), confirmed by the absence of a dependence of the measured values of Q_2^h on the photonic crystal parameters. We use $10 \times 10 \times 1$ mm^3 chips with 25 membranes fabricated with 5 different r_m. The measured resonance frequencies of their fundamental modes agree well with simulations (Fig. 3.3**d**).

We utilize a Polytec MSA400 laser Doppler vibrometer to spatially resolve mode shapes, to obtain resonance spectra, and to acquire time traces from which we extract Q_2^h via ringdown measurements (see Sec. 3.4.3). In Fig. 3.4**a**, we show the mechanical spectrum for three trampoline resonators with nominally the same $r_m = 0.54$, where the fundamental mode (II) is close to a substrate mode (I). The spread in frequency due to fabrication imperfections is < 300 Hz on 115 kHz, which highlights our control over the mechanical frequencies. The inset shows for a particular device the ringdowns of the membrane ($Q_2^h = 1.2 \times 10^6$) and substrate modes.

There is a spread in resonator Q_2^i (see Sec. 3.4.4 and Fig. 3.10) that could obscure an absolute reduction of resonator Q_2^i due to coupling to the substrate mode. We can isolate the effect of the substrate coupling by controlling the substrate Q-factor Q_1^i. By adding carbon tape between substrate and stainless steel sample holder (see Sec. 3.4.3 for the measurement protocol), we reduce [62, 70] Q_1^i from 1.2×10^4 (resting without tape) to $\sim 3 \times 10^3$ (with tape, see Sec. 3.4.2). By comparing the resonator's hybridized Q-factor Q_2^h for an untaped chip (Q_u) to the resonator's hybridized Q-factor for a taped chip (Q_t), we isolate the effect of the

substrate-mode coupling. That is, the ratio Q_t/Q_u should be smaller than 1 only due to the enhanced dissipation by mode coupling.

We plot the ratio Q_t/Q_u for 152 measurements from the resonators spread over 4 chips in Fig. 3.4**b**. Q_t and Q_u are each determined by the average of 3 ringdowns on the same device. The data is then binned by frequency with respect to the substrate mode, for each bin we determine the mean and standard deviation to obtain the errorbars. Circles indicate single devices. Fig. 3.4**b** also shows the theoretical analytical model introduced by Eq. 3.1, the upper bound corresponds a membrane located at a node and thus not coupled, while the lower bound corresponds to a membrane located at an antinode, maximally coupled (simulated mode shape inset in Fig. 3.4**b**). The red dotted line indicates the expected mean reduction in Q-factor.

Close to the substrate mode at ω_1, the average Q_t/Q_u is reduced, and closely matches the theoretical mean, while far away from ω_1 it is close to 1. To gauge the statistical significance of the reduction of Q_t/Q_u, we perform Welch's t-test on the mean Q-factor ratios close to the substrate mode ($\omega_1 - 2\text{kHz} < \omega_2 < \omega_1 + 2\text{kHz}$) and far away from the substrate mode ($\omega_2 < \omega_1 - 7\text{kHz}$). This tests our hypothesis (Q-factor reduced close to ω_2) against the null hypothesis (Q-factor not affected by ω_2). We obtain a probability $p = 0.00072$, so we can reject the null hypothesis. This means the reduction in Q-factor close to the substrate mode is statistically significant. Additionally, the spread in the measured ratio of Q_t/Q_u can be attributed predominantly to the positioning of the resonators on the chip with respect to the nodes or antinodes of the substrate mode (inset of Fig. 3.4**b**). This effect is illustrated by the green shaded area bounded by theory. In some resonators, there is heating and optothermal driving from the laser (1 mW continuous-wave power) which affects the ringdown measurement, and we have excluded these devices (see Sec. 3.4.5, and Fig. 3.10). Summarizing, we find a significant reduction of the average Q_t/Q_u close to the substrate mode ω_1, which quantitatively agrees with the theoretical model of substrate-mode coupling, thus supporting the hypothesis that coupling to the substrate increases dissipation of the membrane mode.

3.2.4. Q-reduction by resonator-resonator coupling

After having investigated the importance of resonator-substrate coupling, we now address the possibility of two resonators on the same chip affecting each other. Such couplings can be relevant in resonator arrays, and have been found in lower-Q devices [107–109]. By measuring their resonance frequencies, we identify two membranes spaced 1.5 mm apart (see Sec. 3.4.6 for details) with resonance frequencies identical to within 2 Hz ($\omega_1/2\pi = 118.828$ kHz and $\omega_2/2\pi = 118.830$ kHz), much closer together than either of them are to the substrate mode, Fig. 3.5**a**. From Lorentzian fits to the spectrum (orange curves), we extract their Q-factors, $Q_1 \simeq 0.6 \cdot 10^6$ and $Q_2 \simeq 0.8 \cdot 10^6$.

By driving at the resonance of one membrane and recording the ringdown, we see oscillatory behavior which we model by two discrete coupled resonators, Fig. 3.5**b** and Sec. 3.4.6 for details. The equation of motion for the resonator

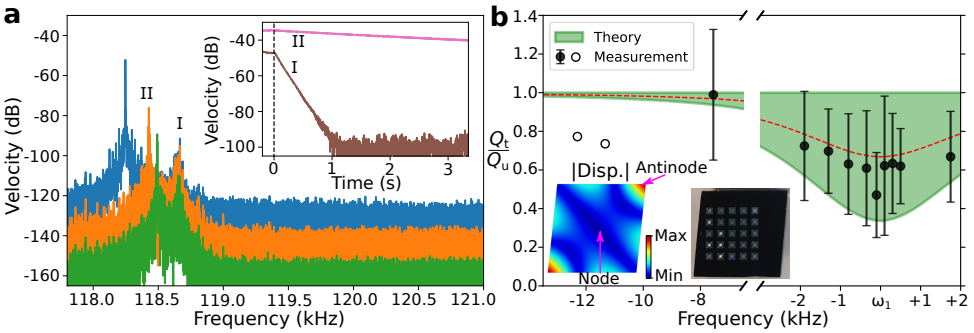

Figure 3.4: **a**: Mechanical velocity spectrum ($20\log_{10}(v/v_{\mathrm{ref}})$ with $v_{\mathrm{ref}} = 1\ \mathrm{m\,s^{-1}}$) of three different devices, showing fundamental mode (II) close to the substrate mode (I) by driving with white noise. Inset: Ringdowns of the untaped device fundamental mode (II) and substrate mode (I), showing the difference in their Q-factors. **b**: Ratio of Q_2^h measured on a taped (Q_{t}) versus untaped (Q_{u}) substrate: the increase in substrate losses causes a decrease in Q_2^h when the modes are close in frequency. Theory curve shows expected reduction in Q_2^h around ω_1 for $Q_1^i = 1.2\times10^4 \rightarrow 3\times10^3$ when applying tape. Insets shows the simulated mode shape of the substrate mode and a photo of the fabricated chip with 25 devices.

positions is

$$\begin{bmatrix} (k_1 - \omega^2 m_1) + i\omega c_1 & J^2 \\ J^2 & (k_2 - \omega^2 m_2) + i\omega c_2 \end{bmatrix} \begin{bmatrix} x_1 \\ x_2 \end{bmatrix} = 0, \tag{3.3}$$

where the coupling between the resonators via the substrate is modeled by the parameter J. The indices 1,2 now both refer to the two membranes, and $J^2 = \frac{k_3^3}{m_1 m_2}$ is the coupling rate between them (Fig. 3.5**b**, inset). By integrating the equations of motion, Eq. (3.3), and plotting the resulting velocity of one of the resonators, we can nearly exactly reproduce the oscillating ringdowns we observe after having adjusted the initial position to get a good fit. The oscillations in the ringdown can be attributed to energy exchange between the spatially separated resonators through the substrate. Based on the periodicity, we extract a coupling rate $J/2\pi \simeq 138$ Hz. When a linear fit is made though the middle of the oscillations, we obtain a Q-factor of $Q_{\mathrm{tot}} = 0.83\cdot10^6$, corresponding reasonably well to the Q-factors from the Lorentzian fits. This measurement demonstrates that the on-chip coupling between Si_3N_4 membranes on the same substrate can present an important coupling channel. Furthermore, the oscillating behavior implies coherence in the energy exchange, which is of interest for information processing [107–110] in particular if a control mechanism to adjust the coupling can be devised. The fact that we see such energy exchange in a passive system suggests it should be taken into account when designing sensors based on resonator arrays [104, 105].

3.3. Conclusion

In conclusion, we demonstrate analytically, numerically and experimentally a mechanism behind the coupling between high-Q resonators and substrate modes, which

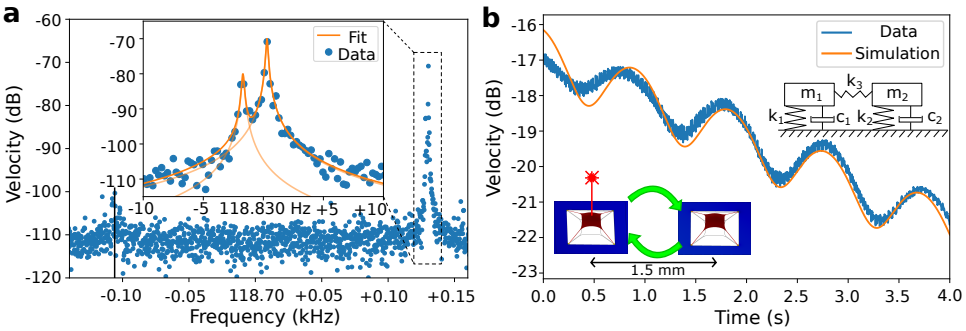

Figure 3.5: **a**: Spectrum measured on one membrane containing both a signature of the substrate mode (black bar) and of a second membrane extremely close in frequency. Inset shows membrane peaks fitted with two Lorentzians (orange, with semi-transparent the separate Lorentzians). **b**: Ringdown (blue) by driving at the resonance of one membrane and recording the time-trace of that same membrane. Oscillations are due to coherent coupling between the two resonators spaced by 1.5 mm (bottom inset). Simulated ringdown (orange) of two coupled resonators (top inset) using fit parameters obtained in **a**.

can reduce the Q-factor of the resonators when their frequencies match. Using a laser Doppler vibrometer to identify resonator and substrate modes, we are able to explain the physics behind this interaction. Interestingly, this interaction is not only limited to resonator and substrate but also exists between spatially separated high-Q resonators under the same frequency-matching condition. These behaviors in a fully passive system show the importance of considering resonator-substrate interactions in future designs of arrays of high-Q mechanical resonators for sensing, actuation, filtering and timing applications. In particular, thin and clamped-down substrates may have a dense spectrum of low-Q modes and suffer from resonator-substrate interaction as a result. To avoid these interactions, our numerical results point towards thick substrates for their increase in mass and stiffness [13], and laterally small chips for a sparser spectrum of substrate modes. We further confirm the result that avoiding tape to mount chips to a sample holder is best to retain high resonator Q-factors. Neither of these effects had been systematically explored before due to the stringent requirements on resonator frequency precision. This chapter thus highlights the substrate and mounting as important parameters to incorporate in future design methodologies.

3.4. Supplementary information

3.4.1. Membrane-on-substrate simulations

We use a COMSOL model to simulate mode frequencies and shapes, and obtain estimates of the Q-factor of the different resonances. The model consists of a 2D shell (Si_3N_4) and a 3D solid (Si) with a solid-shell connection representing the chemical bond between the two, as in Fig. 3.6. Around the patterned membrane, there is a 20 µm cutout in the Si such that the Si_3N_4 is suspended. Upon release, the 1 GPa pre-stress in the Si_3N_4 redistributes (Sec. 3.4.4), to take this into account we first perform a stationary step before calculating the eigenmodes of the system. This

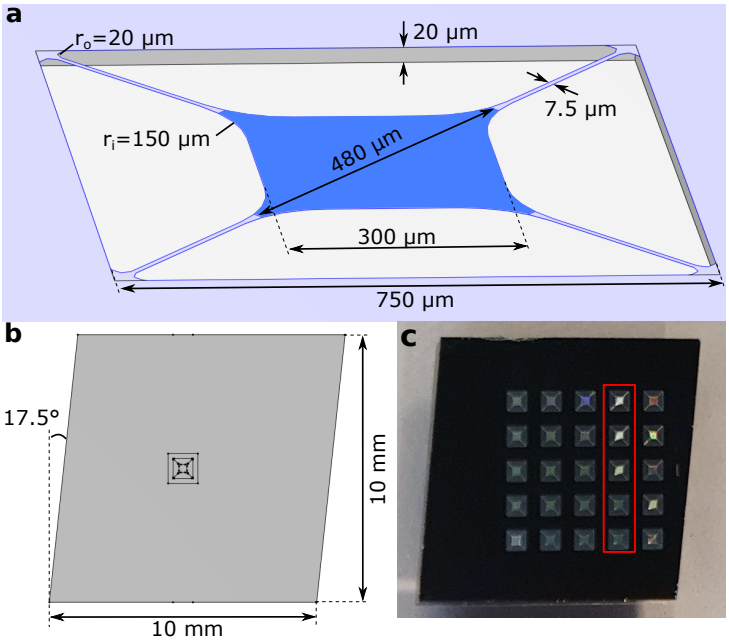

Figure 3.6: **a:** Simulation setup of Si_3N_4 membrane as a shell (light purple/blue) on top of a Si solid (grey), with nominal membrane design parameters. **b:** Full simulation domain, matching closely in size to the actual chips. **c:** Image of chip containing 25 membranes with 5 different designs, one for each column (red).

also accounts for the membrane geometry changing due to the stress redistribution, though this effect is minimal.

The membrane geometry, Fig. 3.6**a**, was designed in a different work [13], though slight modifications were made to account for a new etch process. The diameter of the photonic crystal (480 µm) extends significantly beyond the width of the membrane pad (300 µm). The photonic crystal holes also function as etch release holes, which is crucial to avoid the membrane collapsing. As the tether width increases towards the pad (start at 7.5 µm, with fillet radii of 150 µm), this area is the last to be released. To increase the yield of fabrication, the photonic crystal was extended to cover this area and provide a more equal release of the membrane.

When calculating the eigenmodes of this model, we obtain the free-free modes and discard the rigid-body modes. In the experiment, the chip is placed on a stainless steel sample plate, which constrains the chip motion. Taking this interface properly into account is rather involved, so we neglect this effect. Based on the good agreement in both mode frequency and mode shape between the simulations and measurements, this is a valid simplification.

For most of this chapter, we follow the convention of using square (10×10 mm^2) chips, which would result in symmetric substrate mode shapes. For thick (1 mm) chips in particular, the targeted mode of interest has a large area of low mode

amplitude in a ring around the center of the substrate (cf. Fig. 3.2), which would preclude the majority of membranes from interacting with this mode. To avoid this, we diced these chips at a slight angle, Fig. 3.6**b** and **c**, such that there was a substrate mode of the right frequency with a reasonably flat mode profile across the chip.

In the simulations supporting Fig. 3.2, we sweep the resonator frequency by changing the mass of the resonator. The central pad of the trampoline membrane (blue in Fig. 3.6) is assigned a different virtual material than the rest of the Si_3N_4 surface (light purple in Fig. 3.6); we modify the material density ρ to change the mass, but keep the rest of the material parameters the same. By choosing the material density correctly, we can sweep the resonator mode across any substrate mode of choice. For the different 10×10 mm^2 square chips of 200 µm, 500 µm and 1 mm thickness, we choose modes with the same out-of-plane mode shape, which are at different frequencies for each of the chip thicknesses. This allows for direct comparison of the frequency range over which the resonator Q-factor is reduced due to coupling to the substrate mode.

3.4.2. Substrate modes

We verify the mode shapes we simulate with spatially-resolved mode measurements using the Polytec MSA400 laser Doppler vibrometer. For a nearly-perfectly square 10×10 mm^2 Si chip of 200 µm thickness, we show three modes (149, 201 and 315 kHz) in Fig. 3.7**a**. Simulations of this chip design show excellent agreement in both mode shape and frequency with the measured results, Fig. 3.7**b**. Due to the difference in thickness, these chips have different substrate modes that are considerably easier to measure and visualize than the 1 mm chips used for the experiments in the rest of this chapter.

To motivate the loss factors used for the modeling in this chapter, we fit a Lorentzian to the mechanical modes visible in the substrate spectrum, shown in Fig. 3.7**c**. When the substrate is not taped to the sample holder, the modes have a Q-factor on the order of 10^4, but that is decreased to 10^2 when we add carbon tape. In the latter case, the modes are sufficiently broad that they overlap so we show the sum of the different Lorentzians (solid black line) on top of the detector noise floor (dashed black line) in Fig. 3.7**c**. For some of the more prominent modes, we have denoted the Q-factor in the figure. Note that the substrate mode Q-factors reported here are lower than the ones reported in Sec. 3.2.3, which is due to the thickness of the chip used (200 µm in Fig. 3.7**c** versus 1 mm in Sec. 3.2.3).

For a quantitative match between the analytical theory and the obseved reduction in membrane Q-factor, we must obtain the the substrate Q-factor with and without tape. However, for thicker chips the amplitude of this substrate is too small to reliably measure at any single membrane position. It can be amplified by strong driving with white noise, but obtaining a fit is made difficult by the membrane mode. However, by averaging measurements from all membranes, we can isolate the mode they have in common which should be the substrate mode. We do so in Fig. 3.8, where we plot the spectra of the averaged driven measurement

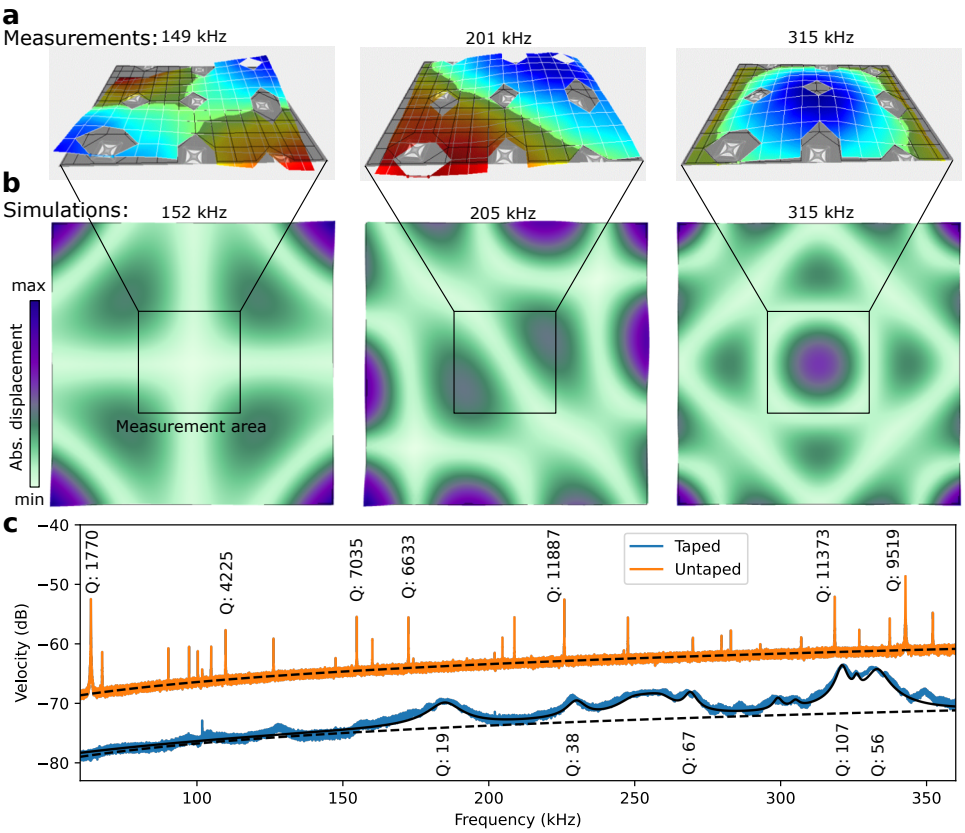

Figure 3.7: **a:** Measured substrate modes on 200 µm substrates, which are easier to visualize than the substrate modes of the 1 mm thick substrates used in Fig. 3.4. **b:** Simulated substrate modes for the 200 µm substrates, showing good agreement in both mode shape and frequency with the measured results. **c:** Spectrum of the measured substrate modes with and without tape, and Q-factors of prominent modes. Dashed lines indicate the detector noise floor, solid black line is Lorentzian fit (only shown for taped case). The curves are vertically offset for clarity.

(grey), and the collective of measurements without driving (blue). The two are offset vertically for clarity. We obtain a Lorentzian fit at 122.85 kHz, with linewidths corresponding to $Q = 1.2 \times 10^4$ (no tape) and $Q = 4 \times 10^3$ (tape), which are the values used in Sec. 3.2.3.

It is worth noting that these fits come with some uncertainty, as we cannot exclude that there is some remaining signal from any of the membrane modes. These fits also represent only a single chip, though the frequencies and Q-factors of the substrate modes of the other chips used in this chapter are similar. Fig. 3.4 combines the results of these three chips, and the confidence interval of that theory fit encompasses the spread in substrate Q-factors of the three chips.

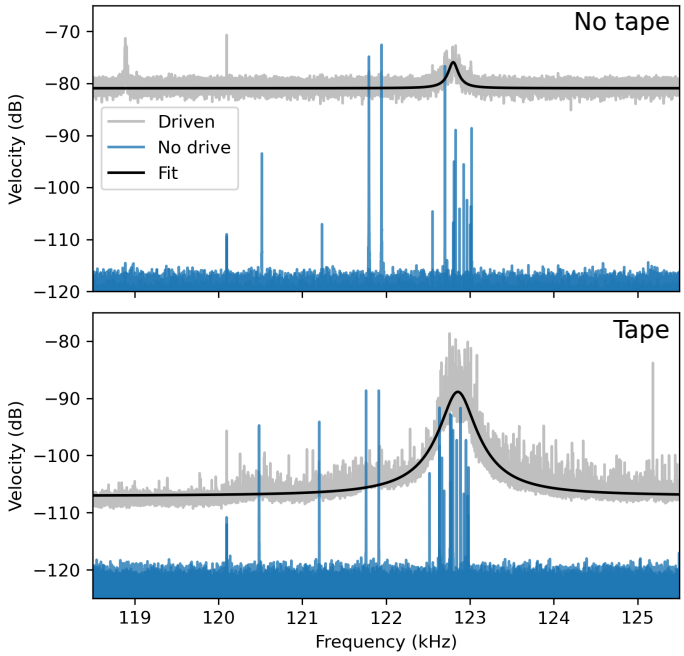

Figure 3.8: Comparison of substrate modes without (top) and with (bottom) tape. Grey curves show the average of white-noise-driven measurements of all devices on a particular chip (offset vertically for clarity). Blue curves show all the individual measurements without drive (stacked), representing all membrane resonances. In black, Lorentzian fit to the substrate mode.

3.4.3. Measurement method and fabrication

The spectra and ringdowns shown in this chapter were obtained using a Polytec MSA400 laser Doppler vibrometer. It uses the Doppler frequency shift of light reflected from a device under test due to the out-of-plane motion to quantify the velocity. The device mechanical spectrum can be obtained by Fourier-transforming the time signal obtained from the vibrometer, and using the scanning stage, mode shapes can be imaged for identification of the modes. To perform a ringdown measurement, we applied a (typically) 10 mV peak-peak sine wave using a Rigol D1032Z signal generator such that we resonantly drive the motion of a particular mode of the device under test. Then we record the time trace after stopping the driving, to observe the energy decay of the driven mode. We perform a short-time Fourier transform on successive parts of the time-signal using scipy's stft function to obtain the temporal behavior of the mechanical spectrum. By making a line-cut along a particular frequency, we can extract peak amplitude as a function of time. In logarithmic scale, we expect a linear curve where the slope b corresponds to the Q-factor via $Q = \frac{2f}{\log 10 b/10}$. This way, we extract the Q-factor.

We performed the experiments by placing a chip containing 25 devices (membrane) on the sample holder inside the vacuum chamber (i.e. without tape). We

operate at a pressure $< 1 \times 10^{-5}$ mbar. For every device, we record the spectrum with and without white noise driving, and determine the frequency of the fundamental mode. Then, we perform three sequential ringdown measurements at that frequency. After every device is measured, we vent the chamber and remove the chip. We then apply a piece of carbon tape to the sample holder, taking care to use a similar-size piece every time. We place the chip such that the carbon tape is in the center of the chip. To create the most repeatable connection between chip, tape and sample holder we gently press down on the outside of the chip with tweezers, to ensure good contact. We then pump down and repeat all the measurements (spectrum with and without white-noise driving, and ringdowns). We perform the data analysis and fit of the Q-factor afterwards.

The trampoline resonators were fabricated on 100 nm thick stoichiometric silicon nitride (Si_3N_4) deposited by low-pressure chemical vapor deposition onto a 1 mm thick silicon substrate. The pattern was first written on a positive tone resist by electron beam lithography and, after the development, transferred on the Si_3N_4 layer using ICP (Inductively Coupled Plasma) etching. The resist was then removed using dimethylformamide followed by two cleaning steps with piranha solution and diluted hydrofluoric acid. Finally, the trampoline resonators were released using an isotropic ICP etch with SF_6 at -120 °C for 30 seconds thus completing the fabrication process.

3.4.4. Stress redistribution due to photonic crystal

We fabricate the devices from a 1 mm thick Si wafer coated with 100 nm Si_3N_4 on both sides, which have a 1 GPa tensile pre-stress. When we release the patterned membranes in a dry-release etch step, the stress redistributes. In sweeping the photonic crystal lattice spacing a and hole radius r, we found that the yield is reduced below a certain mass ratio and that the membranes broke often at the edge of the photonic crystal. We simulate this stress redistribution in our suspended membrane for three different mass ratios, the lowest and highest one used for the measurements in this chapter (Fig. 3.9, top and middle panel) and one where most membranes collapsed (bottom panel).

The redistribution of the stress shows a clear pattern: In the center of the membrane pad, the stress is reduced to zero regardless of the photonic crystal parameters. At the edge of the photonic crystal, the stress greatly increased, because the effective width perpendicular to the tensile axis (diagonal in Fig. 3.9, along the length of the tether) is reduced by the photonic crystal holes. For the lattice spacing and hole radius where the yield was low (bottom panel), the stress in this region approaches the yield stress of Si_3N_4. In the tether itself, the stress is lower the closer we get to this low-yield region. This is likely due to the membrane having less material to pull the tether when the mass ratio of the photonic crystal is low, which results in low tether stress and high stress at the photonic crystal edge. The yield stress of Si_3N_4 thus limits the achievable mass ratio by sweeping the photonic crystal parameters. This corresponds to the photonic crystal edge being a common point of failure of the devices.

Parameters	U_{el}(J)	U_{be}(J)	Q/Q_0
$a = 1372$ nm $r = 475$ nm	$7.6 \cdot 10^{-26}$	$2.4 \cdot 10^{-29}$	3198
$a = 1306$ nm $r = 500$ nm	$4.4 \cdot 10^{-26}$	$1.7 \cdot 10^{-29}$	2628
$a = 1240$ nm $r = 525$ nm	$2.3 \cdot 10^{-26}$	$1.5 \cdot 10^{-29}$	1536

Table 3.1: Q-factor enhancement due to dissipation dilution for the different photonic crystal parameters

In Fig. 3.9, we show the stress distribution depends on the photonic crystal parameters. Since the bending losses of these resonators are governed by dissipation dilution due to stress, we estimate the change in the Q-factor from the different stress distributions. We obtain the elongation (U_{el}) and bending (U_{be}) energies of the fundamental mode of each resonator by integrating over the domain S [61, 63, 64],

$$\begin{aligned} U_{\mathrm{el}} &= t \int \left(\sigma_{xx} u_{z,x}^2 + \sigma_{yy} u_{z,y}^2 + \sigma_{xy} u_{z,x} u_{z,y}\right) \mathrm{d}S, \\ U_{\mathrm{be}} &= \frac{Et^3}{12(1-\nu^2)} \times \int \left(u_{z,xx}^2 + u_{z,yy}^2 + 2\nu u_{z,xx} u_{z,yy} + 2(1-\nu)^2 u_{z,xy}\right) \mathrm{d}S. \end{aligned} \tag{3.4}$$

Here, σ is the stress distribution, u_z the out-of-plane resonator displacement and the comma denotes derivative with respect to that coordinate. We use thickness $t = 80$ nm for the Si_3N_4, which is reduced from the deposited thickness (100 nm) by the etching, $E = 250$ GPa the Young's modulus and $\nu = 0.23$ the Poisson ratio of Si_3N_4. This ratio of these two energies gives us the enhancement of the Q-factor from the intrinsic (bending) Q_0 of unstressed Si_3N_4 due to dissipation dilution, via

$$Q = Q_0 \left(1 + \frac{U_{\mathrm{el}}}{U_{\mathrm{be}}}\right). \tag{3.5}$$

with [61, 111] $Q_0 \simeq 6900t/100$ nm to normalize it to a Si_3N_4 thickness of 100 nm.

From the simulations of the stress redistribution, we calculate the elongation and bending energies of the fundamental membrane mode, and report the expected enhancement in the Q-factor due to the dissipation dilution in Table 3.1. Over the range of parameters with a high fabrication yield, the enhancement of the Q-factor is not too dissimilar (20% change between the top two rows). This validates our assumption that changing the photonic crystal parameters is not the dominant factor in any trends in the Q-factor that we see. Furthermore, when we plot all the Q-factors of the resonators in this chapter, Fig. 3.10, we see that the bending-loss limited Q-factor that follows from the model (dashed black line) is higher than the measured ones, meaning we are likely not in the bending-loss-limited regime.

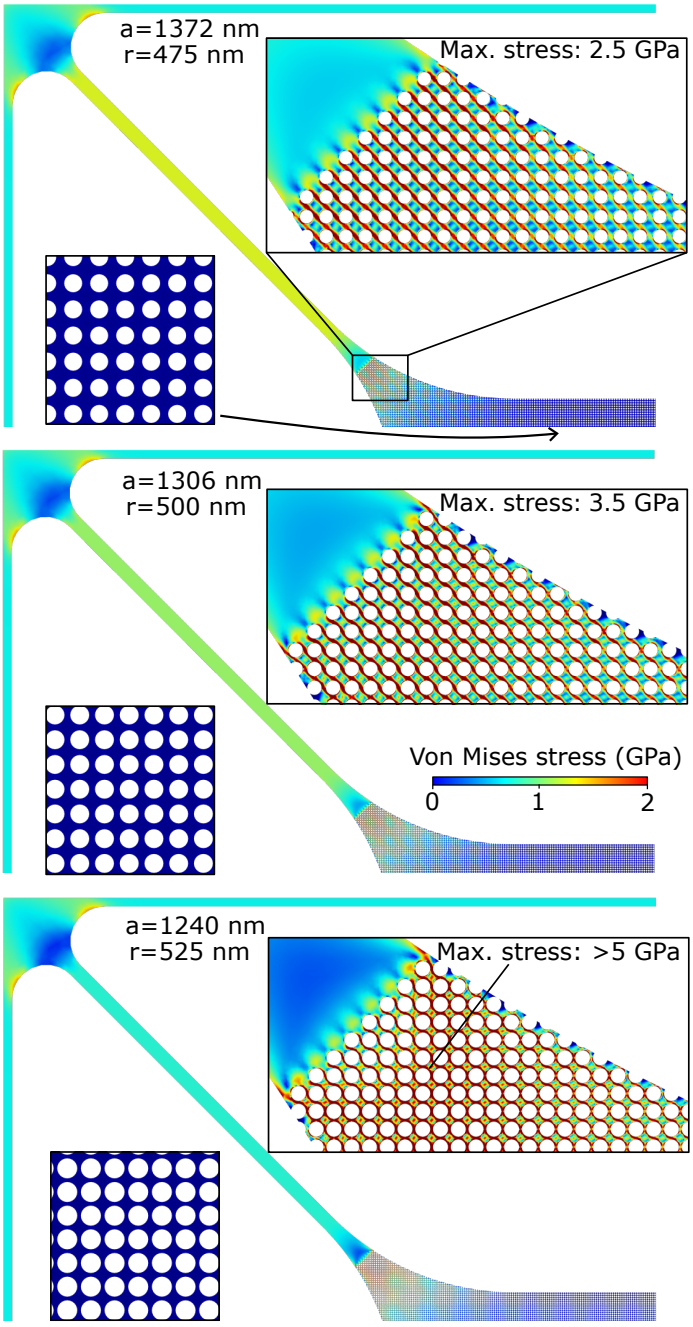

Figure 3.9: Von Mises stress in Si_3N_4 membrane due to 1 GPa initial stress redistributing upon release of suspended structure, for different photonic crystal parameters. The stress is focused at the start of the photonic crystal, depending on the photonic crystal lattice parameter a and hole size r. In the center of the pad, the stress is independent of these parameters. Color scale is the same for all panels.

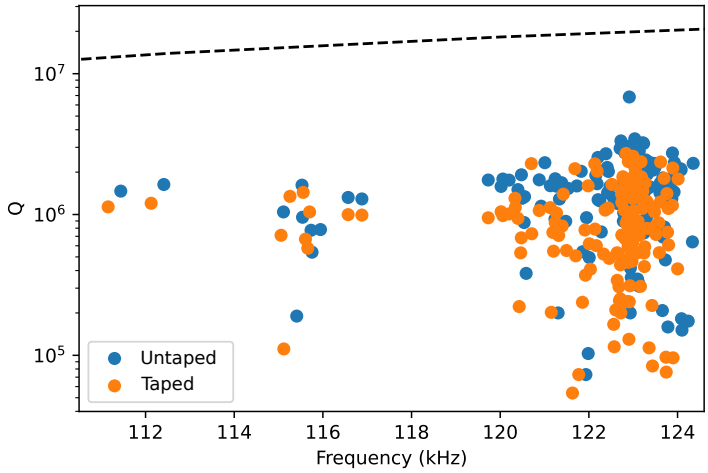

Figure 3.10: Measured Q-factors of the resonators, for the taped and untaped substrate. Black dashed line denotes the bending-loss-limited Q-factor calculated from the dissipation-dilution model described in the text.

3.4.5. Q-reduction by laser heating

We perform ringdown measurements by driving resonators with a sinusoidal excitation at their resonance frequency, which results in a high velocity detected by the Polytec MSA400 vibrometer. In some of the resonators, a significant velocity can be detected without any driving signal applied to the piezoelectric mounted on the sample holder. Some measurements even show negative Q-factors (i.e. increase in resonator displacement while the piezo shaker is not driven), indicating that there is another drive mechanism present in our system. This drive mechanism is the subject of chapter 4, so we limit ourselves to a brief description and focus on the effect it has on resonator Q-factor.

In short, the driving is associated with strong absorption of the 633 nm laser light due to the photonic crystal structures on our membrane. This leads to heating and can cause optothermal self-oscillation if the laser power is sufficiently high [112], which can drive the mechanical motion from an unmodulated continuous-wave laser. In our system, this likely happens due to the heating causing thermal expansion, which modulates the stress in the membrane. This effectively creates an optothermal parametric drive mechanism. It is not easy to distinguish the presence of this second driving mechanism, especially if it is weaker than the piezoelectric driving.

There are two properties we can associate with the presence of the heating and optothermal driving mechanism. The first is that the Q-factors measured when there is optothermal driving tend to show a large variance (between directly sequential measurements on the same device). This originates from the fact that the photonic crystal structures are somewhat position-dependent in our membrane due to the stress redistribution after release (previous section). Because of this, the

absorption, heating and optothermal driving are position-dependent, and Q-factors measured at slightly different positions might be very different. Empirically, we estimated a variance $> 20\%$ between the Q-factors of the three ringdowns performed for each device was a good indicator for the presence of the heating and optothermal driving. Thus we use this as a cutoff, and reject all measurements which show this large variance.

The second property is the presence of integer multiples of our fundamental mode, 'overtones' as named by others [113, 114]. These indicate the resonator is in the nonlinear regime, even though a ringdown measurement might appear linear. Thus we also reject the measurements that display these overtones.

We show an example of such laser-driven ringdown measurement in Fig. 3.11, where we measure the same membrane in directly subsequent measurements, but reduce the laser power by adding a neutral density filter (Thorlabs NE506A, 25% transmission, from 3.6 mW to $\simeq$1.0 mW) in the beam path for the second measurement. We record the time trace, and perform a Fourier transform with a shifting time window to visualize the change in the velocity spectrum over time. In both Figs. 3.11**a** and **b**, we clearly resolve the fundamental mode, but in Fig. 3.11**a**, a second mode at twice the fundamental frequency is present. The presence of this mode demonstrates that the membrane is in the nonlinear regime [113, 114]. We want to stress that this second mode is not related to the transduction nonlinearity common to large displacements in interferometric setups (see e.g. Dolleman et al. [115]), as laser Doppler vibrometers are not affected by these.

We take a horizontal cut of the spectra of Fig. 3.11 to obtain the ringdowns of the modes at the fundamental frequency, and at precisely double the fundamental frequency, which we plot in Fig. 3.11**c,d**. By performing a linear fit, we extract the Q-factor of each of these modes, and the Q-factor from the reduced power measurement (**d**, $Q = 3.83 \cdot 10^6$ at 111.3 kHz) is larger than the Q-factors from the full-power measurement (**c**, $Q = 0.57 \cdot 10^6$ at 111.3 kHz $Q = 0.63 \cdot 10^6$ at 222.6 kHz). The difference in the operating laser power (cf. heating and optothermal driving)is thus related to a large difference in the Q-factor measured by a ringdown.

The ringdowns and Q-factors reported supporting Fig. 3.4 were all taken at the minimum operating laser power of 1 mW. However, the heating and optothermal driving do not appear equally strong in all membranes, and some resonators are still driven into the nonlinear regime even at reduced power. To further reduce the absorption and increase the thermal contact to the substrate, we read out the velocities from the tether foot (closest to the substrate) instead of at the membrane pad. This comes at a cost of reducing the measured velocity, as the tether foot has a much lower displacement amplitude than the center of the membrane, reducing the signal-to-noise ratio. This makes it difficult to gauge if we are in the linear regime, as the mode at twice the fundamental frequency might be hidden by the detector noise.

In summary, there is a heating and optothermal driving effect present in some of our membranes, due to the absorption facilitated by the photonic crystal structures. This driving mechanism happens even at the minimum operating power of the setup, and affects the Q-factors obtained from a ringdown. To exclude these effects,

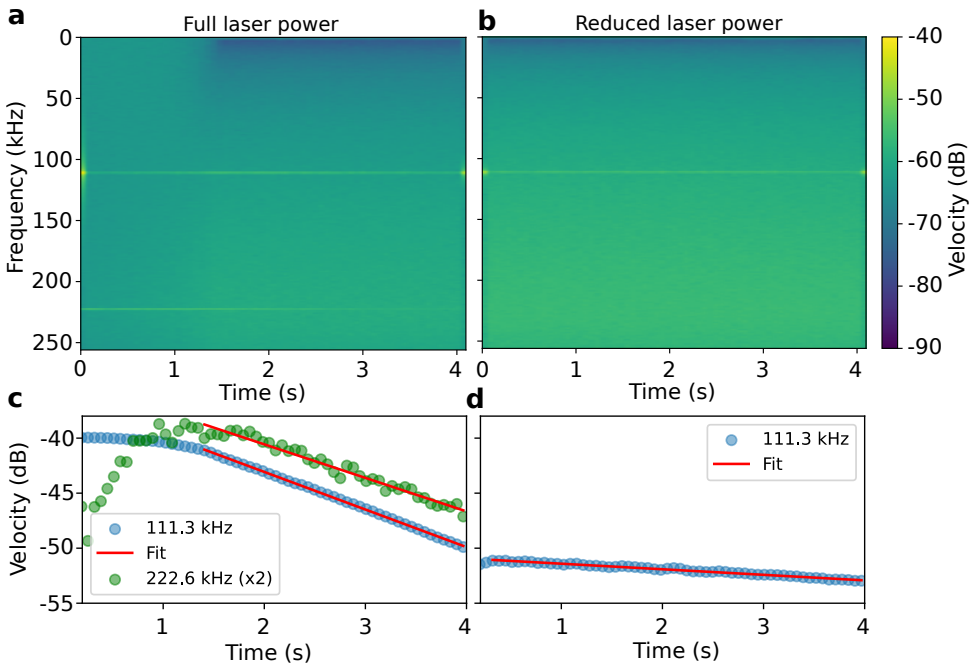

Figure 3.11: **a,b:** Velocity amplitude spectrum plotted as a function of time for full and reduced laser power. In **a**, a second mode at exactly double the fundamental mode frequency is visible, which is absent in **b**. This mode is attributed to the laser driving the resonator into the nonlinear regime. **c,d:** Ringdowns (horizontal time-cuts) of the modes in **a,b** respectively. The mode at twice the fundamental frequency is weaker, so it has been scaled by a factor of two.

we remove the devices from our dataset if they display a large variance ($> 20\%$) in the Q-factors measured in directly sequential ringdowns, or if they display the second mode (overtone) in their spectra.

3.4.6. Resonators coupled via the substrate

In Sec. 3.2.4, we describe two specific resonators coupled to each other via the substrate. To identify which specific membranes are coupled, we compare the resonance frequencies of the set of five resonators with nominally the same design and frequency. By comparing their resonance frequencies, the resonator reported in Sec. 3.2.4 (device 22, blue in Fig. 3.12**a**) was most likely coupled to device 23 (orange in Fig. 3.12**a**). The displayed spectrum of device 22 was taken before the measurements of Sec. 3.2.4, shown in Fig. 3.5**a**, while the spectrum of device 23 was taken after those measurements, and thus approximately one hour after the spectrum of device 22 was measured. It follows that there was likely some creep in the Si_3N_4 that caused a downshift of the spectrum of device 23, meaning it was closer in frequency to device 22 when the coupling was observed.

As the system is fully passive (i.e. there is not mechanism to actively tune the frequency with) and creep is not reversible, it is difficult to a posteriori verify which

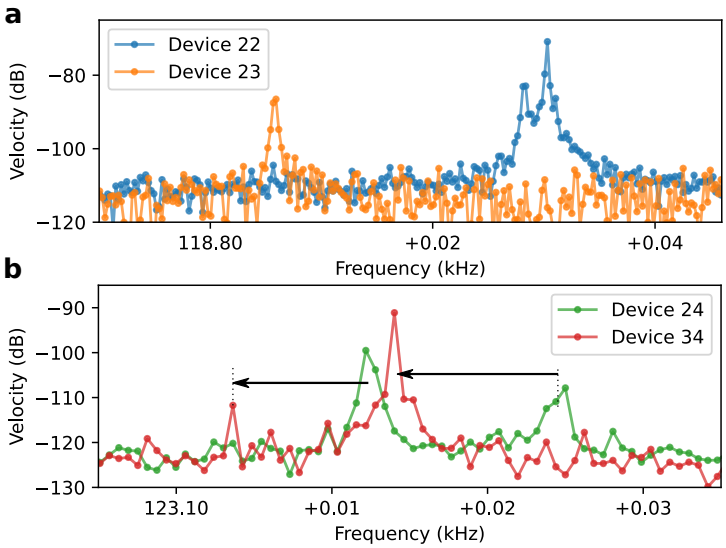

Figure 3.12: **a** Spectra of the two mechanical resonators coupled in Fig. 3.5. The split peak of device 22 shows coupling. Device 23 was measured 1 hour later, the frequency decreased over time due to creep. **b** Spectra of two devices measured in swift succession (20 minutes delay), demonstrating that both devices show the split peak. In this time frame, there is a 9 Hz downwards frequency shift. Arrows identify the shifted peaks, the peak of the mode belonging to the read-out membrane itself is stronger than the one of the coupled membrane.

two resonators were coupled. However, the reported mechanical modes are the fundamental modes of the trampoline resonators, which do not show splitting in case of imperfections. This excludes the possibility of the split peak originating from the same resonator. Furthermore, we have observed similar coupling in more devices, specifically devices 24 and 34 of a different chip. Here, the spectra were measured in quick succession (< 20 minutes delay), plotted in Fig. 3.12**b**. In both spectra, two peaks are visible, shifted by approximately the same amount. We identify the stronger peak as the one belonging to the read-out membrane, as the peak from the coupled membrane is likely weaker.

Based on the observation of a pair of resonator spectra where both show the double peak, and the quantitative match between the two-coupled-resonator model and the data in Fig. 3.5, we consider it clear that there is coupling between two discrete modes. By the arguments above, it is most likely that it is coupling between devices 22 and 23. On the chip, these resonators are separated by 1.5 mm (center-to-center distance).

In the Secs. 3.2.3 and 3.2.4, we use two models to describe coupling between the high-Q resonator and the substrate (Fig. 3.14**a**, stacked model), and between two high-Q resonators (coupled model). For the resonator-substrate coupling, the stacked model provides a straightforward match to the physical system: The Si_3N_4 resonator is on top of the Si substrate on top of the sample holder ('ground'), so any

motion of the substrate automatically affects the position of the Si_3N_4 resonator. Conversely, for the resonator-resonator coupling the positions of the resonators are effectively independent, except for some weak coupling spring that moves energy from one resonator to the other, so the coupled model provides the most straightforward description.

While the two models appear different, their parameters can be related relatively straightforwardly if the damping is small. We use the parameter m_1, m_2 for the effective resonator masses and k_1, k_2 for their spring constants. The coupled model has additional spring k_3 that couples the two resonators, by which we isolate the coupling rate J between the resonators such that $J^2 = \frac{k_3^2}{m_1 m_2}$. In the regime of low damping (i.e. no viscous term accompanying k_3), we can directly relate the parameters of the stacked model to those of the coupled model via

$$\begin{aligned} k_{s,2} &= k_{c,2} + k_{c,3} \\ k_{s,1} &= \frac{k_{c,1} + k_{c,3}}{k_{c,3}^2} k_{s,2}^2 - k_{s,2} \\ m_{s,1} &= \frac{k_{s,2}^2}{k_{c,3}^2} m_{c,1} \\ m_{s,2} &= m_{c,2}, \end{aligned} \tag{3.6}$$

where the subscripts s, c denote the stacked and coupled model parameters respectively. This allows for translation of the coupling strength between the resonators to the coupling strength between resonator and substrate.

To simulate the coupling between the resonators, we start from the equations of motion for the resonator positions from the coupled-resonator model,

$$\begin{aligned} \ddot{x}_1 + \gamma_1 \dot{x}_1 + \omega_1^2 x_1 + J^2 x_2 &= 0 \\ \ddot{x}_2 + \gamma_2 \dot{x}_2 + \omega_2^2 x_2 + J^2 x_1 &= 0. \end{aligned} \tag{3.7}$$

We can write these as a set of four coupled first-order differential equations (for $[x_1, v_1, x_2, v_2]^T$, the positions and velocities of the two resonators respectively) and numerically integrate them. The resulting velocity of one of the resonators can be extracted and compared to the measured velocity, which we show in Fig. 3.13. The envelopes of the two curves match very well.

The resulting time-trace is Fourier-transformed with a shifted time window in exactly the same manner as the measured data, which sacrifices some frequency resolution but allows us to extract the time-dependent behavior of the resonance peaks. This way, we extract a ringdown measurement of a specific mode from the time trace, and the result is shown in Fig. 3.5.

We can further corroborate the existence of coupling between individual resonator on chip by utilizing a finite element model of a substrate with two trampoline resonators, Fig. 3.14**b**. The two resonators are meshed identically to ensure

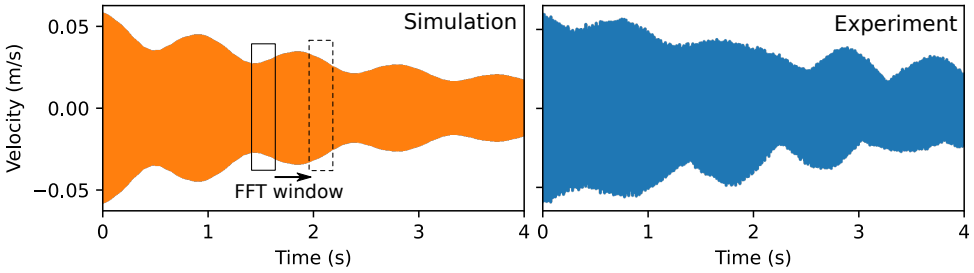

Figure 3.13: Experimentally obtained (right) and simulated (left) velocities of resonator ringdown. Performing a Fourier transform with a shifting time window allows extracting the time-dependent amplitude decay that describes the ringdown of a resonator mode(s).

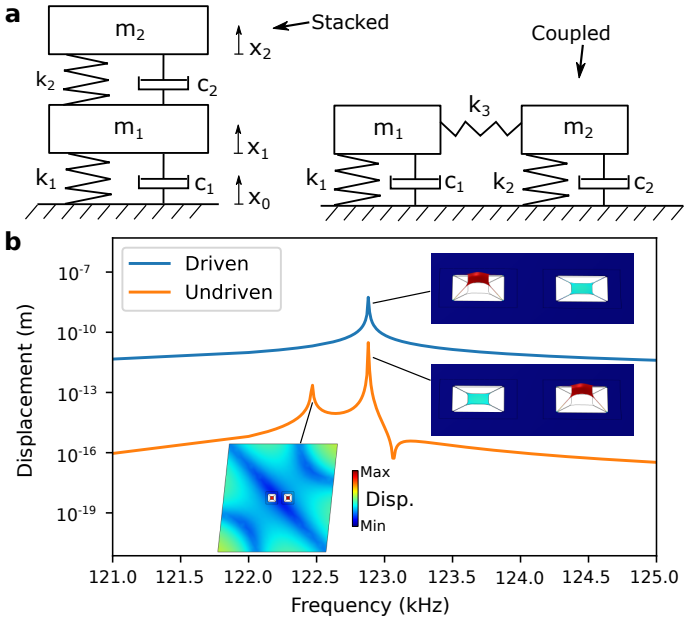

Figure 3.14: **a:** Schematic of stacked 2-DOF (degrees of freedom) model and of coupled two-resonator model. **b:** Frequency response of membrane driven with 1 pN harmonic perturbation (blue) and of the membrane coupled through the substrate. Insets show substrate resonance and degenerate resonator modes.

their eigenmodes are the same, and spaced 1.5 mm apart on the substrate. We evaluate their coupling by adding a 1 pN out-of-plane harmonic perturbation force in the center of one of the resonators, and tracking the resulting displacement in the center of both resonators.

For the driven resonator (Fig. 3.14**b**, blue curve), the resulting displacement spectrum is sharply peaked around the fundamental mode. For the undriven resonator (orange curve) we see two peaks, one associated with the substrate mode and another associated with the resonator mode, shown in the insets. There is also

an antiresonance visible, where the response of the undriven resonator is perfectly out-of-phase with the response of the driven resonator. The peak at resonance means that there is energy transfer from one resonator to the other. At the resonator frequency, the simulated amplitude of the undriven resonator is a factor ~ 180 smaller than that of the driven resonator, which is not too far off of the ratio $\omega_1/J \approx 140$. This suggests that the coupling rate extracted from the fits is a reasonable match with the FEM simulations.

4

Mechanical overtone frequency combs

Mechanical frequency combs are poised to bring the applications and utility of optical frequency combs into the mechanical domain. So far, their main challenge has been strict requirements on drive frequencies and power, which complicate operation. We demonstrate a novel, straightforward mechanism to create a frequency comb consisting of mechanical overtones (integer multiples) of a single eigenfrequency, by monolithically integrating a suspended dielectric membrane with a counter-propagating optical trap. The periodic optical field modulates the dielectrophoretic force on the membrane at the overtones of a membrane's motion. These overtones share a fixed frequency and phase relation, and constitute a mechanical frequency comb. The periodic optical field also creates an optothermal parametric drive that requires no additional power or external frequency reference. This combination of effects results in an easy-to-use mechanical frequency comb platform that requires no precise alignment, no additional feedback or control electronics, and only uses a single, mW *continuous wave laser beam. This highlights the overtone frequency comb as the straightforward future for applications in sensing, metrology and quantum acoustics.*

Put a membrane
in an optical trap
make it sound like a string

This chapter was written together with A. Ganesan, A. Cupertino, S. Gröblacher, and R. A. Norte, is in preparation and can be found at 2207.06401. All measurement data, analysis and calculation scripts, and simulations are available at 10.4121/19821016

4.1. Introduction

Over the last quarter century, optical frequency combs have become key tools for metrology, timing and spectroscopy [116, 117], and are indispensable in many laboratories around the world. The fixed frequency and phase relations between the many different tones of a comb have revolutionized fields as astronomy [118] or cosmology [119], and allowed tests of fundamental physics with atomic clocks [119, 120]. Recently, a new paradigm of frequency combs has appeared in the phononic [121–123] or optomechanical [124, 125] regimes, also called acoustic or mechanical frequency combs. This development began in nonlinear dynamics, where it was realized that mixing in coupled oscillators may lead to a series of sidebands [126], that can be regarded as a frequency comb if there exists a fixed phase relation [122] between these sidebands. Experimental demonstrations have shown mechanical frequency combs exist in different mechanical systems [127–136], and have explored connections to well-known concepts in nonlinear dynamics such as bifurcations [127, 130, 137], 3- or 4-wave mixing [126, 129, 138, 139], and symmetry-breaking [140]. The fixed frequency and phase relation between the comb teeth allows the application of techniques known from optical combs. These can e.g. improve position sensing accuracy in optically opaque materials [141] such as underwater or medical imaging. Mechanical frequency combs can further be used to track and stabilize mechanical resonances [142, 143], and enhance Brillouin microscopy [144, 145]. Recent proposals from the field of quantum acoustics [146] foresee a vital role for mechanical frequency combs in transduction [147] or coupling to multiple qubits [148]. Until now, mechanical frequency combs have been hamstrung by the (generally) nonlinear phononic dispersion relation, which demanded high drive powers, carefully designed mode frequencies or engineered mechanical nonlinearities to obtain an evenly spaced set of modes.

In a different regime of breakthrough physics, optical trapping has allowed us to manipulate and control small particles ranging from single atoms [149, 150] to micrometers [151] in size. These particles are confined by the potential created by a strongly focused laser, which has enabled exploration of cutting-edge fields in both fundamental physics and biology. Using optical traps (tweezers), biologists can precisely manipulate anything from single strands of DNA [152] to whole living cells [153]. Optically trapped ultra-cold atoms and levitated nanoparticles are perfect test beds for fundamental physics involving gravity and mesoscopic quantum mechanics [154–156]. Although optical trapping and frequency combs are widespread techniques, there is little direct overlap between these regimes of physics.

In this chapter, we uniquely interface optical traps with mechanical frequency combs via a novel mechanism that enables frequency combs without requiring feedback control, external drives and frequency references, or precision optics. We observe that due to a weak counterpropagating optical trap [157, 158], strongly driven silicon nitride (Si_3N_4) membranes vibrate not only at their mechanical eigenfrequencies, but at perfect integer multiples of a single frequency, which can form a mechanical frequency comb. The standing-wave optical field exerts a dielectrophoretic force on the membrane, which is modulated by the membrane's motion

as it crosses extrema of the optical field. If the displacement is small, this interaction can suppress mechanical dissipation [159], but if the displacement becomes of the order of a quarter wavelength, it creates integer multiple copies of the original membrane motion ('overtones' [113], see Sec. 4.6.1). These overtones share a fixed frequency and phase relation, and thus form a frequency comb while avoiding all difficulties of engineering a linear mechanical dispersion relation. Strikingly, the overtones are solely dependent on the amplitude of motion and the optical field, and thus independent of drive mechanism. We utilize an optothermal parametric drive based on the same single, unmodulated optical field to bring the membrane to self-oscillation. This allows us to build a mechanical comb without any additional pump tone or frequency reference, which makes overtone combs uniquely simple to generate. We will first describe the mechanism that creates the overtones and study their behavior in the frequency domain. Then, in the the time domain we will show the fixed phase relation that makes the overtones act as a frequency comb.

4.2. Overtone and driving mechanism

In this section, we first describe the physical system and the mechanism that creates the overtone frequency combs, and then introduce a more quantitative model for their dynamics. The system consists of a suspended $t = 80$ nm thick Si_3N_4 trampoline membrane [13] (Sec. 4.6.2), shown schematically in Fig.4.1**a**. It rests ~ 10 µm above a backplane formed by the silicon (Si) substrate, and a laser ($\lambda = 633$ nm, $p \lesssim 3$ mW) from a commercial Polytec MSA400 laser Doppler vibrometer is incident on the membrane. At this wavelength, the Si_3N_4 reflects $\lesssim 30\%$ of the light, and Si reflects about 35%. Part of the light thus forms a standing wave, Fig. 4.1**a**, periodic in the direction of the mechanical motion.

The dielectric Si_3N_4 experiences a dielectrophoretic force proportional to the gradient of the optical intensity, similar to a particle in a counterpropagating-wave optical trap [157, 158]. The trap also exerts a radiation pressure force, but this is negligible in our system ([124] and SI Sec. 4.6.3). If the dielectric moves (e.g. by driving a mechanical eigenmode), it will experience a restoring force from its own elastic potential (blue solid line in Fig. 4.1**b**), with an additional component from the optical field (red solid line). For small motion ($|x| \ll \lambda/4$, cyan line in Fig. 4.1**b**), the optical potential functions as an additional spring [159]. However, if the motion of the membrane is of the order of the optical potential period ($\lambda/2$), the modulated potential generates the overtones.

This can be seen as follows: The restoring force of the mechanical potential switches sign twice per oscillation (arrow pairs in Fig. 4.1**b**). If the motion is large enough (grey, orange lines) for the resonator to cross multiple extrema of the optical field, the optical component of the restoring force switches direction $2n$ times per oscillation (n integer number of optical extrema). If the original motion was at mechanical eigenfrequency ω_0, this effect generates motional components at $n\omega_0$, which are the overtones of the original eigenmode. We will show in Sec. 4.4 that these overtones have a fixed phase relation and thus form a mechanical frequency comb. Because the overtones originate from the combination of the optical and mechanical potential, they completely avoid the difficulties of engineering the me-

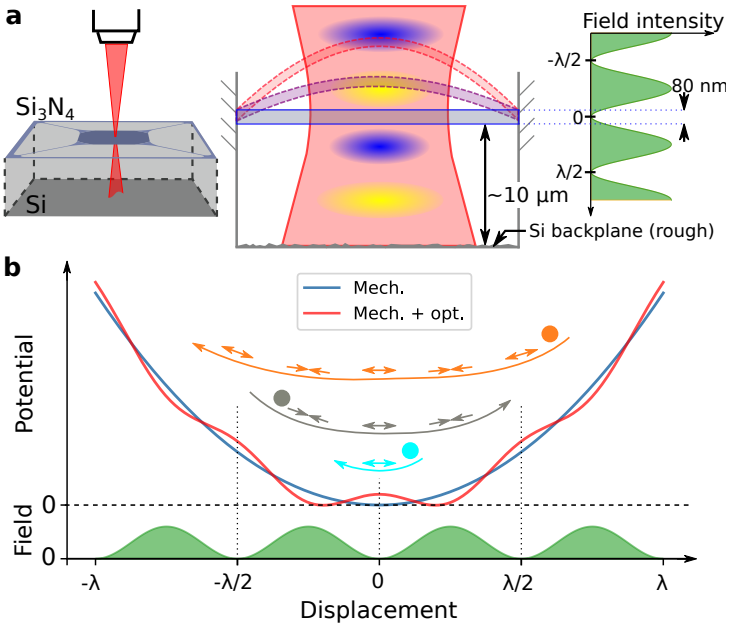

Figure 4.1: **Schematic of overtone frequency comb. a:** The suspended Si_3N_4 membrane is subject to an out-of-plane laser, focused through a microscope objective. Part of the light is reflected from the Si backplane and interferes with the incident light, creating a counterpropagating wave optical trap such that the field intensity (green) is periodic. The membrane is clamped to the substrate, and motion is predominantly out-of-plane (purple, red dashed lines). **b**: The optical field intensity causes a (spatially) periodic modulation of the elastic potential through the dielectrophoretic force (red, blue lines). For small motion of a membrane at frequency ω_0 (cyan), the restoring force component from the optical field switches sign twice per oscillation (arrow pairs), same as the elastic potential. However, for larger membrane motion (grey, orange), more optical extrema are crossed so the optical field component switches sign multiple times per oscillation, efficiently generating frequency components at $n\omega_0$ ($n = 2, 3, 4, ...$) which form an overtone frequency comb.

chanical dispersion while still resulting in perfectly evenly spaced tones. In contrast to other combs, the tones do not exist around some carrier frequency.

We model the overtone frequency comb using a resonator described by displacement $x(t)$ ($x = 0$ mechanical equilibrium), with resonance frequency ω_0 and decay rate γ, where we have divided by the simulated effective mass $m_{\text{eff}} \simeq 12 \times 10^{-12}$ kg. We write the dielectrophoretic force as a proportionality constant F_{o} (units of force) times the gradient of the periodic part of the optical intensity, $\nabla E^2 \propto \sin\left(\frac{4\pi}{\lambda}(x - x_{\text{off}})\right)$. This way we can move finite-size effects of the membrane into F_{o}, which we numerically evaluate in Sec. 4.6.3. We obtain the equation of motion

$$\ddot{x} + \gamma\dot{x} + \omega_0^2 x = \frac{F_{\text{o}}}{m_{\text{eff}}} \sin\left(\frac{4\pi}{\lambda}(x - x_{\text{off}})\right), \tag{4.1}$$

which requires only a suitable initial condition $|x|_{t=0} \gtrsim \lambda/4$ to demonstrate the creation of overtones. This condition is much larger than typical interferometric

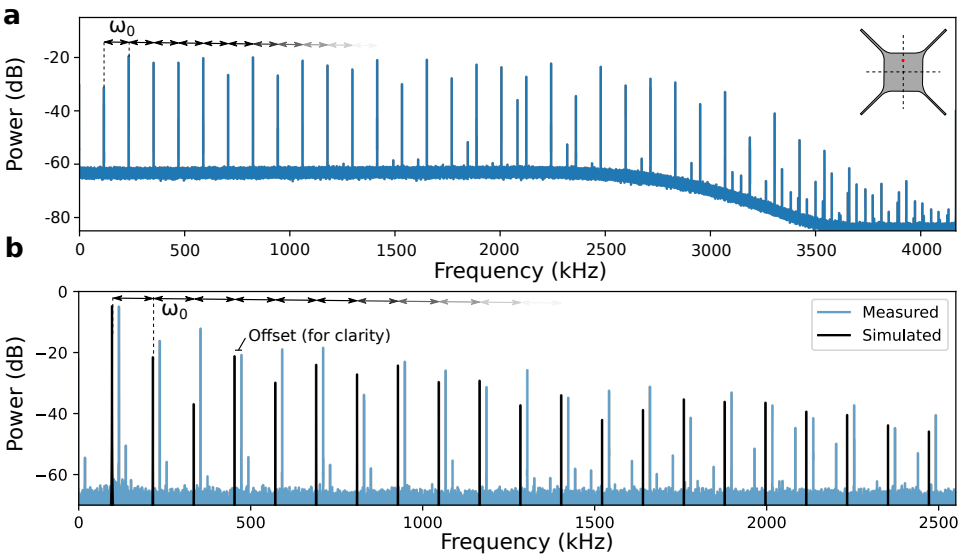

Figure 4.2: **Overtone frequency combs. a**: Measured spectrum of a mechanical frequency comb of the fundamental mode ($\omega_0 = 2\pi \times 118.049$ kHz) of a suspended Si_3N_4 membrane, consisting of 35 peaks spaced by ω_0. The overtones are spectrally flat until ~ 2200 kHz, after which their amplitude drops exponentially. Inset shows the location of the laser spot to generate and read out the comb. The additional peak around 2083 kHz are from a different mechanical mode, see Sec. 4.6.6. **b**: Simulated overtone comb spectrum (black), obtained by integrating Eq. (4.1). The simulation shows quantitative agreement to measured comb (blue), for fit parameters $x_0 = 900$ nm, $v_0 = 0$, $F_0 \simeq 50$ pN, $x_{\mathrm{off}} = 20$ nm.

position measurements, which is why we use a laser Doppler vibrometer that is capable of resolving such large displacements (Sec. 4.6.2). Eq (4.1) also shows that the overtones are independent of the choice of drive (e.g. piezoelectric, electrostatic, thermal). By utilizing the spatially-periodic optical field through optothermal effects [112], we can create a parametric drive powerful enough to bring the membrane to self-oscillation. That is, when the resonator moves through the field, the optical intensity it experiences is modulated at twice the frequency of the original motion. This modulates the resonator frequency through absorption (thermal expansion), thus creating an optothermal parametric drive (see Sec. 4.6.4). Our membranes are patterned with a specific photonic crystal that enhances the absorption of 633 nm laser light. This allows a single, continuous-wave laser beam of mW power to bring the membrane into self-oscillation. While we verify that the overtones can also be generated via inertial (piezo) driving (see Sec. 4.6.5), we leverage the optothermal drive to avoid any external pump tone or frequency reference. This property of overtone combs is unique within the mechanical frequency combs, and allows for significantly simpler setups.

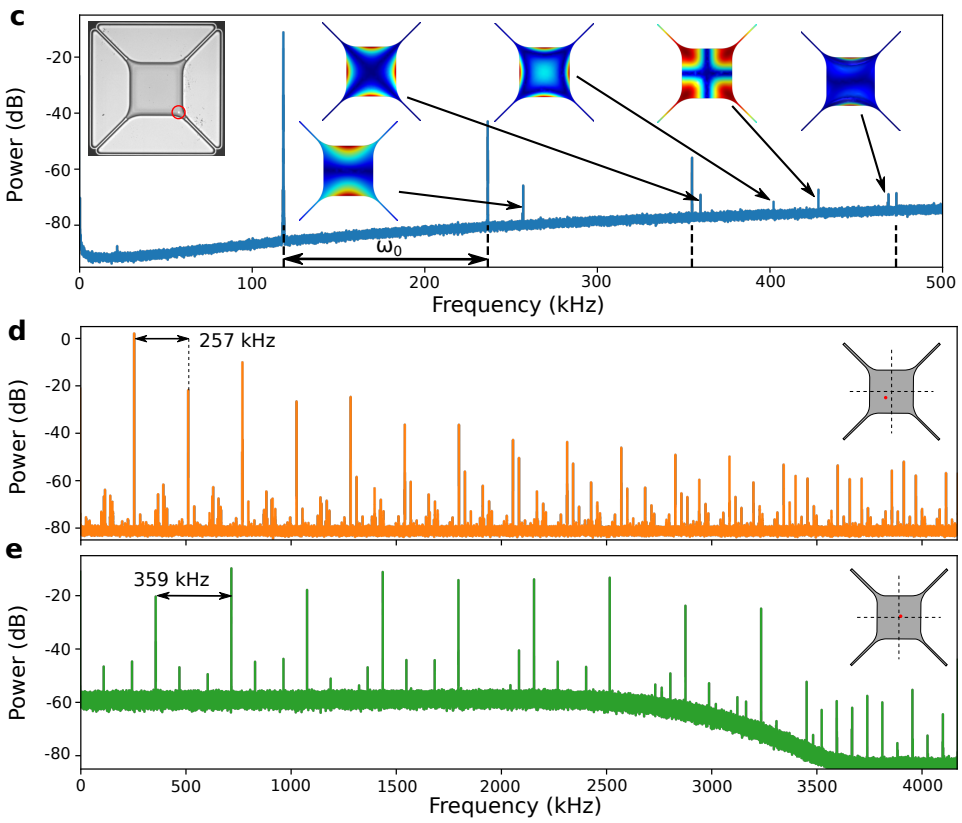

Figure 4.3: **Overtone frequency combs. c**: Simultaneous measurement of fundamental-mode frequency comb (first four teeth) and higher-order mechanical modes of the membrane. Insets: Laser spot position (left) and mode shapes. **d,e** Mechanical frequency combs of the second mode (257 kHz) and third modes (359 kHz). Difference in the noise floor is due to different decoders used due to overloading. The 257 kHz mode has a near-degeneracy, so the comb spectrum is less clean. Insets show the laser position to drive and read out the different modes.

4.3. Overtone frequency comb

We measure the overtone frequency comb for the fundamental mode $\omega_0 = 2\pi \times 118.049$ kHz of our membrane in Fig. 4.2**a**. In the velocity power spectrum, we see a series of 35 peaks spanning the full detection bandwidth of the setup (4.2 MHz), spaced by ω_0. This spacing is perfectly uniform, limited by the spectral resolution of the setup to 4.7×10^{-8} relative spacing difference. A comparison of this comb to other mechanical combs is included in Sec. 4.6.1. Through integration of the velocity signal, we verify the displacement $x \gg \lambda/4$. By numerically integrating Eq. (4.1), we can reproduce the overtone combs, shown in Fig. 4.2**b**, using only the optical potential strength F_o, offset x_{off} and initial conditions $[x_0, v_0]$ as fit parameters (assuming steady state, so $\gamma = F_d = 0$). This highlights that the nonlinearity comes from the optical field, without introducing mechanical nonlinearities previously used

to explain this behavior [113].

The overtones can be distinguished from the other mechanical eigenmodes of the membrane. The mechanical eigenmodes can be detected and identified (Fig. 4.3**c**). When the overtone comb is generated, additional peaks appear in the spectrum (dotted black lines). This demonstrates that the overtones are not affected by the mechanical dispersion relation and do not require engineered nonlinear resonances [122, 129]. Furthermore, it is possible to generate combs from the second and third mechanical eigenmodes, by selecting the right laser position on the membrane, Fig. 4.3**d,e**. This makes the frequency spacing variable, limited by our ability to drive a particular eigenmode. Finally, for some laser positions the overtone comb at ω_0 interacts with a different mechanical eigenmode (ω_h), which could allow extension of the comb bandwidth (Sec. 4.6.6).

We examine Eq. (4.1) to better understand the behavior of this mechanism (details in Sec. 4.6.1). Firstly, when the displacement x increases, more overtones appear due to the increasing number of optical extrema crossed. Each overtone will again be modulated, so they have equal power up to a certain cutoff, which is beneficial for many applications (~ 2200 kHz in Fig. 4.2**a**). Secondly, the strength of the optical field (F_o) controls the power of each overtone relative to the original mode ω_0. Finally, the offset x_off between mechanical and optical zeros determines the relative intensity of the odd and even number overtones. The position offset $x_\mathrm{off} \simeq 40$ nm is consistent between measurements on identical membranes. We can repeatably create the overtone comb in different membranes, and study the effect of the optical beam itself on the membranes and overtone comb in Sec. 4.6.7.

4.4. Comb dynamics

The comb dynamics can be visualized by starting a measurement with the laser spot positioned away from the membrane, as shown in Fig. 4.4**a**. We move the laser to the membrane center at $t = 8.7$ s such that the optothermal parametric driving starts increasing displacement. We analyze the dynamics by cutting the recorded time signal into intervals and performing a Fourier transform on each. Then we concatenate the spectra such that we can study its behavior over time (Fig. 4.4**b**) and monitor the power of individual overtones by taking linecuts (Fig. 4.4**c**).

In Fig. 4.4**b**, the fundamental mode shows a 9 Hz upwards shift in frequency, which is reproduced as an $n \times 9$ Hz upwards shift for the nth overtone (e.g. $n = 5, 15$ in the figure) and likely originates from slow thermalization (Sec. 4.6.4). This illustrates thermal tuning would be an effective mechanism to control and tune the comb spacing, without compromising comb uniformity.

We plot the power of the overtones as the comb grows in Fig. 4.4**c**. We can simulate and reproduce this growth quantitatively by integrating Eq. (4.1). Comparison between the experimental data (markers) and simulation (solid lines) in Fig. 4.4**c** shows good agreement with fit parameters [$F_\mathrm{o} = 3.8$ pN, $x_\mathrm{off} = 40$ nm, $x_0 = 5$ nm, $v_0 = 1$ nm s^{-1}, $\gamma/2\pi = 0.8$ Hz and $F_\mathrm{d} = 2.1$ pN]. Most important for the overtones is F_o, which is in excellent agreement with simulated force on the order of pN (Sec. 4.6.3). All extracted curves share a vertical offset to account for the total detection efficiency. This shows Eq. (4.1) reproduces the dynamics of the

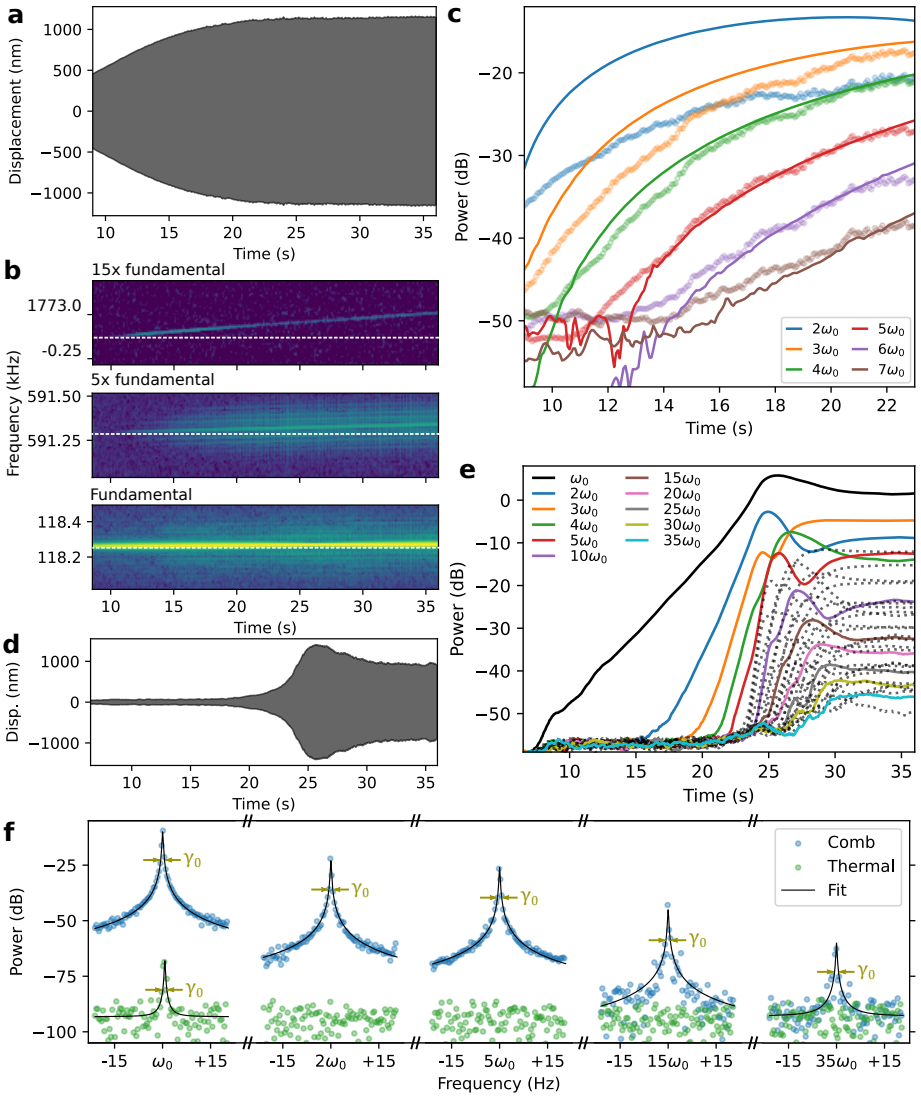

Figure 4.4: **Comb dynamics. a**: Measured displacement of membrane, showing clear growth before reaching a plateau around $t = 24$ s. **b**: Measured spectrum of membrane motion close to fundamental mode and two of its overtones (5th and 15th). A thermal shift of 9 Hz of the fundamental mode is visible as a 5×9 and 15×9 Hz shift in the overtones (white dashed lines are horizontal to guide the eye). Color scale is power (dB), yellow the highest and dark blue the lowest. **c**: First six overtones increasing in power as the membrane displacement increases (markers) in **a**, with simulated dynamics (solid lines) based on integration of Eq. (4.1) matching quantitatively to the highest four. **d**: Membrane displacement of a different device (different chip) than **a**, showing growth from close to thermal regime to steady state. **e**: Overtone amplitudes extracted from the spectrum of measurement of **d**, showing all 35 overtones within the detection bandwidth (black, dotted lines are overtones with numbers between the labeled ones). **f**: Spectrum showing measured fundamental mode and some selected overtones in the comb regime (blue) and thermal (green), along with Lorentzian fit with center frequencies $n\omega_0$ (n integer) and identical linewidths γ_0.

resonator and individual overtones.

In Figs. 4.4**d,e**, we observe the membrane motion from thermal state at $t < 5$ s to the steady state of the comb at $t > 33$ s. Initially, we detect only the fundamental mode ω_0, until the resonator starts crossing multiple optical extrema. Higher overtones appear as the maximum displacement grows. In contrast to Fig. 4.2**a**, the fundamental mode is the most powerful. The detection efficiency likely varies for each overtone due to their shape [113]. The displacement stops growing at $t \simeq 26$ s, and decreases slightly before the system reaches steady state (see Sec. 4.6.8). It is likely limited in amplitude by a mechanical nonlinearity, but the amplitude overshoot and the oscillation of amplitude of overtones suggests that the interaction with the optical field play a role. In the steady state, the fractional frequency stability of the 30^{th} overtone is $7.5 \cdot 10^{-10}$ over a 6-hour period (Sec. 4.6.8), limited by thermal drifts. The frequency of the overtones determined solely by the mechanical frequency, and is thus not affected by drifts in the laser frequency. Changes in the laser power will affect the overtone amplitudes, mainly via the optothermal parametric driving. The uniformity of the comb is not affected by mechanical frequency shifts (nor by the laser), thus uniformity is constant.

We isolate and plot the spectrum around several of the overtones in Fig. 4.4**f**. In the thermal regime (green markers), only the fundamental mode is visible and we can fit a Lorentzian with linewidth $\gamma_0 = 2\pi \times 0.07$ Hz to the peak. For the comb in steady state, the fundamental mode retains its linewidth γ_0, and we can derive that the comb mechanism does not cause additional noise, Sec. 4.6.9. All overtones possess the same linewidth γ_0, which does not match the $n\gamma_0$ scaling expected from a frequency-fluctuation limited linewidth, but matches a decay-rate limited system. These properties combined should allow frequency combs with single-mHz linewidths based on ultra-high-Q membrane resonators [51].

To finally show that the overtones form a comb, i.e. that a fixed phase and frequency relation exists, we show the time-domain signal in Fig. 4.5**a**. Unlike combs centered around a carrier (such as soliton-based mechanical [129] and optomechanical [125] frequency combs), there is no component with periodicity longer than the mechanical period $2\pi/\omega_0$ (Figs. 4.5**b,c**). This highlights the different physical and dynamical processes behind the overtone comb. If the fundamental mode is the dominant component in the comb, we get a sinusoid (Figs. 4.5**b,c**, blue line). When other components are dominant, particularly $2\omega_0$ and $3\omega_0$, we get the peaked curves (Fig. 4.5**c**, green and orange lines), which retain the periodicity of the fundamental mode. The shape of these curves proves that the entire overtone comb is phase-coherent, as they are formed by a sum of cosines with the same phase offset (see Sec. 4.6.10). This behavior is retained not only in the steady-state, but also during comb growth, Fig. 4.5**d**. There we plot the time signal at various stages during the measurement of Fig. 4.4**d,e**, which shows a smooth transition from sinusoidal to peaked behavior as the comb grows. Thus the overtones form a mechanical frequency comb.

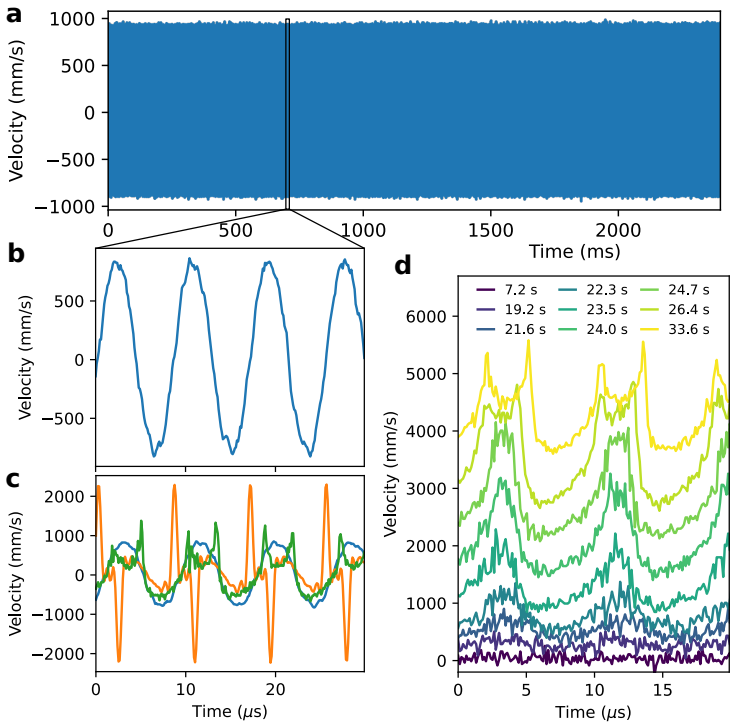

Figure 4.5: **Time domain frequency comb. a**: Measured velocity of resonator in frequency comb regime, displaying no pattern with period longer than $1/\omega_0$. **b**: Zoom-in of time-domain signal in **a**, showing the 118 kHz fundamental mode dominates. **c**: Three different measured time signals in steady state, with varying relative strengths of the overtones (blue: ω_0 dominates, orange: $2\omega_0$ and $3\omega_0$ dominate, green: $1\omega_0$ to $6\omega_0$ similar in strength). All traces can be reproduced only with phase-coherent addition of the different overtones. **d** Time domain signal of comb during growth, same measurement as Fig. 4.4**e** at the indicated times. This shows the smooth transition from thermal regime (bottom) to the comb in steady state (top), traces are offset vertically for clarity.

4.5. Conclusion

We have discovered a mechanism which uniquely interfaces two breakthrough concepts: optical trapping and frequency combs. This allows for mechanical frequency combs whose simplicity stands out from those based on previous mechanisms. This is realized by integrating a suspended dielectric membrane in a weak optical trap. The dielectrophoretic force from the optical field modulates the mechanical potential of the membrane. This modulation creates integer multiple copies (overtones) of the membrane's motion, which forms a frequency comb. We show combs of up to 35 overtones in a 4.2 MHz bandwidth with control over the frequency spacing, excellent uniformity, stability and no added mechanical noise. The integration of the membrane in the optical trap allows us to combine the overtone comb with optothermal parametric driving, which brings the membrane to self-oscillate. We thus realize a frequency comb that requires no external drive or control frequencies

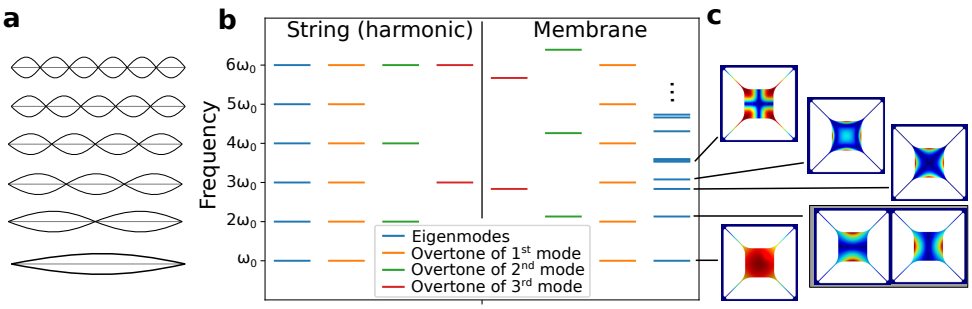

Figure 4.6: **Mechanical overtones.** **a**: Resonator modes of a string. **b**: Frequency diagram of eigenmodes of a harmonic string and the anharmonic Si_3N_4 trampoline membranes used in this chapter. **c**: Si_3N_4 trampoline modes, grey box denotes degenerate modes. The color scale denotes normalized absolute displacement, from minimum (blue) to maximum (red).

and which uses a minimal setup (laser, microscope objective and vacuum chamber). This makes it more versatile and easier to use than other ways of generating these combs. In summary, this mechanism unlocks potential of mechanical frequency combs for sensing, timing and metrology applications at the microscale, and provides native integration with phononic circuits.

4.6. Supplementary information

4.6.1. Mechanical overtones

The motion of a mechanical resonator can typically be described by considering a linear superposition of the normal modes of the structure. In some structures, the normal modes are related by integer multiples of some frequency, and they are said to be *harmonic*. This is the case for a model string (Fig. 4.6**a,b**) and a desirable property for many musical instruments. However for most of the resonators in this chapter, the normal modes are not related by integer multiples, thus the spectrum is *anharmonic*. In Fig. 4.6**c**, we have simulated and plotted the first six eigenmodes of the trampoline membrane resonator, and plotted their frequencies in Fig. 4.6**b**.

In this chapter, we introduce an optics-based nonlinearity to the equation of motion, which affects the description of the resonator motion in terms of the normal modes given by its structure. Briefly summarized, we consider only the lowest frequency normal mode given by the mechanical structure, as a simple harmonic oscillator,

$$\ddot{x} + \gamma\dot{x} + \omega_0^2 x = 0. \tag{4.2}$$

The solutions for this equation are well-known, $x \propto e^{i\omega_0 t}$, which oscillates at the frequency ω_0 of the normal mode. By introducing the gradient force term, $\propto \sin(x)$ (nonlinear), we get terms in our solution that oscillate at integer multiples of ω_0, without being related to the (other) normal modes of the mechanical resonator. To distinguish them from the other normal modes, we will refer to the components at $n\omega_0$ (n integer) as **overtones**. Others have detected these components of the mechanical motion before, and refer to them in a similar manner [113, 114, 160].

They ascribe the origin of these overtones to be mechanical in nature, while we propose an optical origin.

Small displacement

To expand the description of these overtones, we consider the equation of motion as Eq. (4.1), where we have added a resonant drive term F_d and absorbed the effective mass m_eff into F_o and F_d for convenience. The shorthand $\Lambda = 4\pi/\lambda$ is similarly used. We get

$$\ddot{x} + \gamma\dot{x} + \omega_0^2 x = F_\mathrm{o} \sin\left(\Lambda(x - x_\mathrm{off})\right) + F_\mathrm{d} e^{i\omega_0 t}. \tag{4.3}$$

The periodic part of the optical potential is of the form $E \propto \sin\left(\frac{2\pi}{\lambda}(x - x_\mathrm{off})\right)$. The gradient of the optical intensity, $\nabla E^2 \propto \sin\left(\Lambda(x - x_\mathrm{off})\right)$ after some algebra and absorbing the relevant constants into F_o. The constant offset between the potentials, x_off, can be taken out of the sine by

$$\sin\left(\Lambda(x - x_\mathrm{off})\right) = \sin(\Lambda x)\, s_x + \cos(\Lambda x)\, c_x, \tag{4.4}$$

with $s_x = \cos(\Lambda x_\mathrm{off})$ and $c_x = \sin(\Lambda x_\mathrm{off})$. For a small displacement x, we can use the Taylor series and truncate the higher order terms, so $s_x \sin(x) + c_x \cos(x) \simeq c_x + s_x x - \frac{c_x}{2}x^2$. The equation of motion then becomes

$$\ddot{x} + \gamma\dot{x} + \omega_0^2 x = F_\mathrm{o}\left(c_x + s_x \Lambda x - \frac{c_x}{2}\Lambda^2 x^2\right) + F_\mathrm{d} e^{i\omega_0 t}. \tag{4.5}$$

This equation admits solutions of the form

$$x = \sum_{n=0}^{\infty} A_n e^{in\omega_0 t}, \tag{4.6}$$

which are the integer multiples of our original frequency ω_0; the overtones. The term $n = 0$ corresponds to a static position offset from the zero of the mechanical potential. Substituting the solution Eq. (4.6) into Eq. (4.5) and gathering all terms by their frequency ($e^{in\omega_0 t}$ for every n separately) allows us to extract the amplitudes of the individual overtones in terms of the parameters of our system. We get

$$\begin{aligned}
A_0 &\simeq c_x F_\mathrm{o}/\omega_0^2 \\
A_1 &= \frac{F_\mathrm{d}}{i\gamma\omega_0 - \Lambda F_\mathrm{o} s_x + F_\mathrm{o}\frac{c_x}{2}\Lambda^2 A_0}, \\
A_2 &= \frac{F_\mathrm{o}\frac{c_x}{2}\Lambda^2 A_1^2}{3\omega_0^2 - 2i\gamma\omega_0 + F_\mathrm{o} s_x \Lambda - F_\mathrm{o}\frac{c_x}{2}\Lambda^2 A_0}, \\
A_n &= \frac{F_\mathrm{o}\Lambda \sum_{j,k=0}^{\infty} A_j A_k}{(n^2-1)\omega_0^2 - i\gamma n\omega_0 + F_\mathrm{o} s_x \Lambda - F_\mathrm{o}\frac{c_x}{2}\Lambda^2 A_0},
\end{aligned} \tag{4.7}$$

where the summation contains only the terms where $j + k = n$. This sequence of overtone amplitudes is monotonically decreasing (see Fig. 4.7): Every $A_n < A_{n-1}$. In the small-displacement case, the overtones will be negligible compared to A_1.

Large displacement

If instead the displacement is not small, we can still use the same method. We need to keep all the terms of the Taylor expansion,

$$\sin(x) = \sum_{n=0}^{\infty} \frac{(-1)^n x^{2n+1}}{(2n+1)!}, \quad \cos(x) = \sum_{n=0}^{\infty} \frac{(-1)^n x^{2n}}{(2n)!}. \tag{4.8}$$

We can use the same ansatz of Eq. (4.6), and extract the amplitudes by collecting all terms of the same frequency. For $n = 0$, the solution converges to

$$A_0 \simeq c_x F_\mathrm{o}/\omega_0^2, \tag{4.9}$$

as the contribution from the higher order terms of the expansion scale with $1/\Lambda^n$. Similarly, the denominator for $n > 0$ can be truncated to obtain

$$\begin{aligned} A_1 &= \frac{F_\mathrm{d}}{i\gamma\omega_0 - \Lambda F_\mathrm{o} s_x + F_\mathrm{o}\frac{c_x}{2}\Lambda^2 A_0} \\ A_n &= \frac{F_\mathrm{o}\sum_j \left(s_x s_j \sum_{k,\ell,\ldots=0}^{\infty} A^j_{k,\ell,\ldots} + c_x c_j \sum_{k,\ell,\ldots=0}^{\infty} A^j_{k,\ell,\ldots} \right)}{(n^2-1)\omega_0^2 - i\gamma n\omega_0 + \Lambda F_\mathrm{o} s_x - F_\mathrm{o}\frac{c_x}{2}\Lambda^2 A_0}, \end{aligned} \tag{4.10}$$

with $s_j = \frac{(-1)^{(j-1)/2}\Lambda^j}{j!}$ for odd j ($s_j = 0$ for even j) and $c_j = \frac{(-1)^{j/2}\Lambda^j}{j!}$ for even j ($c_j = 0$ for odd j). The summation only contains the terms of j amplitudes ($A_k, A_\ell, \ldots$) whose indices $k, \ell, \ldots$ add up to n. To clarify, for $n = 3$, we sum over $A_1A_1A_1$, A_1A_2, A_2A_1, A_3A_0, A_0A_3 as well as many terms with more A_0's. For every n, we get an infinite number of contributions to each term. The denominator contains at most two terms that depend on n, but the rest is constant and the whole denominator converges for each n; thus we can truncate the denominator, as we have done in Eq. (4.10). In contrast, to evaluate the numerator we can take sequentially higher terms in the Taylor expansion (i.e. increase j), find all combinations of j integers that sum to n, and add them to the term of frequency $n\omega_0$.

It is difficult to analytically express all the combinations of j integers that sum up to n, so we numerically evaluate the overtone amplitudes in Fig. 4.7. Here, we take the expansion up to 13^{th} order, which results in close to $2.5 \cdot 10^6$ terms contributing to $n = 12$. We fix the terms with $n = 0, 1$ to a constant value, in the experiment we do not directly apply a resonant drive (A_1) and there are radiation pressure effects that could result in a static position offset (A_0). From the numerical evaluations, we consistently see that for small displacement, the power in each subsequent overtone drops exponentially. However, for large displacement this is no longer true, and the higher-order terms from the expansion cause strong overtones that decrease much slower in amplitude with overtone number. This is reproduced in the experiments shown in Fig. 4.2.

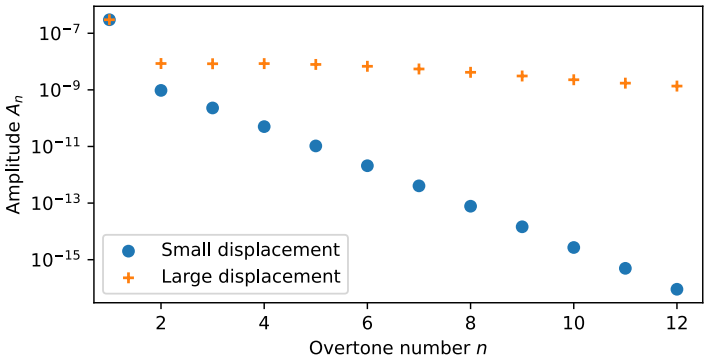

Figure 4.7: **Overtone amplitudes.** Numerically evaluated overtone amplitudes A_n for small and for large displacements. The terms $A_0 = 1 \cdot 10^{-7}$ and $A_1 = 3 \cdot 10^{-7}$ are taken constant, with F_o corresponding to 100 pN. For large displacement, the overtones have much higher amplitude than in the small displacement case. The amplitude also decays more slowly with mode number.

Numerical simulation of overtones

So far, we have derived analytically that the addition of an optical $\sin(x)$ nonlinearity to a mechanical harmonic oscillator creates components of mechanical motion at integer multiples of the original frequency ω_0. If the displacement is large enough, these overtones have significant amplitude and form a frequency comb. We have made some simplifying assumptions (e.g. $x_{\text{off}} = 0$), which do not necessarily hold in practice. To remedy that, we perform numerical simulations. These allow us to better understand the roles of resonator displacement x, the the optical (dielectrophoretic) force F_o, and the position offset x_{off} of the optical potential with respect to the mechanical potential.

First, we investigate the dependence of the frequency comb on displacement x. In Fig. 4.8**a**, we simulate the motion of the resonator starting from the value initial amplitude x_0 ($v_0 = 0$) indicated in the legend. We include dissipation but it is sufficiently small that the amplitude does not significantly decrease within the simulation time. For small amplitude of motion ($x_0 < x_{\text{off}}$), we cross no optical extrema and only the fundamental mode is visible, no higher overtones appear. Once the motion is large enough to cross one optical extremum (100 nm), several overtones appear with exponentially decreasing power, as derived previously. If the motion is large enough to cross multiple optical extrema ($x_0 > \lambda/4 \simeq 150$ nm), more overtones appear. The lower overtones have approximately equal amplitude (empirically until $\omega = 3x_0/(\lambda/4) \times \omega_0$), since these also interact with the optical potential and get modulated to drive higher overtones. Note that the lower overtones have the same amplitude regardless of the resonator displacement. The higher overtones, above $\omega = 3x_0/(\lambda/4) \times \omega_0$, have an amplitude that decays exponentially.

Secondly, we study the dependence of the frequency comb on dielectrophoretic force F_o. For identical initial position x_0, we plot the frequency comb for various values of F_o in Fig. 4.8**b**. For $F_o = 0$ N, we see the dominant fundamental mode but also some higher harmonics ($3\omega_0$, $5\omega_0$, $7\omega_0$, ...). These are from the nu-

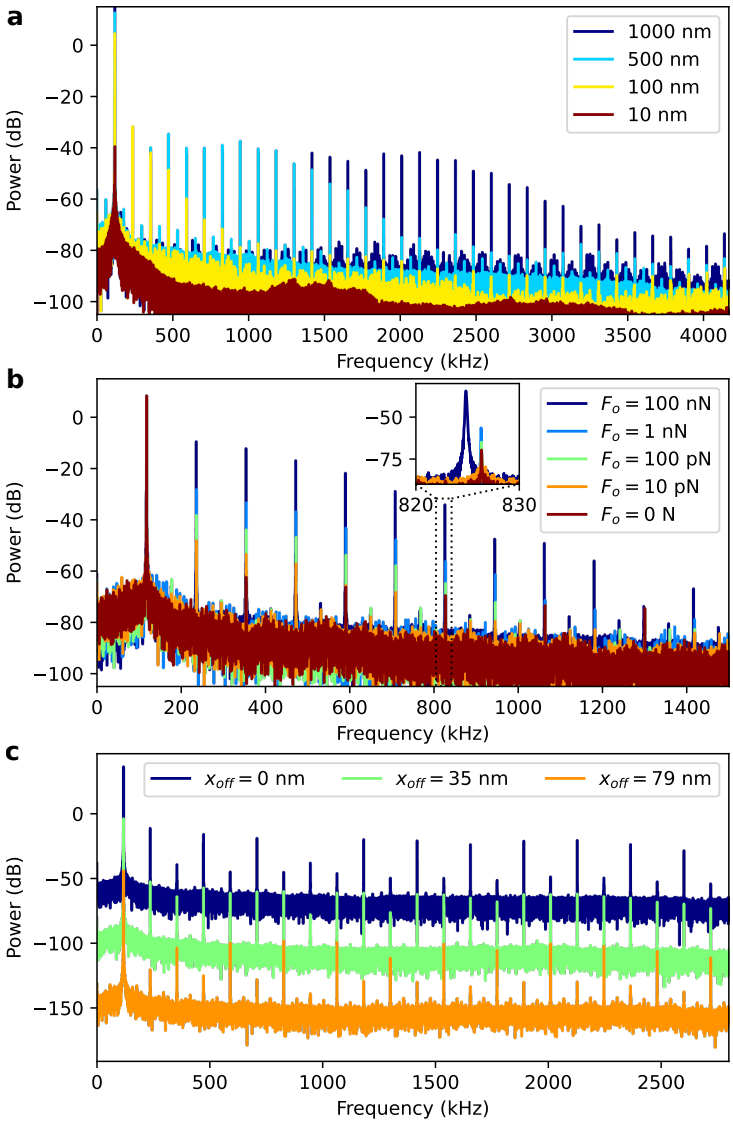

Figure 4.8: **a**: Numerical simulation of overtones generated depending on initial amplitude. Parameters $F_o = 100$ pN, $\omega_0 = 2\pi \times 118.049$ kHz, $\gamma = 2\pi \times 0.02$ Hz, $F_d = 0$ N, $x_{off} = 30$ nm. **b**: Simulation of overtones generated depending on optical force F_o, for $x_o = 200$ nm. Other parameters identical to **a**. Inset shows the frequency shift for stronger optical fields. **c**: Simulation of overtones depending on offset x_{off}. For $x_{off} = 0$ nm, we predominantly drive the even overtones through the cosine-expansion, while for $x_{off} = \lambda/8 = 79$ nm we predominantly drive the odd overtones through the sine-expansion. At $x_{off} = 35$ nm, odd and even modes are approximately equal in power. Individual traces are offset vertically, $x_0 = 1000$ nm and other parameters are identical to **a**.

merical accuracy of our simulation, they do not follow the exponentially decaying trend of the other curves. For increasing values of F_o, the amplitude of each of the individual overtones increases linearly, but the exponential fall-off for higher overtone numbers is unchanged. At some point, the nonlinearities start to shift the frequency of the modes, but this trap strength is well beyond the regime of our setup ($F_o = 100$ nN corresponds to approximately 6 W of incident laser power).

Finally, we report on the dependence of the frequency comb on position offset x_{off}. In the analytical case, we simplified using $x_{off} = 0$ nm, retaining only the cosine terms so the even overtones are strong (dark blue). By shifting the optical potential with respect to the mechanical zero by $\lambda/8 = 79$ nm, we see mainly the odd-numbered overtones appear. For this value of x_{off}, we can rewrite the cosine into a sine, such that the Taylor-series expansion only contains odd terms. At other values of x_{off}, we have a weighted average of the two series expansions. In the middle, at $x_{off} = 35$ nm, we see odd and even numbered modes with approximately equal power.

To summarize: The addition of an optical $\sin(x)$ nonlinearity to a mechanical harmonic oscillator creates components of mechanical motion at integer multiples of the original frequency ω_0, which we call the overtones of ω_0. These overtones can have significant amplitude, if the mechanical displacement is large enough. The displacement x controls the number of overtones visible, while the dielectrophoretic force F_o determines their power relative to the fundamental mode of the comb. Based on the offset between the optical and mechanical potential x_{off}, we can control the relative power in the even- or odd-numbered overtones. We have thus derived an analytical model for the overtone frequency comb, and expanded our qualitative understanding with numerical simulations.

Exclusion of mechanical nonlinearity

We have introduced an optical nonlinearity to explain the mechanical frequency combs, but we have not excluded conventional mechanical nonlinearities (e.g. a Duffing term, $\propto x^3$). These nonlinearities can also lead to mechanical frequency combs, even in the absence of other modes to couple to [113, 135]. In Fig. 4.9**a**, we have simulated and plotted the spectrum of a mechanical resonator with a Duffing term $c_{duff}x^3$, such that the equation of motion is

$$\ddot{x} + \gamma\dot{x} + \omega_0^2 x + c_{duff}x^3 = 0. \tag{4.11}$$

We start from an initial condition of $x_0 = 500$ nm for all traces. For a sufficiently strong nonlinearity, we see a frequency comb. However, due to the nonlinearity, the frequency is shifted away from ω_0. This is expected behavior for nonlinear resonators, oscillating at ω_0 for small amplitude frequency shifting for larger amplitudes where the nonlinearity becomes dominant. The sign of c_{duff} controls the direction of the frequency shift, and a hardening nonlinearity (increasing frequency) is expected for most mechanical resonators.

In Fig. 4.9**b**, we have plotted the fundamental mode during the measurement shown also in Fig. 4.4**e**. At the start of the measurement, the amplitude is small and there is no frequency comb, whereas at the end the amplitude is large and the

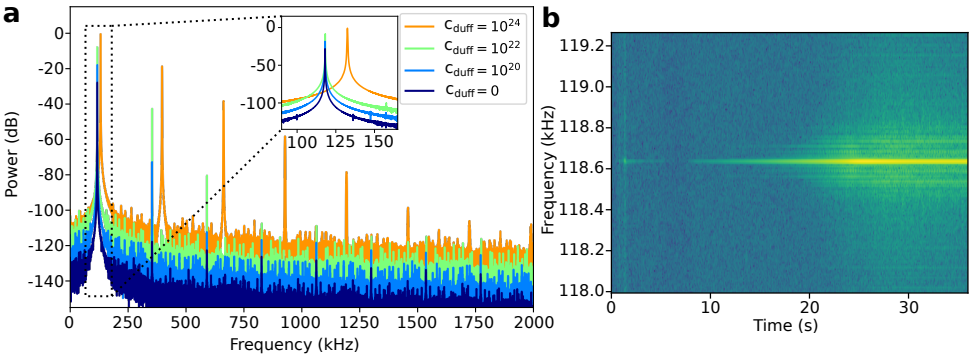

Figure 4.9: **Frequency comb by mechanical nonlinearity. a**: Simulated displacement spectrum of a mechanical resonator with a Duffing nonlinearity. All traces share the same initial displacement, $x_0 = 500$ nm, with different Duffing coefficients. For a sufficiently large nonlinearity, the frequency comb appears, but the frequency of the fundamental mode (and comb spacing) is changed. **b**: Measured frequency of the fundamental mode of Fig. 4.4**e**, showing no shift in frequency between low displacement (no comb) and high displacement (comb).

comb is clear. There is no shift of the frequency of the fundamental mode visible in this measurement, which excludes the explanation of a Duffing nonlinear term being the origin of the comb.

It was proposed by others that strong, higher order nonlinearities (e.g. $\propto x^3$, x^5, x^7, etc.) could be the origin of this comb [113]. However, to reproduce the frequency comb without a similar frequency shift as in the Duffing case, one would need strong nonlinear terms of very high orders. Rather than assuming as many nonlinear terms as we have overtones (up to 35), we have introduced an optical nonlinearity that can explain all overtones from a single effect.

Comparison to other combs

There have been demonstrations of mechanical frequency combs generated via different mechanisms in literature. For applications, the comb properties are more important than the generation mechanism, and we have summarized a large part of the combs available from literature in Table 4.1. The entries are sorted by material/geometry platform, and multiple publications with subtle difference in the comb generation mechanism may be present within the individual categories.

The overtone comb of this chapter has a bandwidth on par with the largest available in literature (limited by the setup), but also has a relatively large resolution. The bandwidth is given by a combination of the maximum displacement and mechanical frequency, both can easily be engineered. We estimate the optothermal parametric drive is limited to $\lesssim 500$ kHz in our membrane, which would constrain the mechanical frequencies that can be operated without an external drive. The frequency resolution could be enhanced by lowering the mechanical frequency (i.e. make the membrane tethers longer and thinner), and can likely be tuned thermally. A further benefit is that the overtone combs are spectrally flat (same amplitude in different overtones), in contrast to other mechanical combs.

	Electro-mech. [121]	Nano strings [128]	Free-beam [129]	Coupled beams [130]	Bulk acoustic [132]	Circular 2D [134]	This work
Bandwidth (Hz)	20–100	$10-25$ $(\times 10^3)$	$60-150$ $(\times 10^3)$	$10-200$	20	$2-11$ $(\times 10^6)$	4.2 $(\times 10^6)$
Resolution (Hz)	0.005–10	$0.5-10$ $(\times 10^3)$	$2-10$ $(\times 10^3)$	$1-30$ [162]	$0.7-2$	$75-400$ $(\times 10^3)$	$118-359$ $(\times 10^3)$
Ext. drive (dBm)	−15 [127]	−2.5 [135]	5 [139]	−26	−67	10 [140]	None
Uniformity (-)	$1 \cdot 10^{-9}$		$5 \cdot 10^{-6}$ [161]				$4.7 \cdot 10^{-8}$
Stability (-)			$1 \cdot 10^{-8}$ [161]				$7.5 \cdot 10^{-10}$
Footprint (μm^2)	$3 \cdot 1$–$150 \cdot 50$	$55 \cdot 0.27$	$1.1 \cdot 0.35$ (mm^2)	$500 \cdot 50$	$23 \cdot 1$ (mm^2)	$5-8$ (diam.)	$750 \cdot 750$

Table 4.1: **Mechanical frequency comb performance.** Overview of reported mechanical frequency comb properties from literature, organized by platform (irrespective of comb mechanism). The overtone comb has a bandwidth (frequency span) on par with the largest combs, but also a relatively large resolution (frequency spacing). We report the absolute frequency stability over a 6-hour period (see Sec. 4.6.8), whereas [161] computes the Allan deviation over a 10 s period. Our work is the only mechanical frequency comb that does not require any external drive.

The main benefit of the overtone comb is that it does not require an external drive, which is unique for a mechanical comb. This greatly simplifies the necessary setup to operate the comb. In terms of uniformity of the frequency spacing, overtone combs come close to the level of electromechanical combs, where the uniformity is given by the electric drives directly. However, our measured uniformity is limited by the detection setup. Overtone combs are also among the most stable, especially comparing our 6-hour frequency stability (Sec. 4.6.8) to the 10 s Allan deviation of Ref. [161].

4.6.2. Trampoline membranes and setup

Laser Doppler Vibrometer

The setup used in this chapter is shown in Fig. 4.10**a**. It consists of a commercial laser Doppler vibrometer (LDV), Polytec MSA400, which is depicted schematically. Light from the LDV goes through a microscope objective, which focuses it on the chip containing the membrane resonators. This chip is placed in a vacuum chamber and pumped down until the pressure is $< 5 \times 10^{-6}$ mbar, to reduce gas damping. There is a piezoelectric shaker mounted to the sample holder, by which we can drive the membrane, though for the majority of the measurements we use the thermal parametric driving described in Sec. 4.6.4. The reflected light from the membranes is Doppler-shifted due to their out-of-plane motion, which is then detected by the LDV. To extend the time we can continuously measure, we add a Rohde & Schwarz RTB2004 digital oscilloscope to readout the LDV decoder. Using the history function of this oscilloscope, we can chain 16 measurements of 20 million data points each, which allows 38 s of time signal at 8.33 MHz sampling rate. However, this method for reading out the velocity comes at a cost of the calibrated readout that the LDV

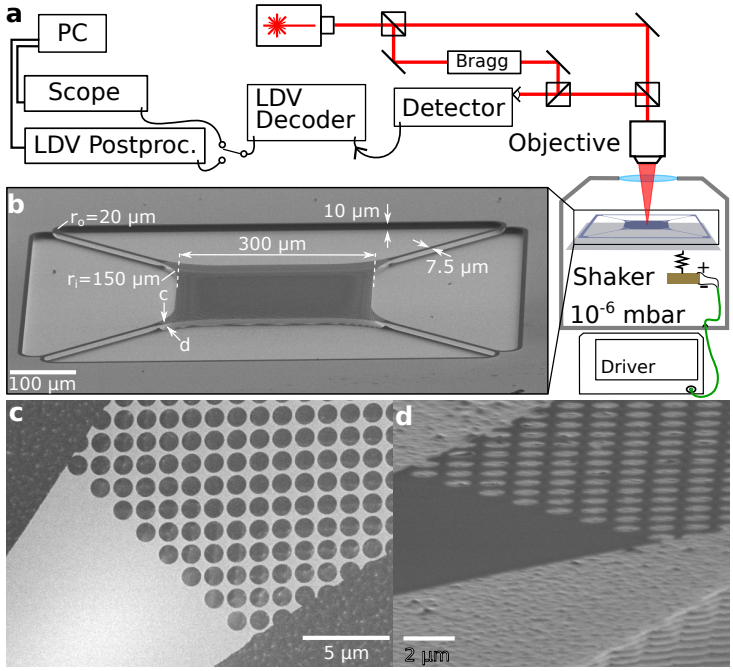

Figure 4.10: **Setup and membranes.** **a**: Schematic of the laser Doppler vibrometer (LDV) setup, where we access the chip containing the membranes using a microscope objective directly outside a vacuum chamber. **b**: SEM (scanning electron microscope) image of the suspended membrane, with nominal design parameters in white. **c**: Top-down view of corner of the membrane, highlighting the interface of the photonic crystal with the tether. **d**: Tilted view to show Si surface below **c**, to illustrate etch roughness and an etched imprint of the photonic crystal pattern (bottom right).

postprocessing offers.

The LDV outputs a voltage signal proportional to velocity or displacement, depending on the LDV decoder used. If using the LDV postprocessing, it can easily be Fourier-transformed and exported. If using the oscilloscope and history function, we sequentially read out the measurements afterwards and concatenate them in the correct order in post-processing. We can then further extract information from this signal either by integrating (to obtain the displacement), or by using Scipy's short-time Fourier transform function to obtain the time-varying behavior of the comb spectrum.

Higher harmonics in LDVs

There are several mechanisms by which spurious higher harmonics can appear in measurements from a LDV [163]. In the following paragraphs, we will discuss these mechanisms and show that we can exclude them as the source of the observed frequency comb. We will treat all parts of the setup shown in Fig. 4.10: the optical parts, the photodetector, the decoder and the data acquisition.

Multi-path interferences may happen when the LDV laser beam is reflected by

more than one surface [164]. The geometry of our system facilitates having multiple reflection sources, since both the trampoline membrane and the substrate contribute to the reflection. We assume an ideal LDV, with an incident electrical field with amplitude E_0, a moving membrane, and a stationary substrate, as shown in Fig. 4.11**a**. The directly reflected (desired) beam from the membrane has power $R_{\mathrm{SiN}}|E_0|^2$ ($R_{\mathrm{SiN}} = 0.3$). Assuming no scattering ($T + R = 1$, for transmission T and reflection R), the substrate contributes $T_{\mathrm{SiN}}^2 R_{\mathrm{Si}}|E_0|^2 \simeq 0.17|E_0|^2$ ($R_{\mathrm{Si}} = 0.35$). Only the membrane contribution has a Doppler shift due to its motion, $+v$. Neglecting effects from beam divergence, multiply-reflected beams contribute $T_{\mathrm{SiN}}^2 R_{\mathrm{Si}}^2 R_{\mathrm{SiN}}$, $T_{\mathrm{SiN}}^2 R_{\mathrm{Si}}^3 R_{\mathrm{SiN}}^2$, and so on. These terms have Doppler shifts with the opposite sign to the directly reflected beam, as they interact with the membrane from the opposite direction. The first term has a Doppler shift equal in magnitude to the desired signal ($-v$), while subsequent terms have multiple times the Doppler shift ($-2v, -3v, \ldots$). These terms thus directly affect the magnitude of the velocity that the LDV senses. For harmonic membrane motion $v(t) = v_0 \cos(\omega_0 t)$, the multiply-reflected beams lead to an error in v_0, but their Doppler shift does not contribute directly to higher harmonics of the observed membrane motion.

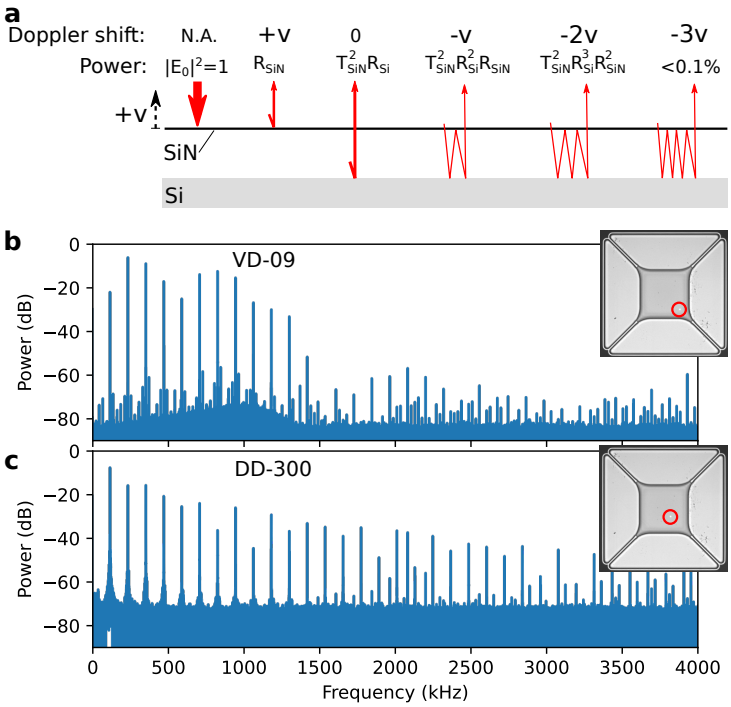

Figure 4.11: **Sources of higher harmonics. a**: Schematic of reflected components of a single optical beam on our device (red arrows). For each component, the Doppler shift due to membrane velocity v is shown, as well as the relative power. **b**: Frequency comb measured using the VD-09 decoder (maximum bandwidth set to 1.5 MHz to allow maximum detectable amplitude). Inset shows microscope image with laser position highlighted by the red circle. **c**: Frequency comb measured using the DD-300 decoder, measured on the same device at a slightly different position.

In a non-ideal laser Doppler vibrometer, multi-path interferences can be identified by presence of ripples and spikes in the velocity signal. We can compare the measured velocity signals with simulated signals using the model of [164]. For a harmonic oscillator with $\omega_0 = 118$ kHz, maximum displacement amplitude $x_{\max}$, the demodulated velocity signal has the form

$$v(t) = -\frac{1}{2}\omega_0 x_{\max}\left(\frac{\theta_2 - 1}{2\theta\cos\left(\frac{4\pi}{\lambda}\cos(\omega t) + \Delta\phi\right) + \theta^2 + 1}\right)\sin(\omega t). \tag{4.12}$$

Here, θ is the electric field ratio of the correct and the unwanted reflected signals ($\theta = \infty$ for an ideal vibrometer), $\Delta\phi$ is the phase offset between the two beams (constant). In the worst-case scenario ($R_{\mathrm{SiN}} = 0.3$, $R_{\mathrm{Si}} = 0.35$, no scattering losses), $\theta \simeq 1.33$. The unwanted beam likely suffers from scattering losses more than the correct beam, since its path crosses the Si_3N_4 domain twice and reflects of the etch-roughened Si surface (see Fig. 4.10**d**).

We simulate the velocity signal with multi-path interferences, and compare it with the observed velocity signal in Fig. 4.12. The simulated signal of Fig. 4.12**b** ($\theta = 10$) has the characteristic ripples of multi-path interference. By comparing the simulated signal to the measured signal (Fig. 4.12**a**), one sees that the characteristic ripples are absent. While it is unlikely that the multi-path interference effect is completely absent in our setup, it can be corrected by a combination of amplitude- and phase-locked loops [165]. Either way, the observed velocity signal does not correspond to multi-path interference effects.

We can further exclude multi-path interferences as the source of the comb by measuring outside the membrane, on the Si chip. At the position indicated on the microscope image of Fig. 4.12**d**, the Si and Si_3N_4 layers are touching and thus have the same motion. The multi-path interference as described in Ref. [164] does not happen. We use a second beam ('drive beam' in Fig. 4.12**d**) to generate a comb of the fundamental mode of the membrane. At the measurement position outside the membrane, we can detect this comb, red curve in Fig. 4.12**c**. For verification, without the drive beam present (blue curve), no comb is detected while the fundamental mode is visible. Thus we can exclude multi-path interference effects as the source of the observed frequency combs.

High-aperture effects can occur when the LDV is operated with a microscope objective, based on the Guoy phase delay of the optical beam [163, 166]. The majority of the measurements in this chapter were done using a Mitutoyo Plan APO 5x objective with a numerical aperture of 0.14. With this numerical aperture, the amplitude error and harmonic distortion should be limited to $< 1\%$ [163]. Additionally, we compare the frequency combs obtained from the same device using different lenses (different numerical apertures), which show no clear relation between the numerical aperture and frequency comb. Thus we can exclude high-aperture effects as the source of the observed frequency comb.

The electronic parts of the LDV (sketched in Fig. 4.10**a**) may contribute to a nonlinear response that would generate harmonics [163]. We record frequencies well below the 20 MHz specified maximum frequency of the detector, thus this com-

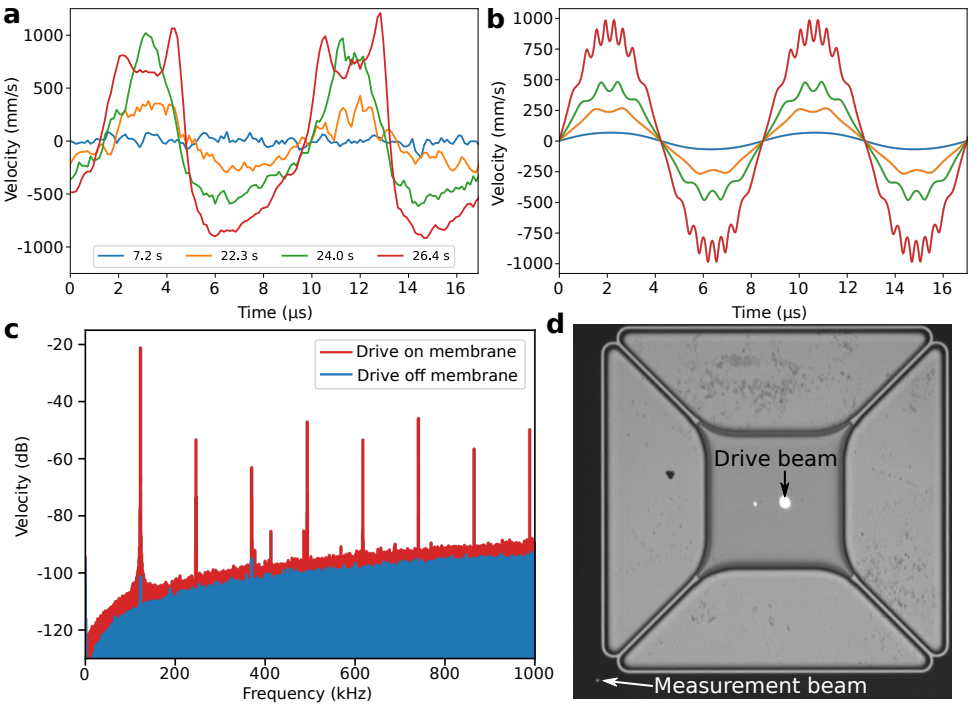

Figure 4.12: **Exluding multi-path interferences. a**: Measured velocity signal for different times in Fig. 4.5b. The data has been smoothed with a first order Savitzky-Golay filter of width 3, to emphasize the presence of ripples. **b**: Simulated velocity signal of a resonator with frequency 118 kHz with multi-path interferences present. The characteristic ripples of the interference are visible at the extrema of the velocity curve in **b**, but absent in **a**. **c**: Measured velocity spectrum outside the membrane, on chip. A second (drive) beam generates a frequency comb of the membrane's fundamental mode, which we detect at the position indicated on the microscope image **d**. Without this beam on the membrane, no comb is observed.

ponent should not contribute higher harmonics.

In a conventional heterodyne interferometer, harmonics of a signal would naturally arise for sufficiently large displacement. The interferometer phase is linear only in a limited regime, typically $x \ll \lambda$. However, a Doppler vibrometer measures the frequency shift of the reflected light rather than its phase. The frequency shift can be extracted with a frequency-to-voltage converter, in the LDV decoder. This allows an LDV to measure velocities associated with displacements much larger than the optical wavelength, without suffering from the harmonics expected in a displacement interferometer.

There are two LDV decoders available in our setup, the VD-09 velocity decoder and the DD-300 displacement decoder. The VD-09 has a lower maximum operating frequency ($1.5 - 2.5$ MHz), while the DD-300 has a lower detection maximum. In Fig. 4.11**b,c**, we show the frequency combs measured from the same device with the different decoders. These measurements show that the frequency comb is not a decoder artifact. Thus we can exclude the electronic parts of the measurement

setup as a source of the observed frequency comb.

In summary, we have described common mechanisms that yield higher harmonics in laser Doppler vibrometer measurements. All these mechanisms can be excluded as the cause of the frequency combs, by qualitative arguments and the measurements shown in Figs. 4.11, 4.12 and 4.23. In combination with the fact that there is a visible change in the membrane when the frequency comb occurs (Fig. 4.21), we conclude that the observed mechanical frequency comb is a real, physical phenomenon and not an artifact of the measurement setup.

Trampoline membranes

The membrane structures used in this chapter are fabricated out of 100 nm thick stoichiometric low-pressure chemical vapor deposition Si_3N_4 on top of a 1 mm Si chip. This was done by writing the pattern using electron beam lithography and an inductively coupled plasma (ICP) etch to transfer that pattern to the Si_3N_4. The membranes are then released using a second ICP etch, at −120 °C for 30 s, resulting in about 10 µm of undercut and a final Si_3N_4 thickness of 80 nm. A SEM (scanning electron microscope) image of a released trampoline is shown in Fig. 4.10**b**, with the nominal design parameters added in white. The resulting trampolines have well-characterized mechanical properties [13] and Chapter 3, with fundamental mode frequencies at 120 kHz and Q-factors typically of 1 million.

The membranes are pattered with a periodic array of holes (Fig. 4.10**c**) that forms a photonic crystal, though it is not designed to have a high reflectivity at the operating wavelength of our LDV ($\lambda = 633$ nm). Instead, the holes function as etch release holes to evenly release the membrane in the final ICP etch, which is essential for the fabrication yield. For these membranes, the periodic array of holes functions as a method to control the mass and resonance frequencies (Chapter 3), and possesses internal optical resonances that facilitate absorption which we detail in Sec. 4.6.4. Finally, the release etch imprints the photonic crystal pattern on the Si backplane, which roughens the surface. Fig. 4.10**d** shows the final Si surface roughness from the release etch (top left half) and the imprint below the periodic hole pattern (bottom right half).

4.6.3. Membrane in an optical trap

Optical traps can be used to confine small particles, as the light exerts a force proportional to the gradient of the optical intensity [157, 167]. For uncharged dielectric particles, the electrical field polarizes the particles, and any change in field (from a gradient) will result in a dielectrophoretic force acting on that particle [168]. In this section, we will simulate a laser incident on a dielectric (Si_3N_4) membrane, and evaluate the dielectrophoretic and radiation pressure forces. We will show that the optical gradient is sufficient for the dielectrophoretic force to affect the mechanical motion, while the radiation pressure force does not affect the dynamics significantly.

Dielectrophoretic force

We simulate the physical system consisting of a $t \simeq 80$ nm thin Si_3N_4 slab suspended in air above a much thicker Si slab, shown in Fig. 4.13**a**. We study a 2D-

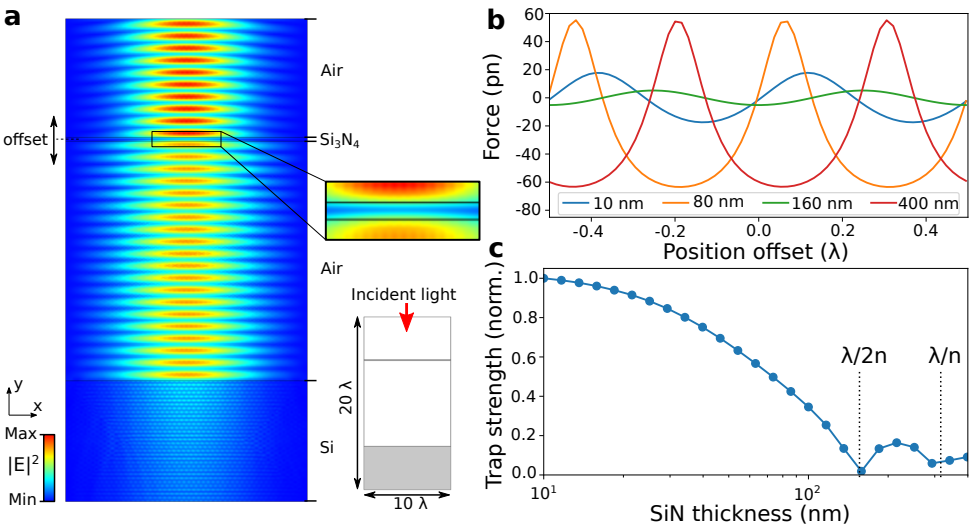

Figure 4.13: **Simulation of optical trap. a:** Electric field norm of incident 633 nm light on 100 nm Si_3N_4 membrane suspended ~6 µm above a Si backplane. The reflected light forms a standing wave pattern. Zoom shows center of the Si_3N_4 membrane. Bottom inset shows the simulation geometry schematically. **b:** Force exerted by the optical field on the Si_3N_4 domain as the position of the membrane is varied. The colors represent different membrane thicknesses. **c:** Normalized strength of the trap for different Si_3N_4 thicknesses.

axisymmetric domain centered around our laser spot, which is incident from the top of the figure. We assume that our laser Doppler vibrometer emits a Gaussian beam for convenience. For a regular optical trap, the optical gradient and thus the force exerted is weakest along the laser propagation direction, while it is stronger in the plane normal to the propagation direction. However, the Si backplane in our geometry reflects part of the light and produces a standing wave (Fig. 4.13**a**), producing a periodic optical intensity. Combined with the fact that the membranes are much larger than the optical gradient laterally ($\sim 750 \times 750$ µm^2), we have a one-dimensional counterpropagating-wave optical trap in the out-of-plane direction. A simple (unpatterned) Si backplane has been shown before to be sufficient to create an interference pattern for such an optical trap [158].

We consider only motion in the out-of-plane direction of the membrane, so we are interested in the gradient of the electric field norm in the y-direction (Fig. 4.13**a**). The total force F_{de} induced by the optics on the dielectric Si_3N_4 structure can then be found by integrating this gradient over the membrane domain,

$$F_{\mathrm{de}} = \int_{V_{SiN}} \alpha \frac{\partial |E|^2}{\partial y} \mathrm{d}V, \tag{4.13}$$

with α the polarizability. For a linear isotropic material, the constant $\alpha = P_x/E_x$ can be found from the simulation by dividing the polarization in any direction P_x by the electric field in that direction E_x.

We need relate the equation for F_{de} (units of force) to the coefficient F_{o} (units of force) used in Eq. (4.1). The expression for F_{de} depends on the position of the resonator with respect to the Si backplane, Fig. 4.13**b**, whereas F_{o} is a constant. $F_{\mathrm{de}}(x)$ in Fig. 4.13**b** shows the periodic behavior expected from an optical trap (i.e. periodic sign change), as well as a slight asymmetry due to radiation pressure. It shares the periodicity that we have separately introduced in Eq. (4.1), $\sin\left(\frac{4\pi}{\lambda}(x-x_{\mathrm{off}})\right)$, but does not exactly follow the same curve due to the finite size (thickness) of the membrane with respect to the wavelength. To simplify the dynamical calculations, we have thus chosen to separate out the periodic behavior and leave it proportional to the optical intensity, $\sin\left(\frac{4\pi}{\lambda}(x-x_{\mathrm{off}})\right)$, and keep F_{o} as a constant equal to the maximum of $|F_{\mathrm{de}}(x)|$. Thus for a $t = 80\,\mathrm{nm}$ membrane subject to our 3.6 mW laser, we expect a maximum out-of-plane force in the order of 60 pN. This confirms the values of F_{o} used in the numerical simulations of Fig. 4.2 and in Sec. 4.6.1, which show that the dynamics of our membrane can be significantly altered by the presence of the optical field.

The different curves of Fig. 4.13**b** illustrate that the total optical force exerted on the membrane does not decrease monotonically with membrane thickness. When we calculate the effective strength of the trap (peak-to-peak force difference divided by the thickness of the membrane, in Fig. 4.13**c**), we see that it decreases for increasing Si_3N_4 thickness. There are minima around $t = \lambda/(2n_{\mathrm{SiN}})$ where n_{SiN} the index of refraction; the half-integer number of optical periods leads to a total cancellation of the net force on the membrane F_{de}.

Radiation pressure force

In an optical cavity, the interaction between radiation pressure and a mechanically compliant element can lead to optomechanical frequency combs [124]. The radiation pressure of an optical cavity coupled to a mechanical resonator can result in an effective cubic nonlinearity, and by sufficiently driving the optical cavity one can bring the system in the self-oscillation regime. This creates an optical frequency comb with a spacing equal to the mechanical frequency. We must thus distinguish the frequency combs from the dielectrophoretic force from those originating from the radiation pressure.

We follow the analysis of Ref. [124] as they analyze the stability of a mechanically compliant end-mirror optomechanically coupled to an optical cavity. Our Si_3N_4 membrane functions as the compliant end mirror, while the Si substrate is the other (fixed) end mirror. For a given set of parameters, we evaluate whether the frequency comb will appear through equations (9a,b) of [124], which amounts to checking the Routh-Hurwitz stability criterion. For completeness, the conditions for stability are

$$\begin{aligned} 3\mathcal{G}^2 + 4\Delta\mathcal{G} + \Delta^2 + \kappa^2/4 > 0, \\ \mathcal{G}^4 + d_1\mathcal{G}^3 + d_2\mathcal{G}^2 + d_3\mathcal{G} + d_4 > 0, \end{aligned} \tag{4.14}$$

with coefficients

$$\begin{aligned} d_1 =& 4\Delta, \\ d_2 =& \gamma\kappa + 6\Delta^2 + \gamma^2 - 6\omega_0^2 + \frac{\kappa^2}{2} - \frac{2\gamma\omega_0^2}{\kappa} - \frac{2\omega_0^2\kappa}{\gamma}, \\ d_3 =& \Delta\left(2\gamma\kappa + 4\Delta^2 + 2\gamma^2 - 8\omega_0^2 + \kappa^2 - \frac{2\gamma\omega_0^2}{\kappa} - \frac{2\omega_0^2\kappa}{\gamma}\right), \\ d_4 =& \Delta^2\left(\Delta^2 + \gamma^2 + \gamma\kappa - 2\omega_0^2 + \frac{\kappa^2}{2}\right) + \frac{\gamma^2\kappa^2}{4} \\ &+ \gamma\omega_0^2\kappa + \frac{\gamma\kappa^3}{4} + \left(\omega_0^2 + \frac{\kappa^2}{4}\right)^2. \end{aligned} \tag{4.15}$$

The key quantity is the static optomechanical frequency shift $\mathcal{G} = \frac{2g_0^2}{\omega_0}|a|^2$, with $g_0 = 2\pi \times 1$ Hz the vacuum optomechanical coupling strength typical for these membranes (see chapter 6). Additionally, $a = \left(\frac{\kappa P_\ell/4\hbar\omega_\ell}{(\kappa/2+i\Delta)}\right)^{1/2}$ is the average optical field amplitude in the cavity, determined by the cavity decay rate κ, laser power and frequency P_ℓ, ω_ℓ and detuning Δ. Finally, the mechanical frequency $\omega_0 = 2\pi \times 120$ kHz and linewidth $\gamma = 2\pi \times 0.1$ Hz are rounded from the values measured and reported throughout this chapter.

To estimate κ, we calculate the finesse of the Fabry-Pérot cavity formed by a 10 µm distance between an $R = 0.3$ Si_3N_4 and an $R = 0.35$ Si backplane. This is a low estimate for κ, as the Si surface is rough from fabrication (Fig. 4.10**d**), and we do not consider additional losses from that. We obtain $\kappa \sim 2\pi \times 430$ GHz. We assume the optimal detuning to reach the frequency comb regime, which is around $\Delta = -\kappa/4$. Combining these values, we can evaluate the expressions for the stability and determine a minimum input laser power to reach the frequency comb regime. This is at approximately 1.5 kW, several orders of magnitude larger than the 3.6 mW measured laser power output of our laser Doppler vibrometer. Thus the optomechanical (radiation pressure) instability is not the origin of our frequency combs.

In conclusion, we have simulated the behavior of a Si_3N_4 membrane subject to an incident laser. Due to the Si backplane, reflected light forms a standing wave which leads to a counterpropagating optical trap. We have calculated the force exerted on the membrane by the optical trap, its dielectrophoretic part is sufficient to generate the overtone frequency comb as described throughout this chapter. We have also verified that the optical cavity formed between the Si_3N_4 membrane and Si backplane is not good enough to lead to an optomechanical frequency comb based on the radiation pressure.

4.6.4. Optothermal parametric driving

Driving the trampoline resonators to sufficiently large amplitudes to see the frequency comb from the optical trapping potential requires a strong driving mechanism. We have previously used a piezo shaker to drive these membranes (Chapter 3,

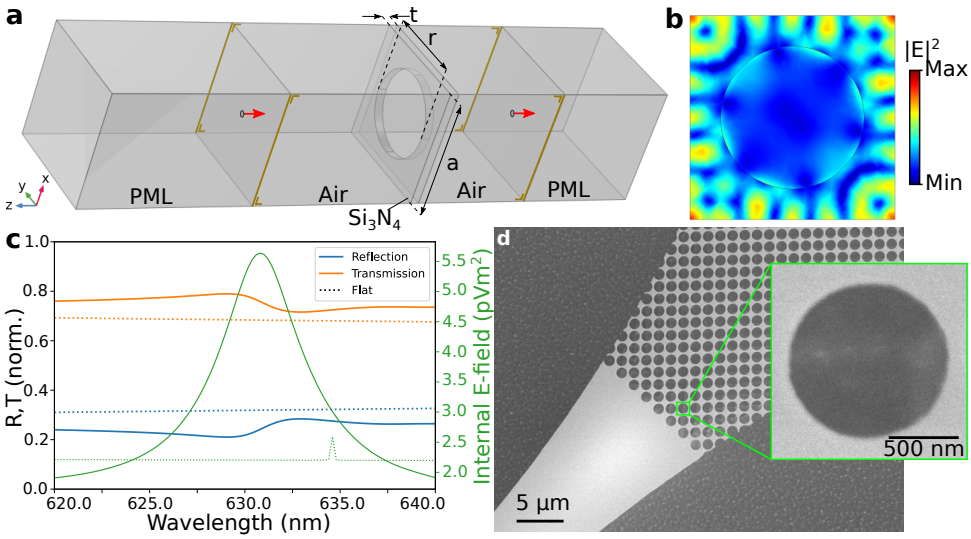

Figure 4.14: **Optical behavior of photonic crystal. a:** Schematic of simulation setup, consisting of a Si_3N_4 photonic crystal unit cell in air, with a plane wave incident in the out-of-plane direction (red arrows). There are periodic boundary conditions on the outer surfaces, with the brown markings indicating one of the surface pairs. **b:** Norm of the E-field along the mid-surface of the Si_3N_4 domain, showing a standing wave for $\lambda = 630.8$ nm. **c:** Reflection and transmission of the photonic crystal as a function of wavelength, and that of a flat Si_3N_4 surface for comparison (dotted lines). The feature in the reflection/transmission is correlated with the mode of the photonic crystal shown in **b**, indicated by the total E-field integrated over the Si_3N_4 domain (green). This feature is also absent for an unpatterned surface (green, dotted). **d**: SEM image of photonic crystal at the membrane edge, with inset showing single hole.

also described in Sec. 4.6.5), but for the majority of this chapter we use a optothermal parametric drive mechanism where the membrane reaches the self-oscillation regime [112]. That means that we can use a continuous-wave laser without power or frequency modulation, and do not require any additional signal or connection to the chip containing the resonator.

In the following subsections, we study the optothermal parametric driving. Since it is based on absorption, which is normally not too large for $\lambda = 633$ nm in Si_3N_4, we first show the absorption is enhanced by our photonic crystal structure. Then, we simulate the slow (> 0.1 s) thermal dynamics from steady state absorption and the fast ($\ll 0.1$ s) thermal dynamics due to modulated intensity from the standing wave optical field. Finally, we compare the simulated changes in temperature to the optothermal self-oscillation theory [112] and other effects from literature.

Absorption in the photonic crystal

Si_3N_4 is a often-used optical material because of its low absorption at telecom wavelengths, with typical absorption coefficients $\mu = 1 - 2$ cm^{-1} at 1550 nm [169]. However at 633 nm, absorption is higher and sensitive to deposition parameters (reports vary from $\mu = 2$ cm^{-1} [170] to $\mu = 5000$ cm^{-1} [171]. Works using a similar setup but low-stress Si_3N_4 measured 0.5 % absorption for a 50 nm film

($\mu = 100$ cm^{-1}) [93], so for simulation purposes we assume 1 % for our 80 nm film. It is difficult to verify the accuracy of this assumption, especially since our trampoline resonators are patterned with an array of circular holes that form a photonic crystal [34] and previously cited absorption coefficients cover unpatterned films. These works suggest absorption should be dependent mainly on material properties (Si_3N_4 deposition parameters) thus be the same for all membranes on a chip. However, we experience quite a variance in the response of our membranes to our laser beam (Sec. 4.6.7), and also depending on the exact positioning of the laser on the membrane, so we propose a different effect.

Photonic crystal patterns can be designed to yield a certain reflectivity at a target wavelength [34], but for the resonators in this chapter the photonic crystal functions as a mechanism to accurately control the resonance frequency (Chapter 3), as well as allowing their smooth undercut. Due to this, the photonic crystal parameters (lattice spacing $a = 1356$ nm, hole radius $r = 481$ nm) are larger than the wavelength, which allows standing waves in the Si_3N_4 domain that couple to waves incident on the plane of the membrane. These modes enhance the field inside the Si_3N_4 and thus could increase the absorption while being subject to fabrication imperfections such that not all membranes or locations on membranes absorb equally, leading to the variance in the observed optothermal self-oscillation.

We simulate the behavior of the photonic crystal in COMSOL by taking a unit cell with the photonic crystal parameters (a, r, and Si_3N_4 thickness $t = 100$ nm), as shown in Fig. 4.14**a,d**. We use $n = 2.016$ for the Si_3N_4 domain and $n = 1$ for vacuum. Parallel to the plane of the membrane we define two periodic ports, for input (reflection) and output (transmission), which are located sufficiently far away from the Si_3N_4 domain. These ports border a perfectly-matched layer that absorbs scattered light that is not absorbed by the periodic ports. The incident wave is an plane wave with normal incidence to the slab, with a polarization in the $x + y$ direction, and the entire simulation domain has periodic boundary conditions in x and y directions (brown lines in Fig. 4.14**a**.

From this simulation, we find that a standing wave pattern forms in the plane of the Si_3N_4 membrane, shown in Fig. 4.14**b**. When we evaluate the reflection and transmission of this photonic crystal, we see only a small feature around $\lambda = 630.8$ nm, Fig. 4.14**c**. However, the field integrated over the Si_3N_4 domain is much enhanced. These modes are sensitive to material thickness, a and r, and not unique to the parameters chosen for our simulation. We propose that standing waves of this form cause strong(er) absorption of light in some of our structures, depending on fabrication imperfections and precise laser position.

Slow thermal behavior

To build our understanding of the effects of the absorbed light, we simulate the effect of a heat source on the photonic crystal membrane (Fig. 4.15**a**). The membrane structure is symmetric, so we can reduce the simulation domain to only a quarter of a membrane. The outer edges of the domain connect the suspended Si_3N_4 connects to the (much more massive) Si substrate, so we apply a fixed temperature condition (purple). The heating due to the laser light is considered as an

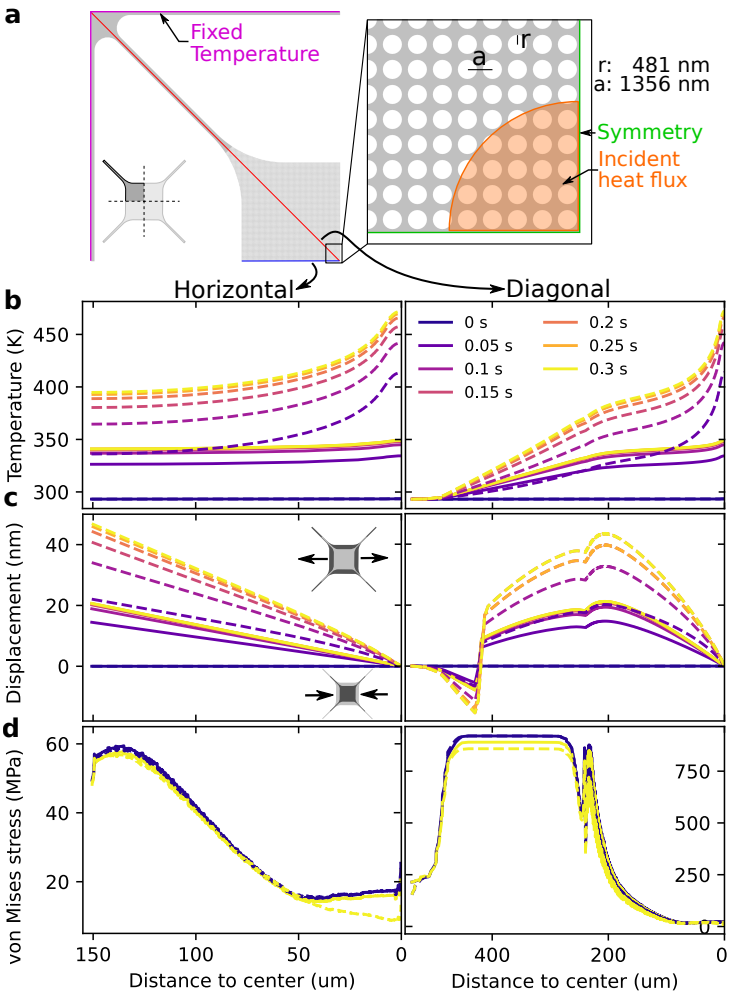

Figure 4.15: **Thermal behavior of photonic crystal. a:** Schematic of simulation of the laser heating the suspended membrane. Boundary conditions and geometry are described in the text. Results are extracted along two linecuts, horizontal (left column) and diagonal (right column) in **b, c, d**. Starting from room temperature, an incident heat flux representing absorption from the laser light heats up the membrane over time. Colors indicate time, solid lines assume thermal conductivity $k = 20\,\mathrm{W\,m^{-1}\,K^{-1}}$, dashed lines use $k = 2\,\mathrm{W\,m^{-1}\,K^{-1}}$. **b:** Temperature along the linecuts shows heating in the center, which settles within 0.3 s. **c** Displacement of the geometry away from (positive) or towards (negative) the center of the domain due to thermal expansion. The maximum displacement is ~ 45 nm. **d:** Von Mises stress (smoothed, only first and last timestep shown). Left and right panel have different y-axis scale.

incident heat flux in the center of the membrane (orange), defined via the total deposited heat as $P\mu_{\mathrm{Si_3N_4}}$ with laser power $P = 3.6$ mW and absorption coefficient $\mu_{\mathrm{Si_3N_4}} = 0.01$. The heat can be lost through the fixed temperature boundary condition at the outer edges of the domain, but also through radiative transfer in the

out-of-plane direction, where we assume the environment is at room temperature. We use a surface emissivity of 0.1, which is valid for room temperature and a film thickness of 100 nm [108], and noticeably different than the $0.6 - 0.9$ value used for bulk Si_3N_4.

The choice of material parameters of Si_3N_4 is important for our simulation. The Young's Modulus $E = 250$ GPa, Poisson's ratio $\nu = 0.23$ and density $\rho = 3100$ kg m^{-3} are relatively well-known, and the fabrication pre-stress is known to be 1.0 GPa. The thermal properties reported in literature vary (see [93] and references therein), we take the specific heat $C_p = 700$ J kg^{-1} K^{-1} and thermal expansion coefficient $\Upsilon = 2.3 \times 10^{-6}$ K^{-1}. Literature values for the thermal conductivity vary between $k = 0.34$ W m^{-1} K^{-1} [172] and $k = 20$ W m^{-1} K^{-1} [173]. We simulate using both values and plot the results as solid ($k = 20$ W m^{-1} K^{-1}) or dashed lines ($k = 2$ W m^{-1} K^{-1}) in Fig. 4.15**b,c,d**.

The simulation results show that for both thermal conductivities, the temperature (Fig. 4.15**b**) reaches a steady state after $\lesssim 0.3$s, though the temperature is significantly higher for the low thermal conductivity case (470 K) than for the high thermal conductivity case (349 K). Due to this, the material expands by 20 (45) nm for the high (low) thermal conductivity case ((Fig. 4.15**c**). On a lateral dimension of 150 µm of the membrane this is negligible as it corresponds to approximately a 0.2 (0.4) nm increase in the lattice spacing a. Because of the width of the pad (middle of membrane) with respect to the tether, the stress in the pad is strongly reduced from the initial film stress (1 GPa), to < 20 MPa. By the heating, this can be reduced to close to zero stress (compare yellow-dashed line in Fig. 4.15**d** to the blue line). Overall, these changes are not so significant and unlikely to change the dynamics of the membrane by themselves.

Fast thermal behavior

After simulating the steady state in temperature, material deformation and stress described in the previous subsection, we will now include the time-modulated optical intensity. We assume that the resonator moves initially in its fundamental mode at 120 kHz, so the optical field intensity is modulated by the $\sin$ term of Eq. (4.1). We make sure to keep the time-averaged power the same as in our steady-state simulation. We simulate a full period, and plot the incident heat flux (grey) and resulting temperature averaged over circular domains at various distances from the center (colors) in Fig. 4.16**a**.

The incident heat flux modulates the temperature of the membrane with an amplitude of about 0.3 K and a delay on the order of a microsecond. This delay is smallest in the domain where the heat flux is directly incident (blue), and increases as we move further away from the center (orange through red). The change in temperature also decreases as we move further away, which indicates that the effect is local to the laser beam spot. We can also extract the average von Mises stress, Fig. 4.16**b**, according to $\sigma_{\text{avg}} = 1/\sqrt{2}\sqrt{(\sigma_{xx} - \sigma_{yy})^2 + 6\sigma_{xy}}$, with $\sigma_{xx,yy,xy}$ representing the stress components in the respective coordinates. This shows a clear inverse correlation with the temperature, and follows the trend of decreasing

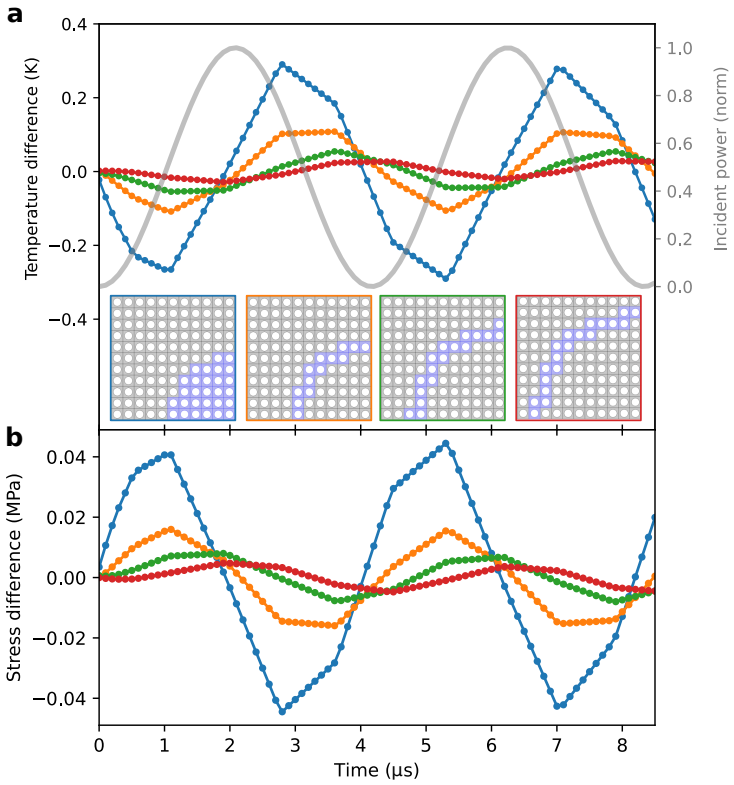

Figure 4.16: **Fast thermal dynamics. a:** Incident laser power (grey) and average temperature difference with respect to steady state ($\simeq$ 348 K for 120 kHz motion through standing wave optical trap field. Colors represent integration over domains depicted in the insets. **b:** Resulting stress change with respect to steady state.

in amplitude and increasing in delay as we move further away from the incident laser beam spot.

The resulting stress difference is relatively small compared to the total local steady-state stress ($\sim$ 24 MPa). However, it can forms a parametric driving mechanism since stress is modulated at double the frequency of the original motion, guaranteed by the optical standing wave. This optothermal parametric driving is thus automatically frequency-matched to the dominant motion. The delay between heat flux and stress suggests that this mechanism of driving is limited in our case to $\lesssim$ 500 kHz, which corroborates with the fact that only observe combs based on the first few eigenmodes.

Self-oscillation

We have shown so far that the motion of the membrane through the optical standing wave results in a modulated stress via the absorption. However, this alone is not sufficient to drive the resonator to larger amplitudes since dissipation is also

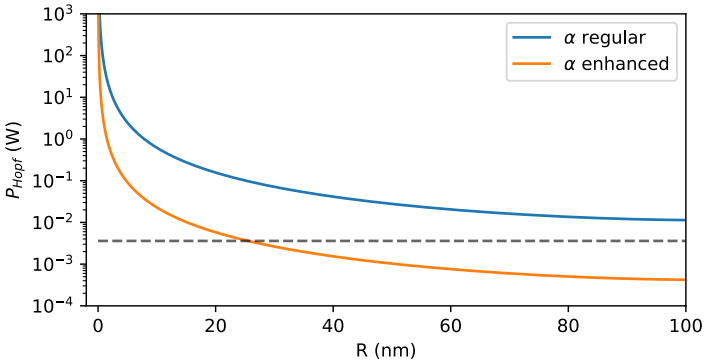

Figure 4.17: Simulated optical power necessary to create a limit-cycle of amplitude R, using the absorption expected for a bare Si_3N_4 membrane, and with one enhanced by absorption through internal standing waves due to the photonic crystal. Black dashed lines indicate maximum laser power used in experiments, 3.6 mW.

present (though small). To estimate whether this effect is strong enough to bring our resonator into limit-cycle oscillations under a $P \lesssim 3$ mW drive, we follow the model of [112]. There, the authors derive the minimum incident laser power to bring a resonator into the self-oscillation regime (Hopf bifurcation),

$$P_{\mathrm{Hopf}} = \frac{3(B^2+1)(B^2+4)}{2\pi^2 AQ\psi K}, \tag{4.16}$$

where

$$\begin{aligned} K &= \eta_1\lambda^4R^4 + \eta_2\lambda^2R^2 + \eta_3, \\ \eta_1 &= -4\pi^2(B^2+1)C, \\ \eta_2 &= -24\pi^2(B^2+1)x_{\mathrm{off}}^2C/\lambda^2 - 24\pi^2(B^2+4)x_{\mathrm{off}}D/\lambda \\ &\quad + 3(B^2+1)C, \\ \eta_3 &= -4D(B^2+4)(8\pi^2x_{\mathrm{off}}^2/\lambda^2 - 3)x_{\mathrm{off}}/\lambda. \end{aligned} \tag{4.17}$$

Here, A describes the heating due to the laser (units $\mathrm{K\,W^{-1}}$), B is a dimensionless constant, C represents the stiffness change due to temperature (units $\mathrm{K^{-1}}$), D is the optothermal forcing term (units $\mathrm{K^{-1}}$), Q is the mechanical Q-factor of our resonator, and ψ is the fraction of optical field that forms a standing wave. These equations give the laser power necessary to create a limit-cycle of amplitude R.

The authors of [112] give helpful guide on how to estimate the parameters of Eq. (4.16) from the simulations earlier in this section. To estimate the thermal parameters A and B, we require the steady state temperature at the point of illumination (center) of Fig. 4.15, T_{dc} (difference with respect to the room temperature environment), and the amplitude of the temperature change due to the standing

wave optical field from Fig. 4.16, T_{ac}. Using

$$A = BT_{\mathrm{dc}}$$
$$B = \frac{T_{\mathrm{ac}}\omega}{\sqrt{T_{\mathrm{dc}}^2 - T_{\mathrm{ac}}^2}} \tag{4.18}$$

and the values of T_{dc} and T_{ac} reported in the previous subsections, we get $A = 222425\ \mathrm{K\,W^{-1}}$ (independent of thermal conductivity k), and $B = 1257$ ($k = 2\ \mathrm{W\,m^{-1}\,K^{-1}}$) or $B = 3971$ ($k = 20\ \mathrm{W\,m^{-1}\,K^{-1}}$).

The forcing parameters C (parametric) and D (direct) can be estimated from other simulations. By calculating the difference between eigenfrequencies of our structure at the minimum and maximum temperatures of Fig. 4.16, $\Delta\omega_0$ for the fundamental membrane mode, we can use $C = 2\Delta\omega_0/(\omega_0 T_{\mathrm{ac}})$. We extract $\Delta\omega = 2\pi \times 200$ Hz from a simulation where we impose only the stress change due to the thermal behavior, which gives $C \simeq 0.01\ \mathrm{K^{-1}}$. The parameter D should be zero, because the tensile stress means that a temperature change does not lead to a direct out-of-plane displacement. This is true if the out-of-plane heat gradient is small enough, the tensile stress does not reach zero, and as long as our entire structure has the same thermal expansion coefficient (i.e. is from the same material). The latter is what distinguishes us from previous work on the optothermal excitation (bolometric backaction) driving a cantilever into self-oscillation [174], where the gold layer induces deflection under temperature change such that $D \neq 0$.

Finally, the we take mechanical quality factor $Q = 1 \times 10^6$ and $\psi = 1$. The latter we implicitly assumed already in Fig. 4.16, as the standing wave field cancels out fully (modulated power goes to zero). This is likely an overestimation due to losses and transmission through the Si backplane. The assumptions behind the derivation of [112] leading to Eq. (4.16) are somewhat different than for our system, since they use small displacement $x \ll \lambda$.

We evaluate Eq. (4.16) and plot the power necessary for a limit-cycle of radius R in Fig. 4.17. We distinguish between the absorption that we expect for an unpatterned Si_3N_4 film (1% light absorption, blue), and if it would be enhanced a factor 3 by the standing wave (orange). For non-zero limit cycle amplitude R, the orange curve lies below the (maximum) power we send in, 3.6 mW indicated by the black dashed line, which shows that our membrane can be driven to self-oscillation by the optothermal parametric effect. This requires a slightly higher absorption than would be expected based on the material parameters, which can be achieved due to the internal standing optical waves shown in the previous section. Fig. 4.17 shows that limit cycles with amplitudes larger than $R \simeq 30$ nm can exist. For $R \to 0$, no limit cycle appears which is due to $D = 0$ in our system. By evaluating the second derivative of P with respect to R, $\mathrm{d}^2P/\mathrm{d}R^2$, we find that the Hopf bifurcation is supercritical and thus our limit-cycle is stable [112].

The optothermal parametric drive forms an effective periodic modulation, which could also lead to a frequency comb, similar to the dielectrophoretic force. By including a periodic variation in the frequency ω_0, we simulate this effect. The

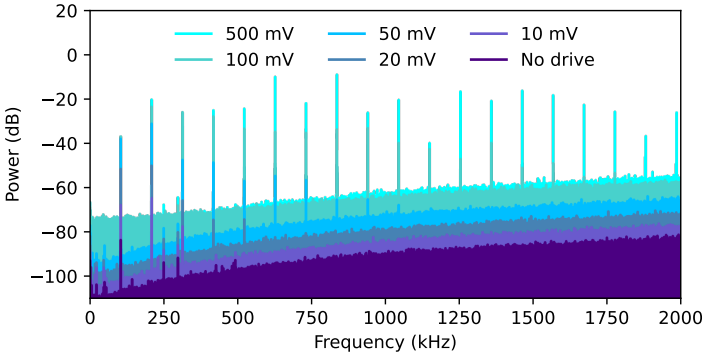

Figure 4.18: **Comb with sine drive.** Observed velocity power spectra for different drive powers of a 104.524 kHz sine wave. The overtones appear when the resonator is driven with high powers on resonance, such that the displacement amplitude is large. The individual traces are offset by 5 dB vertically.

equation of motion is

$$\ddot{x} + \gamma\dot{x} + \omega_0^2(1 + F_{\text{th}} \sin 2\omega_0 t)x = 0, \tag{4.19}$$

such that the parametric term oscillates at twice the frequency of motion. With $F_{\text{th}} = 1 \cdot 10^{-5}$, we are close to the simulated frequency shift $\Delta\omega$. Numerically integrating Eq. (4.19) yields an increase of velocity over time (even in the presence of damping $\gamma/2\pi = 0.2$ Hz). However, the higher harmonics generated by the inclusion of this parametric drive are negligible, 60 dB lower than the fundamental mode. Higher harmonics (above $2\omega_0$) do not appear visibly in the spectrum. While the optothermal parametric drive is sufficiently strong to drive the membranes to self-oscillation, it is not strong enough to result in a frequency comb without the dielectrophoretic force.

To conclude this section, we have simulated the optical and thermal behavior of our resonators and analyzed the possibility of self-oscillation. We find that the motion of the membrane through the standing wave optical field modulates the absorbed light intensity, which in turn modulates the tensile stress in the material. This is sufficiently strong to drive our resonator to self-oscillation, if the absorption is slightly higher than what is expected based on purely the material parameters.

4.6.5. Overtone comb with piezo driving

In this section, we demonstrate that it is possible to generate the overtone frequency comb through inertial driving with a piezo shaker. We do this by using several membranes that do not show any sign of overtones when the laser is positioned anywhere on the membrane for at least five minutes. This way, we exclude thermal parametric driving. The piezo shaker is mounted on the back-side of the sample holder and driven via an Agilent 33220A arbitrary waveform generator and a a FLC A400 voltage amplifier with $20\times$ gain.

In Fig. 4.18, we show the velocity power spectrum of a device that is driven on resonance by a sine wave of varying power. Without any drive, the fundamental mode (104.524 kHz) can be observed, together with the second and third modes above 250 kHz. At higher powers, the power in the first mode grows and overtones appear. For the highest drive powers, we retrieve a comb similar to the one reported in Fig. 4.2. This demonstrates that using an external drive tone, we can utilize the overtone mechanism to generate a frequency comb.

If the comb can be generated with the piezo by applying a white noise drive, it would be possible to avoid an external frequency reference that must be matched to the device. In Fig. 4.19**a**, we apply a white noise drive of varying peak-to-peak amplitude. Again, the overtone comb is absent for lower drive powers, but clearly present once the drive is sufficiently strong. Fig. 4.19**b** shows the fundamental mode for the lowest and highest drive cases.

We perform a similar analysis of the white-noise driven comb dynamics as for the optothermal parametrically driven comb of Fig. 4.2. The displacement of the mechanical resonator over time as we increase the drive power is shown in Fig. 4.19**c**, starting from 0 V at $t \leq 2.5$ s to 3 V at $t \geq 25$ s. Compared to those obtained via thermal parametric driving, the white noise drive results in a less smooth displacement signal. The amplitude is also noticeably smaller, which may be related to using a different displacement encoder, which is not impedance-matched to the oscilloscope used to record the time signal. By extracting the different overtones, Fig. 4.19**d**, we see the fundamental mode increase in power first, the first and second overtone grow some seconds later and the higher overtones only appear once the amplitude has grown sufficiently. This matches the behavior of the comb shown in Fig. 4.4. The bumps between $t = 20$ s and $t = 28$ s are due to the waveform generator internal switches.

We have shown that we can generate the overtone frequency comb using different driving mechanisms. Using inertial driving via a piezoelectric shaker, we observe qualitatively the same comb behavior as when using the thermal parametric drive. However, the white noise drive results in a noisier displacement signal and comb teeth powers. To highlight this, we show the displacement power spectrum around the first three tones in Fig. 4.19**e**, where the vertical lines indicate fast changes of comb power. This, combined with the added complexity of requiring a piezoelectric shaker, voltage source and amplifier, motivates the choice of using thermal parametric driving for the majority of the measurements in this chapter.

4.6.6. Extension via comb interactions

The bandwidth (span) of a frequency comb is an important property for many applications. While the overtone comb already performs on-par with the largest bandwidth mechanical combs (Table 4.1), we illustrate how the bandwidth can be extended further. This can be done by letting the frequency comb interact with a higher-order mechanical eigenmode ω_h of the membrane, to generate a comb with frequency spacing ω_0 centered around ω_h. This comb around ω_h has harmonics appearing on both sides of ω_h. In contrast, the comb of ω_0 has harmonics only on one side. This means that the interaction with ω_h could double the span.

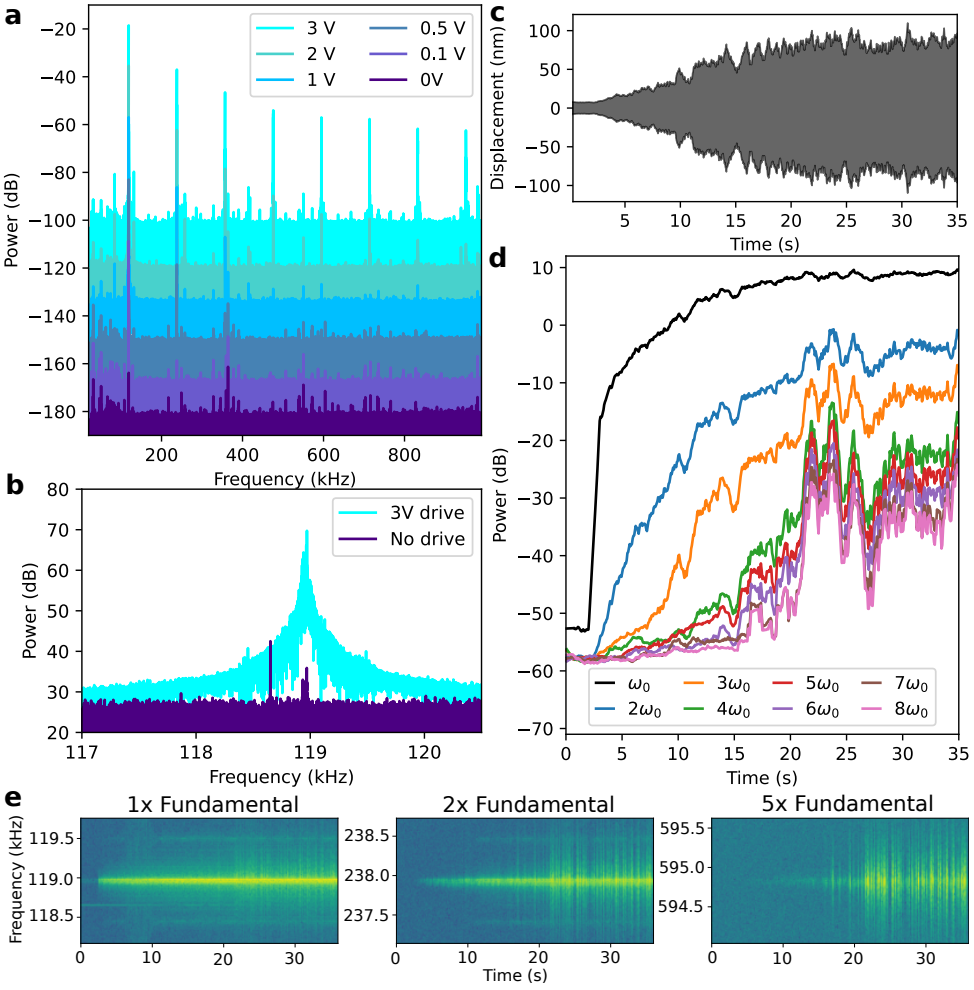

Figure 4.19: **Overtone frequency comb through piezo driving. a:** Displacement power spectrum for various white noise driving powers. The overtone frequency comb only appears for the highest driving powers. **b:** Fundamental mechanical mode without and with driving. **c:** Displacement of the resonator as the drive power is slowly increased from 0 to 3 V. The displacement shows a less smooth signal than those obtained through thermal parametric driving. **d:** Extracted strengths of the individual comb teeth over time from the signal shown in **c**. Jumps around 25 s likely originate from the waveform generator internal switches. **e:** spectral maps of fundamental and first two overtones. The jumps observed in **d** cause the vertical lines.

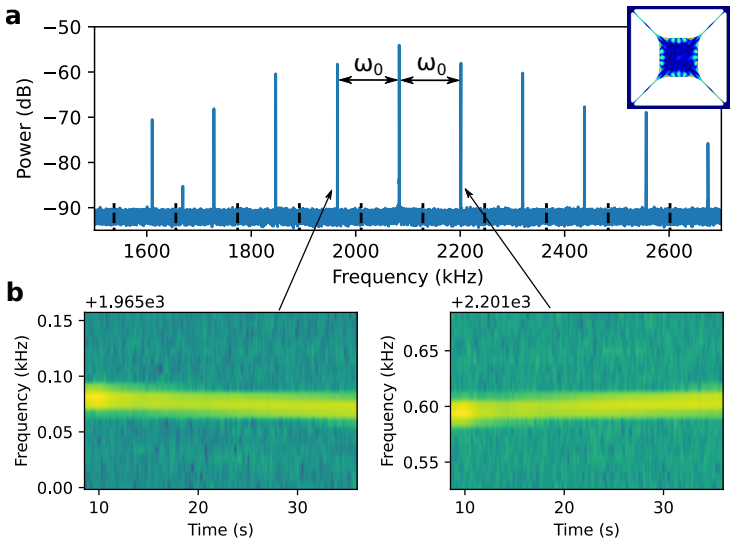

Figure 4.20: **Comb interactions. a**: Spectrum around a higher-order mechanical mode, showing a symmetrized copy of frequency comb of the fundamental mode, ω_0. The teeth are offset from the integer multiples of the original mode (dashed lines), but still equally spaced by ω_0. Inset shows mode shape of the (5,5) mode expected to be the center peak at 2083.3 kHz. Readout position is identical to Fig. 4.2**c**, where the (5,5) mode has considerable amplitude. **b**: The teeth of the secondary comb follow the 9 Hz shift of the fundamental comb mode as in Fig. 4.4, and shift symmetrically away from the center peak.

We observe a copy of the fundamental mode overtone comb (ω_0 spacing) symmetrically around the higher-order mode of the system. In Fig. 4.20**a**, we plot the spectrum around a higher order at $\omega_h = 2083.3$ kHz which we designate as the (5,5) mode shown in the inset. The simulated frequency of the (5,5) mode is at 2046 kHz, and this is the closest mode with significant mode amplitude at the readout position (same as in Fig. 4.2**c**). The symmetric pattern of ω_0-spaced comb teeth is offset from the overtones of ω_0 (black dashed lines).

To corroborate this interaction between the frequency comb as a whole and a higher-order mode of the membrane, we closely study the frequency of two of the comb teeth over time. Originating from the same measurement as Fig. 4.4, the fundamental mode at ω_0 has a 9 Hz upwards frequency shift over the duration of the measurement. In Fig. 4.20**b**, we plot the spectrum of two of the comb teeth (the first ones symmetrically around the central peak). These peaks show the same shift in frequency, but one shifts upwards while the other shifts downwards in frequency; they are clearly spaced around the central (5,5) mode peak by ω_0. The teeth further away from the center follow the $9n$ Hz scaling of the fundamental mode comb as described in Fig. 4.4. This interaction thus unlocks the possibility of shifting the overtone comb upwards in frequency and thereby extend its span.

4.6.7. Effect of optics on comb and membrane

In this section, we demonstrate the overtone frequency comb on multiple devices to corroborate the measurements shown earlier in this chapter. Additionally, we also describe the visible changes in the membranes under an optical microscope when driven into the overtone comb regime, and we study the effect of the optics (power and focus) on the frequency comb.

Comb prevalence and visible deformation

We observe the overtone frequency comb behavior on multiple devices, shown in Fig. 4.21**a**. We fabricated two nominally identical chips containing 25 membranes each. The membranes are identical with the exception of the photonic crystal parameters, as described in earlier in this thesis (Chapter 3). All of the designs feature the same internal modes that allow for strong absorption of $\lambda = 633$ nm light as in Sec. 4.6.4, albeit at slightly different wavelengths. Each chip contains the same set of 5 photonic crystal designs, oriented as marked in Fig. 4.21**a**.

Of the 45 surviving devices on the two chips, 27 demonstrated the frequency comb behavior based on optothermal parametric driving (Sec. 4.6.4), and the remainder could be driven into the overtone comb regime by sufficient piezoelectric shaking (Sec. 4.6.5). This confirms the generality of the overtone mechanism.

We can corroborate the relation of the overtone comb and (powerful) heating through absorption by studying the membranes using the microscope of the laser Doppler vibrometer. The presence of the optothermal parametrically driven frequency comb behavior is correlated with visible changes in the membrane structure. We show this by taking a microscope image immediately after the laser spot is moved to the center of the membrane (Fig. 4.21**b**, left column), and > 30 s later when the system has reached steady state (Fig. 4.21**b**, right column). There is an interference pattern at the edges of the membrane, which is likely from the change in photonic crystal pattern due to a stress-gradient from the edge of the Si_3N_4. The laser beam heats the membrane and via the thermal expansion of the Si_3N_4, the stress changes such that this edge deforms and the interference pattern changes.

We show three devices to illustrate different changes observable in this interference pattern in Fig. 4.21**b**. In some devices (top row), the pattern disappears completely, which suggests these have the strongest absorption: The deformation is larger than in other devices and the steady-state temperature is thus high. Simultaneously, these devices show strong frequency combs. In other devices (Fig. 4.21**b**, middle row), the interference pattern disappears only partially. This is typically along one diagonal, which suggests that the stress along the other diagonal is not fully removed; we can switch between the diagonals by positioning our laser spot. The steady-state temperature is likely less than in the case where the pattern disappears completely, and also the frequency comb appears less pronounced. Finally, a few devices show a small discoloration around the laser spot, which suggests that the interference pattern is modified only slightly. These devices display only weak frequency combs. These behaviors corroborate that the thermal parametric driving through absorption of the light is the origin of the frequency combs that we observe.

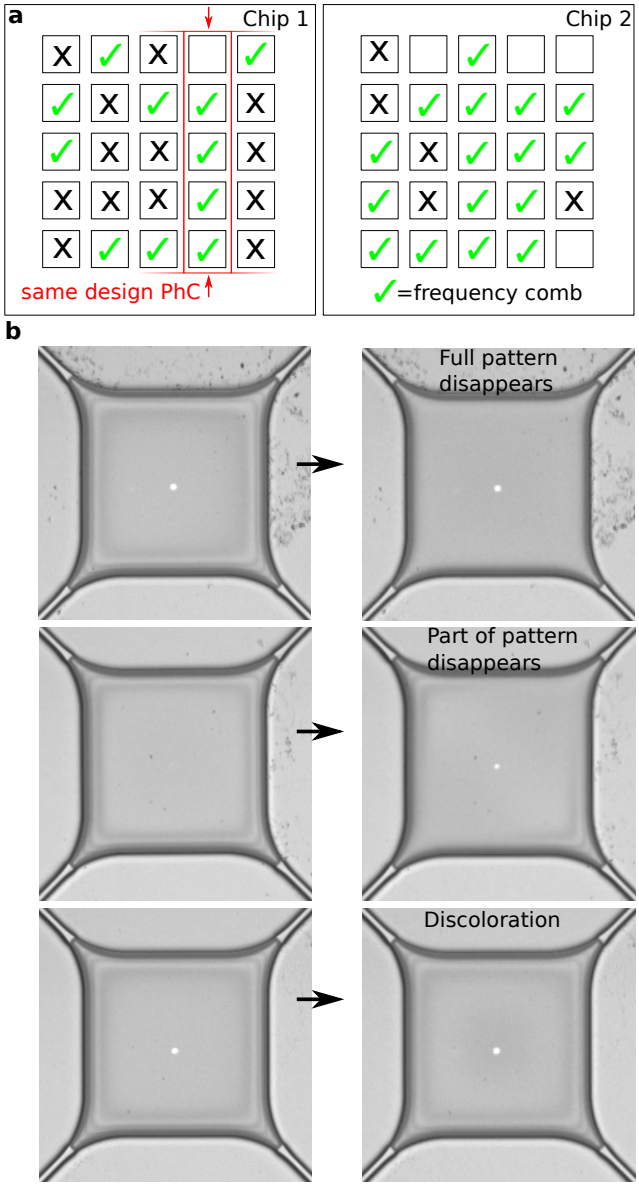

Figure 4.21: **Visual changes in membrane structure. a:** Schematic sample maps of two nominally identical chips containing 25 membrane devices each, using 5 different photonic crystal designs. Green checkmarks indicate which devices show frequency comb behavior when optically addressed, blank squares show membranes collapsed during fabrication. **b**: Microscope images of three different devices before (left) and during (right) frequency comb behavior, showing visible changes. The color pattern along the outer edge of the membrane either disappears fully (top), partially (middle) or shows as a slight discoloration centered around the laser spot (bottom), indicating induced change in the photonic crystal lattice spacing and hole radius.

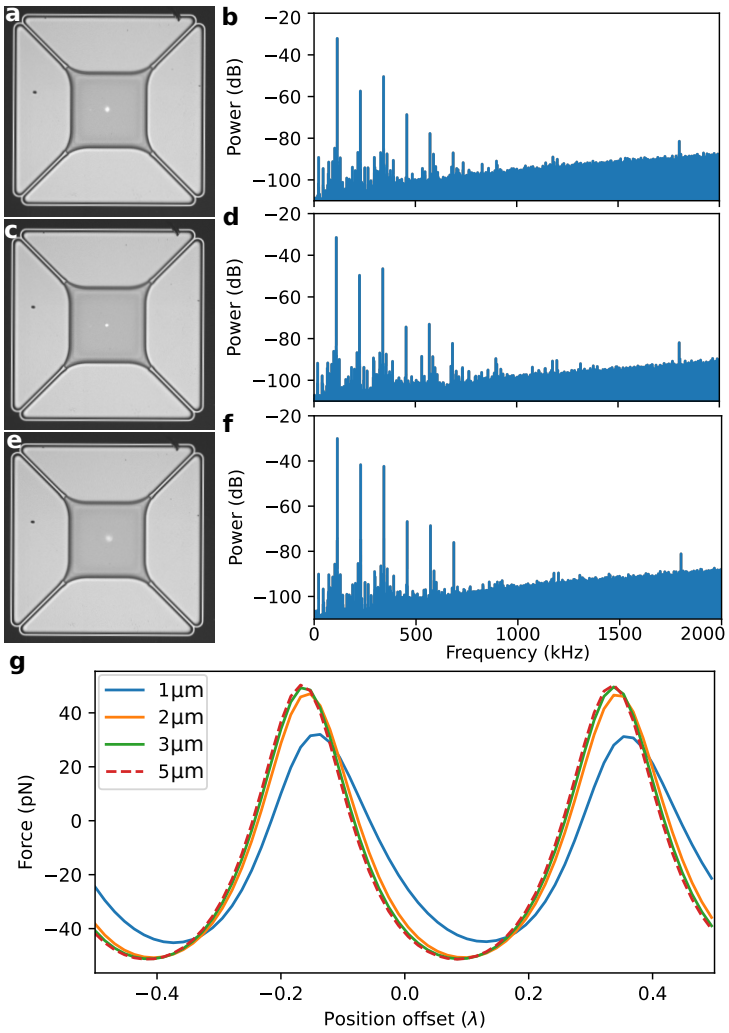

Figure 4.22: **Comb dependence on laser focus. a,c,e:** Microscope images of the same device with the laser focus before (**a**), at (**c**) and after (**e**) the plane of the membrane structure. **b,d,f:** Frequency comb spectra measured with the respective laser foci, showing no major change. **g:** Simulated trapping force as a function of beam waist for constant total beam power.

Comb dependence on optical focus

We study the effect of laser focus on the frequency comb behavior. By deliberately defocusing the laser beam, and using a membrane that has a weak frequency comb behavior, we expect the focus to change the number of overtones appearing in the spectrum.

In Fig. 4.22**a,c,e**, we show microscope images of the laser focus before, at and after the plane of the membrane. In **b,d,f**, we plot the velocity power spectrum

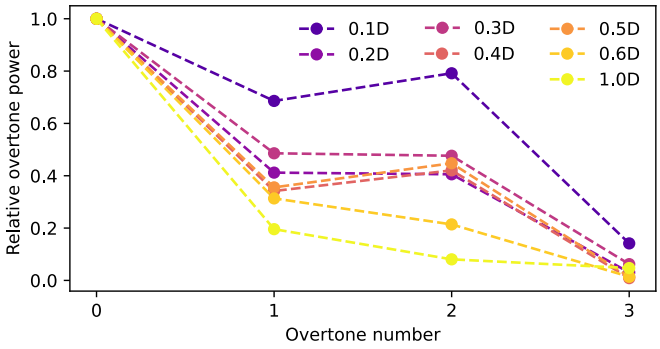

Figure 4.23: **Comb dependence on optical power.** Relative powers in the individual overtones, normalized the overtone powers without filter and to the power of the fundamental mode for each filter setting. With less optical power, the overtones decrease in power with respect to the fundamental mode, as simulated in Fig. 4.8. The labeled optical densities correspond to a transmission of $0.1\mathrm{D} : 79\%$, $0.2\mathrm{D} : 63\%$, $0.3\mathrm{D} : 50\%$, $0.4\mathrm{D} : 32\%$, $0.5\mathrm{D} : 32\%$, $0.6\mathrm{D} : 25\%$, $1.0\mathrm{D} : 10\%$.

measured from the devices with their respective foci, which are nearly identical. This shows that the formation of the frequency comb does not depend significantly on the laser focusing. Simulations of the optical trapping force as a function of beam waist (Fig. 4.22**g**) confirm this behavior: The trapping force does not change for beam waists > 3 µm. Simultaneously, the thermal parametric force is limited to the area of the beam spot, so as long as the total beam power is constant, the changes in power density and beam area will cancel and the thermal parametric driving will be constant. This shows that the generation of an overtone frequency comb does not require a tightly focused laser beam.

Comb dependence on optical power

We also study the effect of laser power on the frequency comb. We can add an absorptive neutral density filter to reduce the power of the optical beam. This decreased F_o and should decrease the power of the overtones with respect to the fundamental mode, as simulated in Fig. 4.8. In Fig. 4.23, we show the relative overtone powers measured on a single device, for various filter strengths. The power in every overtone is normalized to the overtone power for the measurement without optical filter. Subsequently, the powers of the individual filter traces are then normalized for the power in their respective fundamental mode (overtone number 0). F_o affects the power relative to the fundamental mode, not the absolute power.

From Fig. 4.23, we see a trend where the higher optical density filters lead to lower relative overtone powers. This matches the simulations shown in Fig. 4.8. For higher density filters and higher overtone numbers ($n \geq 4$), the signal quality is too poor extract a meaningful relative overtone power. Nonetheless, it is a clear validation of the model of Eq. (4.1) as the correct description of the source of the frequency combs.

4.6.8. Comb properties

An important property of a frequency comb is the stability of the comb teeth over time, both in amplitude and in frequency. To gain insight in how our overtone frequency comb performs, we park our laser on a single device and measure the spectrum on various timescales. From each spectrum, extract the frequency and amplitude of some of the overtones, and plot them in Fig. 4.24.

In Fig. 4.24**a**, we plot the power of the overtones at ω_0, $5\omega_0$, $15\omega 0$ and $30\omega_0$, offset vertically for clarity. On the timescales > 1 min, the amplitude of the individual overtones fluctuates around a constant mean with a 95% confidence interval between 2.0 dB and 2.5 dB. On shorter timescales, a correlation between the amplitudes is visible which can be reproduced by simulations if decay is included.

In Fig. 4.24**b**, we show the frequency of the same set of overtones, where the width of the displayed part of the spectrum is proportional to the overtone number. The color indicates power and is the same for the bottom three rows, but multiplied by a factor 10 for the top row for clarity. All comb teeth display the same frequency shift over time, scaled by overtone number. This correspondence is *exact*, to within the resolution of our measurement. On short timescales (< 16 s), the frequency of the fundamental mode is stable to within the resolution of our measurement (0.78 Hz). However, we can use the exact frequency correspondence and observe a slight shift of the overtone at $30\omega_0$, 4.68 Hz over the measurement time, or $7.9 \times 10^{-8}\,\mathrm{s}^{-1}$ relative frequency stability. This is likely limited by the environment temperature causing a frequency shift of the mechanical mode. That shift is clearly visible as the slow drift on longer timescales, as the right-most column was measured overnight and the frequency seems to stabilize. There are also oscillations on a 10 min timescale, which we attribute to the room air conditioning. If we select the most stable 6-hour period of our overnight measurement, the fractional stability reaches $7.5 \times 10^{-10}\,\mathrm{s}^{-1}$.

4.6.9. Noise in overtone frequency combs

We study fluctuations in the frequency comb as a response to (thermal) noise. By starting from Eq. 4.1 and including a Langevin force noise term $\xi(t)$, we obtain

$$\ddot{x} + \gamma\dot{x} + \omega_0^2 x = F_\mathrm{o} \sin\left(\frac{4\pi}{\lambda}(x - x_\mathrm{off})\right) + F_\mathrm{d} e^{i\omega_d t} + \xi(t), \tag{4.20}$$

Where the noise has zero mean $\langle\xi(t)\rangle = 0$ and is correlated $\langle\xi(t)\xi(t')\rangle = 2\gamma T\delta(t - t')$ such that we have assumed Markovian noise at temperature T, valid since resonator $Q = \frac{\omega_0}{\gamma} \gg 1$ [175]. We expand the sine-squared nonlinear term in the same way as in Sec. 4.6.1, where we keep all the terms since the displacement is not small. We can rewrite this to

$$\ddot{x} + \gamma\dot{x} + \omega_0^2 x = \sum_n^\infty \alpha_n x^n + F_\mathrm{d} e^{i\omega_d t} + \xi(t), \tag{4.21}$$

such that if $x_\mathrm{off} = 0$, all odd coefficients (α_1, α_3, α_5,...) are zero. Let us first consider the oscillation of only the first harmonic term, $x = \frac{1}{2}\left(Ae^{i\omega_0 t} + A^* e^{-i\omega_0 t}\right)$.

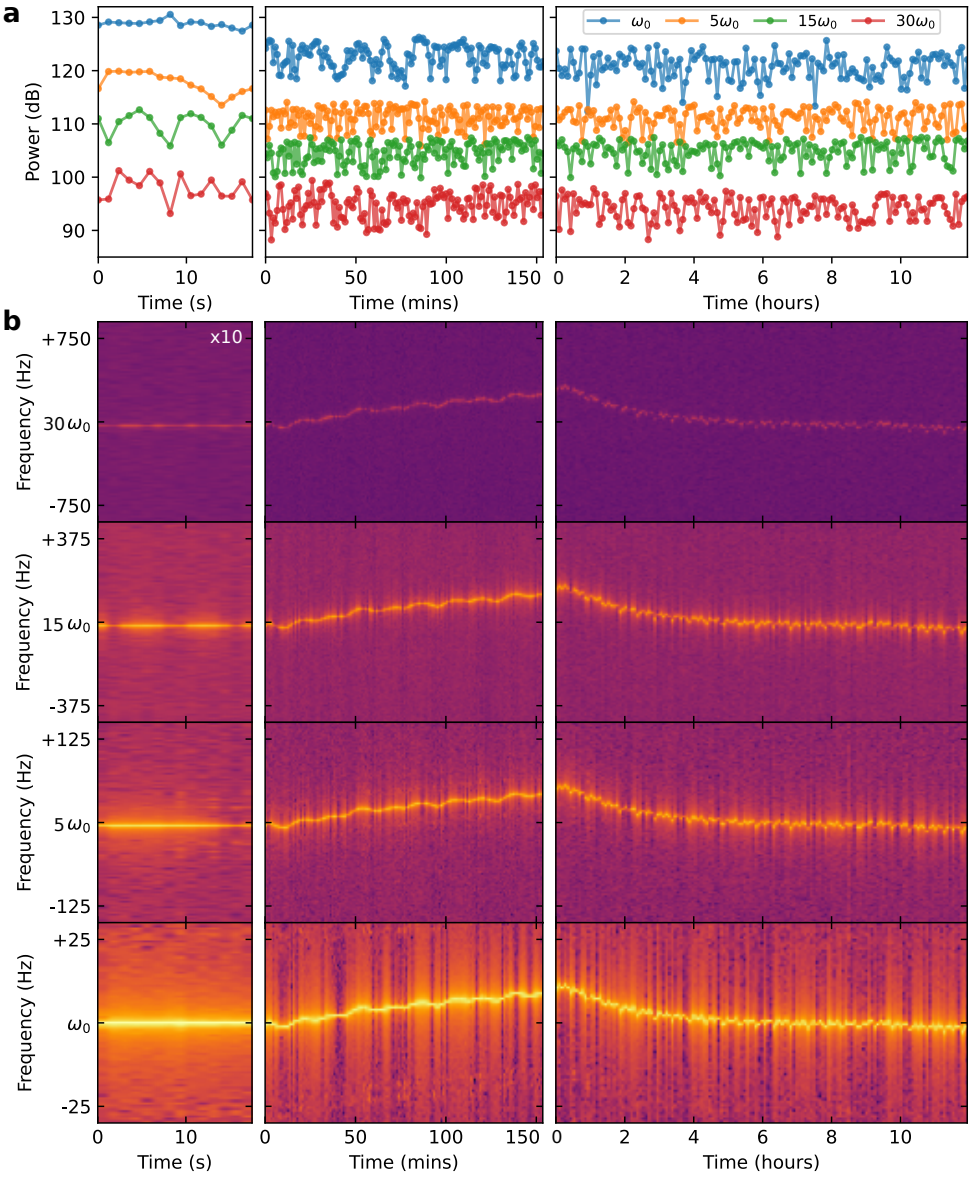

Figure 4.24: **Comb stability. a**: Extracted power of different overtones (ω_0, $5\omega_0$, $15\omega_0$ and $30\omega_0$), measured on the same device for several timescales. There is no correlation in the amplitudes on timescales longer than a minute, but there appears to be a beating pattern on short timescales. **b:** Frequency of different overtones, measured for several timescales. The frequency is stable on short timescales, but drifts due to temperature on timescales longer than a minute. The drift is the same (scaled by overtone number) for all overtones.

Then expand the series of $\alpha_n x^n$ and truncate all the tones that are not resonant. The first few terms read

$$\begin{aligned}
\alpha_1 x &= \frac{\alpha_1}{2}\left(Ae^{i\omega_d t} + A^* e^{-i\omega_d t}\right) \Rightarrow \alpha_1 x \\
\alpha_2 x &= \frac{\alpha_2}{4}\left(A^2 e^{2i\omega_d t} + 2|A|^2 + A^{*2} e^{-2i\omega_d t}\right) \Rightarrow 0 \\
\alpha_3 x &= \frac{\alpha_3}{8}\left(\begin{array}{c} A^3 e^{3i\omega_d t} + 3|A|^2 A e^{i\omega_d t} \\ + 3|A|^2 A^* e^{-i\omega_d t} + A^{*3} e^{-3i\omega_d t} \end{array}\right) \Rightarrow \frac{3\alpha_3}{4}|A|^2 x \\
\alpha_4 x &= \frac{\alpha_4}{16}\left(\begin{array}{c} A^4 e^{4i\omega_d t} + 4|A|^2 A^2 e^{2i\omega_d t} + 6|A|^4 \\ + 4|A|^2 A^{*2} e^{-2i\omega_d t} + A^{*4} e^{-4i\omega_d t} \end{array}\right) \Rightarrow 0.
\end{aligned} \tag{4.22}$$

We can thus rewrite Eq. (4.21) as

$$\ddot{x} + \gamma\dot{x} + \omega_0^2 x = \left[\alpha_1 x + 0 + \frac{3\alpha_3}{4}|A|^2 x + 0 + \frac{5\alpha_5}{8}|A|^4 x + \ldots\right] + F_{\mathrm{d}} e^{i\omega_d t} + \xi(t). \tag{4.23}$$

Now we can introduce a new set of coefficients β_n such that $\beta_1 = 1,\ \beta_2 = 0,\ \beta_3 = \frac{3}{4},\ \beta_4 = 0,\ \beta_5 = \frac{5}{8}$. Rearranging the terms now gives us

$$\begin{aligned}
\ddot{x} + \gamma\dot{x} + \left[1 - \sum_n \alpha_n \beta_n |A|^{n-1}\right]\omega_0^2 x &= F_{\mathrm{d}} e^{i\omega_d t} + \xi(t) \\
\ddot{x} + \gamma\dot{x} + \Omega_0^2 x &= F_{\mathrm{d}} e^{i\omega_d t} + \xi(t).
\end{aligned} \tag{4.24}$$

This way, we work with the frequency of the first harmonic, Ω_0, taking into account the shift due to the nonlinearity. In the case where $x_{\mathrm{off}} = 0$, all odd $\alpha_n = 0$, and all even $\beta_n = 0$ in general, which implies that the frequency of the first harmonic is not shifted by the nonlinearity. Intuitively, that makes sense since the electric field is symmetric around the resonator rest position for $x_{\mathrm{off}} = 0$.

We obtain the amplitude of the first harmonic by switching off the noise $\xi(t)$, and get

$$|A|^2 = \frac{F_d^2}{\left(\left[1 - \sum_n \alpha_n \beta_n |A|^{n-1}\right]\omega_0^2 - \omega_d^2\right)^2 + \gamma^2 \omega_d^2}. \tag{4.25}$$

Similarly, we can find the amplitude response to fluctuations $\xi(t)$ by turning off the coherent drive,

$$\ddot{x} + \gamma\dot{x} + \Omega_0^2 x = \xi(t). \tag{4.26}$$

In Fourier space, we then get

$$X(\omega) = \frac{\xi(\omega)}{\Omega_0^2 - \omega^2 + i\gamma\omega} \tag{4.27}$$

with autocorrelation

$$\langle X(\omega) X(\omega')\rangle = \frac{2\gamma k_{\mathrm{B}} T \delta(\omega + \omega')}{(\Omega_0^2 - \omega^2 + i\gamma\omega)(\Omega_0^2 - \omega'^2 + i\gamma\omega')}. \tag{4.28}$$

Then we can find the mean square amplitude response to fluctuations as

$$\begin{aligned}\overline{\delta x^2} = \langle X(t)^2 \rangle &= \int \frac{\mathrm{d}\omega}{2\pi}\frac{\mathrm{d}\omega'}{2\pi} \langle X(\omega)X(\omega')\rangle\, e^{i(\omega+\omega')t} \\ &= \frac{2k_\mathrm{B}T}{\Omega_0^2}.\end{aligned} \tag{4.29}$$

Thus the mean square amplitude of the first harmonic due to thermal fluctuations depends on the optical nonlinearity via Ω_0^2.

Now to obtain the net motion we consider both driving and noise terms (use Eq. (4.21)) and make the ansatz that our solution consists of a set of harmonics with a perturbation δx

$$x = \sum_{n=1}^{\infty} A_n e^{in\omega_0 t} + \sum_{n=1}^{\infty} A_n^* e^{-in\omega_0 t} + \delta x = B + \delta x. \tag{4.30}$$

The nonlinear term $\sum_n \alpha_n x^n$ from Eq. (4.21) can then be expanded and simplified by neglecting higher-order noise terms and keeping only the linear one. If $\delta x \ll B$, $(B+\delta x)^n \simeq B^n + nB^{n-1}\delta x$. Now if we let the sum in the nonlinear term go to a reasonable finite number N_max, we split the sum and shift the index of one of the two,

$$\begin{aligned}\sum_{n=1}^{\infty} \alpha_n (B^n + nB^{n-1}\delta x) &= \sum_{n=1}^{N_\mathrm{max}} \alpha_n B^n + \sum_{n=0}^{N_\mathrm{max}-1} \alpha_{n+1}(n+1)B^n\delta x \\ &= \alpha_1\delta x + \sum_{n=1}^{N_\mathrm{max}-1} B^n(\alpha_n + \alpha_{n+1}(n+1)\delta x) + \alpha_{N_\mathrm{max}} B^{N_\mathrm{max}}.\end{aligned} \tag{4.31}$$

If we then have $\alpha_n \simeq \alpha_{n+1}$ for all reasonable n, and small noise such that $\delta(n+1) \ll 1$, we can then absorb the term at N_max back into the sum,

$$\sum_{n=1}^{\infty} \alpha_n (B^n + nB^{n-1}\delta x) \simeq \alpha_1\delta x + \sum_{n=1}^{N_\mathrm{max}} \alpha_n B^n. \tag{4.32}$$

Thus we obtain the same solution in terms of the harmonics as we would do without considering fluctuations δx, with only the additional term $\alpha_1\delta x$. The equation of motion thus becomes

$$\begin{aligned}\sum_{n=1}^{\infty} A_n \left(\omega_0^2 - n^2\omega_d + in\gamma\omega_d\right) e^{in\omega_d t} + \ddot{\delta x} + \gamma\dot{\delta x} + \omega_0^2\delta x = \\ \alpha_1\delta x + \sum_{n=1}^{N_\mathrm{max}} \alpha_n B^n + F_d e^{i\omega_d t} + \xi(t)\end{aligned} \tag{4.33}$$

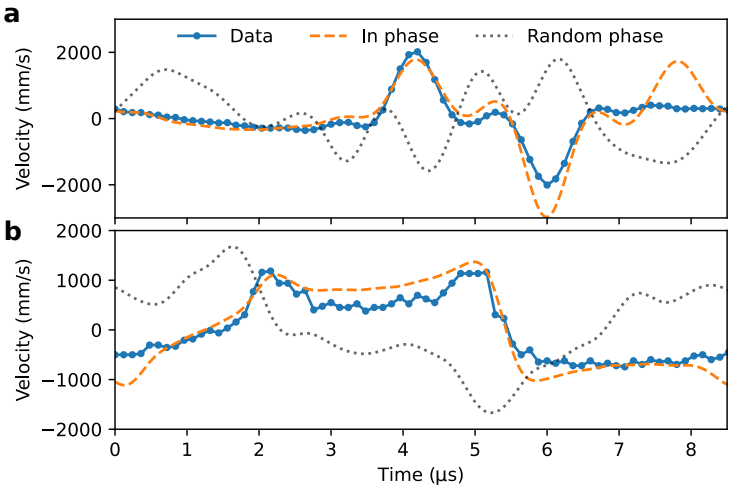

Figure 4.25: **Phase coherence of overtone comb. a,b**: Single period (blue) of the measured time signals of Fig. 4.5**c**, together with fits containing the sum of the first 16 cosines (overtones, at ω_0, ..., $16\omega_0$). In orange, the cosines all have the same phase offset, while in black the phase offset is random. This shows the phase-coherence of our overtone comb.

Based on the previous analysis, we can linearize this to

$$\sum_{n=1}^{\infty} A_n \left(\omega_0^2 - n^2\omega_d + in\gamma\omega_d\right) e^{in\omega_d t} + \ddot{\delta x} + \gamma\dot{\delta x} + \Omega_0^2 \delta x + F_d e^{i\omega_d t} + \xi(t) \quad (4.34)$$

where $\Omega_m^2 = \left[1 - \sum_n \alpha_n \beta_n |A|^{n-1}\right] \omega_0^2$. While the amplitudes A_n are obtained in Sec. 4.6.1, this analysis shows that the root-mean square fluctuations stay constant at $\frac{2k_B T}{\Omega_m^2}$ for all values of n. This indicates that the comb generation does not cause additional fluctuations or noise.

Thus we have confirmed our observations of Fig. 4.4**f**: The Lorentzian linewidth of our resonator fundamental mode is the same in the thermal regime as it is when driven into the overtone comb, since the optical nonlinearity does not add noise to the system.

4.6.10. Phase-coherence

To show the phase-coherence of all tones within the comb, we take a closer look at the time domain signal. When the overtones at $2, 3, 4, \ldots \times \omega_0$ have considerable amplitude, we can extract the phases of each component separately from the shape of a single period in the time domain. To do so, fit the sum of the first n cosine terms with amplitude coefficients $a_1, \ldots, a_n$ and phase offsets $\phi_1, \ldots, \phi_n$ using

$$\begin{aligned} A(t) = {} & a_1 \cos(2\pi\omega_0 t + \phi_1) + a_2 \cos(4\pi\omega_0 t + \phi_2) + \ldots \\ & + a_{16} \cos(32\pi\omega_0 t + \phi_n). \end{aligned} \quad (4.35)$$

When all phase offsets are the same, $\phi_1 = \phi_2 = ... = \phi_n$, the overtone comb is phase-coherent.

To fit Eq.(4.35), we extract the amplitudes of the first $n = 16$ overtones from the measurement of the whole time signal (~ 36 s). This we use as an initial guess for a fit that optimizes them to the final amplitudes that best describe a single period (~ 8 µs). We calculate two curves, one where all phase offsets $\phi_1, ..., \phi_{16}$ are the same (orange in Fig. 4.25**a,b**) and one where all the phase offsets are random (black). From this, it is clear that all overtones have the same phase offset and thus the overtone comb is phase-coherent.

5

Ringing ringdowns of near-degenerate mechanical resonances

Mechanical resonators that possess coupled modes with harmonic frequency relations have recently sparked interest due to their suitability for controllable energy transfer and non-Hermitian dynamics. Here, we show coupled high Q-factor ($>10^4$) modes with a nearly 1:1 frequency relation in spatially-symmetric microresonators. We develop and demonstrate a method to analyze their dynamical behavior based on the simultaneous and resonant detection of both modes, and validate this with experimental results. The frequency difference between the modes modulates their ringdown, and creates a ringing (beat) pattern in the linear decay. This method applies both to the externally driven and the Brownian motion (thermal) regime, and allows characterization of both linear and nonlinear resonator parameters. The mechanism behind this method renders it broadly applicable to both optical and electrical readout, as well as to different mechanical systems. This will aid studies using near-degenerate mechanical modes, for e.g. optomechanical energy transfer, synchronization and gyroscopic sensors.

I saw a mode
or two
talk in the light

This chapter was written together with with A. Cupertino, D. Shin, S. Gröblacher, F. Alijani, P. G. Steeneken and R. A. Norte, is in preparation and can be found at 2211.09636. All raw data, simulations, calculations and other supporting information can be found at 10.4121/21428517

5.1. Introduction

The dynamics of coupled resonators have been intensely studied from numerous perspectives over the last centuries. With the advent of ultra-high Q mechanical resonators ([13, 61, 99, 176] as recent examples), the regime of linear coupling between modes [103, 106, 177] has seen renewed interest, due to the sensitivity to small perturbations. High-Q resonators can be utilized for their long coherence- and lifetimes [97, 110, 178], but they often feature spatial symmetries that naturally predisposes them to have (near) degenerate or harmonically related eigenmodes (e.g. [179–182]). This makes them ideal candidates for various schemes in optomechanics, such as synchronization and phonon lasing [76, 81, 183–185], heat and energy transport [80, 186, 187], mechanical squeezing [188–191] and noise cancellation [192–194] (see also chapter 6). Mechanical systems with near-degenerate eigenmodes are an attractive platform for studying exceptional points, non-reciprocal coupling and other phenomena of non-Hermitian (open) systems [195–199]. An exceptional point, for example, requires the frequencies of the eigenmode to be degenerate while the decay rates are opposite (e.g. one mode is driven, the other decays). Additionally, near-degenerate mechanical resonances feature direct applications to sensors such as gyroscopes [200, 201].

Due to the development of suspended micro- and nano-scale resonators, some recent studies have focused on the nonlinear behavior of coupled mechanical modes. Coupled nonlinear modes [202, 203] can lead to stabilization [204] and low-noise oscillators. Strong coupling [205] can be used in mechanical signal processing, while coherent [206, 207] and nonlinear decay paths [208–210] could be leveraged for controlling energy transfer between modes [211].

In this chapter, we leverage our fabrication precision to design and study high Q-factor mechanical modes with a 1:1 frequency relation. Based on the spatial symmetries, we find pairs of modes whose shapes are identical except for a rotation by 90° in the plane of the suspended structures, separated in frequency by less than 6 parts per million (ppm). The energy decay shows evidence of coupling between the modes, which we extract using a characterization method based on the simultaneous, resonant detection of the modes. The detector has a bandwidth larger than the frequency spacing between the modes, such that we measure their superposition. Based on the frequency difference and relative mode amplitudes, we observe a characteristic beating pattern by performing ringdown measurements, from which we can extract the linear resonance parameters (frequency ω, damping γ and coupling strength J). We then use this method to observe the frequency shift due to a small Duffing nonlinearity, and to investigate the resonator phase decoherence in the thermal (Brownian) motion regime.

5.2. Results

5.2.1. Coupling and ringing

We study the dynamics of near-degenerate mechanical modes using optical interferometers, shown schematically in Fig. 5.1**a**. Two types of resonators are studied,

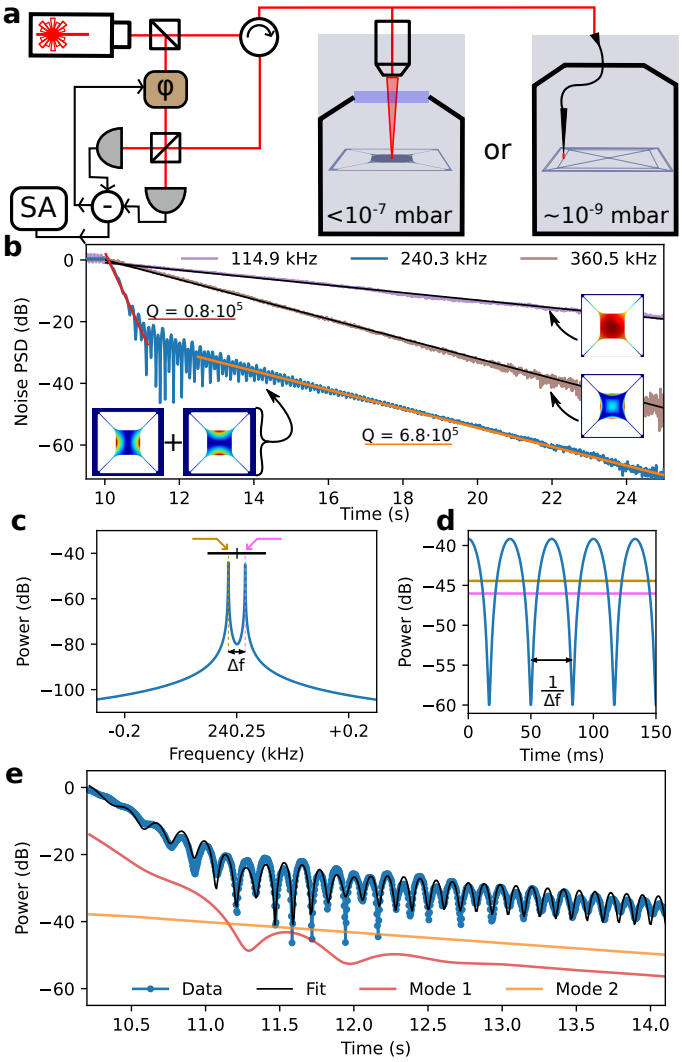

Figure 5.1: **a**: Schematic of the two homodyne detection setups used to measure the mechanical motion of membranes (left) or spiderwebs (right). SA: Spectrum analyzer, ϕ phase shifter. The sketched laser positions match experimental conditions. **b**: Ringdowns of first three membrane modes (inset: mode shape, red indicates maximum displacement). They are aligned to the time where the driving is stopped, at $t = 10$ s. The fundamental (purple) and third (brown) mode can be fit with single linear slopes (black), while the second mode shows two distinctly different linear slopes (red, orange, with fitted Q-factors) and a characteristic ringing pattern. The second mode consists of the two near-degenerate modes, 1 and 2, indicated in the inset. **c**: Simulated spectrum of two modes that exist as distinct spectral peaks separated by less than the detection bandwidth (black bar). **d:** The frequency difference Δf leads to a characteristic beat ('ringing') in the ringdown signal. The relative amplitudes of the modes (gold, pink horizontal lines) determine the amplitude of the ringing pattern. **e**: Simulated amplitudes of the near-degenerate modes 1 and 2 based on extracted decay rates from **b**, reconstructed signal with the ringing pattern (black) and the measured data (blue). Mode amplitudes are vertically offset for clarity.

trampoline membranes [13] and spiderweb resonators [61]. A free-space readout system is used for trampoline membranes (Fig. 5.1**a**, left), while the narrow beams of the spiderwebs necessitate a lensed-fiber readout (Fig. 5.1**a**, right). Applying a resonant drive to a piezo shaker mounted on the sample holder excites mechanical eigenmodes of the resonator. By stopping the drive and letting the amplitude decay, we perform a ringdown experiment that allows precise measurement of the decay rate.

The amplitude of a linear harmonic oscillator decays exponentially, which we observe in the motion of the fundamental and third eigenmodes of the trampoline membranes (Fig. 5.1**b**, purple and brown lines). These fit well to a straight line (black) when plotted in log-scale. The ringdown trace at 240 kHz shows significantly different behavior, corresponding to two different slopes, two different decay rates. The extracted Q-factors (red, orange lines indicate fits) differ by almost an order of magnitude. We will show that this peculiar ringdown behavior is due to the near-degeneracy of two membrane modes (simulated mode shapes inset in Fig. 5.1**b**). This near-degeneracy is present for the second mode of the membranes due to symmetry, but absent for the fundamental and third modes. In the following, we refer to the two near-degenerate (second) modes with indices 1,2.

To model the ringdown of two near-degenerate modes, we use modal coordinates x_1, x_2, decay rates γ_1, γ_2, resonance frequencies ω_1, ω_2 and a linear coupling between the modes, rate J [106]. The coupling can for instance occur via the substrate to which the resonator is anchored (Refs. [212, 213] and Chapter 3). In a ringdown measurement, we only observe the decay so our model does not need driving terms or noise sources; the initial amplitudes $x_1(t=0), x_2(t=0)$ of both modes are non-zero. Thus we obtain the following set of equations of motion,

$$\begin{aligned} \ddot{x}_1 + \gamma_1 \dot{x}_1 + \omega_1^2 x_1 + J^2 x_2 &= 0 \\ \ddot{x}_2 + \gamma_2 \dot{x}_2 + \omega_2^2 x_2 + J^2 x_1 &= 0. \end{aligned} \tag{5.1}$$

It bears mention that the system of Eq. (5.1) can always be diagonalized into eigenmodes ω_1', ω_2' with coordinates y_1, y_2 such that they are decoupled (see also Sec. 5.4.1). Both descriptions yield the same dynamics if their parameters are properly matched. We are in the weakly-coupled regime, so the modes we observe are close to the bare frequencies ω_1, ω_2 and thus we use the description of Eq. (5.1).

The near-degenerate modes of our resonator can be resolved as two distinct peaks separated by 9 Hz, as schematically shown in Fig. 5.1**c** (see also Sec. 5.4.2). This frequency difference is smaller than the detection bandwidth of our spectrum analyzer during the ringdown measurement (SA in Fig. 5.1**a**), such that both modes are captured in the single ringdown trace. This condition explains the observation of two different slopes in the same ringdown, if the two modes we observe have different decay rates.

In the kink between the two slopes (red, orange), we observe a particular ringing pattern. Such patterns commonly indicate energy exchange between two modes [106, 177]. However, the coupling strength necessary to create a ringing pattern with the frequency we observe would mean the modes are in the strong coupling regime (see Sec. 5.4.3). This regime is incompatible with the observation

of the two (different) slopes, since strong coupling allows the energy to decay via the fastest-decaying mode, i.e. one would only see the steepest slope.

Instead, we propose a different effect that contributes to the ringing pattern. The signal measured in a ringdown measurement is the total displacement of the resonator, which is the sum of the displacement of both modes at the detection spot (Fig. 5.1**a**). The total displacement power is thus of the form

$$x^2 = |e^{i\omega_1 t}\bar{x}_1 + e^{i\omega_2 t}\bar{x}_2|^2, \tag{5.2}$$

where we have split the mode coordinates x_1, x_2 into envelopes $\bar{x}_1, \bar{x}_2$, and fast-oscillating terms $e^{i\omega_1 t}, e^{i\omega_2 t}$. The bandwidth of our detector (100 Hz) makes it much slower than the frequencies ω_1, ω_2 ($\simeq 240$ kHz). However, the frequency difference $\Delta_f = \omega_2 - \omega_1$ (gold, pink in Fig. 5.1**c,d**) creates a beat with period $1/\Delta f$, which is slow enough to be detected. This means the detected displacement power x^2 gains a periodic modulation. This effect applies to different detection mechanisms (optical, electrical), as it only requires the bandwidth of the resonant detector to encompass both modes. It is analogous to electronically or optically down-mixing a signal by sending in a different tone and observing the beat pattern. In this instance, it is passively obtained based on the frequency difference and choice of measurement bandwidth.

To correctly fit the measured ringdown (Fig. 5.1**e**), we require both the linear coupling and the ringing effect. Without the latter, the frequency of the ringing pattern would indicate strong coupling, but this is incompatible with the presence of two slopes [106]. Without the former, the ringing pattern would only briefly appear in the ringdown as the mode amplitudes cross (Sec. 5.4.3), whereas it extends much further in Fig. 5.1**e**. A nonlinear coupling between the modes ($\propto x^3$) would lead to a ringing pattern that is qualitatively different to the one observed: the ringing would slow down in frequency as the amplitude decays (see Sec. 5.4.3 for a comparison of the linear and nonlinear models).

We obtain the individual mode frequencies $\omega_1 = 2\pi \times 240,331.9$ Hz and $\omega_2 = 2\pi \times 240,341.1$ Hz from a separate spectrum measurement (Sec. 5.4.2) which also allows us to calibrate the detection efficiencies for either mode. From the linear parts of the ringdown, we extract decay rates $\gamma_1 = 2\pi \times 6.0$ Hz and $\gamma_2 = 2\pi \times 0.7$ Hz. We can simulate the ringdown using only three fit parameters: the initial positions of the resonators x_{10}, x_{20} and coupling strength J. The optimized fit (black) to the data (blue) is shown in Fig. 5.1**e**, with dimensionless initial positions $x_{10} = 0.089 \pm 0.001$, $x_{20} = 0.071 \pm 0.001$ and coupling $J/(2\pi) = 320 \pm 5$ Hz. The frequency shift due to the linear coupling, J^2/ω_1, would correspond to 0.4 Hz if $\omega_1 = \omega_2$, so we are in the weakly-coupled regime. Nonetheless, there is sufficient coupling to observe energy exchange between the reconstructed mode powers (red, orange lines in Fig. 5.1**e**). For example, between 11.3 s and 11.5 s, mode 1 gains energy from mode 2, shown by the increase of the reconstructed power. The power in mode 2 correspondingly decreases, but this is not clearly visible in Fig. 5.1**e** due to the difference in detection efficiency between the modes. We numerically verify that the reconstructed power always decreases over time. Our measurement thus marks the observation of purely linear coupling between mechanical modes with a 1:1 frequency relation, without

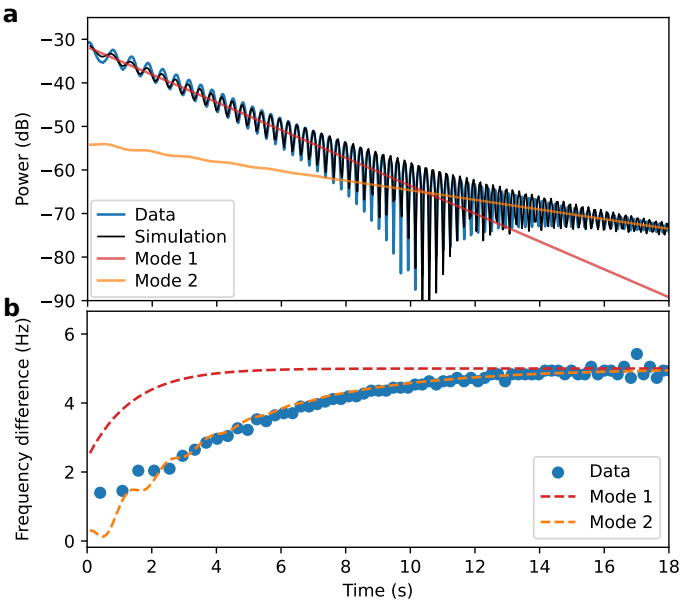

Figure 5.2: **a**: Ringdown with a prominent beating pattern, measured (blue) and simulated (red, orange, black). This experiment is performed on a different device than those of Fig. 5.1, but in the same experimental setup. Two separate, linear slopes can be distinguished, but they are similar since the decay rates of both modes are similar. **b**: Frequency difference between the two near-degenerate mode as the ringdown progresses, determined from the distance between subsequent minima of **a**. The fit (orange) is an exponential described in the text.

driving either mode to show nonlinear power decay.

5.2.2. Frequency shift

The ringing pattern is periodic with the inverse of the frequency difference between the two near-degenerate modes. Careful observation of Fig. 5.1**e** shows that this period is not constant; it changes with time. This means that the frequency difference is not constant, and that either one or both modes change in frequency over time. In the previous section, the energy decay was observed to be linear, sufficiently so that no nonlinearity is necessary to describe the ringdown completely. However, a small nonlinearity might still be present and lead to a frequency shift without measurably affecting the energy decay. Since the period of the ringing is inversely proportional to the frequency difference between the two modes, analyzing this periodicity provides a measure sensitive to small nonlinearities of the modes.

From the ringdown shown in Fig. 5.2**a**, we extract the frequency difference by finding the minima of the ringing pattern and taking the inverse of their time differences. We plot the frequency difference in Fig. 5.2**b** (blue), which shows an exponential trend towards $\Delta f = 5.0$ Hz. It is likely that the drive pulled the frequencies of the two modes together [214], which indicates the presence of a

nonlinearity. Assuming a small Duffing nonlinear term ($\propto x^3$), the frequency shift due to frequency pulling is of the form [214]

$$\omega_{nl} = \omega_0 + \frac{3}{8}\frac{\alpha}{m_{\text{eff}}\omega_0}\tilde{x}^2, \tag{5.3}$$

with Duffing coefficient α, effective mass m_{eff} and displacement amplitude $\tilde{x}$.

By observing the change in the frequency difference, we can extract which of the two modes is nonlinear, and whether it is softening or hardening. The linear mode parameters are extracted by the same procedure as before (via Eq. (5.1)), and we find $\omega_1 = 2\pi \times 240,302.5$ Hz, $\gamma_1 = 2\pi \times 0.7$ Hz, $\omega_2 = 2\pi \times 240,307.5$ Hz, $\gamma_2 = 2\pi \times 0.22$ Hz, and coupling $J = 2\pi \times 20$ Hz (independent of the value of α). We calculate the frequency shift as the mode amplitude decays from Eq. (5.3), which is consistent with mode 2 being frequency-pulled by the drive. This implies a softening nonlinearity ($\alpha < 0$), which is usually associated with an external (e.g. electrical or optical) force source. However, curvature of the membrane in the out-of-plane direction could also lead to a softening nonlinearity. Although the suspended membrane is nominally flat due to the tensile stress, some curving at the membrane edges can be observed under microscope. In the absence of any external sources of (softening) nonlinearity, this curvature could be responsible for the observed change in periodicity of the ringing pattern. An estimate for α based on the onset of the Brownian motion regime yields a value $\alpha_2 = -3\times10^{-21}$ m^{-2} s^{-2}, but a more accurate value should be obtained after calibration of the displacement and detection efficiency. The nonlinear term is sufficiently small compared to the coupling J that it is negligible for the measured ringdowns. Despite this, we can observe and measure the frequency shift due to the nonlinearity.

5.2.3. Resonator decoherence

Frequency shifts of resonators due to external factors are associated with resonator phase decoherence [178] or dephasing. This is detrimental for coherent control [97, 110], which is important for many quantum mechanical applications. Classically, one can observe the spectral width integrated over sufficient time to obtain the phase decoherence time [178]. We will describe how the ringing effect provides another mechanism to evaluate the phase decoherence time by utilizing the second mode as a frequency reference.

In spiderweb resonators [61], there is a set of modes extremely close to degeneracy, $\omega_1 = 2\pi \times 120,725.52$ Hz, $\omega_2 = 2\pi \times 120,726.14$ Hz (< 6 parts per million difference), as shown in Figs. 5.1**a** and 5.3**a**. These modes have linewidths below the resolution of the spectrum analyzer in this setup (0.01 Hz). We estimate their spectral linewidths to be 2.5 mHz and 2.3 mHz respectively (full width at half maximum, corresponding to $Q \simeq 25 \times 10^6$), which matches to the Q-factor extracted from a linear fit to the ringdown measurement, $Q = 21.1 \times 10^6$.

The ringdown measurement (Fig. 5.3**b**), shows the ringing pattern both in the strongly driven regime (blue) and in the Brownian motion regime (green). The dynamics of x_1, x_2 are much faster than our detection bandwidth, and our experiment is at room temperature, so we cannot directly resolve the thermal decoherence

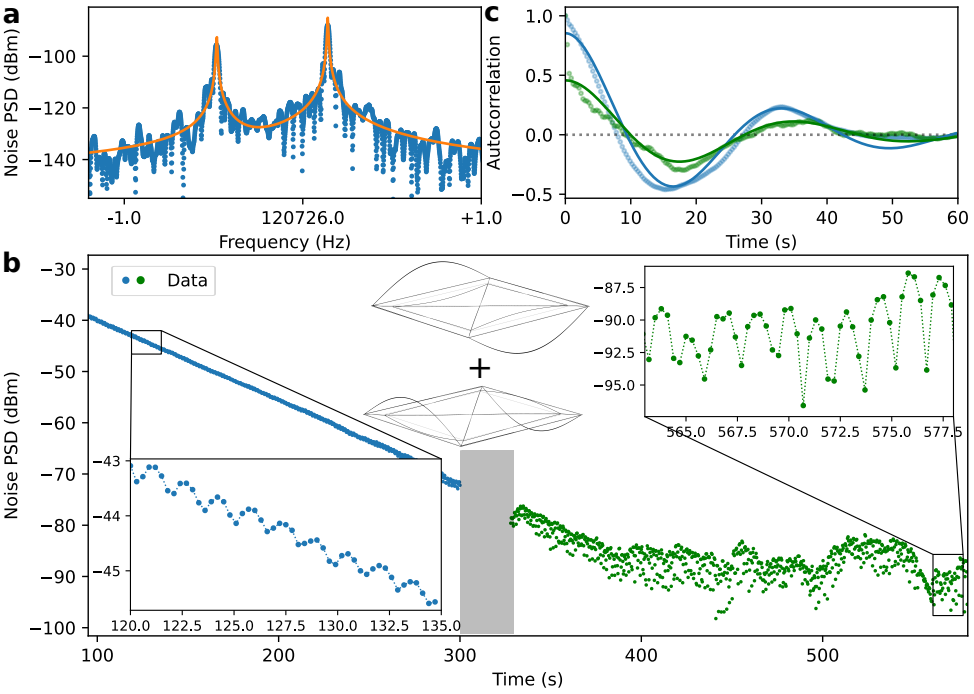

Figure 5.3: **a**: Mechanical spectrum of near-degenerate modes of a spiderweb resonator (blue), with Lorentzian fits (orange). **b**: Two consecutive ringdowns performed on the same device, one showing the decay from the driven state (blue), the other showing the last part of the ringdown and subsequent transition towards a Brownian motion driven state (green). Insets highlight the ringing behavior (dotted line drawn as a guide to the eye), which continues even in the Brownian-motion regime. Grey-colored region denotes the cut between the two ringdowns. The two simulated mode shapes are shown schematically. **c** Autocorrelation functions of the signal in the ringdown (blue) and Brownian-motion regime (green), showing a coherence time of 24 ± 2 s. Points indicate the experimental data, solid lines indicate the fit.

rate [97]. However, the ringing pattern is sensitive to fluctuations in the frequencies of the two modes. A phase-shift in the ringing pattern corresponds to a frequency shift between the two resonators. Thus monitoring the ringing pattern phase allows us to observe frequency shifts, which correspond to resonator phase decoherence. We can do so by calculating the autocorrelation of the ringing signal of Fig. 5.3**b**, which we plot in in Fig. 5.3**c**. It shows the behavior of a single, underdamped particle on a spring undergoing Brownian motion, which has an autocorrelation given by [215]

$$C(t) = \frac{\Gamma k_B T}{m_{\text{eff}}} e^{-\Gamma t} \left(\frac{1}{\Gamma} \cos(\delta t) - \frac{1}{\delta} \sin(\delta t) \right), \tag{5.4}$$

with $\delta = \sqrt{\Omega^2 - \Gamma^2}$. Here the frequency Ω is the frequency of the ringing pattern, and decay Γ is related to the phase decoherence time, i.e. when the amplitude of the autocorrelation drops by half. We fit a $1/\Gamma = 24.5 \pm 1.8$ s (24.8 ± 2.8 s) in the driven (thermal) regime respectively. This is close to the linear (energy) decay time

($Q/\omega_{1,2} \simeq 27.8$ s) extracted from the ringdown directly. This is the expected behavior for a linear harmonic oscillator: the phase decoherence time (measured via the ringing pattern) should be similar to the energy decay time (measured directly from the ringdown). Additionally, we fit $\Omega = 0.195 \pm 0.001$ Hz ($\Omega = 0.185 \pm 0.002$ Hz) in the driven (thermal) regime, which matches well with the frequency difference of the two modes $|\omega_1 - \omega_2|/\pi$. This illustrates that the ringing effect can provide a measurement of the phase decoherence of (near-) degenerate modes of a mechanical resonator.

5.3. Conclusion

We have experimentally studied high Q-factor mechanical modes of spatially symmetric microresonators that have a 1:1 frequency relation. We demonstrate linear coupling between these modes, present without driving the modes to nonlinearity. This is in contrast to previous studies, that generally require a quadratic or cubic term for coupling. To detect this linear coupling, we developed a characterization method based on a single, resonant detector. This detector has a detection bandwidth that encompasses both spectral peaks, such that we can see both modes decay in a single ringdown measurement. When the modes are nearly degenerate, an interference effect occurs that leads to a particular beating pattern. The relative amplitudes of the individual modes control the beating pattern amplitude, while their frequency difference controls the beating period. From the beating pattern, we can monitor the amplitudes of the individual modes and find their coupling rate. The beating period provides a sensitive measure to the relative frequency difference between the two modes. This allows us to observe slight frequency shifts due to nonlinearities, which would be difficult to observe using other methods. Our Si_3N_4 trampoline membranes feature a softening nonlinearity, which we attribute to out-of-plane curving. The beating period can additionally be used to monitor frequency shifts associated with phase decoherence of the modes. In Si_3N_4 spiderweb resonators, we find the phase decoherence time is similar to the energy decay time, as expected for linear harmonic oscillators.

Our characterization method is applicable to both optical and electrical readout schemes, and is particularly suited to high Q-factor mechanical resonators. This type of resonators is highly relevant for e.g. sensing, optomechanics and forms an attractive platform to study non-Hermitian systems. We have thus developed a broadly applicable method to characterize near-degenerate resonators, which can be immediately applied to studies in different fields.

5.4. Supplementary Information

5.4.1. Decoupling the EOM

It is convenient to obtain the relation between the parameters of the coupled and decoupled equations of motion for our system of near-degenerate modes. We start from the Fourier-transform of Eq. (5.1), where we have simplified $\omega_1 = \omega_0$, $\omega_2 = \omega_0 + \nu$ and $(\omega_0 + \nu)^2 \simeq \omega_0^2 + 2\nu\omega_0$ (thus assuming small ν). Thus we start

the equation of motion

$$\begin{bmatrix} \omega_0^2 + i\gamma_1 - \omega^2 & -J^2 \\ -J^2 & \omega_0^2 + 2\nu\omega_0 + i\gamma_2 - \omega^2 \end{bmatrix} \begin{bmatrix} x_1 \\ x_2 \end{bmatrix} = \begin{bmatrix} 0 \\ 0 \end{bmatrix}, \tag{5.5}$$

which is of the form $\mathbf{A}\vec{x} = \vec{0}$. It is straightforward to obtain the eigenvectors $\vec{e}_1$, $\vec{e}_2$ of matrix $\mathbf{A}$, and we put them in a 2x2 matrix $\mathbf{U} = [\vec{e}_1\ \vec{e}_2]$. Then we can obtain the diagonalized matrix $\mathbf{B}$ using $\mathbf{B} = \mathbf{U}^{-1}\mathbf{A}\mathbf{U}$. The coordinates in which the modes are decoupled are then given by $\vec{y} = \mathbf{U}^{-1}\vec{x}$. The eigenvalues (diagonal elements) of $\mathbf{B}$ are then given by

$$\begin{aligned} (\omega'_{1,2})^2 &= \omega_0^2 + \nu\omega_0 + \frac{i}{2}(\gamma_1 + \gamma_2) \pm \frac{\tau}{2}, \\ \tau &= \sqrt{4J^4 + 4\nu^2\omega_1^2 - \gamma_1^2 - \gamma_2^2 + 2\gamma_1\gamma_2 + 4i\nu\omega_0(\gamma_1 + \gamma_2)}. \end{aligned} \tag{5.6}$$

These $\omega'_{1,2}$ are the frequencies of the decoupled ('dressed') modes, which are the frequencies we observe in the spectrum. If we measure the splitting $2\pi\Delta f = \Delta\omega = |\omega'_1 - \omega'_2|$ and want to know the detuning of the coupled ('bare') modes $\nu = |\omega_1 - \omega_2|$ for a given coupling J, we use

$$\nu = \frac{1}{2}\left(\Delta\omega^2 + i\gamma_1 - i\gamma_2\right) - \sqrt{\Delta\omega^2(\omega_0^2 + i\gamma_1) - J^4}. \tag{5.7}$$

which allows us to find the frequencies of the coupled modes, $\omega_{1,2}$, from the decoupled modes and coupling strength J.

5.4.2. Spectrum and detection efficiency

A typical membrane device spectrum is shown in Fig. 5.4**a**. The the near-degenerate modes of interest show up at 240.3 kHz as two very closely spaced peaks separated by 9 Hz, as in Fig. 5.4**b**. The laser spot of our interferometer is large enough to capture the majority of the membrane pad and thus detect both the near-degenerate modes. In the high-Q limit, the expected PSD for a harmonic oscillator is a Lorentzian around its resonance [43]. The mechanical mode shapes are identical except rotated by 90°, so their effective mass m_{eff} is the same (barring fabrication imperfections) and their response to thermal or white-noise driving should result in equal displacement (power) in both modes [45]. Modeling this requires the linear decay rates of the modes, which we extract from the piecewise linear parts of the ringdown measurement, Fig. 5.1**b**. We obtain decay rates of $\gamma_1 = 2\pi \times 6.0$ Hz and $\gamma_2 = 2\pi \times 0.7$ Hz respectively for the modes at $\omega_1 = 2\pi \times 240331.9$ Hz and $\omega_2 = 2\pi \times 240341.1$ Hz.

Reconstructing the expected power spectrum results in the black lines of Fig. 5.4**b**. These suggest that instead of the detection efficiency (DE) being equal (dotted line), the lower-frequency mode is detected a factor 20 less efficiently (solid line). This is likely determined by the precise position of the laser beam on the membrane. From the (room-temperature) thermally driven amplitude ($\lesssim$2 pm), we deduce that the maximum driven amplitude $\simeq$2 nm, well within the linear regime

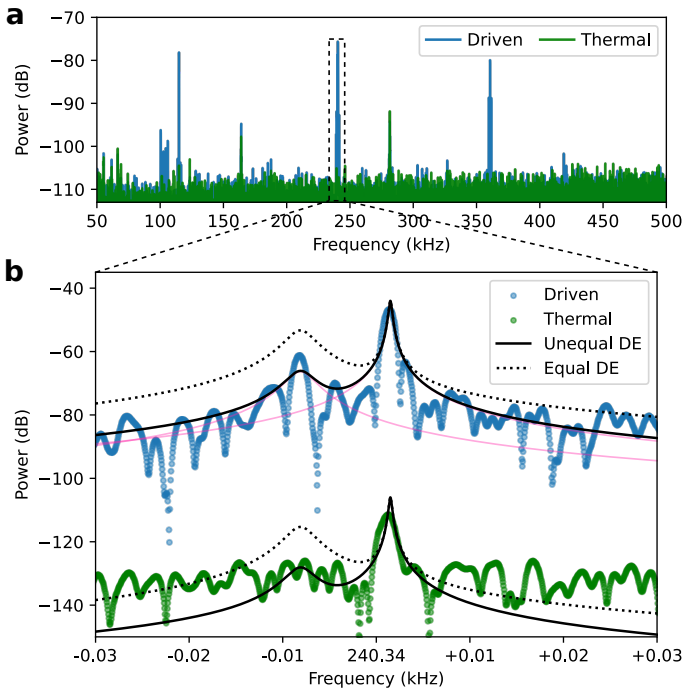

Figure 5.4: **a**: Spectrum of a typical mechanical resonator, showing the first three modes (114.9 kHz, 240.3 kHz and 360.5 kHz identified by their growth under white noise driving (blue) vs thermal driving (green). **b**: Spectrum around the near-degenerate modes (vertically offset for clarity). Rounded peaks are the result of the 1 Hz measurement bandwidth used. Black line indicates Lorentzian fit of the sum of the modes, dotted for equal detection efficiency and solid for the factor 20 less efficient detection of the lower-frequency mode. Pink lines indicate the individual Lorentzian components.

of the interferometer. In that same comparison, no frequency shift of the peak is visible which confirms that we are in the linear regime of mechanical motion and the Duffing nonlinearity is small. The rounded shape of the peaks is determined by the minimum detection bandwidth of the spectrum analyzer, 1 Hz.

5.4.3. Linear and nonlinear coupling

To distinguish between the coupling and ringing effects, we simulate and show ringdowns in Fig. 5.5 for various values of the coupling strength J. All simulations share the same initial condition as Fig. 5.1**e**. In Fig. 5.5**a**, there is no coupling between the modes, $J = 0$. In the absence of the ringing effect (dashed line), there is a smooth transition between two slopes. With the presence of ringing effect (solid line), the kink between the slopes gains the characteristic pattern.

In Fig. 5.5**b**, we replicate the ringdown of Fig. 5.1**e**. Without the ringing effect (dashed line), there is some oscillation present that is indicative of energy exchange between the modes. It appear superimposed on the ringing pattern (solid line), illustrating that the effects are independent and both are necessary to describe the

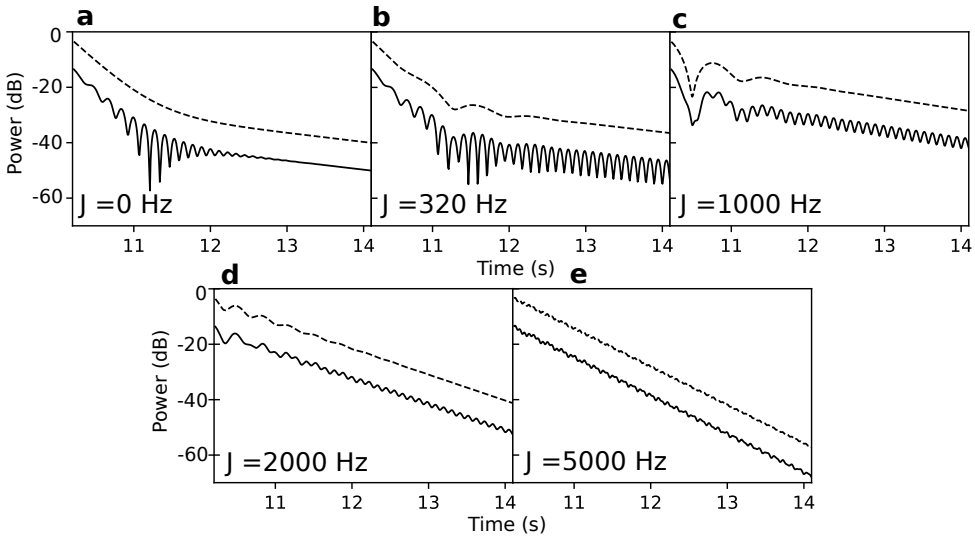

Figure 5.5: Simulated ringdowns with (solid) and without (dashed) the ringing pattern due to downmixing, for different values of coupling strength J. All simulations share the same initial values as Fig. 5.1**e**, the dashed lines are vertically offset by 10 dB for clarity.

observations.

In Figs. 5.5**c-e**, the coupling strength is increased until the strong-coupling regime is reached ($J = 5000$ Hz corresponds to a splitting of 104 Hz if $\omega_1 = \omega_2$). The oscillations due to the energy exchanged via the coupling increase in frequency, while the ringing effect decreases in amplitude. The two different slopes also transform into one slope in the strong coupling regime. Here, energy predominantly leaves the system via the fast-decaying resonator.

The ringing observed in ringdowns could also be related to energy exchange between nonlinear resonators with a 1:1 resonance [209]. The equations describing this are [209]

$$\begin{aligned}\dot{a}_1 &= -i\left(\delta_1 a_1 - \frac{3}{2}\alpha_1 a_1 |a_1|^2 + J a_2\right) - \frac{\gamma_1}{2} a_1 \\ \dot{a}_2 &= -i\left(\delta_2 a_2 - \frac{3}{2}\alpha_2 a_2 |a_2|^2 + J a_1\right) - \frac{\gamma_2}{2} a_2.\end{aligned} \tag{5.8}$$

Here, a_1, a_2 are the complex mode amplitudes, δ_1, δ_2 describes the detuning of each of the modes with respect to the rotating frame we choose (we pick $\delta_1 = 0, \delta_2 = 9$ Hz to match the 9 Hz difference between our two modes), α_1, α_2 are the Duffing nonlinearities of the modes, and J and γ_1, γ_2 are the mode coupling and linear decay rates.

We simulate our system using Eq. (5.8), and show the results in Fig. 5.6. In the absence of coupling or nonlinearities ($J = 0, \alpha_1 = \alpha_2 = 0$), Eq. (5.8) gives identical results to the model introduced earlier in this chapter. The detuning δ takes the role of the ringing effect, if we plot $|a_1 + a_2|^2$. This illustrates the generality of

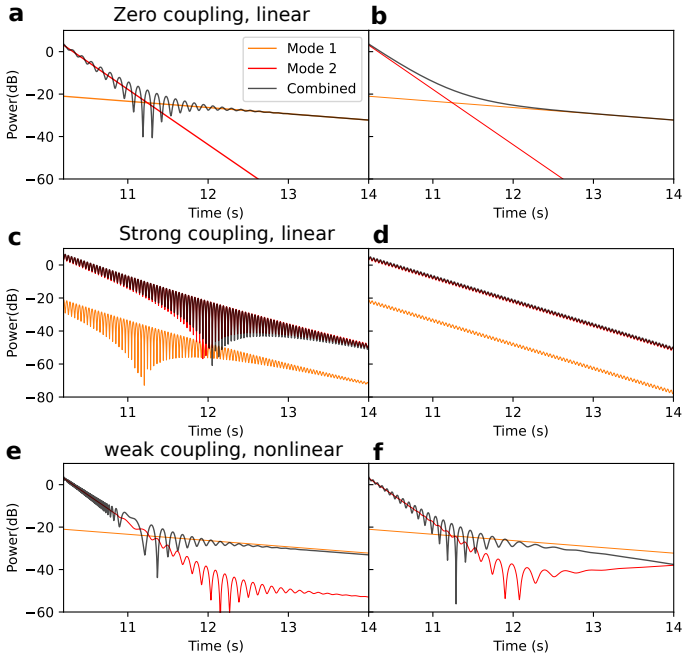

Figure 5.6: Simulated ringdowns using the nonlinear 1:1 coupling model of Ref. [209]. Left column (**a,c,e**) include the ringing, equivalent to the detuning in the model of Ref. [209], while the right column (**b,d,f**) excludes this effect. **a,b**: Ringdowns for zero coupling between linear resonators, replicating the result in Fig. 5.5. **c,d**: Ringdowns in the strong, linear coupling regime for different values of coupling strength J. **d** matches to Fig. 5.5, but **c** has an enhanced beat pattern due to the frequency splitting of the strong coupling. **e,f**: Ringdowns for nonlinear resonators, showing a ringing pattern that slows down as the amplitudes decay. All simulations share the same initial values as Fig. 5.1**e**.

the effect, as a_1, a_2 exist in a rotating frame (similar to the center frequency of our detector bandwidth). Figs. 5.6**a,d** thus match closely with simulated results of Fig. 5.5**a**. In the strong coupling regime (Figs. 5.6**b,e**), there is a difference due to the large frequency split. The model introduced earlier in this chapter explicitly contains the frequencies observed from a measurement of the spectrum (ω_1, ω_2), and thus constrains the frequency difference to this value. In contrast, Eq. (5.8) does not constrain this frequency splitting. Nonetheless, both models predict a single slope with fast, small oscillations.

In Figs. 5.6**c,f**, we introduce nonlinearity in the resonators $(\alpha_1 \neq 0, \alpha_2 \neq 0)$. This creates an oscillating pattern, where the frequency of oscillation decreases as the resonators decay. This trend is general (i.e. not dependent on the sign or values of α), and different from the trends observed in Figs. 5.1 and 5.2. In Fig. 5.1**e**, the ringing pattern stays constant in frequency, while in Fig. 5.2**a**, it increases in frequency. Thus these observations are inconsistent with a model whereby the ringing originates from the nonlinearity of the resonators.

Finally, the two linear slopes observed in the ringdowns could alternatively be

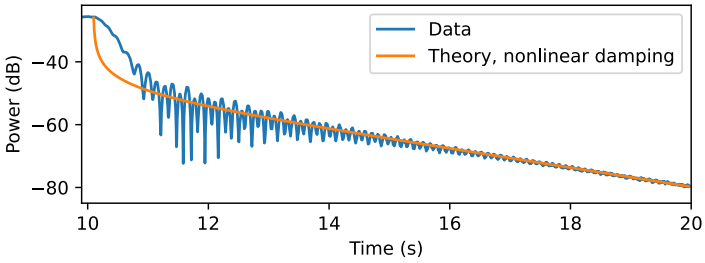

Figure 5.7: Simulated ringdown (orange) for a resonator with nonlinear damping, with the observed ringdown (blue) for comparison.

explained by a single resonator that has nonlinear damping [208], of the form

$$\ddot{x} + 2(\gamma_1 + \gamma_{\mathrm{nl}} x^2)\dot{x} + \omega^2 x = 0. \tag{5.9}$$

Here, γ_1 the linear damping and γ_{nl} the nonlinear damping. This term causes a fast decay directly after the driving stops, and returns the slow decay for lower amplitude. Qualitatively, the kink that results from this transition could have the same shape as the observed kink. However, the fast decay of the nonlinear damping region is much steeper than the fast decay we observe as show in Fig. 5.7, which rules out this nonlinear damping as an alternative explanation.

6

Coherent mechanical noise cancellation and cooperativity competition

Studying the interplay between multiple coupled mechanical resonators is a promising new direction in the field of optomechanics. Understanding the dynamics of the interaction can lead to rich new effects, such as enhanced coupling and multi-body physics. In particular, multi-resonator optomechanical systems allow for distinct dynamical effects due to the optical cavity coherently coupling mechanical resonators. Here, we study the mechanical response of two Si_3N_4 membranes and a single optical mode, and find that the cavity induces a time delay between the local and cavity-transduced thermal noises experienced by the resonators. This results in an optomechanical phase lag that causes destructive interference, cancelling the mechanical thermal noise by up to 20 dB *in a controllable fashion, matching our theoretical expectation. Based on the effective coupling between membranes, we further propose, derive and measure a collective effect, cooperativity competition on mechanical dissipation, whereby the linewidth of one resonator depends on the coupling efficiency (cooperativity) of the other resonator.*

Message on a trampoline
will travel lightly
just takes a while

This chapter has been published together with J. Li, C. Gärtner, R. A. Norte and S. Gröblacher in Optica **9**, 170-176 (2022). All data, measurements and analysis scripts in this work are available at 10.5281/zenodo.5782970.

6.1. Introduction

Cavity optomechanics [2] addresses the interaction between electromagnetic fields and mechanical motion. In recent years, multi-mode optomechanics, such as multiple mechanical resonators interacting with a common cavity field, has received significant attention and offered a platform for studying rich physics, including hybridization [216–219] and synchronization [76, 185, 220] of mechanical modes, mechanical state swapping [75], coherent [221] and topological [186] energy transfer, and two-mode squeezed mechanical states [190, 222, 223]. In particular, optomechanical systems consisting of multiple Si_3N_4 membranes have seen considerable progress towards the enhancement of their single-photon coupling rate [33, 37, 90, 224], and have been the subject of many theoretical proposals [183, 188, 225–227]. Compared to the relatively simple description of the standard optomechanical system, arrays of mechanical resonators coupled to a common optical mode offer the prospect of studying complex new physical effects and the ability to achieve individual control over each constituent of a multi-element system.

In this work, we study two mechanical resonators coherently coupled to a common cavity mode, that couples the thermal mechanical noise of the two resonators in an effective mechanical beam-splitter interaction [226, 228] that can be used to swap the mechanical states [75, 229] or topologically transfer energy between them [186]. By operating in the side-band unresolved regime, the optomechanically scattered photons that mediate this effective mechanical beam-splitter interaction can remain coherent in the cavity, which adds a stochastic time delay to this process. This results in a time delay in the effective (local and transduced) noise experienced by each resonator, which causes destructive interference when the mechanical resonator spectra overlap. We measure up to 20 dB cancellation of mechanical noise, matching well with our theoretical model. This provides a new interference mechanism distinct from that attributed to direct mechanical coupling between two resonators [216, 230], to multiple optical modes [231, 232] or optical modulation [192], which can clearly be excluded in our system.

We further propose and derive another new collective effect, resulting in a cooperativity competition of the mechanical dissipation, which we also observe in our measurements. This competition arises between the dissipation dynamics of two mechanical resonators coupled to the same optical field and leads to a linewidth broadening of one resonator that depends on the optomechanical cooperativity of the other resonator.

6.2. Theory and experimental setup

Our system consists of an array of two nominally identical 200 nm thick Si_3N_4 membranes (Fig. 6.1**a**) with fundamental frequencies $\omega_{1,2} \simeq 2\pi \times 150$ kHz and linewidths $\gamma_{1,2} \simeq 2\pi \times 0.1$ Hz. They are patterned with a photonic crystal with 35 % reflectivity at 1550 nm [34], characterized in a previously described setup [13]. The double-membrane chip is placed close to the center of a 49.6 mm long Fabry-Pérot cavity (free spectral range 3.023 GHz, beam waist 33 µm), with an empty-cavity

optical linewidth (full width at half maximum) of $\kappa_e = 2\pi \times 128$ kHz, in principle putting us into the optomechanical sideband resolved regime (total linewidth $\kappa \lesssim \omega_j$). The membranes cause additional optical loss when placed inside the cavity due to scattering and small imperfections in the alignment, resulting in a linewidth $\kappa \gtrsim 2\pi \times 300$ kHz, with a strong dependence on the exact position [233] and alignment [34] of the membranes. The mechanical motion of the membranes is coupled to the optical cavity frequency ω_c with vacuum optomechanical coupling rates $g_{0,1}$ and $g_{0,2}$ respectively. A laser at frequency ω_ℓ is coupled to the cavity with coupling strength $E = \sqrt{P_\ell \kappa_e / \hbar \omega_\ell}$, where P_ℓ is the laser power and κ_e the external coupling rate of the cavity.

The behavior of the membranes is investigated using a homodyne detection setup, schematically shown in Fig. 6.1**b**, for which we lock the laser wavelength ($\lambda = 1549.62$ nm) to the cavity length using a Pound-Drever-Hall (PDH) locking scheme [86]. By tuning the parameters of our PID (proportional-integral-derivative) controller, we can lock the laser beam slightly off-resonant with our cavity, and the red (blue) detuned laser can be used to cool (amplify) our optomechanical system.

The Hamiltonian describing our system is given by

$$\hat{H}/\hbar = \omega_c \hat{a}^\dagger \hat{a} + \sum_{j=1,2} \left(\frac{\omega_j}{2} \left(\hat{x}_j^2 + \hat{p}_j^2 \right) - g_{0,j} \hat{a}^\dagger \hat{a} \hat{x}_j \right) + iE \left(\hat{a}^\dagger e^{-i\omega_\ell t} - \text{H.c.} \right) \tag{6.1}$$

with $\hat{a}$ ($\hat{a}^\dagger$) the annihilation (creation) operator of the cavity mode, $\hat{x}_j$ and $\hat{p}_j$ the dimensionless position and momentum of the j^{th} mechanical resonator. We are interested in the fast fluctuations of the mechanical operators ($\delta\hat{x}_j$, $\delta\hat{p}_j$) and optical field, which are described by the quantum Langevin equations (QLEs, see Sec. 6.5.1 for details),

$$\begin{aligned} \delta\dot{\hat{x}}_j &= \omega_j \delta\hat{p}_j \\ \delta\dot{\hat{p}}_j &= -\omega_j \delta\hat{x}_j - \gamma_j \delta\hat{p}_j + g_j^* \delta\hat{a} + g_j \delta\hat{a}^\dagger + \hat{\xi}_j \\ \delta\dot{\hat{a}} &= -(i\Delta + \kappa/2)\, \delta\hat{a} + i \sum_{j=1,2} g_j \delta\hat{x}_j + \sqrt{\kappa}\hat{a}^{\text{in}} \end{aligned} \tag{6.2}$$

where $\hat{\xi}_j$ and $\hat{a}^{\text{in}}$ are the mechanical and optical noise terms. We have further introduced an effective detuning $\Delta = \omega_c - \omega_\ell - \sum_j \frac{g_{0,j}^2}{\omega_j} |\langle\hat{a}\rangle|^2$ and the effective optomechanical coupling rate $g_j = g_{0,j}\langle\hat{a}\rangle = g_{0,j} E/(\kappa/2 + i\Delta)$, with $\langle\hat{a}\rangle$ being the average cavity field amplitude. We can solve these equations by taking the Fourier transform and deriving the expected power spectral density (PSD) detected from the cavity output field (Sec. 6.5.2).

6.3. Results

6.3.1. Interference from optomechanical phase lag

In this section, we motivate the introduction of the optomechanical phase lag, and show that it leads to interference in the dynamics of the two mechanical resonators. To simplify the following analysis, we take the phase of $\langle\hat{a}\rangle$ such that the g_j are

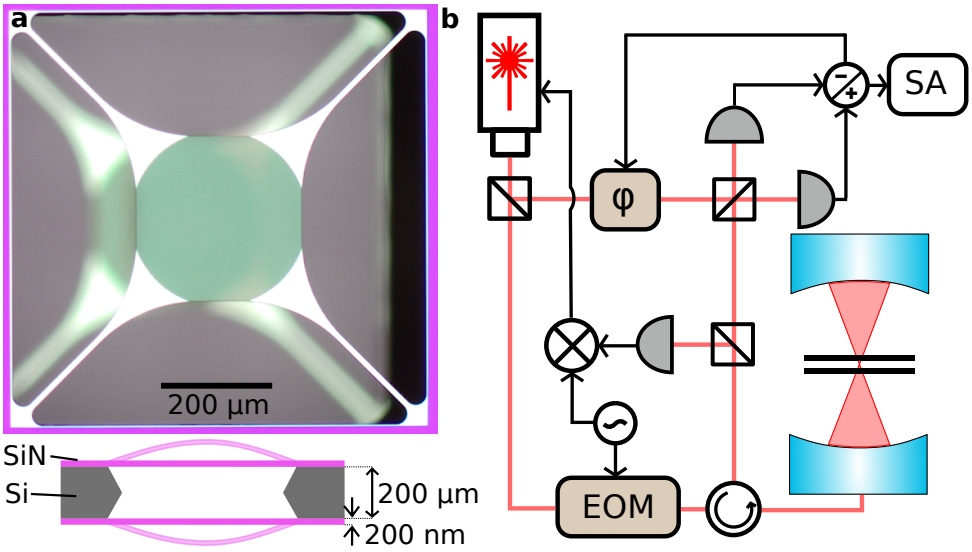

Figure 6.1: **a:** (top) Microscope image of a double-membrane device. Due to fabrication imperfections, the membranes are laterally offset by about 20 µm, which does not cause additional losses as the cavity beam waist is sufficiently small. (bottom) Cross-section of the double-membrane chip, with the Si_3N_4 membranes on either side of the Si substrate. The 200 µm spacing between the two membranes is rigid, fixed by the substrate. **b:** Schematic of the experimental setup. The laser wavelength is locked to the cavity length using a Pound-Drever-Hall locking scheme and the mechanics of the membranes are measured via homodyne detection. SA: Spectrum analyzer, φ: Fiber stretcher, EOM: Electro-optic modulator.

real (the full derivation keeping any complex values of g_j is given in Sec. 6.5.1). If we solve the QLEs, Eq. (6.2), the position fluctuations for example for resonator 1 take the form

$$\delta\hat{x}_1 = \chi_1^{\mathrm{eff}}(\omega)\left\{\frac{\begin{array}{c}-g_1 g_2\left[\chi_c(\omega)-\chi_c^*(-\omega)\right]\chi_2(\omega)\hat{\xi}_2 \\ +\,ig_1\sqrt{\kappa}\left[\hat{a}^{\mathrm{in}}\chi_c(\omega)+\hat{a}^{\mathrm{in},\dagger}\chi_c^*(-\omega)\right]\end{array}}{i+g_2^2\,\chi_2(\omega)\left[\chi_c(\omega)-\chi_c^*(-\omega)\right]}+\hat{\xi}_1\right\}, \tag{6.3}$$

where we have introduced the natural susceptibility of the mechanical resonators, $\chi_j(\omega) = \frac{\omega_j}{\omega_j^2-\omega^2-i\gamma_j\omega}$, and of the cavity field, $\chi_c(\omega) = \frac{1}{\kappa/2+i(\Delta-\omega)}$ ($\chi_c^*(-\omega) = \frac{1}{\kappa/2-i(\Delta+\omega)}$), and an effective susceptibility that incorporates the optomechanical effects on the susceptibility of the mechanical resonator,

$$\chi_1^{\mathrm{eff}}(\omega) = \left[\frac{1}{\chi_1(\omega)}+\frac{g_1^2\left(\chi_c(\omega)-\chi_c^*(-\omega)\right)}{i+g_2^2\,\chi_2(\omega)\left(\chi_c(\omega)-\chi_c^*(-\omega)\right)}\right]^{-1}. \tag{6.4}$$

Eq. (6.3) features terms that contain the different noise sources, the optical noises $\hat{a}^{\mathrm{in}}, \hat{a}^{\mathrm{in},\dagger}$ and the mechanical noises of both resonators, $\hat{\xi}_1, \hat{\xi}_2$. If we neglect the optical noises, which is a valid assumption if the system is at room temperature,

we can see that the position fluctuations of the resonator depend on an effective mechanical noise, $\hat{\xi}^{\text{eff}}$,

$$\hat{\xi}_1^{\text{eff}}(\omega) = \hat{\xi}_1 + M_1\hat{\xi}_2, \quad \hat{\xi}_2^{\text{eff}}(\omega) = \hat{\xi}_2 + M_2\hat{\xi}_1 \tag{6.5}$$

with

$$\begin{aligned} M_1(\omega) &= \frac{i\chi_2(\omega)g_1g_2\left(\chi_c(\omega) - \chi_c^*(-\omega)\right)}{1 - ig_2^2\chi_2(\omega)(\chi_c(\omega) - \chi_c^*(-\omega))} \\ M_2(\omega) &= \frac{i\chi_1(\omega)g_1g_2\left(\chi_c(\omega) - \chi_c^*(-\omega)\right)}{1 - ig_1^2\chi_1(\omega)(\chi_c(\omega) - \chi_c^*(-\omega))}. \end{aligned} \tag{6.6}$$

This is the crucial point: The position fluctuations of any (one) of the two resonators are not only dependent on its local thermal bath, but also on the thermal bath of the other via the optical field (Fig. 6.2**a**), as is well-understood for general coupled resonators [234]. This cross-term between the resonators is the effective mechanical beam-splitter interaction used for state-swapping and energy transfer between the mechanical resonators[75, 186, 226, 228, 229]. It represents photons that have been scattered with phonon transfer (i.e. optomechanically scattered) from one resonator, and subsequently re-scattered from the other. While this is a second-order optical process, it is linear in the mechanical operators, so it is not eliminated by the linearization of the QLEs (Eq. (6.2)). We quantify the rate of this process in the Sec. 6.5.3, and show that the transduced noise can be similar in amplitude to the local noise.

To evaluate these expressions and obtain a power spectral density (PSD) such as the one we detect in our experimental setup, conventionally, one assumes each of the mechanical baths to be Markovian (if $Q_j = \frac{\omega_j}{\gamma_j} \gg 1$ [175, 235]), with autocorrelators for $\hat{\xi}_j$ as

$$\left\langle \hat{\xi}_j(t)\hat{\xi}_j(t') + \hat{\xi}_j(t')\hat{\xi}_j(t) \right\rangle /2 \approx \gamma_j(2\bar{n}_j + 1)\delta(t - t'), \tag{6.7}$$

with $\bar{n}_j$ the mean thermal phonon number (Sec. 6.5.4). Based on Eq. (6.5), we can write an autocorrelator for the effective noise, which will contain terms from both thermal baths.

It is here that we introduce new physics. In Eq. (6.5), both noises have an *immediate* effect on the position fluctuations of the resonator: $\delta\hat{x}_1(t)$ is dependent on $\hat{\xi}_1(t)$ and $\hat{\xi}_2(t)$. For the local noise, this is correct, but the transduced noise *must* have a finite time delay due to the separation of the resonators (thermal baths) and the non-zero travel time of the photons between them: $\delta\hat{x}_1(t)$ must depend on $\hat{\xi}_1(t)$ and $\hat{\xi}_2(t - \bar{t})$ for an average photon travel time $\bar{t}$. The well-established framework of Eq. (6.2) breaks down: it does not contain this time delay. It predicts an immediate response of e.g. resonator 1 when resonator 2 is moved, regardless of the finite photon travel time. Note that the noise transduced by the cavity is first experienced by the other resonator from its own thermal bath (Fig. 6.2**a**).

We introduce the time delay of the transduced noise with respect to the local noise in the autocorrelation of the effective thermal noise experienced by a res-

onator (e.g. resonator 1),

$$\frac{\langle\hat{\xi}_1^{\text{eff}}(t)\hat{\xi}_1^{\text{eff}}(t')+\hat{\xi}_1^{\text{eff}}(t')\hat{\xi}_1^{\text{eff}}(t)\rangle}{2} = \left\langle\left(\hat{\xi}_1(t)+M_1(t)*\hat{\xi}_2(t)\right)\left(\hat{\xi}_1(t')+M_1(t')*\hat{\xi}_2(t')\right)\right\rangle$$
$$\Rightarrow \left\langle\left(\hat{\xi}_1(t)+M_1(t)*\hat{\xi}_2(t-\bar{t})\right)\left(\hat{\xi}_1(t')+M_1(t')*\hat{\xi}_2(t'-\bar{t})\right)\right\rangle, \tag{6.8}$$

where $M(t) = \mathcal{F}^{-1}\{M_1(\omega)\}$ from the inverse Fourier transform, the time delay between the local and transduced noise is $\bar{t}$, and $*$ denotes convolution. We have explicitly introduced the delay time $\bar{t}$ only in the transduced noise term; by property of the convolution we could have distributed the time delay freely between $M_1(t)$ and $\hat{\xi}_2(t)$ without affecting the result. In the frequency domain, using the time-shift property of the Fourier transform, we get a phase shift,

$$\langle\hat{\xi}_1^{\text{eff},'}(\omega)\hat{\xi}_1^{\text{eff},'}(\omega')+\hat{\xi}_1^{\text{eff},'}(\omega')\hat{\xi}_1^{\text{eff},'}(\omega)\rangle/2 =$$
$$\left\langle\left(\hat{\xi}_1(\omega)+e^{-2i\pi\bar{t}\omega}M_1(\omega)\hat{\xi}_2(\omega)\right)\left(\hat{\xi}_1(\omega')+e^{-2i\pi\bar{t}\omega}M_1(\omega')\hat{\xi}_2(\omega')\right)\right\rangle \tag{6.9}$$

where we have denoted the effective noise with added time delay by $\hat{\xi}_j^{\text{eff},'}$. The frequency range of interest is close to the mechanical frequencies ($\omega \sim \omega_1 \simeq \omega_2$), so we can consider it as a constant phase factor $e^{-2i\pi\bar{t}\omega} \simeq e^{i\phi_1}$. We call this the *optomechanical phase lag* that the transduced noise experiences with respect to the local noise. This modifies Eq. (6.5) to

$$\hat{\xi}_1^{\text{eff},'}(\omega) = \hat{\xi}_1 + \alpha_1 e^{i\phi_1}M_1\hat{\xi}_2, \quad \hat{\xi}_2^{\text{eff},'}(\omega) = \hat{\xi}_2 + \alpha_2 e^{i\phi_2}M_2\hat{\xi}_1, \tag{6.10}$$

where we have introduced the amplitude fit factors α_1 and α_2 to account for imperfect alignment between the two membranes.

Some closer considerations of this time delay and phase lag are warranted. An optomechanically scattered photon traveling the distance between resonators 1 and 2 (200 µm) takes about 670 fs, which should be negligible on the time scale of the mechanical motion, so we would expect the phase lag to be negligibly small as well. However, due to the optical cavity and the fact that $g_{0,j}$ is small, the chance for a scattered photon to directly interact with the other resonator is very small. It is much more likely to exit the cavity without interacting with the other membrane, as $\kappa \gg g_{0,j}$. The photons that *do* interact with the other membrane (i.e. the ones that have not exited the cavity) will thus have an average travel time equal to the lifetime of the cavity $\bar{t} = \tau = 1/\kappa$. In the regime $\kappa \simeq \omega_j$, this time lag represents a significant fraction of the mechanical period, meaning that the contributions to the effective noise of a resonator can be perfectly out of phase. When that happens, the effective noise term that resonator 1 experiences is reduced due to the coupling to resonator 2 and its thermal bath (and vice versa). In other words, the local noise and the noise transduced by the optical field from the other resonator interfere. We estimate the optomechanical phase lag for systems from literature (Sec. 6.5.5) and distinguish interference due to the this effect from other interference mechanisms (Sec. 6.5.6).

6.3.2. Experimental observation of interference

We study the behavior of our optomechanical system by measuring the mechanical power spectral density (PSD) with our homodyne setup. This allows us to test the theory curves obtained with the inclusion of the time delay and the curves obtained for two completely independent membranes (i.e. g_j set to zero while $g_{i\neq j} \neq 0$, for either membrane with the resulting spectra summed), shown in Fig. 6.2**b**. As these measurements are in the frequency domain, we shall refer to the optomechanical phase lag rather than the time delay.

The theory curve for the independent resonators (orange, solid line) clearly shows two Lorentzians, one at ω_1 which is broadened due to optomechanical cooling, and one which is less coupled at ω_2, and therefore less broad. The theory curve with the added optomechanical phase lag (red, solid line) follows the other theory curve for most of the frequency domain: because the Lorentzian at ω_2 is narrow, the noise contribution from $\hat{\xi}_2$ to $\hat{\xi}_1^{\text{eff}}$ is only relevant for a small frequency range around ω_2 (inset). Here, the interference between the noise terms results in a characteristic Fano-lineshape [236] in the theory curve where the spectra of the individual mechanical resonators would overlap.

Comparing both theory curves to the experimental data (blue, solid line), we see a clear drop in the PSD around ω_2, which the theory that includes the optomechanical phase lag describes well, while the model without it does not. Note that the peak of the Fano-lineshape is absent from the experimental data as well, which we attribute this to experimental imperfections.

To further study how this interference based on the optomechanical phase lag behaves, we adjust the optomechanical coupling rates of the resonators. This changes the frequency range over which the interference is observable, and also its strength. By varying the position of the chip within the cavity, the optical field intensity that each membrane experiences is changed, which allows us to control the optomechanical coupling rate of each of the membranes. We consider four cases, one shown in Fig. 6.2**b** ($g_{0,1} \gg g_{0,2}$), and three in Fig. 6.3**a-c**, $g_{0,1} \ll g_{0,2}$, $g_{0,1} < g_{0,2}$ and $g_{0,1} \simeq g_{0,2}$. For the latter three, we also show optomechanically induced transparency (OMIT) measurements and fits [191, 237, 238] (for details see the Sec. 6.5.7), by which we independently obtain all optomechanical parameters. In these OMIT measurements (Fig. 6.3**a-c** bottom row), we observe an additional feature not captured by our fit. Due to its frequency, it likely stems from the resonator's thermal noise.

In the case where one of the resonators has very weak coupling to the optical field, as shown in Fig. 6.2**b** and Fig. 6.3**a**, the PSD of the more strongly-coupled resonator takes the expected Lorentzian form. At the frequency of the weakly-coupled resonator, we observe a consistent dip in the PSD (Figs. 6.2**b** right panel, 6.3**d**), where the noise drops $15-20$ dB below the level of the spectrum of the other mode. The optomechanical parameters ($\omega_1 = 2\pi \times 149.89$ kHz, $\omega_2 = 2\pi \times 150.80$ kHz, $\kappa \simeq 2\pi \times 600$ kHz, $\Delta = 2\pi \times 10$ kHz, $g_{0,1} = 2\pi \times 2.2$ Hz and $g_{0,2} = 2\pi \times 0.2$ Hz for Fig. 6.2**b**) are also obtained through the separate OMIT measurement and fit.

When one of the resonators is less coupled, but not very weakly, Fig. 6.3**b,d**,

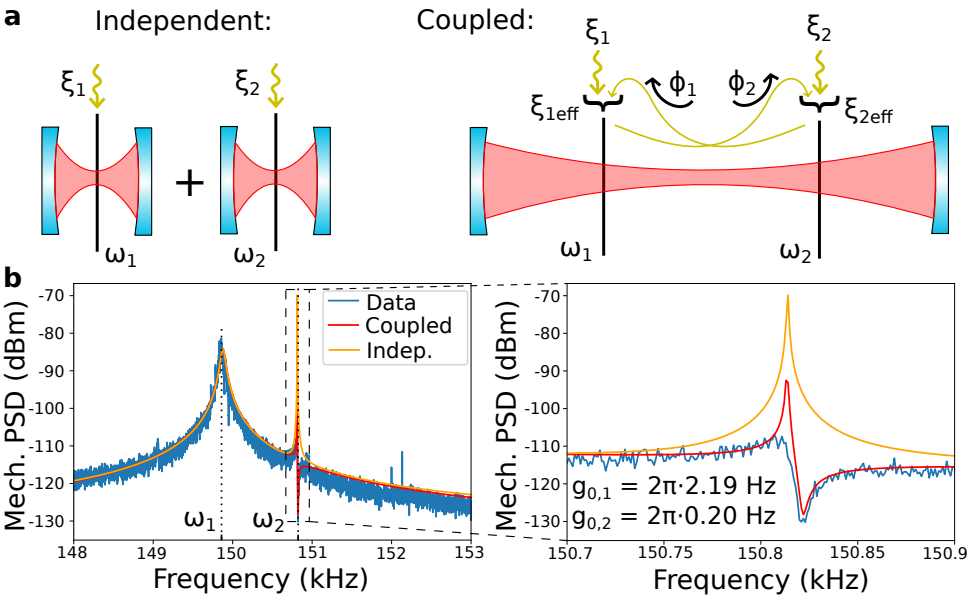

Figure 6.2: **a:** Schematic of mechanical noise contribution for two independent (left) or cavity-coupled (right) resonators. **b:** Measured mechanical spectra for two membranes in a single cavity, where one membrane (ω_1) is significantly stronger coupled (more damped) than the other (ω_2). Theory models are fitted for the independent (uncoupled) and the coupled membranes case including optomechanical phase lag.

we see a clear Fano-lineshape in the PSD. If both resonators are approximately equally coupled (cf. Fig. 6.3**c**), the measured spectrum exhibits a pronounced anti-resonance [239], clearly signaling destructive interference. There is an additional mode at 147 kHz that is not included in the fits in Fig. 6.3. Combined, these measurements show that our model with phase lag consistently describes the experimental data much better (20 dB, a factor 100 difference) than the theory without the phase lag.

The most important factor governing the phase lag is the cavity linewidth κ. As we change the position of the chip in the cavity, κ changes due to scattering and misalignment losses. We plot the expected phase lag as a function of the chip position in Fig. 6.3**e**, by way of the fits (red circles) to the spectra of Figs. 6.2, 6.3 and 6.4, and the calculated values (green crosses) based on the average κ measured directly before and after each experiment. Unfortunately, κ is the main source of uncertainty in the theory curves, as it has a significant uncertainty from the OMIT fits and a spread ($275 - 600$ kHz) when measured directly from a laser wavelength scan before and after OMIT and PSD measurements. This is likely due to our imperfect stabilization of the laser to the cavity frequency, smeared out by the averaging. To illustrate, we have calculated the expected phase lag for a spread of $\kappa = 275 - 600$ kHz (green shaded area) all observed from measurements at the same wavelength and chip position. We have calculated the expected linewidths

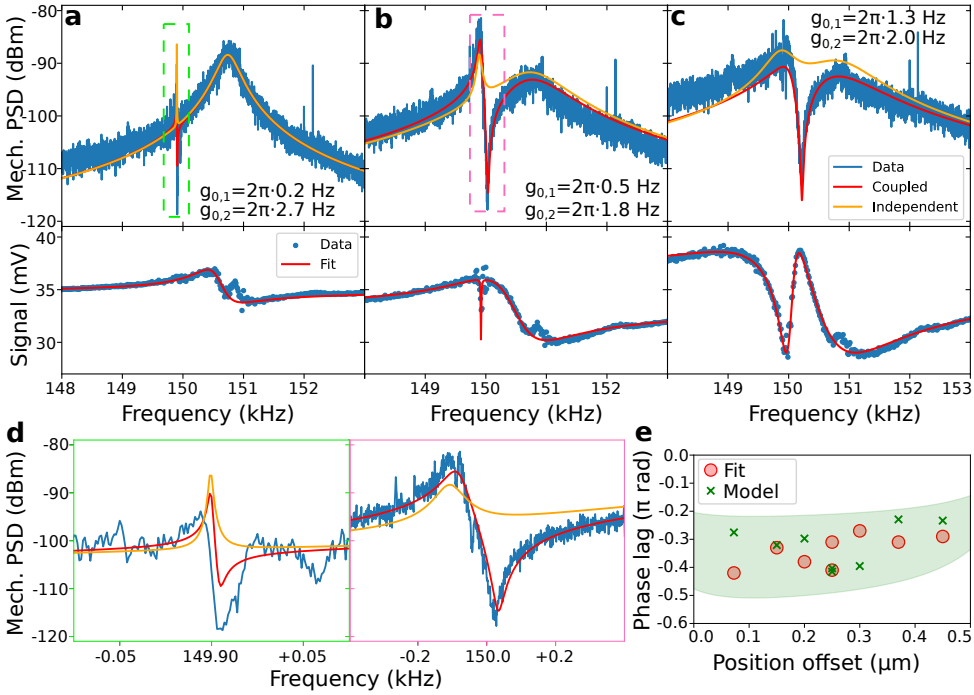

Figure 6.3: **a-c**, Top panels: Measured PSD for the two-membrane system for various coupling ratios (blue), and the expected behavior with interference (red) and considering independent membranes (orange). The measured coupling rates are shown, their ratios being 0.07, 0.28 and 0.65, respectively. Bottom panels: OMIT data (blue dots) and fits (red line) used to extract the optomechanical parameters. **d:** Zoom-in on dashed regions of **a** and **b** showing narrow spectral features at the mechanical frequency of the less-coupled resonator. **e** Extracted phase lag from the fit (red circles) and expected phase lag based on the cavity linewidths (green crosses). The green shaded area shows the phase lag bounds based on the cavity linewidths, see main text.

based on this spread using a model of a Fabry-Pérot cavity with lossy membranes (Sec. 6.5.8). There is reasonable agreement between the fitted and calculated values, and all values fall well within the band based on the spread in κ.

6.3.3. Cooperativity competition

Independently of the optomechanical phase lag, we predict that if two mechanical resonators are coupled to the same optical field, the effective mechanical dissipation of one does not only depend on its local environment but also on the optomechanical cooperativity of the other resonator. We refer to this effect as *cooperativity competition* (for details see Sec. 6.5.9). From the solution to Eq. (6.2), we can rewrite the position fluctuations in terms of the effective susceptibility $\chi_i^{\text{eff}}(\omega)$. We can further define the effective mechanical linewidths, which reduce to the simple expressions

$$\gamma_1^{\text{eff}} \approx \gamma_1\left(1+\frac{C_1}{C_2}\right), \qquad \gamma_2^{\text{eff}} \approx \gamma_2\left(1+\frac{C_2}{C_1}\right). \tag{6.11}$$

Here we assume identical mechanical frequencies and optimal cooling, $\Delta = \omega_1 = \omega_2$, side-band resolution, $\kappa \lesssim \omega_j$ and large optomechanical cooperativities, $C_j = 2g_j^2/(\kappa\gamma_j) \gg 1$. These equations describe how the effective mechanical dissipation of one resonator is reduced with respect to those of two independent modes, where $\gamma_j^{\text{eff}} \simeq \gamma_j(1 + C_j)$ $(j = 1, 2)$ [38, 91, 240]. While Eq. (6.11) describes a simplified model, for our experiments we use the full model (see Sec. 6.5.9) to obtain γ_j^{eff}. Although both the optomechanical phase lag and the cooperativity competition originate from cavity-mediated coupling between the mechanical resonators, they are essentially different effects with their own characteristics, embodied by noise cancellation and competition in dissipation dynamics respectively.

To observe cooperativity competition in our system, we vary cooperativities C_1 and C_2 (see Eq. (6.11)) by changing the coupling ratio $g_{0,1}/g_{0,2}$ or by changing the optical power. With $g_{0,1}/g_{0,2} = 0.74$ to keep the effect of the interference on the shape of our PSD constant, we measure at different powers, Fig. 6.4**a** (blue). The optomechanical parameters are determined as before, which we then use to fit our coupled (red) and independent (orange) models. The cooperativity competition manifests itself as a change in linewidth of the two resonances, which is difficult to gauge from the shape of the PSD, as it is dominated by the interference. Therefore we have plotted the fitted linewidths in terms of the cooperativity in Fig. 6.4**b** for both the coupled case (solid curves), which contains both the interference and the cooperativity competition, and the independent case (dashed curve) which contains neither. This shows an appreciable reduction in linewidth for higher cooperativities as predicted.

We can further corroborate cooperativity competition by analyzing the fitted linewidths for various coupling ratios, shown in Fig. 6.4**c**. We compare the total linewidth (sum of both linewidths), and expect a straight line as a function of C_1/C_2 in the independent case (orange, dashed), while cooperativity competition predicts a cooperativity-ratio-dependent reduction of the total linewidth (red, solid). The reduction is maximal when the cooperativities are approximately equal where the competition is most intense, and the curve is symmetric around $C_1/C_2 = 1$, which can be seen by switching the labels $1,\ 2$ of the resonators. The fitted linewidths are normalized to account for the cooling efficiency by re-scaling the total linewidth by the maximum reduction expected due to cooperativity competition for the fitted κ, Δ and cooperativities of each data point. The results match with the expected decrease associated with the cooperativity competition as a function of C_1/C_2. This shows the effective optomechanical coupling leading to a competition on the mechanical dissipation of the resonators.

6.4. Conclusion

We have introduced an optomechanical phase lag between the local and cavity-transduced thermal noises of the two resonators, originating from the time-delay of noise transduced via the cavity. We have observed interference stemming from this phase lag by measuring the mechanical power spectral density of a double-membrane device. The interference coherently cancels mechanical noise of the two resonators where their (broadened) frequency spectra overlap, leading to a

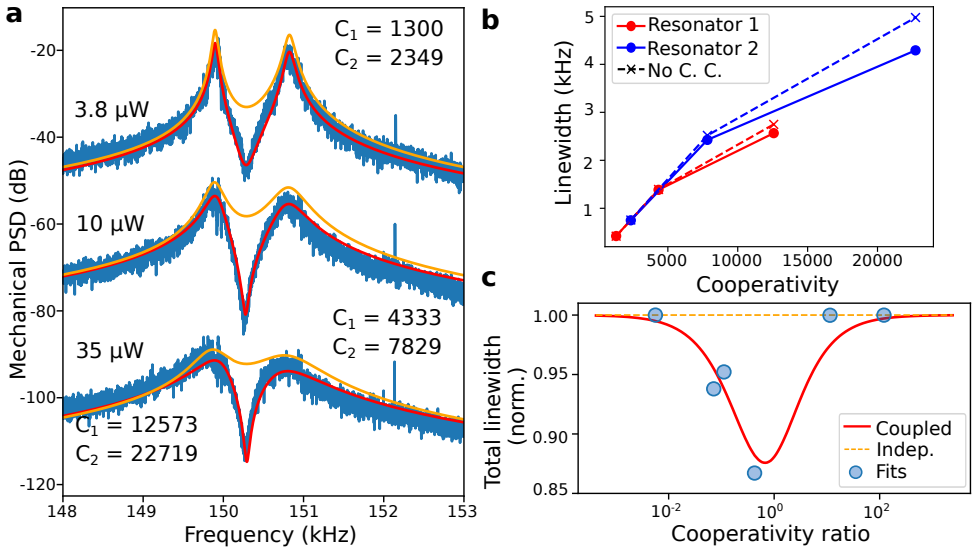

Figure 6.4: **a:** PSD for a fixed $g_{0,1}/g_{0,2} = 0.74$ and various powers (blue), with theory fits for the coupled-resonator (red) and independent-resonator models (orange). textbfb: Fitted mechanical linewidths as a function of cooperativity. Solid lines include the effect of cooperativity competition while dashed lines do not. **c** Normalized total (sum) linewidths for various coupling ratios (blue), showing a decrease due to cooperativity competition.

20 dB decrease in mechanical noise. This could create an interesting new method of controllably reducing unwanted mechanical noise by introducing a second resonator, which would allow cancellation of mechanical noise in a specific frequency range (Sec. 6.5.10).

In addition, we have proposed and experimentally verified another new collective effect in the same system, where the effective susceptibility of the coupled resonators causes a competition on the mechanical dissipation. The dissipation rates of two mechanical resonators can get significantly reduced when their optomechanical cooperativities are comparable. This novel collective effect paves the way for long-range control of phonon dynamics [241] and the results of this work can be applied directly to multi-resonator ($N > 2$) optomechanical systems, where we expect more prominent and even richer collective effects.

6.5. Supplementary

This section contains the derivation of the equations of motion for a set of two mechanical resonators coupled to a single optical mode, as well as the derivation of the mechanical power spectral density observable from this system in a homodyne detection setup. We also include the full analytical derivation for cooperativity competition. We provide supporting material and calculations for the experiments and conclusions drawn in the main text, i.e. a quantitative estimate of the rate of the scattering-rescattering process (effective mechanics-mechanics beam-splitter), the

effective temperature of our mechanical resonators due to optomechanical cooling, a comparison of optomechanical phase lag expected in other systems in literature, qualitative and quantitative arguments that allow exclusion of other interference mechanisms as explanations of the observations in the main text, a classical model of a Fabry-Pérot cavity that allows us to model optical and optomechanical parameters, a derivation of multi-mode optomechanically induced transparency (OMIT) and a proposal for application of the optomechanical phase lag to a sensor.

6.5.1. Equations of motion for the coupled resonator system

We consider a system where two mechanical modes (each the fundamental mechanical mode of a membrane) are coupled to an optical cavity via radiation pressure. There is no direct coupling between the two mechanical modes, but they are indirectly coupled by the mediation of light. The Hamiltonian of the system is given by

$$\frac{H}{\hbar} = \omega_c \hat{a}^\dagger \hat{a} + \sum_{j=1,2} \left[\frac{\omega_j}{2} (\hat{x}_j^2 + \hat{p}_j^2) - g_{0,j} \hat{a}^\dagger \hat{a} \hat{x}_j \right] + iE\left(\hat{a}^\dagger e^{-i\omega_\ell t} - \text{H.c.}\right), \tag{6.12}$$

where $\hat{a}$ ($\hat{a}^\dagger$) is the annihilation (creation) operator of the cavity field, $\hat{x}_j$ and $\hat{p}_j$ are, respectively, the dimensionless position and momentum of the j^{th} ($j = 1, 2$) mechanical resonator, and thus we have $[\hat{a}, \hat{a}^\dagger] = 1$ and $[\hat{x}_j, \hat{p}_j] = i$. The resonance frequencies ω_c, ω_j are of the cavity and the j^{th} mechanical resonator, respectively, and $g_{0,j}$ is the single-photon optomechanical coupling rate related to the j^{th} mechanical resonator. The last term in the Hamiltonian denotes the laser driving for the cavity, where $E = \sqrt{P_\ell \kappa_e / \hbar \omega_\ell}$ is the coupling between the cavity with external decay rate κ_e and the driving laser with frequency ω_ℓ and power P_ℓ.

In the frame rotating at the drive frequency ω_ℓ and by including input noises and dissipation of the system, we obtain the following quantum Langevin equations (QLEs), which govern the system dynamics

$$\begin{aligned} \dot{\hat{x}}_j &= \omega_j \hat{p}_j, \\ \dot{\hat{p}}_j &= -\omega_j \hat{x}_j - \gamma_j \hat{p}_j + g_{0,j} \hat{a}^\dagger \hat{a} + \hat{\xi}_j, \qquad (j = 1, 2) \\ \dot{\hat{a}} &= -(i\Delta_0 + \kappa/2)\hat{a} + i \sum_{j=1,2} g_{0,j} \hat{x}_j \hat{a} + E + \sqrt{\kappa} \hat{a}^{\text{in}}, \end{aligned} \tag{6.13}$$

where $\Delta_0 = \omega_c - \omega_\ell$, κ is the total cavity decay rate ($\kappa > \kappa_e$), γ_j is the mechanical damping rate, $\hat{a}^{\text{in}}$ denotes vacuum input noise for the cavity, whose mean value is zero and the only nonzero correlation is

$$\langle \hat{a}^{\text{in}}(t)\, \hat{a}^{\text{in},\dagger}(t') \rangle = \delta(t - t'). \tag{6.14}$$

Here, $\hat{\xi}_j$ is the Langevin force operator, which accounts for the Brownian motion of the j^{th} mechanical resonator and is auto-correlated as

$$\langle \hat{\xi}_j(t) \hat{\xi}_j(t') + \hat{\xi}_j(t') \hat{\xi}_j(t) \rangle / 2 \simeq \gamma_j (2\bar{n}_j + 1) \delta(t - t'), \tag{6.15}$$

where a Markovian approximation has been made. This is valid for a large mechanical Q-factors $Q_j = \omega_j/\gamma_j \gg 1$ [175, 235], and $\bar{n}_j \simeq \frac{k_B T}{\hbar\omega_j}$ is the mean thermal phonon number in the high temperature limit, with k_B the Boltzmann constant and T the environmental temperature.

In the experiment, the cavity is strongly driven which leads to a large amplitude of the cavity field $|\langle\hat{a}\rangle| \gg 1$. This allows us to linearize the system dynamics around the semi-classical averages by writing any operator as $\hat{O} = \langle\hat{O}\rangle + \delta\hat{O}$ ($\hat{O} = \hat{a}, \hat{x}_j, \hat{p}_j$) and neglecting second-order fluctuation terms. We obtain the linearized QLEs for the quantum fluctuations $(\delta\hat{x}_j, \delta\hat{p}_j, \delta\hat{a})$

$$\begin{aligned}
\delta\dot{\hat{x}}_j &= \omega_j \delta\hat{p}_j, \\
\delta\dot{\hat{p}}_j &= -\omega_j \delta\hat{x}_j - \gamma_j \delta\hat{p}_j + g_j^* \delta\hat{a} + g_j \delta\hat{a}^\dagger + \hat{\xi}_j, \\
\delta\dot{\hat{a}} &= -(i\Delta + \kappa/2)\delta\hat{a} + i\sum_{j=1,2} g_j \delta\hat{x}_j + \sqrt{\kappa}\hat{a}^{\text{in}}
\end{aligned} \tag{6.16}$$

where (complex) $g_j = g_{0,j}\langle\hat{a}\rangle$ is the effective optomechanical coupling rate, $\langle\hat{a}\rangle = \frac{E}{\kappa/2+i\Delta}$, and $\Delta = \Delta_0 - \sum_j \frac{g_{0,j}^2}{\omega_j}|\langle\hat{a}\rangle|^2$ is the effective detuning.

By taking the Fourier transform of each equation in Eq. (6.16) and solving *separately* the two equations for each mode in the frequency domain, we obtain the following solutions

$$\delta\hat{p}_j = -i\frac{\omega}{\omega_j}\delta\hat{x}_j, \tag{6.17}$$

$$\delta\hat{x}_j = \chi_j(\omega)\left[g_j^*\delta\hat{a} + g_j\delta\hat{a}^\dagger + \hat{\xi}_j\right], \tag{6.18}$$

$$\delta\hat{a} = \chi_c(\omega)\left(\sum_{j=1,2} i g_j \delta\hat{x}_j + \sqrt{\kappa}\hat{a}^{\text{in}}\right), \tag{6.19}$$

$$\delta\hat{a}^\dagger = \chi_c^*(-\omega)\left(\sum_{j=1,2} -i g_j^* \delta\hat{x}_j + \sqrt{\kappa}\hat{a}^{\text{in},\dagger}\right), \tag{6.20}$$

where we have introduced the natural susceptibility of the mechanical resonators, $\chi_j(\omega)$, and of the cavity field, $\chi_c(\omega)$, given by

$$\chi_j(\omega) = \frac{\omega_j}{\omega_j^2 - \omega^2 - i\gamma_j\omega}, \tag{6.21}$$

$$\chi_c(\omega) = \frac{1}{\kappa/2 + i(\Delta - \omega)}, \tag{6.22}$$

$$\chi_c^*(-\omega) = \frac{1}{\kappa/2 - i(\Delta + \omega)}. \tag{6.23}$$

Solving Eq. (6.18) for $\delta\hat{x}_2$ (i.e. taking $j = 2$) and Eq. (6.19) and Eq. (6.20) for $\delta\hat{a}$ and $\delta\hat{a}^\dagger$, and inserting their solutions into Eq. (6.18) of $\delta\hat{x}_1$ (i.e. taking $j = 1$), we obtain

$$\delta\hat{x}_1 = \chi_1^{\text{eff}}(\omega)\left\{\frac{-\left[g_1^* g_2 \chi_c(\omega) - g_1 g_2^* \chi_c^*(-\omega)\right]\chi_2(\omega)\,\hat{\xi}_2 + \sqrt{\kappa}\left[(c_1 + i g_1^* \chi_c(\omega))\hat{a}^{\text{in}} + (c_2 + i g_1 \chi_c^*(-\omega))\hat{a}^{\text{in},\dagger}\right]}{i + g_2^* g_2\,\chi_2(\omega)\left[\chi_c(\omega) - \chi_c^*(-\omega)\right]} + \hat{\xi}_1\right\}, \tag{6.24}$$

with

$$\begin{aligned} c_1 &= \chi_2 \chi_c(\omega)\chi_c^*(-\omega) g_2^* \left(g_1 g_2^* - g_1^* g_2\right) \\ c_2 &= \chi_2 \chi_c(\omega)\chi_c^*(-\omega) g_2 \left(g_1 g_2^* - g_1^* g_2\right) \end{aligned} \tag{6.25}$$

which is fully solved and a function of only input noise operators $\left(\hat{\xi}_1, \hat{\xi}_2, \hat{a}^{\text{in}}, \hat{a}^{\text{in},\dagger}\right)$. Eq. (6.24) recognizes three noise sources for the first mechanical resonator: the noise from its own thermal bath, the optomechanical back-action noise from the cavity field, and the thermal noise from the second mechanical resonator transduced through the cavity field. We have defined the effective susceptibility

$$\chi_1^{\text{eff}}(\omega) = \left[\frac{1}{\chi_1(\omega)} + \frac{g_1^* g_1}{\frac{i}{\chi_c(\omega) - \chi_c^*(-\omega)} + g_2^* g_2\,\chi_2(\omega)} + d_1\right]^{-1} \tag{6.26}$$

with

$$d_1 = \frac{\chi_2(\omega)\chi_c(\omega)\chi_c^*(-\omega)\left(g_1 g_2^* - g_1^* g_2\right)^2}{i g_2^* g_2 \chi_2(\omega)\left(\chi_c(\omega) - \chi_c^*(-\omega)\right) - 1}, \tag{6.27}$$

which identifies the coupling to the cavity field and the *indirect* coupling to the second mechanical resonator mediated by the light. Taking $g_2 = 0$, i.e. the second mechanical resonator is decoupled from the cavity field, we obtain

$$\chi_1^{\text{eff}}(\omega) = \left[\frac{1}{\chi_1(\omega)} - i g_1^* g_1\left[\chi_c(\omega) - \chi_c^*(-\omega)\right]\right]^{-1}, \tag{6.28}$$

which is exactly the effective mechanical susceptibility provided in Ref. [91] (note: their definitions of g and κ are slightly different from ours), which studied a single mechanical resonator coupled to cavity field. Owing to the symmetry of the two mechanical resonators, we therefore get the effective susceptibility of the second mechanical resonator

$$\begin{aligned} \chi_2^{\text{eff}}(\omega) &= \left[\frac{1}{\chi_2(\omega)} + \frac{g_2^* g_2}{\frac{i}{\chi_c(\omega) - \chi_c^*(-\omega)} + g_1^* g_1\,\chi_1(\omega)} + d_2\right]^{-1} \\ d_2 &= \frac{\chi_1(\omega)\chi_c(\omega)\chi_c^*(-\omega)\left(g_1 g_2^* - g_1^* g_2\right)^2}{i g_1^* g_1 \chi_1(\omega)\left(\chi_c(\omega) - \chi_c^*(-\omega)\right) - 1}. \end{aligned} \tag{6.29}$$

By neglecting the optical input noise, which is small compared to the room temperature thermal noise in our system, we can express the position fluctuation in terms of an effective susceptibility and effective noise

$$\delta\hat{x}_1 = \chi_1^{\text{eff}}(\omega)\hat{\xi}_1^{\text{eff}} = \chi_1^{\text{eff}}\left(\hat{\xi}_1 + M_1\hat{\xi}_2\right) \tag{6.30}$$

with

$$M_1 = \frac{i\chi_2(\omega)\left(g_1^* g_2 \chi_c(\omega) - g_1 g_2^* \chi_c^*(-\omega)\right)}{1 - ig_2 g_2^* \chi_2(\omega)(\chi_c(\omega) - \chi_c^*(-\omega))} \tag{6.31}$$

describing the transduction of the mechanical noise from resonator $2 \rightarrow 1$ through the cavity field, as in the main text. Note that we have considered the general situation of complex couplings g_j in M_1. Using the same approach, we can write the position fluctuation $\delta\hat{x}_2$ in a similar form as Eq. (6.30).

6.5.2. Homodyne detection of mechanical fluctuations

We derive the expected power spectral density (PSD) that we would detect in our homodyne detection setup based on the fluctuations of the mechanical operators, $\delta\hat{x}_j$ and $\delta\hat{p}_j$ and the optical field $\delta\hat{a}$. We start from Eqs. (6.17)-(6.20), which we solve for the fluctuations $\delta\hat{x}_j$, $\delta\hat{p}_j$ and $\delta\hat{a}$ in terms of the noise operators $\hat{\xi}_j$ and $\hat{a}^{\text{in}}$.

We use a homodyne detection setup that is sensitive to the optical field output from our cavity, so we are interested in finding the PSD of that field rather than the PSD of the mechanical fluctuations. Using input-output theory, we can obtain the output field as

$$\delta\hat{a}^{\text{out}} = \sqrt{\kappa_e}\delta\hat{a} - \hat{a}^{\text{in}}. \tag{6.32}$$

Using the results from the previous section, we have

$$\begin{aligned}\delta\hat{a} &= \chi_c\left(ig_1\chi_1^{\text{eff}}(\hat{\xi}_1 + M_1\hat{\xi}_2) + ig_2\chi_2^{\text{eff}}(\hat{\xi}_2 + M_2\hat{\xi}_1) + \sqrt{\kappa}\hat{a}^{\text{in}}\right)\\ \delta\hat{a}^\dagger &= \chi_c^*\left(-ig_1^*\chi_1^{\text{eff}}(\hat{\xi}_1 + M_1\hat{\xi}_2) - ig_2^*\chi_2^{\text{eff}}(\hat{\xi}_2 + M_2\hat{\xi}_1) + \sqrt{\kappa}\hat{a}^{\text{in},\dagger}\right)\end{aligned} \tag{6.33}$$

To consider the fact that we have a homodyne detection where our local oscillator might have a phase offset ϕ with regards to the signal returned from the cavity, we observe a general quadrature $\delta\hat{z}^{\text{out}}$, given by

$$\delta\hat{z}^{\text{out}} = \frac{1}{\sqrt{2}}\left(\delta\hat{a}^{\text{out}}e^{-i\phi} + \delta\hat{a}^{\text{out},\dagger}e^{i\phi}\right). \tag{6.34}$$

We can reorganize the expression for $\delta\hat{z}^{\text{out}}$ in the form of coefficients of these noise terms,

$$\delta\hat{z}^{\text{out}} = \delta\hat{z}_a^{\text{out}}\hat{\xi}_1 + \delta\hat{z}_b^{\text{out}}\hat{\xi}_2 + \delta\hat{z}_c^{\text{out}}\hat{a}^{\text{in}} + \delta\hat{z}_d^{\text{out}}\hat{a}^{\text{in},\dagger}. \tag{6.35}$$

The quantity of interest is the spectrum of these fluctuations of the generalized output quadrature, which can be obtained by calculating

$$S_z(\omega) = \frac{1}{2\pi}\int_\infty^\infty \frac{1}{2}\langle\delta\hat{z}^{\text{out}}(\omega)\delta\hat{z}^{\text{out}}(\omega') + \delta\hat{z}^{\text{out}}(\omega')\delta\hat{z}^{\text{out}}(\omega)\rangle e^{-i(\omega+\omega')t}\mathrm{d}\omega'. \tag{6.36}$$

When we rewrite this equation in terms of the coefficients of the noise operators, we obtain terms containing the correlations of the noise, which we already know (Eqs. (6.14) and (6.15)). From there it is straightforward, if tedious, to calculate the PSD from only the cavity and mechanical parameters.

6.5.3. Quantitative estimation of scattering-rescattering rate

The scattering-rescattering process that forms the effective mechanics-mechanics beam-splitter interaction between the resonators is a second-order optical effect, but it is linear in the mechanical operators. To illustrate its relation to other optomechanical processes happening in our system, we have sketched it in Fig. 6.5**a**. The process of interest is (4), the scattering and subsequent rescattering of a single photon to/from a resonator.

To estimate the rate of this interaction, and corroborate that this can be of the order of the mechanical noise, we make a quantitative estimate of the size of this effect. We can calculate the strength of the first-order scattered fields with respect to the laser-driven cavity field by using Eqs. (60) and (61) of [2],

$$\begin{aligned} a &\simeq a_0 + a_1 \\ a_0 &= a_{\text{in}} \frac{\sqrt{\kappa_e}}{i\Delta + \kappa/2} \\ a_1 &= \frac{g_0 x_0}{2x_{\text{ZPF}}} a_0 \left(\frac{1}{i(\Delta - \omega_j) + \kappa/2} - \frac{1}{i(\Delta + \omega_j) + \kappa/2} \right) \\ &= a_{\text{aS}} + a_{\text{S}}, \end{aligned} \tag{6.37}$$

where a is the total cavity field, split in the laser carrier field a_0 and the first-order scattered field a_1 (containing both anti-Stokes and Stokes sidebands, $a_{\text{aS}} + a_{\text{S}}$). Here we neglect the time-dependence of these fields, as we are only interested in their amplitude. We have mechanical motional amplitude x_0, zero-point motion x_{ZPF} and optical input field $a_{\text{in}}\sqrt{\kappa_e}$ which is simply the input field (laser) we have previously denoted by $E = \sqrt{P_\ell \kappa_e / \hbar\omega_\ell}$. We can calculate the zero-point motion via $x_{\text{ZPF}} = \sqrt{\hbar/(2m_{\text{eff}}\omega_j)}$ for $m_{\text{eff}} \approx 29$ ng the effective mass of the fundamental mode obtained from a COMSOL model (cf. Fig. 6.7), taking into account the correct normalization [45]. Similarly, by utilizing the equipartition theorem we estimate the motional amplitude $x_0 \approx 7$ pm at room temperature.

For the parameters of Table 6.1, but simplifying $\omega_1 = \omega_2 = 150$ kHz and $g_{0,1} = g_{0,2} = 2\pi \times 1.6$ Hz, we calculate a ratio $a_{\text{S}}/a_0 = 0.017$, $a_{\text{aS}}/a_0 = 0.020$. By treating the first-order scattered fields each as a new 'main' field, we can repeat this and calculate the scattered-rescattered fields $a_{2\text{s}} = (a_{\text{aS}})_{\text{S}} + (a_{\text{S}})_{\text{aS}}$ with $(a_{\text{aS}})_{\text{S}}$ the Stokes-rescattered (2nd order) sideband of the (1st order) anti-Stokes field. The ratio of the (sum of) these fields with respect to the original cavity field is $a_{2\text{s}}/a_0 = 9.2 \times 10^{-4}$. This is much weaker than the main cavity (laser driven) field. Similarly, we can calculate the amplitude ratio of the other second-order sidebands, $(a_{\text{aS}})_{\text{aS}}$ and $(a_{\text{S}})_{\text{S}}$ with the original field. We get a ratio of 4.4×10^{-4}.

As the photons that go through the scattering-rescattering process end up around the laser frequency, $\omega_\ell \pm (\omega_1 - \omega_2)$, we cannot separate them from low-

Param.	Value	Param.	Value	Param.	Value
ω_1	$2\pi \times 149.90$ kHz	$g_{0,1}$	$2\pi \times 1.3$ Hz	α_1	1.4
ω_2	$2\pi \times 150.83$ kHz	$g_{0,2}$	$2\pi \times 2.0$ Hz	α_2	1.7
κ	$2\pi \times 320$ kHz	Δ	$2\pi \times 23.5$ kHz	$\phi_1 = -\phi_2$	-0.27

Table 6.1: Optomechanical parameters used in Fig. 6.3**c** and Fig. 6.6 for simulation of the PSD.

frequency noise in our homodyne detection. We can however detect other second order sidebands (cf. (2) in Fig. 6.5**a**) that should have a comparable amplitude based on the calculation above. For a different set of resonators (lower frequency) but with comparable cavity parameters and driving power, we can clearly detect both the first-order scattering process (Fig. 6.5**b**) at $\omega_{1,2}$ and the second-order scattering process (right) at $2\omega_1$, $2\omega_2$ and $\omega_1 + \omega_2$. This is different from first-order scattering from the second mode of the mechanical resonators, which happens around 240 kHz. When we lock the laser frequency (far) away from the center of the cavity resonance, the signal from the mechanics becomes very weak (orange curve in Fig. 6.5**b**) and we can no longer see the second-order scattering process. This power difference between the detected first- and second-order sidebands corresponds well with the calculations above, confirming our estimation of the strength of the scattering-rescattering process.

To see if this process is also a reasonable explanation for the transfer and subsequent cancellation of thermal noise of our two resonators, we have to compare the rate of photons going through this scattering-rescattering process with the thermal phonon diffusion rate of our resonators. If the rate of photons going through this process is similar to the rate of thermal phonons, it is reasonable for the phonons from resonator 2 to be transferred to resonator 1 (or vice versa), causing cancellation of their mechanical noise (if they are perfectly out of phase). To calculate this, we must multiply the photon number $n = \langle a_{2\mathrm{s}}^* a_{2\mathrm{s}} \rangle$ with the cavity decay rate κ to gain the number of photons per second. However, the amplitude of the scattered fields depends on the position fluctuations x_0, which depend on the effective mode temperature. By optomechanical cooling, we drastically reduce the mode temperature, and thus the sideband strength. We have calculated the steady-state effective temperature of the resonators as described in the next section (approximately 0.1 K) which reduces our motional amplitude to 128 fm. This amounts to approximately 7.6×10^6 photons per second going through the scattering-rescattering process to exchange mechanical noise between the resonators. By comparing this with the average thermal phonon number per second for one of the mechanical resonators, about 4.2×10^6 (calculated for a 150 kHz resonator at 0.1 K effective mode temperature with a 3 kHz effective linewidth conforming to the optomechanical cooling achieved for a system with the parameters of Table 6.1), we can clearly see that a significant fraction of thermal phonons can be transduced between the resonators (and therefore experience this phase delay) within the thermal decoherence time of that resonator.

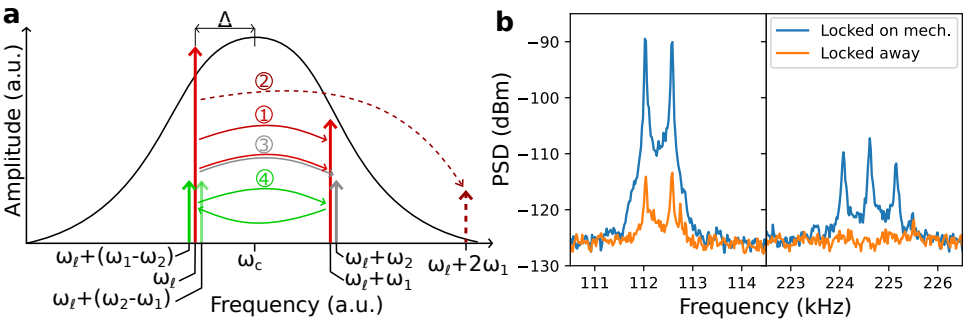

Figure 6.5: **a**: Schematic of (some) processes in the optomechanical system: (1) First-order Anti-Stokes scattering from laser (ω_ℓ) to mechanical sideband ($\omega_\ell + \omega_1$). (2) Second-order Anti-Stokes scattering to $\omega_\ell + 2\omega_1$. (3) Simultaneous first-order Anti-Stokes scattering to both resonators ω_1 and ω_2. (4) Subsequent scattering (Anti-Stokes then Stokes) to ω_1 and ω_2, and to ω_2 and ω_1. **b**: Mechanical PSD showing first (left) and second (right) order scattering processes from a different set of resonators with lower resonance frequencies, for comparable cavity and laser drive parameters. We clearly resolve the two first-order processes at ω_1 and ω_2. While the second order peaks at $2\omega_1$, $2\omega_2$ and $\omega_1 + \omega_2$ are much smaller than the first, they are still detectable.

6

6.5.4. Effective temperature of mechanical resonators

The autocorrelation of the mechanical noise of the resonators, Eq. (6.15), contains the mechanical linewidth γ_j and mean thermal phonon number of the resonator, $\bar{n}_j$. Both of these parameters are affected by the optomechanical cooling, and we use the effective (optomechanically broadened) γ_j^{eff} and $\bar{n}_j^{\text{eff}}$ [38, 91, 240] to fit our experimental data. To obtain these values, we adopt an approach solving the Lyapunov equation [242]. We start from the QLEs for the fluctuations of our system, Eq. (6.16), and we write it in a matrix form such that $\dot{u}(t) = Au(t) + n(t)$, where $u(t)$ is the vector of our system coordinates, A is the drift matrix and $n(t)$ contains only the noise terms. We get

$$\begin{pmatrix} \delta\dot{\hat{x}}_1 \\ \delta\dot{\hat{p}}_1 \\ \delta\dot{\hat{x}}_2 \\ \delta\dot{\hat{p}}_2 \\ \delta\dot{\hat{a}} \\ \delta\dot{\hat{a}}^\dagger \end{pmatrix} = \begin{pmatrix} 0 & \omega_1 & 0 & 0 & 0 & 0 \\ -\omega_1 & -\gamma_1 & 0 & 0 & g_1^* & g_1 \\ 0 & 0 & 0 & \omega_2 & 0 & 0 \\ 0 & 0 & -\omega_2 & -\gamma_2 & g_2^* & g_2 \\ ig_1 & 0 & ig_2 & 0 & -(i\Delta + \kappa/2) & 0 \\ -ig_1^* & 0 & -ig_2^* & 0 & 0 & -(-i\Delta + \kappa/2) \end{pmatrix} \begin{pmatrix} \delta\hat{x}_1 \\ \delta\hat{p}_1 \\ \delta\hat{x}_2 \\ \delta\hat{p}_2 \\ \delta\hat{a} \\ \delta\hat{a}^\dagger \end{pmatrix} + \begin{pmatrix} 0 \\ \xi_1 \\ 0 \\ \xi_2 \\ \sqrt{\kappa}\hat{a}^{\text{in}} \\ \sqrt{\kappa}\hat{a}^{\text{in},\dagger} \end{pmatrix}. \tag{6.38}$$

Then, we can define the diffusion matrix D in terms of the entries of our noise vector,

$$\frac{1}{2}\langle n_i(t)n_j(t') + n_j(t')n_i(t)\rangle = D_{ij}\delta(t-t') \tag{6.39}$$

and we can use the correlation functions of our noises, Eqs. (6.14) and (6.15), to get the matrix D as

$$D = \begin{pmatrix} 0 & 0 & 0 & 0 & 0 & 0 \\ 0 & \gamma_1(2\bar{n}_1+1) & 0 & 0 & 0 & 0 \\ 0 & 0 & 0 & 0 & 0 & 0 \\ 0 & 0 & 0 & \gamma_2(2\bar{n}_2+1) & 0 & 0 \\ 0 & 0 & 0 & 0 & 0 & \kappa/2 \\ 0 & 0 & 0 & 0 & \kappa/2 & 0 \end{pmatrix}. \tag{6.40}$$

Similarly, we can identify the covariance matrix V in terms of our system coordinates $u(t)$ as

$$V_{ij} = \frac{1}{2}\langle u_i(t)u_j(t') + u_j(t')u_i(t)\rangle. \tag{6.41}$$

The steady-state expression for the covariance matrix can be found by solving the Lyapunov equation,

$$AV + VA^T = -D \tag{6.42}$$

under the condition that all eigenvalues (real parts) of the matrix A are negative (equivalent to the the Routh-Hurwitz criterion for stability) [242]. For our system this would result in a matrix of the form

$$V = \begin{pmatrix} \langle\delta\hat{x}_1^2\rangle & \langle\delta\hat{p}_1\delta\hat{x}_1\rangle & & \cdots & \\ \langle\delta\hat{x}_1\delta\hat{p}_1\rangle & \langle\delta\hat{p}_1^2\rangle & & & \cdots \\ & \vdots & \langle\delta\hat{x}_2^2\rangle & \langle\delta\hat{p}_2\delta\hat{x}_2\rangle & \\ & & \langle\delta\hat{x}_2\delta\hat{p}_2\rangle & \langle\delta\hat{p}_2^2\rangle & \cdots \\ & \vdots & & \vdots & \ddots \end{pmatrix} \tag{6.43}$$

where the first four diagonal terms contain the autocorrelations of the position and momentum fluctuations of our two mechanical resonators. These are related to the effective thermal phonon number via

$$\bar{n}_i^{\text{eff}} = \frac{\langle\delta\hat{x}_i^2\rangle + \langle\delta\hat{p}_i^2\rangle - 1}{2}. \tag{6.44}$$

Since our matrices A and D contain only known parameters, it is straightforward to numerically solve Eq. (6.42) and obtain an expression for $\bar{n}_i^{\text{eff}}$. In our notation, $\langle\delta\hat{x}_j^2\rangle = \langle\delta\hat{p}_j^2\rangle = 0.5$, which yields $\bar{n}_j^{\text{eff}} = 0$ for the mechanical ground state.

6.5.5. Estimation of the phase lag in other systems

We can assess how the optomechanical phase lag would appear in different parameter regimes than the one we operate in, and specify some conditions necessary to see it. Firstly, in sideband-resolved systems, $\kappa \ll \omega_j$, the optomechanically scattered light would be outside the cavity linewidth and would not form a standing wave, so the photons do not remain in the cavity for a significant time (cf. the system in [75] if their detuning would be small, $|\Delta| \ll \omega_j$). This would make the average time-delay between the transduced and local noises negligible, because it

would be equal to the spatial separation of the resonators. In the opposite limit, $\kappa \gg \omega_m$, the photons exit the cavity sufficiently quickly such that again the time delay becomes negligible. Ideally, both the laser carrier field ω_ℓ and the sidebands $\omega_\ell \pm \omega_j$ fall within the cavity linewidth (i.e. $|\Delta| \ll \omega_j$) such that the effective coupling between the resonators is maximal. For example, if one operates with the laser carrier outside the cavity, the Stokes-rescattering of the anti-Stokes sideband (i.e. the second leg of process (4) in Fig. 6.5**a**) is weak.

Secondly, the optomechanical phase lag requires two mechanical resonators that are very close in frequency. Specifically, the mechanical (thermal) noise peaks must overlap to see interference between $\hat{\xi}_1$ and $\hat{\xi}_2$. This means that the difference in frequency must be smaller than the mechanical linewidths, $\omega_1 - \omega_2 < \gamma_1, \gamma_2$, which is a challenging condition. It can be eased by operating in the regime of optomechanical cooling (as we do), where the linewidths are broadened.

Finally, the effective coupling rate must be significantly greater than the decoherence rate of the mechanical resonators. If the coupling rate is too small, the thermal decoherence of the resonators causes effectively a random phase relation between the local and transduced noise. On top of that, by utilizing a large cavity photon number, the g_j become large and in that limit $M_1(M_2) \to \frac{g_1}{g_2}(\frac{g_2}{g_1})$; the transduced noise becomes similar in size to the local noise and the interference between them is maximal.

The conditions on seeing interference due to optomechanical phase lag are three-fold:

- $\kappa > \omega_j$ and $|\Delta| \ll \omega_j$, we must be sideband-unresolved and operate the laser carrier within the cavity for the maximum coupling between the resonators.
- $\omega_1 \simeq \omega_2$ (to within their effective linewidths), as otherwise the thermal noises do not overlap, and they cannot show interference.
- The effective coupling rate ($\propto g_1 g_2$) must be much greater than the effective decoherence rate ($\approx \gamma_1^{\text{eff}}, \gamma_2^{\text{eff}}$), such that there is significant thermal noise that is transduced, and the phase relation between the resonator (noises) doesn't become random due to thermal decoherence.

We have summarized the relevant parameters for related work in Table 6.2, determined which of the above criteria they meet (✓/ ×) and how large the optomechanical phase lag ϕ_{om} would be. Since $\omega_1 \simeq \omega_2$ is a challenging condition and subject to how the system is operated (i.e. mechanical frequencies can be changed by optomechanical cooling, thermal tuning, etc.), we have also calculated the phase lag for publications that are close to meeting this criterion (~ in Table 6.2). It is clear from the table that in all other publications to date, the optomechanical phase lag is small and therefore unlikely to be detected.

6.5.6. Exclusion of other interference mechanisms

Ref.	$\omega_j/(2\pi)$	$\omega_1 \simeq \omega_2$?	$\kappa/(2\pi)$	$\kappa > \omega_j$?	ϕ_{om} (π rad)
[186]	788.04 kHz 788.49 kHz	✓	177 kHz	×	-
[223]	10.0 MHz 11.3 MHz	×	1.38 MHz	×	-
[216]	13.6 MHz	✓	6.9 GHz	✓	3.1×10^{-4}
[218]	6.999 MHz 7.005 MHz	~	>20 MHz	✓	0.055
[185]	50.283 MHz 50.219 MHz	~	>1 GHz	✓	2.7×10^{-3}
[220]	6.53 MHz 6.61 MHz	~	>3 GHz	✓	3.0×10^{-4}
[76]	1.2 MHz	✓	2 MHz	✓	0.095
[221]	116.4 kHz 110.0 kHz	~	1.8 MHz	✓	0.01
This work	149.90 kHz 150.83 kHz	✓	$250 - 600$ kHz	✓	$0.1 - 0.4$

Table 6.2: Estimation of optomechanical phase lag in related works that meet (✓) or come close to meeting (~) the conditions to see optomechanical phase lag ($\omega_1 \simeq \omega_2$ and $\kappa > \omega_j$). Many related works operate in the resolved-sideband regime ($\kappa < \omega_j$) and have not been included.

Interference from effective mechanical frequency crossing

In certain optomechanical parameter regimes (κ, Δ, $g_{0,j}$, input laser power P_ℓ), the mechanical spectrum measured in our experiments can take a Fano-lineshape without the inclusion of optomechanical phase lag. As this looks qualitatively similar to the spectra we have reported in the main text, we will discuss how these phenomena are different. To illustrate this, we calculate the PSD using the parameters fitted to the data of Fig. 6.3**c**, shown in Table 6.1. When the optical input power is increased, we can distinguish the different behavior with and without optomechanical phase lag in Fig. 6.6.

For a low input laser power (100 nW, blue curves), the PSD looks the same without **a** and with **b** the optomechanical phase lag. The two mechanical resonances are clearly distinguishable as thermal peaks. As we increase the optical input power (orange through red curves), we see the peaks get broadened by optomechanical cooling. Without the optomechanical phase lag, Fig. 6.6**a**, the peaks continue to be broadened as we increase the power, until the effective mechanical frequencies cross (dashed lines) at higher powers. Around this crossing, the PSD changes and shows a dip left of a pronounced peak, forming a Fano-lineshape. Comparing this with the PSD simulated with optomechanical phase lag, we see a dip appear in the curves of higher power ($\simeq$20 µW, purple through pink). This somewhat symmetric dip between the two mechanical peaks is notably absent when excluding optomechanical phase lag, and is a key feature of the spectra that we observe. For the highest power (grey curve), we enter the strong-coupling regime ($g_j > \kappa, \omega_j$) and

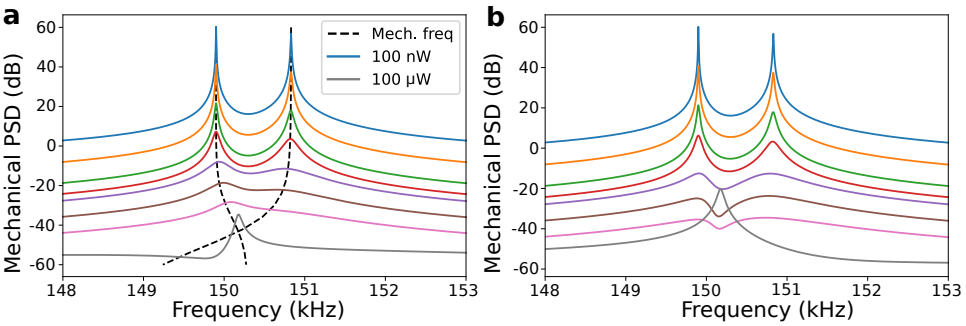

Figure 6.6: Simulated PSD without (**a**) and with (**b**) optomechanical phase lag, for various powers (top lowest power, 100 nW, bottom highest power, 100 μW, offset vertically), with dashed black lines the effective mechanical frequencies for the different power curves.

we see a dark-mode peak appear while the bright mode becomes heavily damped.

The interference seen without optomechanical phase lag seems to be related to the effective mechanical frequencies crossing, and can be compared to the work of Ref. [216]. Though the mechanism behind the interference effect is different in that work, their mechanical modes cross in a similar manner to the simulations shown in Fig. 6.6. As can be seen from the data reported in Fig. 6.4**a** of the main text (where we increase the laser input power while keeping $g_{0,1}/g_{0,2}$ constant), mechanical frequencies have not crossed and the curves resemble those of Fig. 6.6**b** much more than they resemble the curves of Fig. 6.6**a**. Furthermore, the optomechanical parameters κ, Δ, $g_{0,j}$ and ω_j follow from independent measurement of the cavity and OMIT (see below). Based on these considerations, the interference effect we see is significantly different from the one that originates from the effective mechanical mode crossing.

Interference from direct mechanics-mechanics coupling

If there is a direct mechanical coupling between the resonators, an interference effect can also be seen in the mechanical PSD [216]. Such a coupling would be described by a term of the form $c\hat{x}_1\hat{x}_2$ in the Hamiltonian (c some coupling constant), which is absent in our Eq. (6.12). To validate this, we estimate the direct mechanical coupling between the membranes (through the Si chip) via a finite element method (FEM) simulation in COMSOL. Our model consists of two 2D-shell physics nodes representing the suspended membrane and the Si_3N_4 layer on each side of the chip, while a 3D solid mechanics physics node represents the bulk of the Si chip (Fig. 6.7**a**). The in-plane stress in the Si_3N_4 layer is included in the model, and we capture the stress redistribution from the release step of the fabrication by including a stationary step in the model to ensure the stress distribution and geometry of our model match the physical sample. We ensure the mesh in the two membranes is identical, and sufficiently fine to have a converging solution.

We apply a 1 μN harmonic perturbation to the middle of one of the membranes (Fig. 6.7**a**, blue arrow), and obtain the displacement both at this center point and the center point of the other, undriven membrane (green arrow). The difference in

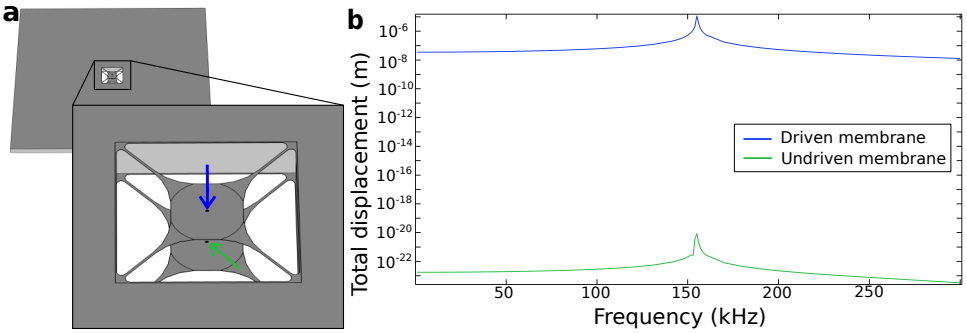

Figure 6.7: **a**: COMSOL model of our double-membrane device. The inset shows an area around the membranes and the hole through the chip, with the blue arrow denoting the location of a simulated driving force and the green arrow denoting the readout point in the center of the other membrane. **b**: Frequency-response simulation showing negligible displacement of the undriven membrane.

displacement amplitude gives an indication of the coupling strength between the membranes. From the 15 orders-of-magnitude difference in displacement plotted in Fig. 6.7**b**, we can confidently say that the direct mechanical coupling is negligibly small. From that, we conclude that the interference mechanism studied in [216] is not present in our system.

Interference from back-action cancellation

There are several publications describing interference in optomechanical systems through back-action cancellation, e.g. [192, 231, 232]. In general, this requires either multiple optical cavities/optical modes, or a second beam to drive the system. In this work, we explicitly only have a single optical cavity mode, which we verify by scanning the laser wavelength across the cavity resonance; we see a single resonance within the scanning window ($\pm$60 MHz). There are other modes from the Fabry-Pérot cavity, the longitudinal modes are separated by the free spectral range (FSR, 3 GHz) and the transversal modes are separated by >100 MHz. Both of these are considerably larger than the mechanical frequency ($\sim$150 kHz), which precludes them from being relevant in back-action cancellation schemes such as in Ref. [231].

The mode-matching is about 92% to the longitudinal mode, so the transversal modes are considerably smaller (measured in the empty cavity). The largest contribution is the second transversal mode, due to a slight mismatch in beam size between the incident laser beam and the cavity. This further allows us to exclude other optical modes as a mechanism for interference.

The incident laser beam consists of a single tone around 1550 nm, with two sidebands at 30 MHz generated for the Pound-Drever-Hall scheme. During operation, these sidebands are well outside the cavity window, and do not match with other frequencies of the system (i.e. ω_j). Thus we can also exclude back-action cancellation schemes relying on optical drives such as [192]. For the OMIT measurements (next section), we do use a drive tone that we sweep across the mechanical frequency, but this is turned off when measuring the mechanical spectra that show

optomechanical phase lag and the resulting interference.

6.5.7. Multi-mode OMIT

We use optomechanically induced transparency (OMIT) [237] as a way to fit and extract the optomechanical parameters of our system. Since we have multiple mechanical resonators and cannot operate our cavity in the sideband-resolved limit, we adopt the approach of Ref. [191] to fit our measured OMIT curves. We start by neglecting all input noises, and keeping only the strong pump term $\sqrt{\kappa_e}a_d$. We choose a phase reference such that the average cavity field $\langle\hat{a}\rangle$ is real and positive, such that g_1 and g_2 are also real and positive. We use the equations

$$\begin{aligned}\langle\hat{x}_j\rangle &= \chi_j(\omega)g_j\left(\langle\hat{a}\rangle + \langle\hat{a}\rangle^*\right)\\ \langle\hat{a}\rangle &= \chi_c(\omega)\left(\sum_{j=1,2} ig_j\langle\hat{x}_j\rangle + \sqrt{\kappa_e}a_d\right)\\ \langle\hat{a}\rangle^* &= \chi_c^*(-\omega)\left(\sum_{j=1,2} -ig_j\langle\hat{x}_j\rangle + \sqrt{\kappa_e}a_d^*\right).\end{aligned} \tag{6.45}$$

We solve this set of equations for the cavity field, and at the output we measure, $S(\omega) = \sqrt{\kappa_e}(\langle\hat{a}\rangle + \langle\hat{a}\rangle^*)$, and obtain

$$S(\omega) = \frac{\kappa_e\left(\chi_c(\omega)a_d + \chi_c^*(-\omega)a_d^*\right)}{1 - i\left(\chi_c(\omega) - \chi_c^*(-\omega)\right)\left(\chi_1(\omega)g_1^2 + \chi_2(\omega)g_2^2\right)}. \tag{6.46}$$

This result is similar to the one obtained in Ref. [191]. It contains terms both at $+\omega$ and $-\omega$, which represent the anti-Stokes and Stokes signal generated by our mechanical resonators, which we need to take into account due to the level of sideband resolution in our system ($\kappa \gtrsim \omega_j$). When comparing to the expressions in the fully sideband-resolved limit [237], we see that those do not contain both of these terms.

To detect our OMIT signal, we add an additional electro-optic modulator (EOM) to our setup, and we connect a vector network analyzer (VNA) to it to provide a frequency sweep of the drive together with the read-out. We connect the VNA in place of the spectrum analyzer (SA) to the home-built homodyne detector, as shown schematically in Fig. 6.8**a**. To measure OMIT, we lock the frequency of our laser to our cavity, and we turn on the small drive from the VNA. Due to the small linewidth of our mechanical resonators ($\simeq$1 Hz without optomechanical cooling), the filter bandwidth of the VNA is set very narrowly and we integrate for several minutes.

In OMIT measurements shown in the main text, we see an additional feature not expected from the spectrum derived in Eq. (6.46). This happens at exactly the mechanical frequencies of the resonators, and takes the shape of a peak in the OMIT curve. Because of the frequency at which this happens, we ascribe this to

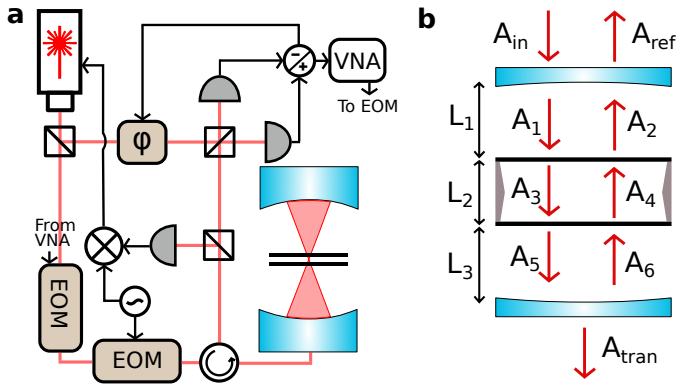

Figure 6.8: **a**: Setup to measure OMIT from our system. A VNA drives an additional phase EOM in the frequency range close to our mechanical resonances, and reads the reflected homodyne signal. **b**: Cavity fields for our Fabry-Pérot cavity containing the double-membrane system.

mechanical (thermal) noise from the resonators that we neglected in the derivation above. For a sufficiently strong pump $\hat{a}_{\mathrm{d}}$, the mechanical noise would be negligible, but such a pump would also affect our system. The frequency locking of the cavity is experimentally challenging, and a pump strong enough to neglect the mechanical noise would not allow us to obtain a stable lock. For the fits of the OMIT spectrum of Eq. (6.46), the frequency of these mechanical noise features make it difficult to exclude them, leading to some uncertainty in the fit parameters, in particular the detuning Δ.

6.5.8. Fabry-Pérot cavity with two lossy reflecting membranes

To model the behavior of our system, we use a known model [90] to describe our cavity in terms of the optical field amplitudes. The reason for this is twofold: Firstly, we control the optomechanical coupling of both of the membranes by controlling the position of the membrane-chip and the length of the cavity. Together with the (tunable) wavelength of the light that we send in, this gives us control over the resonance conditions of the three sub-cavities in our system. Secondly, by including lossy membranes in the model, we can take into account how the cavity linewidth changes as a function of membrane position. This gives us bounds on the optomechanical phase lag that we can expect.

We use the model

$$
\begin{aligned}
A_1 &= itA_{\mathrm{in}} + rA_2 e^{ikL_1} & A_5 &= it_m A_3 e^{ikL_2} - r_m A_6 e^{ikL_3} \\
A_2 &= it_m A_4 e^{ikL_2} - r_m A_1 e^{ikL_1} & A_6 &= rA_5 e^{ikL_3} \\
A_3 &= it_m A_1 e^{ikL_1} - r_m A_4 e^{ikL_2} & A_{\mathrm{ref}} &= itA_2 e^{ikL_2} + rA_{\mathrm{in}} \\
A_4 &= it_m A_6 e^{ikL_3} - r_m A_3 e^{ikL_2} & A_{\mathrm{tran}} &= itA_5 e^{ikL_3}
\end{aligned}
\tag{6.47}
$$

with the field amplitudes A_{in}, A_{refl}, A_{tran} and A_{1-6} and lengths L_1, L_2 and L_3 defined as in Fig. 6.8**b**. Furthermore, we have mirror reflectivity $r^2 = 99.995\%$ and

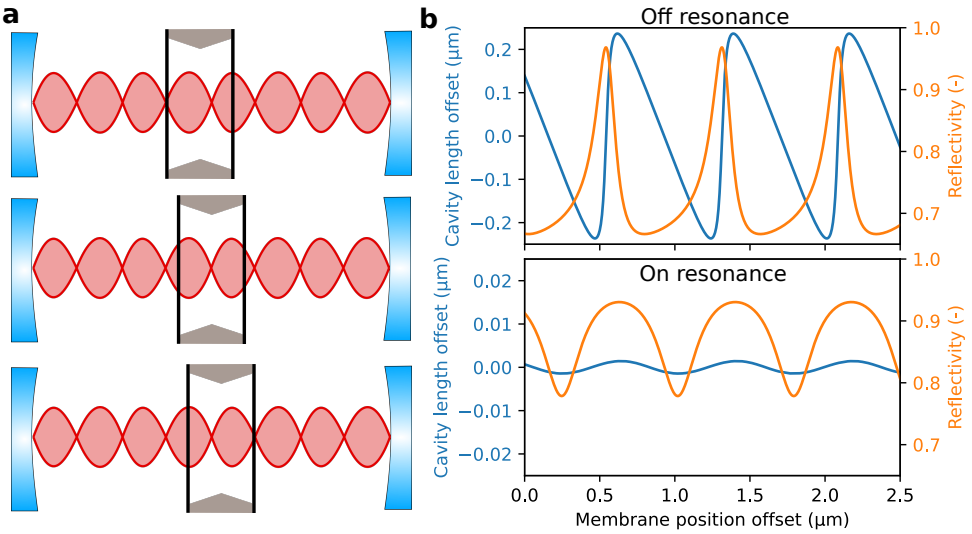

Figure 6.9: **a**: Sketch of control of (linear) optomechanical coupling g_0 by changing the position of the membranes within the cavity. From top to bottom: left resonator maximally coupled, right resonator not (linearly) coupled; both resonators approximately equally coupled; and left resonator not coupled, right resonator fully coupled. **b**: Simulated dispersion curve of cavity resonance versus chip position, and the associated reflectivity of the (lossy) cavity. Top panel for the slightly off-resonant case in this work, bottom panel for the case where the intra-membrane cavity is at resonance.

transmissivity $t^2 = 1 - r^2$ and membrane reflectivity $r_m^2 \approx 35\%$ and transmissivity $t_m^2 \approx 65\%$. This means we have lossless mirrors, which is a relatively good approximation for our setup. For the membranes, the loss due to absorption is much smaller than the losses due to e.g. scattering [34], imperfect alignment, fabrication imperfections, etc., so it can be ignored. We can take non-absorption losses into account by reducing the reflectivity and transmissivity slightly from their stated values, using a value of 0.98 ($= r_m^2 + t_m^2$) for the losses. This reduces the transmission of the cavity, but does not change the shape of the dispersion curve, i.e. it does not affect the optomechanical coupling rate. We have a photonic crystal pattern on our membranes [34] that changes the index of refraction away from that of bare Si_3N_4, which differs from the assumptions in Ref. [90].

We analytically solve Eq. (6.47) for the fields A_{1-6}, A_{in}, A_{refl} and A_{tran} and perform numerical calculations using the resulting equations. We vary the position of the membrane chip and calculate the position of the cavity mirrors required to see a cavity resonance for every position of the membrane. This gives a dispersion curve of the cavity resonance, Fig. 6.9**b** (blue lines), in exactly the same way as we perform experimentally. This dispersion curve takes a sinusoidal shape when the inter-membrane cavity is resonant (bottom plot), but is skewed when we are off-resonant with the inter-membrane cavity (top plot). Since the membrane reflectivity is much lower than the mirror reflectivity, the cavity can still be resonant even when the inter-membrane cavity is off-resonance. When comparing these numerical

simulations to the measurements in Fig. 6.10, we see from the skewness of the dispersion curve that we are not on resonance with the inter-membrane cavity. The regime of inter-membrane cavity resonance is of significant interest due to enhancement of the optomechanical coupling [37, 90, 224], but unfortunately out of reach due to limited laser tunability.

In Fig. 6.9**b**, we also plot the reflectivity of the cavity as a whole (orange lines). The plotted reflectivity gives the depth of the dip in cavity reflection at the resonance, i.e. the minimum reflection. The closer this value is to 1, the less we see of the cavity resonance due to losses in the cavity. We utilize this as a simple model to estimate the expected cavity linewidth to calculate the optomechanical phase lag. We estimate a lower (275 kHz) and upper (600 kHz) bound for the linewidth at the point of the lowest reflectivity, based on averaged measurements of the cavity linewidth over various measurement runs. Then, we scale these linewidths based on the reflectivity calculated and plotted in Fig. 6.9**b** to incorporate the effect of cavity losses on the expected optomechanical phase lag, thereby neglecting any contribution from the cavity lock.

When varying the position of the chip, we can choose for either of the membranes to be at a node/antinode of the field, as depicted in Fig. 6.9**b**. As we sweep the position of the membrane, our resonance traces out the dispersion curve and we can smoothly vary the coupling to either membrane. We do so in a measurement, plotted in the main window of Fig. 6.10. At several points (colored diamonds) we measure the PSD and we can deduce the coupling situation of each of the membranes from that. For the green (orange) diamond, we are predominantly coupled to the higher (lower) frequency resonator, given by its broadened linewidth in the noise spectrum. In the purple diamond case, we are coupled approximately equally to both membranes. As is visible in the main window, these three colored diamonds are in the mostly-linear regime where the cavity frequency shift is linear with membrane position, hence our optomechanical coupling is linear. The red diamond shows a measurement done in the quadratic regime, which shows a markedly different noise spectrum (no interference).

In the main window of Fig. 6.10, we can see approximately three periods of the dispersion curve. When comparing the noise spectra at identical points on the different curves (black circle, cross and triangle), we see a difference in features around 147 kHz and 153 kHz, which we ascribe to some other mechanical mode (not necessarily of our membranes). The difference in these features between the three periods of the dispersion curve we attribute to different amplitudes in the solutions to the field equations, Eq. (6.47). All measurements done in the main text were performed at a branch of the dispersion curve where both noise features (147 and 153 kHz) were mostly absent.

6.5.9. Analytical treatment of cooperativity competition

To clarify the effect of the cooperativity competition, we derive an analytical expression using some simplifying assumptions. In the derivation below, we have chosen a phase reference such that $\langle \hat{a} \rangle$ (and thus g_j) is real and positive. In all the numerical evaluations throughout this work, we have kept the complex behavior of g_j.

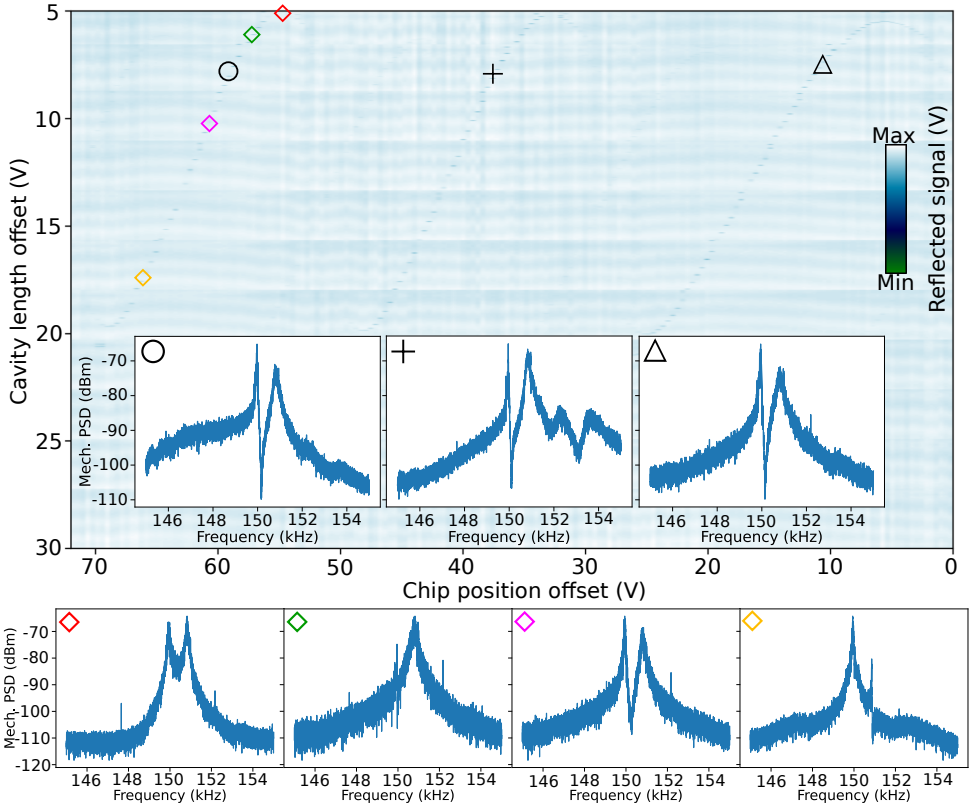

Figure 6.10: Cavity resonance as a function of membrane position. The main figure shows the dispersion curve of the resonance, which shifts in frequency ($\omega_c \propto V_{\text{mirror}}$) when the chip position is varied. Insets with black symbols show the homodyne spectrum at similar points on different branches of the dispersion curve. Insets with colored diamonds show the homodyne spectrum at different points on the same branch of the dispersion curve. Horizontal stripes are artifacts of the measurement.

From the real part of $\left(\chi_1^{\text{eff}}\right)^{-1}$ in Eq. (6.26), we can extract the effective mechanical frequency, where we can recognize the so-called "optical-spring" effect, given by

$$\omega_1^{\text{eff}}(\omega) = \left[\omega_1^2 + \frac{2g_1^2\Delta\omega_1\left[A(\omega) - (\Delta^2 + \kappa^2/4 - \omega^2)\right]}{\left[A(\omega) - (\Delta^2 + \kappa^2/4 - \omega^2)\right]^2 + \left[\kappa\omega + B(\omega)\right]^2}\right]^{\frac{1}{2}}, \tag{6.48}$$

where

$$\begin{aligned} A(\omega) &:= \frac{2g_2^2\Delta\omega_2(\omega_2^2 - \omega^2)}{(\omega_2^2 - \omega^2)^2 + \gamma_2^2\omega^2}, \\ B(\omega) &:= \frac{2g_2^2\Delta\omega_2\gamma_2\omega}{(\omega_2^2 - \omega^2)^2 + \gamma_2^2\omega^2}. \end{aligned} \tag{6.49}$$

From the imaginary part of $\left(\chi_1^{\text{eff}}\right)^{-1}$ in Eq. (6.26), we can extract the effective mechanical damping rate

$$\gamma_1^{\text{eff}}(\omega) = \gamma_1 + \frac{\omega_1}{\omega}\frac{2g_1^2\Delta\left[\kappa\omega + B(\omega)\right]}{\left[A(\omega) - (\Delta^2 + \kappa^2/4 - \omega^2)\right]^2 + \left[\kappa\omega + B(\omega)\right]^2}. \tag{6.50}$$

Eqs. (6.48) and (6.50) clearly reveal that both the effective frequency and damping rate of the first mechanical resonator are modified by the presence of the second mechanical resonator, reflected in the fact that $A(\omega), B(\omega) \neq 0$ when $g_2 \neq 0$. Instead, if we take $g_2 = 0$, Eqs. (6.48) and (6.50) become exactly the same form as those reported in Ref. [91] for a single resonator.

We now focus on the effect of the coupling to the second mechanical resonator on the damping rate of the first mechanical resonator. The expression of $\gamma_1^{\text{eff}}(\omega)$ is still quite involved, but it takes a simpler form under specific interesting conditions. By assuming the mechanical resonators with equal frequencies $\omega_1 = \omega_2 \equiv \omega_0$, working in the optimal mechanical cooling regime $\Delta = \omega_0$ (the cavity is resonant with two anti-Stokes sidebands), and looking at $\omega = \omega_0$ in the spectrum, we obtain

$$A(\omega_0) = 0, \quad B(\omega_0) = \frac{2g_2^2\omega_0}{\gamma_2}, \tag{6.51}$$

and thus

$$\gamma_1^{\text{eff}}(\omega_0) = \gamma_1 + \frac{2g_1^2\left(\kappa + \frac{2g_2^2}{\gamma_2}\right)}{\frac{\kappa^4}{16\omega_0^2} + \left(\kappa + \frac{2g_2^2}{\gamma_2}\right)^2}. \tag{6.52}$$

By assuming a large cooperativity of the second resonator, $C_2 = 2g_2^2/(\kappa\gamma_2) \gg 1$, we achieve

$$\gamma_1^{\text{eff}}(\omega_0) \simeq \gamma_1 + \frac{2g_1^2\kappa C_2}{\kappa^2\left(\frac{\kappa^2}{16\omega_0^2} + C_2^2\right)}, \tag{6.53}$$

and by further assuming $\kappa < 4\omega_0$, thus $(\kappa/4\omega_0)^2 < 1 \ll C_2^2$, we obtain a rather simple expression

$$\gamma_1^{\text{eff}}(\omega_0) \simeq \gamma_1 + \frac{2g_1^2}{\kappa C_2} = \gamma_1\left(1 + \frac{C_1}{C_2}\right), \tag{6.54}$$

where $C_1 = 2g_1^2/(\kappa\gamma_1)$ is the cooperativity of the first mechanical resonator, which does not have to be large to derive the above equation. It is interesting to compare γ_1^{eff} with and without the second mechanical resonator. By taking $g_2 = 0$ in Eq. (6.52) (only one mechanical resonator is coupled to the cavity), we have

$$\gamma_1^{\text{eff}}(\omega_0) = \gamma_1 + \frac{2g_1^2}{\kappa\left(\frac{\kappa^2}{16\omega_0^2} + 1\right)}, \tag{6.55}$$

and it becomes the well-known result in the resolved sideband limit $\kappa \ll \omega_0$ [38, 91, 240],

$$\gamma_1^{\text{eff}}(\omega_0) \simeq \gamma_1(1 + C_1). \tag{6.56}$$

Note that here the condition $\kappa \ll \omega_0$ is more demanding on the cavity linewidth than $\kappa < 4\omega_0$ used for deriving Eq. (6.54), because the latter is only used to keep $(\kappa/4\omega_0)^2 < 1 \ll C_2^2$. Comparing the damping rates with and without the second mechanical resonator, i.e. Eqs. (6.54) and (6.56), we see that the effective damping rate γ_1^{eff} is significantly reduced due to the presence of the second mechanical resonator because a large $C_2 \gg 1$ is assumed in Eq. (6.54), and for the special case $C_1 = C_2$, it reduces to twice its natural damping rate $\gamma_1^{\text{eff}} = 2\gamma_1$.

Similarly, owing to the symmetry of the two mechanical resonators, we obtain the effective damping rate of the second mechanical resonator

$$\gamma_2^{\text{eff}}(\omega_0) \simeq \gamma_2\left(1 + \frac{C_2}{C_1}\right), \tag{6.57}$$

under the condition $C_1 \gg 1$. Eqs. (6.54) and (6.57) are the main results of the work. They reveal a dissipation competition mechanism between the two mechanical resonators: the effective damping rate of each mechanical resonator is reduced by the presence of the other mechanical resonator, with the extent depending on the ratio of their cooperativities C_1/C_2, and the mechanical resonator with a larger cooperativity dissipates faster, i.e.

$$C_1 > C_2 \;\Rightarrow\; \gamma_1^{\text{eff}}(\omega_0) > \gamma_2^{\text{eff}}(\omega_0), \tag{6.58}$$

if the two natural damping rates are assumed equal $\gamma_1 = \gamma_2$ (in our system, these two damping rates are very close). This can be understood intuitively: both the mechanical resonators dissipate through the same optical channel and the one that is more strongly coupled to the optical field takes advantage in dissipating energy via light into the environment. We call this phenomenon cooperativity competition on the mechanical dissipation.

6.5.10. Mechanical noise cancellation for sensors

The ability to cancel mechanical (thermal) noise by insertion of a second mechanical resonator hints at potential applications in sensing. The straightforward way of implementing this would be to consider a resonant signal (force) $\hat{q}_1$ acting on the position fluctuations of one of the membranes. An example of this would be a laser beam at an incident angle such that it does not form a cavity mode, which is modulated at a specific (signal) frequency. This can be described by modifying Eqs. (6.17)-(6.18) to

$$\begin{aligned} \delta\hat{p}_j &= -j\frac{\omega}{\omega_j}\delta\hat{x}_j, \\ \delta\hat{x}_j &= \chi_j(\omega)\left[g_j^*\delta\hat{a} + g_j\delta\hat{a}^\dagger + \hat{\xi}_j + \hat{q}_1\right]. \end{aligned} \tag{6.59}$$

One can retrieve the solutions from earlier in this document by substituting $\hat{\tilde{\xi}}_1 = \hat{\xi}_1 + \hat{q}_1$, which shows that the signal we would want to detect is canceled by the mechanical noise cancellation, similar to the thermal noise. That is, in the transparency window (where the mechanical noise is canceled), the signal would appear

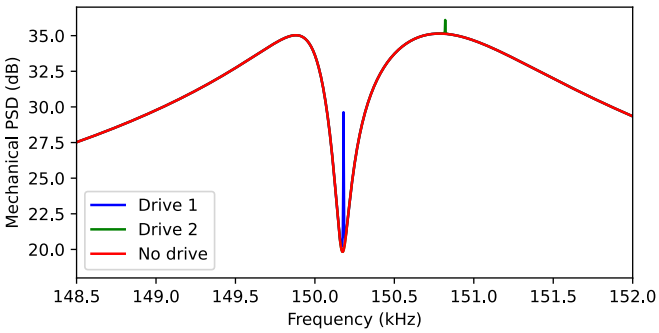

Figure 6.11: PSD with optical signal in cancellation window (blue), outside cancellation window (green), and without driving (red). The contrast between the signal peak and (thermal) noise floor is enhanced when it falls within the cancellation window.

above the thermal noise with the same prominence as outside the transparency window.

Conversely, if we work with a signal that is present in the optical mode rather than on the mechanics side, we introduce the $\hat{q}_1$ signal in Eqs. (6.19)-(6.20) instead,

$$\begin{aligned}\delta\hat{a} &= \chi_c(\omega)\left(\sum_{j=1,2} ig_j\delta\hat{x}_j + \sqrt{\kappa}\hat{a}^{\text{in}} + \hat{q}_1\right)\\ \delta\hat{a}^\dagger &= \chi_c^*(-\omega)\left(\sum_{j=1,2} -ig_j^*\delta\hat{x}_j + \sqrt{\kappa}\hat{a}^{\text{in},\dagger} + \hat{q}_1^\dagger\right).\end{aligned} \tag{6.60}$$

We can take it through the same process as described earlier in this work to calculate the resulting PSD. We assume a narrow-frequency signal with a Lorentzian distribution centered at frequency ω_q, with linewidth γ_q and with power P_q. If the signal is in the transparency window (Fig. 6.11 blue curve), it is much better resolved above the noise than if the signal is present outside the transparency window (green curve). We have used realistic parameters close to those of Table 6.1 to obtain these spectra. A particular use-case for such a signal could be in a gravitational wave interferometer [243] if one wants to detect a signal that is at the same frequency as a mechanical mode of that system. In that case, the fluctuations originating from (unwanted) mechanical modes can be suppressed in a specific frequency range by the inclusion of this second resonator in the cavity.

7

Conclusion

Well, that was quite an adventure. In this thesis, we have investigated the dynamical behavior of trampoline membranes. In chapter 3, we have found that the dissipation of the membrane mechanical modes can be increased by coupling to the substrate mode. Additionally, we have also shown that the modes of different membranes can be coupled via the substrate. In chapter 4, we have discovered a mechanism to generate mechanical frequency combs consisting of integer multiple overtones of a mechanical mode. The periodic optical field generated by reflection from the Si chip exerts a dielectrophoretic force on the Si_3N_4 membrane, which creates the overtones. The same periodic optical field also causes optothermal self-oscillation, which generates the large displacements necessary to see the frequency comb. In chapter 5, we have described and modeled an interference mechanism between two near-degenerate modes that leads to a particular ringing pattern in a ringdown measurement. This can be used to characterize the linear and non-linear properties of those modes. Finally, in chapter 6, we have found that there is a time-delay associated with the effective interaction between two membranes coupled through an optical cavity. This time delay causes destructive interference of their mechanical response, and thus leads to cancellation of the mechanical noise. Additionally, the coupling of both membranes to the single optical field leads to a competition effect on their optomechanical cooperativity.

So far, most of the results presented were not what we set out to discover or build. Truth be told, chapter 3 was the only part of this thesis where we found what we intended to look for; that the mechanical dissipation can increase due to coupling to a substrate mode. During this investigation, the membranes displayed curious behavior under the influence of the laser of our vibrometer, which turned out to be the frequency combs of chapter 4. Similarly, in the quest to demonstrate enhanced optomechanical coupling in multi-membrane arrays [33], the mechanical spectra also behaved unexpectedly. This turned out to be due to a cavity-induced time-delay in their coupling, which is the main point of chapter 6. And during characterization measurements of the membranes of chapter 6, as well as the spiderweb structures

of Ref. [61], an unforeseen ringing pattern appeared in their ringdowns. Modeling and understanding this effect is the core of chapter. 5.

For the future, there are some clear paths forward. There is work being done towards the enhanced coupling in optomechanical arrays, which could be an important result in the field if sufficient enhancement is achieved. Furthermore, the setup has a (so far) unused second optical beam that can be used to cool, drive or shift the mechanical modes. This is good for a curiosity-driven exploration, but likely leads in the direction of exceptional points [186], hybridization [218], synchronization [76] or other interesting dynamical behaviors. However, one can also think to further explore the time-delayed interaction between the membranes. What are the limits of the noise cancellation? How does it extend to three-membrane arrays? Does it affect the non-Hermitian dynamics around an exceptional point? There are plenty of questions both for theory and experiment to answer.

One can also think about continuing the investigation of dissipation in membranes. In particular, engineering the substrate such that the coupling to the membrane mode is reduced without the use of phononic crystal. Or investigating the coupling between the substrate and the outside world through clamping. However, the more interesting path forward is likely the one of the frequency combs. What are the limits on the number of comb lines? How to the individual lines behave in the presence of growth or decay of the whole comb? Can we guide the modes into an on-chip phononic waveguide or structure? Is it possible to engineer a structure in-plane to display frequency combs with similar origin? There is a wide range of opportunities to explore this effect.

This thesis has the title ”Dynamical behavior of trampoline membranes”, and that is indeed what is covered inside. But looking back, and looking forward, I think there is a lot yet to be discovered.

8

Acknowledgements

A PhD project is never done completely alone, even though only one person (usually) gets their name on the thesis. There are a lot of people I want to thank for supporting me over the past four years. Without all of you, I would not have been able to complete this project. I would not have had the opportunity to learn as many things, or have as much fun as I have had.

First, I would like to thank my promotor, **Simon Gröblacher**. Simon, I think you have a wonderful talent for hiring and supervising people, because I have seldom seen such a hard-working and successful team as the Glab. It has been an amazing four years! I've learned so much, and grown both as a person and as a scientist. You've always been the steady, calm factor that keeps the project going straight for the goal, even when we run into difficulties. That's what keeps the team together, and I'm looking forward to what comes out of the labs in the coming years!

Then, I would like to thank my co-promotor, **Richard Norte**. Richard, you seem to possess an incredible source of ideas, creativity, and a talent to find interesting collaborations. These skills made working with you so pleasant over the past four years, and I feel I learned a lot every time we discussed science. It's been an experience seeing the group grow from just you and me, where we could have a meeting in the library (and you would buy me coffee), to a team of people large enough to fill the PME meeting room. You've been highly successful in starting and driving all the new projects in the lab, and I think the Norte lab has become ready to make amazing science with you at the helm!

Even though the job I originally applied for was under your supervision, **Peter Steeneken**, you've been more of a mentor to me over the past years. I could always count on you to be the calm voice of reason that would advise me on the way forward even if I didn't see any. I think you have a positive influence on everyone in the department, either as a supervisor or as a mentor and adviser. If I succeed in an academic career, I know who I will model my behavior on! You've kept my head on straight and brought be back down to earth when I struggled with things during my project, and I want to thank you for that.

I'd like to thank **Gary Steele** for always keeping me on my toes! By challenging the things that I thought I knew (but didn't), you've made me go down scientific rabbit holes that were very valuable to explore. These worthwhile experiences were fun, looking back, and I feel they made me a better scientist!

I met **Wolfgang Löffler** when I was at my first conference, not even 2 months into my PhD, and the only other person I knew was Simon. Meeting someone who is both an incredibly nice person to talk to, and who was also working on topic similar to my own, suddenly made the whole conference seem less scary. Thanks you for that!

Thanks, **Silvan Schmid**, for helping me understand mechanical dissipation! Your works and talks were always enlightening when I was stuck understanding the finer details of damping. I would have loved to visit your group in Vienna, but travel was somewhat impeded over the last few years. I'm looking forward to all the sensing applications of trampoline membranes that will come from Vienna in the future!

I want to thank **Albert Schliesser** for inspiring me, and a lot of other people in Delft! You've shown us all how to include phononic crystals in our membranes, and why one should do so. When we met at GRC in Ventura, it was both refreshing and inspiring to talk to you! I hope we may collaborate somewhere in the future!

Special gratitude must to be given to **Andrea Cupertino** and **Nina Codreanu**, for being my paranymphs! **Andrea**, it's been nice working together because you're fundamentally a nice person. You're patient, hard-working and are truly a fabrication expert: very few people can make resonators with such high Q-factors! The endurance and attention to detail necessary to fabricate devices that make my own $Q = 10^6$ resonators 'not so high Q' is impressive! I also want to thank you for making nearly all the resonators used in these last few years, without which this thesis would be rather short. I'm looking forward to what you will make in the future!

Nina, you're not only a diamond fabrication genius, you're also a diamond of a person! Every time we talked, it felt like you made me a better, kinder, person. Thank you for all the time we spent together! Like me, you also spend your time in between two research groups, and I wish you the best of luck in the coming years!

This whole adventure started with the double-membrane project, which is actually still on-going! I would like to thank **Joao Moura**, **Claus Gärter** and **Jie Li** for teaching me the lab and how to do measurements, the cleanroom and how to make membranes and the theory of optomechanics. Thanks also to **Klara Knupfer** for your cavity design, to **Jingkun Guo** for being the best lab-mate one can have and to **Jin Chang** and **Xiong Yao** for taking over the project! Hopefully the future will bring enhanced coupling, or even better, more unexpected physics in double membranes!

I think my PhD project wouldn't have been successful if I hadn't been embedded in such an amazing group of people as the Glab (past and present)! I'm very happy we kept each other sane by lunching every day at 1.5 m distance during Covid times. Even though some of you have left the Glab before me (or joined the Glab after me), I'd like to thank all of you: For all the help in the lab, for all the fun times

and all the crazy experiences. So thanks, **Igor Marinkovic**, **Andreas Wallucks**, **Maarten Leeuwenhoek**, **Moritz Forsch**, **Rob Stockill**, **Bas Hensen**, **Niccolò Fiaschi**, **Nina Codreanu**, **Rodrigo Benevides**, **Amirparsa Zivari**, **Stefanos Andreou**, **Alexander Korsch**, **Yong Yu**, **Liu Chen**, and **Gaia da Prato**!

A lot of the projects that I've done wouldn't be successful if not for the people in the Norte lab. **Andrea Cupertino**, **Dongil Shin**, **Minxing Xu**, **Yufan Li**, and **Lucas Norder**, the Norte lab became a little better when every one of you joined, and I'm sad to have to leave such a relaxed, supportive environment. Thank you for all the help and advice, all the trouble-shooting and idea-bouncing that we had. I'm looking forward to what the future will bring for the Norte lab! I'd also like to give special thanks to my two master students, **Malte ten Wolde** and **Lauran Leermakers**. I'm extremely proud of the both of you, for all the things you learned and the hard work you did! You kept me on my toes with all the questions, and it was an amazing time supervising you two!

There are many people to thank for having such an supportive environment as PME. The lunch breaks we all took together were the highlight of many days! I'd like to thank **Satadal Dutta**, **Martin Robin**, **Hadi Arjmandi-Tash**, **Abilash Chandrashekar**, **Xiangfeng Chen**, **Ata Keskekler**, **Zichao Li**, **Irek Roslon**, **Makars Siskins**, **Martin Lee**, **Ali Sarafraz**, **Hanqing Liu**, **Maurits Houmes**, **Gabriele Baglioni**, **Tufan Erdogan**, **Yuheng Yan**, **Yang Yang**, **Farbod Alijani**, **Gerard Verbiest**, **Sabina Caneva**, **Wouter Westerveld**, **Ruben Guis**, **Arthur Givois**, **Tomás Manzaneque Garcia**, **Sabiju Valiya Valappil**, and **Nils Hermann**!

When I started my PhD in QN, I found a set of amazing colleagues. Thanks for all the fun times, the random chats in hallways and all the parties! **Adrià Sanz Mora**, **Sarwan Peiter**, **Jean-Paul van Soest**, **Robin Dekker**, **Sonakshi Arora**, **Thijs van Gogh**, **Luigi Maduro**, and **Sonia Conesa-Boj**, thank you for making QN a better place!

Behind the scenes of every science department, there is a great team of people that keep the show running. I was lucky enough to have two departments worth of people taking care of the administration and help with the technical support, and on top of that I also had the cleanroom team for their expertise! I'd like to thank:
PME: **Lisette Janse**, **Eveline Matroos**, **Gaby Offermans**, **Marli Guffens**, **Birgit Rademakers**, **Marianne Stolker**, **Annemieke van Ast**, **Sylviane Roso**, **Rob Luttjeboer**, **Patrick van Holst**, **Spiridon van Veldhoven**, **Bradley But**, **Gideon Emmaneel**, **Alex van den Boogaard**,
QN: **Etty van der Leij**, **Maria Roodenburg**, **Heleen Woldhuis**, **Erika van Verseveld**, **Lizzy Grootte**, **Irma Peterse**, **Dorine Verhoeven**, **Tino Kool**, **Ronald Bode**, **Tom de Kruijff**,
Kavli Nanolab Delft: **Marc Zuiddam**, **Charles de Boer**, **Roald van der Kolk**, **Eugene Straver**.

I'd also like to thank **Romy** and **Simone** of 't Je van het Loket, for their excellent lunches!

Although some colleagues are friends, I've been blessed with many friends who are not colleagues. Friends allow you to blow off steam when the pressure gets too

high, and a necessity in any PhD project!

Gentlemen, most of the adventures in my life have been thanks to, and with, you! **Wouter Kessels**, **Tomas Peeters**, **Wout Stapel**, **Jelle Rieske**, **Robin Blok**, **Jolan Samwel**, and **Kavish Kowlesar**, I could not have imagined the amount of fun we would have when we started as a group of 13, just over 10 years ago. I would not be the same without you, and I would not have been where I am today.

Being around like-minded people makes one feel at home. Thanks, **Koen van der Poll**, **Koen van Hoof**, **Maarten Seerden**, **Pepijn Baart**, **Sarah Veldhuizen**, **Alies Scharroo**, **Jelte Dijkstra**, **Stephan Olde**, **Tim Vroomans**, **Alexander Bruschke**, **Anne Poot**, **Anneriet Krol**, **Arent Kievits**, **Florian Huisman**, **Sep Driessen**, **Nina Sneeboer**, **Hidde Keizers**, **Judith van Looveren**, **Jurjen Oude Luttikhuis**, **Justin Oosterbaan**, **Laura Muntenaar**, **Luna Pennings**, **Mark van Leeuwen**, **Micha Burrichter**, **Onno Twisk**, **Oxana Oosterlee**, **Rens van Lierop**, **Robin Dekker**, **Roemer Hendrikx**, **Sasha Ivlev**, **Siem Aarts**, **Tristan Widjojoatmodjo**, and **Wietske Beers** for making me feel so at home in Delft! Thanks for all the invigorating discussions that filled the evenings, for the many trips and events we went to and all the fun activities of the past decade.

All of us started physics at the same time here in Delft, and I wouldn't have believed that we would still be good friends 10 years later. Thanks, **Fabian Fool**, **Luka Bavdaz**, **Alexander Geenen**, **Mike van Iersel**, **Roland Stolk**, and **Wendy Blonk**, for going through the TU Delft physics education with me, for being annoyed at the same professors and exercises, and delighted when we understood something new.

Als laatste, en allerbelangrijkste, wil ik graag degenen bedanken die het meeste voor mij hebben betekend, niet alleen tijdens mijn PhD maar ook in alle jaren daarvoor. Ik denk niet dat er genoeg woorden zijn om uit te drukken hoeveel ik van jullie allemaal hou, **Pap**, **Mam**, **Pieter**, **Irthe**, **Jorn**, **Anke** (en **Yfke**).

Curriculum Vitae

Matthijs Hendrik Jan DE JONG

24-02-1994 Born in Gouda, the Netherlands

Education

2006-2012 High School
Coornhert Gynmasium, Gouda, the Netherlands

2012-2016 B.Sc. Technische Natuurkunde
Delft University of Technology, the Netherlands,

2016-2018 M.Sc. Applied Physics
Delft University of Technology, the Netherlands,
Thesis: Fabrication and characterization of Josephson parametric amplifiers
Supervisor: Prof. Dr. G.A. Steele

2018-2022 Ph.D. Physics & Mechanical Engineering
Delft University of Technology, the Netherlands,
Thesis: Dynamical behavior of trampoline membranes
Promotor: Prof. Dr. S. Gröblacher
Copromotor: Dr. R.A. Norte

List of publications

* indicates equal contribution

5. **M.H.J. de Jong**, A. Cupertino, D. Shin, S. Gröblacher, F. Alijani, P.G. Steeneken, and R.A. Norte, *Ringing ringdowns of near-degenerate mechanical resonances*, manuscript in preparation.

4. **M.H.J. de Jong**, A. Ganesan, A. Cupertino, S. Gröblacher, and R.A. Norte, *Mechanical overtone frequency combs*, manuscript in preparation, preprint: Arxiv 2207.06401.

3. **M.H.J. de Jong**, M.A. ten Wolde, A. Cupertino, S. Gröblacher, P.G. Steeneken, and R.A. Norte, *Mechanical dissipation by substrate-mode coupling in SiN resonators*, Appl. Phys. Lett. **121**, 032201 (2022).

2. **M.H.J. de Jong***, J. Li*, C. Gärtner, R.A. Norte, and S. Gröblacher, *Coherent mechanical noise cancellation and cooperativity competition in optomechanical arrays*, Optica **9**, 170-176 (2022).

1. D. Shin, A. Cupertino, **M.H.J. de Jong**, P.G. Steeneken, M.A. Bessa*, and R.A. Norte*, *Spiderweb nanomechanical resonators via Bayesian optimization: Inspired by nature and guided by machine learning*, Adv. Mater. **34**, 2106248 (2022).

References

[1] M. Myllys, H. Häkkänen, J. Korppi-Tommola, K. Backfolk, P. Sirviö, and J. Timonen, *X-ray micro-tomography and laser ablation in the analysis of ink distribution in coated paper,* J. Appl. Phys. **117**, 144902 (2015).

[2] M. Aspelmeyer, T. J. Kippenberg, and F. Marquardt, *Cavity optomechanics,* Rev. Mod. Phys. **86**, 1391 (2014).

[3] S. Gröblacher, J. B. Hertzberg, M. R. Vanner, G. D. Cole, S. Gigan, K. C. Schwab, and M. Aspelmeyer, *Demonstration of an ultracold micro-optomechanical oscillator in a cryogenic cavity,* Nat. Phys. **5**, 485 (2009).

[4] S. Gröblacher, K. Hammerer, M. R. Vanner, and M. Asplemeyer, *Observation of strong coupling between a micromechanical resonator and an optical cavity field,* Nature **460**, 724 (2009).

[5] J. D. Thompson, B. M. Zwickl, A. M. Jayich, F. Marquardt, S. M. Girvin, and J. G. E. Harris, *Strong dispersive coupling of a high-finesse cavity to a micromechanical membrane,* Nature **452**, 72 (2008).

[6] D. Kleckner, B. Pepper, E. Jeffrey, P. Sonin, S. M. Thon, and D. Bouwmeester, *Optomechanical trampoline resonators,* Opt. Express **19**, 19708 (2011).

[7] B. M. Zwickl, W. E. Shanks, A. M. Jayich, C. Yang, A. C. Bleszynski Jayich, J. D. Thompson, and J. G. E. Harris, *High quality mechanical and optical properties of commercial silicon nitride membranes,* Appl. Phys. Lett. **92**, 103125 (2008).

[8] D. J. Wilson, C. A. Regal, S. B. Papp, and H. J. Kimble, *Cavity optomechanics with stoichiometric SiN films,* Phys. Rev. Lett. **103**, 207204 (2009).

[9] C. H. Bui, J. Zheng, S. W. Hoch, L. Y. T. Lee, J. G. E. Harris, and C. W. Wong, *High-reflectivity, high-Q micromechanical membranes via guided resonances for enhanced optomechanical coupling,* Appl. Phys. Lett. **100**, 021110 (2012).

[10] U. Kemiktarak, M. Durand, M. Metcalfe, and J. Lawall, *Cavity optomechanics with sub-wavelength grating mirrors,* New J. Phys. **14**, 125010 (2012).

[11] C. Stambaugh, H. Xu, U. Kemiktarak, J. Taylor, and J. Lawall, *From membrane-in-the-middle to mirror-in-the-middle with a high-reflectivity sub-wavelength grating,* Ann. Phys. **527**, 81 (2015).

[12] K. Makles, T. Antoni, A. G. Kuhn, S. Deléglise, T. Briant, P.-F. Cohadon, R. Braive, G. Beaudoin, L. Pinard, C. Michel, V. Dolique, R. Flaminio, G. Cagnoli, I. Robert-Philip, and A. Heidmann, *2D photonic-crystal optomechanical nanoresonator,* Opt. Lett. **40**, 174 (2015).

[13] R. A. Norte, J. P. Moura, and S. Gröblacher, *Mechanical resonators for quantum optomechanics experiments at room temperature,* Phys. Rev. Lett. **116**, 147202 (2016).

[14] C. Reinhardt, T. Müller, A. Bourassa, and J. C. Sankey, *Ultralow-noise SiN trampoline resonators for sensing and optomechanics,* Phys. Rev. X **6**, 021001 (2016).

[15] H. J. Kimble, *The quantum internet,* Nature **453**, 1023 (2008).

[16] C. A. Regal and K. W. Lehnert, *From cavity electromechanics to cavity optomechanics,* in *Journal of Physics: Conference Series*, 22nd International Conference on Atomic Physics, Vol. 264 (2011) p. 012025.

[17] R. W. Andrews, R. W. Peterson, T. P. Purdy, K. Cicak, R. W. Simmonds, C. A. Regal, and K. W. Lehnert, *Bidirectional and efficient conversion between microwave and optical light,* Nat. Phys. **10**, 321 (2014).

[18] T. Bagci, A. Simonsen, S. Schmid, L. G. Villanueva, E. Zeuthen, J. Appel, J. M. Taylor, A. Sørensen, K. Usami, A. Schliesser, and E. S. Polzik, *Optical detection of radio waves through a nanomechanical transducer,* Nature **507**, 81 (2014).

[19] A. P. Higginbotham, P. S. Burns, M. D. Urmey, R. W. Peterson, N. S. Kampel, B. M. Brubaker, G. Smith, K. W. Lehnert, and C. A. Regal, *Harnessing electro-optic correlations in an efficient mechanical converter,* Nat. Phys. **14**, 1038 (2018).

[20] B. M. Brubaker, J. M. Kindem, M. D. Urmey, S. Mittal, R. D. Delaney, P. S. Burns, M. R. Vissers, K. W. Lehnert, and C. A. Regal, *Optomechanical ground-state cooling in a continuous and efficient electro-optic transducer,* Phys. Rev. X **12**, 021062 (2022).

[21] G. J. Milburn, K. Jacobs, and D. F. Walls, *Quantum-limited measurements with the atomic force microscope,* Phys. Rev. A **50**, 5256 (1994).

[22] R. Fisher, D. P. McNally, C. Reetz, G. G. T. Assumpção, T. Knief, Y. Lin, and C. A. Regal, *Spin detection with a micromechanical trampoline: towards magnetic resonance microscopy harnessing cavity optomechanics,* New J. Phys. **21**, 043049 (2019).

[23] D. Hälg, T. Gisler, Y. Tsaturyan, L. Catalini, U. Grob, M.-D. Krass, M. Héritier, H. Mattiat, A.-K. Thamm, R. Schirhagl, E. C. Langman, A. Schliesser, C. L. Degen, and A. Eichler, *Membrane-based scanning force microscopy,* Phys. Rev. Applied **15**, L021001 (2021).

[24] J. Manley, D. J. Wilson, R. Stump, D. Grin, and S. Singh, *Searching for scalar dark matter with compact mechanical resonators,* Phys. Rev. Lett. **124**, 151301 (2020).

[25] J. Manley, M. D. Chowdhury, D. Grin, S. Singh, and D. J. Wilson, *Searching for vector dark matter with an optomechanical accelerometer,* Phys. Rev. Lett. **126**, 061301 (2021).

[26] D. Carney, G. Krnjaic, D. C. Moore, C. A. Regal, G. Afek, S. Bhave, B. Brubaker, T. Corbitt, J. Cripe, N. Crisosto, A. Geraci, S. Ghosh, J. G. E. Harris, A. Hook, E. W. Kolb, J. Kunjummen, R. F. Lang, T. Li, T. Lin, Z. Liu, J. Lykken, L. Magrini, J. Manley, N. Matsumoto, A. Monte, F. Monteiro, T. Purdy, C. J. Riedel, R. Singh, S. Singh, K. Sinha, J. M. Taylor, J. Qin, D. J. Wilson, and Y. Zhao, *Mechanical quantum sensing in the search for dark matter,* Quantum Sci. Technol. **6**, 024002 (2021).

[27] R. W. Peterson, T. P. Purdy, N. S. Kampel, R. W. Andrews, P.-L. Yu, K. W. Lehnert, and C. A. Regal, *Laser cooling of a micromechanical membrane to the quantum backaction limit,* Phys. Rev. Lett. **116**, 063601 (2016).

[28] M. Underwood, D. Mason, D. Lee, H. Xu, L. Jiang, A. B. Shkarin, K. Børkje, S. M. Girvin, and J. G. E. Harris, *Measurement of the motional sidebands of a nanogram-scale oscillator in the quantum regime,* Phys. Rev. A **92**, 061801 (2015).

[29] A. Noguchi, R. Yamazaki, M. Ataka, H. Fujita, Y. Tabuchi, T. Ishikawa, K. Usami, and Y. Nakamura, *Ground state cooling of a quantum electromechanical system with a silicon nitride membrane in a 3D loop-gap cavity,* New J. Phys. **18**, 103036 (2016).

[30] S. Bose, K. Jacobs, and P. L. Knight, *Scheme to probe the decoherence of a macroscopic object,* Phys. Rev. A **59**, 3204 (1999).

[31] M. Bonaldi, A. Borrielli, A. Chowdhury, G. Di Guissepe, W. Li, N. Malossi, F. Marino, B. Morana, R. Natali, P. Piergentili, G. A. Prodi, P. M. Sarro, E. Serra, P. Vezio, D. Vitali, and F. Marin, *Probing quantum gravity effects with quantum mechanical oscillators,* Eur Phys J D **74**, 178 (2020).

[32] Y. Liu, J. Mummery, J. Zhou, and M. A. Sillanpää, *Gravitational forces between nonclassical oscillators,* Phys. Rev. Applied **15**, 034004 (2021).

[33] A. Xuereb, C. Genes, and A. Dantan, *Strong coupling and long-range collective interactions in optomechanical arrays,* Phys. Rev. Lett. **109**, 223601 (2012).

[34] C. Gärtner, J. P. Moura, W. Haaxman, R. A. Norte, and S. Gröblacher, *Integrated optomechanical arrays of two high reflectivity SiN membranes,* Nano Lett. **18**, 7171 (2018).

[35] J. P. Moura, *Making light jump: Photonic crystals on trampoline membranes for optomechanics experiments*, phdthesis, Delft University of Technology (2019), iSBN: 978-90-8593-390-8.

[36] C.-M. Gärtner, *Advanced membrane architectures for multimode optomechanics*, Ph.D. thesis, University of Vienna, Faculty of Physics (2020).

[37] P. Piergentili, L. Catalini, M. Bawaj, S. Zippilli, N. Malossi, R. Natali, D. Vitali, and G. Di Giuseppe, *Two-membrane cavity optomechanics,* New J. Phys. **20**, 083024 (2018).

[38] F. Marquardt, J. P. Chen, A. A. Clerk, and S. M. Girvin, *Quantum theory of cavity-assisted sideband cooling of mechanical motion,* Phys. Rev. Lett. **99**, 093902 (2007).

[39] J. Guo, R. Norte, and S. Gröblacher, *Feedback cooling of a room temperature mechanical oscillator close to its motional ground state,* Phys. Rev. Lett. **123**, 223602 (2019).

[40] J. Guo and S. Gröblacher, *Coherent feedback in optomechanical systems in the sideband-unresolved regime,* Quantum **6**, 848 (2022).

[41] C. Whittle, E. D. Hall, S. Dwyer, N. Mavalvala, V. Sudhir, R. Abbott, A. Ananyeva, C. Austin, L. Barsotti, J. Betzwieser, C. D. Blair, A. F. Brooks, D. D. Brown, A. Buikema, C. Cahillane, J. C. Driggers, A. Effler, A. Fernandez-Galiana, P. Fritschel, V. V. Frolov, T. Hardwick, M. Kasprzack, K. Kawabe, N. Kijbunchoo, J. S. Kissel, G. L. Mansell, F. Matichard, L. McCuller, T. McRae, A. Mullavey, A. Pele, R. M. S. Schofield, D. Sigg, M. Tse, G. Vajente, D. C. Vander-Hyde, H. Yu, H. Yu, C. Adams, R. X. Adhikari, S. Appert, K. Arai, J. S. Areeda, Y. Asali, S. M. Aston, A. M. Baer, M. Ball, S. W. Ballmer, S. Banagiri, D. Barker, J. Bartlett, B. K. Berger, D. Bhattacharjee, G. Billingsley, S. Biscans, R. M. Blair, N. Bode, P. Booker, R. Bork, A. Bramley, K. C. Cannon, X. Chen, A. A. Ciobanu, F. Clara, C. M. Compton, S. J. Cooper, K. R. Corley, S. T. Countryman, P. B. Covas, D. C. Coyne, L. E. H. Datrier, D. Davis, C. D. Fronzo, K. L. Dooley, P. Dupej, T. Etzel, M. Evans, T. M. Evans, J. Feicht, P. Fulda, M. Fyffe, J. A. Giaime, K. D. Giardina, P. Godwin, E. Goetz, S. Gras, C. Gray, R. Gray, A. C. Green, E. K. Gustafson, R. Gustafson, J. Hanks, J. Hanson, R. K. Hasskew, M. C. Heintze, A. F. Helmling-Cornell, N. A. Holland, J. D. Jones, S. Kandhasamy, S. Karki, P. J. King, R. Kumar, M. Landry, B. B. Lane, B. Lantz, M. Laxen, Y. K. Lecoeuche, J. Leviton, J. Liu, M. Lormand, A. P. Lundgren, R. Macas, M. MacInnis, D. M. Macleod, S. Márka, Z. Márka, D. V. Martynov, K. Mason, T. J. Massinger, R. McCarthy, D. E. McClelland, S. McCormick, J. McIver, G. Mendell, K. Merfeld, E. L. Merilh, F. Meylahn, T. Mistry, R. Mittleman, G. Moreno, C. M. Mow-Lowry, S. Mozzon, T. J. N. Nelson, P. Nguyen, L. K. Nuttall, J. Oberling, R. J. Oram, C. Osthelder, D. J. Ottaway, H. Overmier, J. R. Palamos, W. Parker, E. Payne, R. Penhorwood, C. J. Perez, M. Pirello, H. Radkins, K. E. Ramirez, J. W. Richardson, K. Riles, N. A. Robertson, J. G. Rollins, C. L. Romel, J. H. Romie, M. P. Ross, K. Ryan, T. Sadecki, E. J. Sanchez, L. E. Sanchez, T. R. Saravanan, R. L. Savage, D. Schaetz, R. Schnabel, E. Schwartz, D. Sellers, T. Shaffer, B. J. J. Slagmolen, J. R. Smith, S. Soni, B. Sorazu, A. P. Spencer, K. A. Strain, L. Sun, M. J. Szczepańczyk, M. Thomas, P. Thomas, K. A. Thorne, K. Toland, C. I. Torrie, G. Traylor, A. L. Urban, G. Valdes, P. J. Veitch, K. Venkateswara, G. Venugopalan, A. D. Viets, T. Vo, C. Vorvick, M. Wade, R. L. Ward, J. Warner, B. Weaver, R. Weiss, B. Willke, C. C. Wipf, L. Xiao, H. Yamamoto, L. Zhang, M. E. Zucker, and J. Zweizig, *Approaching the motional ground state of a 10 kg object,* Science **372**, 1333 (2021).

[42] R. Wolfson, *Essential university physics*, 2nd ed. (Pearson Education Inc., 1301 Sansome St., San Francisco, 9411 USA, 2012).

[43] L. D. Landau and E. M. Lifshitz, *Mechanics*, 3rd ed., Course of Theoretical Physics, Vol. 1 (Reed Educational and Professional Publishing Ltd., Linacre House, Jordan Hill, Oxford OX2 8DP, 1976).

[44] E. I. Green, *The story of Q,* Am. Sci. **43**, 584 (1955).

[45] B. D. Hauer, C. Doolin, K. S. D. Beach, and J. P. Davis, *A general procedure for thermomechanical calibration of nano/micro-mechanical resonators,* Ann. Physics **339**, 181 (2013).

[46] M. V. Salapaka, H. S. Berg, J. Lai, A. Majumdar, and E. McFarland, *Multi-mode noise analysis of cantilevers for scanning probe microscopy,* J. Appl. Phys. **81**, 2480 (1997).

[47] P. T. Törmä, H. J. Sipilä, M. Mattila, P. Kostamo, J. Kostamo, E. Kostamo, H. Lipsanen, N. Nelms, B. Shortt, M. Bavdaz, and C. Laubis, *Ultra-thin silicon nitride X-ray windows,* IEEE Trans. Nucl. Sci. **60**, 1311 (2013).

[48] J. W. M. Jacobs and J. F. C. M. Verhoeven, *Specimen preparation technique for high resolution transmission electron microscopy studies on model supported metal catalysts,* J. Microsc. **143**, 103 (1986).

[49] S. Tagliati, V. M. Krasnov, and A. Rydh, *Differential membrane-based nanocalorimeter for high-resolution measurements of low-temperature specific heat,* Rev. Sci. Instrum. **83**, 055107 (2012).

[50] W. Gao, F. Wang, and O. Sigmund, *Systematic design of high-Q prestressed micro membrane resonators,* Comput. Methods Appl. Mech. Engrg. **361**, 112692 (2020).

[51] D. Høj, F. Wang, W. Gao, U. B. Hoff, O. Sigmund, and U. L. Andersen, *Ultra-coherent nanomechanical resonators based on inverse design,* Nat Commun **12**, 5766 (2021).

[52] M. J. Bereyhi, A. Beccari, S. A. Fedorov, A. H. Ghadimi, R. Schilling, D. J. Wilson, N. J. Engelsen, and T. J. Kippenberg, *Clamp-tapering increases the quality factor of stressed nanobeams,* Nano Lett. **19**, 2329 (2019).

[53] P. Sadeghi, M. Tanzer, S. L. Christensen, and S. Schmid, *Influence of clamp-widening on the quality factor of nanomechanical silicon nitride resonators,* J. Appl. Phys. **126**, 165108 (2019).

[54] J. M. L. Miller, G. D. Vukasin, Z. Zhang, H.-K. Kwon, A. Majumdar, T. W. Kenny, and S. W. Shaw, *Effects of remote boundary conditions on clamping loss in micromechanical resonators,* J Microelectromech S **31**, 204 (2021).

[55] R. O. Pohl, X. Liu, and E. Thompson, *Low-temperature thermal conductivity and acoustic attenuation in amorphous solids,* Rev. Modern Phys. **74**, 991 (2002).

[56] D. R. Southworth, R. A. Barton, S. S. Verbridge, B. Ilic, A. D. Fefferman, H. G. Craighead, and J. M. Parpia, *Stress and silicon nitride: a crack in the universal dissipation behaviour of glasses,* Phys. Rev. Lett. **102**, 225503 (2009).

[57] P. Temple-Boyer, C. Rossi, E. Saint-Etienne, and E. Scheid, *Residual stress in low-pressure chemical vapor deposition SiN_x films deposited from silane and ammonia,* J Vac Sci Technol **16**, 2003 (1998).

[58] S. S. Verbridge, J. M. Parpia, R. B. Reichenbach, L. M. Bellan, and H. G. Craighead, *High quality factor resonance at room temperature with nanostrings under high tensile stress,* J. Appl. Phys. **99**, 124304 (2006).

[59] Q. P. Unterreithmeier, T. Faust, and J. P. Kotthaus, *Damping of nanomechanical resonators,* Phys. Rev. Lett. **105**, 027205 (2010).

[60] S. Fedorov, *Mechanical resonators with high dissipation dilution in precision and quantum measurements*, phdthesis, École Polytechnique fédérale de Lausanne (2021).

[61] D. Shin, A. Cupertino, M. H. J. de Jong, P. G. Steeneken, M. A. Bessa, and R. A. Norte, *Spiderweb nanomechanical resonators via Bayesian optimization: Inspired by nature and guided by machine learning,* Adv. Mater. **34**, 2106248 (2022).

[62] S. Schmid, K. D. Jensen, K. H. Nielsen, and A. Boisen, *Damping mechanisms in high-Q micro and nanomechanical string resonators,* Phys. Rev. B **84**, 165307 (2011).

[63] P.-L. Yu, T. P. Purdy, and C. A. Regal, *Control of material damping in high-Q membrane microresonators,* Phys. Rev. Lett. **108**, 083603 (2012).

[64] S. A. Fedorov, N. J. Engelsen, A. H. Ghadimi, M. J. Bereyhi, R. Schilling, D. J. Wilson, and T. J. Kippenberg, *Generalized dissipation dilution in strained mechanical resonators,* Phys. Rev. B **99**, 054107 (2019).

[65] J. Rieger, A. Isacsson, M. J. Seitner, J. P. Kotthaus, and E. M. Weig, *Energy losses of nanomechanical resonators induced by atomic force microscopy-controlled mechanical impedance mismatching,* Nat Commun **5**, 3345 (2014).

[66] I. Wilson-Rae, *Intrinsic dissipation in nanomechanical resonators due to phonon tunneling,* Phys. Rev. B **77**, 245418 (2008).

[67] D. J. Wilson, *Cavity optomechanics with high-stress silicon nitride films*, phdthesis, California Institute of Technology (2012).

[68] A. Jöckel, M. T. Rakher, M. Koprri, S. Camerer, D. Hunger, M. Mader, and P. Treutlein, *Spectroscopy of mechanical dissipation in micro-mechanical membranes,* Appl. Phys. Lett. **99**, 143109 (2011).

[69] S. Chakram, Y. S. Patil, L. Chang, and M. Vengalattore, *Dissipation in ultrahigh quality factor SiN membrane resonators,* Phys. Rev. Lett. **112**, 127201 (2014).

[70] Y. Tsaturyan, A. Barg, A. Simonsen, L. G. Villanueva, S. Schmid, A. Shliesser, and E. S. Polzik, *Demonstration of suppresed phonon tunneling losses in phononic bandgap shielded membrane resonators for high-Q optomechanics,* Opt. Express **22**, 6810 (2014).

[71] S. A. Fedorov, V. Sudhir, R. Schilling, H. Schütz, D. J. Wilson, and T. J. Kippenberg, *Evidence for structural damping in a high-stress silicon nitride nanobeam and its implications for quantum optomechanics,* Phys. Lett. A **382**, 2251 (2018).

[72] G. S. MacCabe, H. Ren, J. Luo, J. D. Cohen, H. Zhou, A. Sipahigil, M. Mirhosseini, and O. Painter, *Nano-acoustic resonator with ultralong phonon lifetime,* Science **370**, 840 (2020).

[73] B. Nair, A. Naesby, and A. Dantan, *Optomechanical characterization of silicon nitride membrane arrays,* Opt. Lett. **42**, 1341 (2017).

[74] X. Wei, J. Sheng, C. Yang, Y. Wu, and H. Wu, *Controllable two-membrane-in-the-middle cavity optomechanical system,* Phys. Rev. A **99**, 023851 (2019).

[75] M. J. Weaver, F. Buters, F. Luna, H. Eerkens, K. Heeck, S. de Man, and D. Bouwmeester, *Coherent optomechanical state transfer between disparate mechanical resonators,* Nat. Commun. **8**, 824 (2017).

[76] J. Sheng, X. Wei, C. Yang, and H. Wu, *Self-organized synchronization of phonon lasers,* Phys. Rev. Lett. **124**, 053604 (2020).

[77] P. Piergentili, W. Li, R. Natali, N. Malossi, D. Vitali, and G. Di Giuseppe, *Two-membrane cavity optomechanics: non-linear dynamics,* New J. Phys. **23**, 073013 (2021).

[78] C. Yang, J. Sheng, and H. Wu, *Controllable phononic low-pass filter via optomechanical interactions,* Aip Conf Proc **10**, 904467 (2022).

[79] C. Yang, X. Wei, J. Sheng, and H. Wu, *Phonon heat transport in cavity-mediated optomechanical nanoresonators,* Nat. Commun. **11**, 4656 (2020).

[80] J. Sheng, C. Yang, and H. Wu, *Realization of a coupled-mode heat engine with cavity-mediated nanoresonators,* Sci. Adv. **7**, eabl7740 (2021).

[81] Q. Zhang, C. Yang, J. Sheng, and H. Wu, *Dissipative coupling induced phonon lasing with anti-parity-time symmetry,* (2022), arxiv preprint, 2110.12456 .

[82] A. Perot and C. Fabry, *On the application of interference phenomena to the solution of various problems of spectroscopy and metrology,* Astrophys. J. **9**, 87 (1899).

[83] K. T. Knupfer, *Improving the stability of a membrane-in-the-middle setup for cavity optomechanics*, mathesis, Leiden University (2019).

[84] R. V. Pound, *Electronics frequency stabilization of microwave oscillators,* Rev. Sci. Instrum. **17**, 490 (1946).

[85] R. W. P. Drever, J. L. Hall, F. V. Kowalski, J. Hough, G. M. Ford, A. J. Munley, and H. Ward, *Laser phase and frequency stabilization using an optical resonator,* Appl. Phys. B **31**, 97 (1983).

[86] E. D. Black, *An introduction to Pound-Drever-Hall laser frequency stabilization,* Am. J. Phys **69**, 79 (2001).

[87] D. J. Griffiths and D. F. Schroeter, *Introduction to quantum mechanics*, 3rd ed. (Cambridge University Press, 2018).

[88] Y. V. Nazarov and J. Danon, *Advanced quantum mechanics*, 1st ed. (Cambridge University Press, 2013).

[89] M. Aspelmeyer, T. J. Kippenberg, F. Marquardt, A. A. Clerk, K. Hammerer, C. Genes, D. Vitali, P. Tombesi, G. Milburn, C. Simon, D. Bouwmeester, P.-F. Cohadon, R. Schnabel, I. Favero, J. Sankey, E. M. Weig, A. Schliesser, F. Bahl, T. Carmon, H. Tang, W. Pernice, A. H. Safavi-Naeini, O. Painter, K. W. Lehnert, A. O'Connell, A. N. Cleland, D. M. Stamper-Kurn, P. Treutlein, M. Poggio, and P. Rabl, *Cavity optomechanics*, edited by M. Aspelmeyer, T. J. Kippenberg, and F. Marquardt (Springer, 2014).

[90] J. Li, A. Xuereb, N. Malossi, and D. Vitali, *Cavity mode frequencies and strong optomechanical coupling in two-membrane cavity optomechanics,* J. Opt. **18**, 084001 (2016).

[91] C. Genes, D. Vitali, P. Tombesi, S. Gigan, and M. Aspelmeyer, *Ground-state cooling of a micromechanical oscillator: Comparing cold damping and cavity-assisted cooling schemes,* Phys. Rev. A **77**, 033804 (2008).

[92] A. G. Krause, M. Winger, T. D. Blasius, Q. Lin, and O. Painter, *A high-resolution microchip optomechanical accelerometer,* Nat. Photonics **6**, 768 (2012).

[93] M.-H. Chien, M. Brameshuber, B. K. Rossboth, G. J. Schütz, and S. Schmid, *Single-molecule optical absorption imaging by nanomechanical photothermal sensing,* PNAS **115**, 11150 (2018).

[94] G. Gruber, C. Urgell, A. Tavernarakis, A. Stavrinadis, S. Tepsic, C. Magén, S. Sangiao, J. M. de Teresa, P. Verlot, and A. Bachtold, *Mass sensing for the advanced fabrication of nanomechanical resonators,* Nano Lett. **19**, 6987 (2019).

[95] A. Szorkovszky, A. C. Doherty, G. I. Harris, and W. P. Bowen, *Mechanical squeezing via parametric amplification and weak measurement,* Phys. Rev. Lett. **107**, 213603 (2011).

[96] T. P. Purdy, R. W. Peterson, and C. A. Regal, *Observation of radiation pressure shot noise on a macroscopic object,* Science **339**, 801 (2013).

[97] D. J. Wilson, V. Sudhir, N. Piro, R. Schilling, A. Ghadimi, and T. J. Kippenberg, *Measurement-based control of a mechanical oscillator at its thermal decoherence rate,* Nature **524**, 325 (2015).

[98] P.-L. Yu, K. Cicak, N. S. Kampel, Y. Tsaturyan, T. P. Purdy, R. W. Simmonds, and C. A. Regal, *A phononic bandgap shield for high-Q membrane microresonators,* Appl. Phys. Lett. **104**, 023510 (2014).

[99] Y. Tsaturyan, A. Barg, E. S. Polzik, and A. Schliesser, *Ultracoherent nanomechanical resonators via soft clamping and dissipation dilution,* Nat. Nanotechnol. **12**, 776 (2017).

[100] A. H. Ghadimi, S. A. Fedorov, N. J. Engelsen, M. J. Bereyhi, R. Schilling, D. J. Wilson, and T. J. Kippenberg, *Elastic strain engineering for ultralow mechanical dissipation,* Science **360**, 764 (2018).

[101] I. Wilson-Rae, R. A. Barton, S. S. Verbridge, D. R. Southworth, B. Ilic, H. G. Craighead, and J. M. Parpia, *High-Q nanomechanics via desctructive interference of elastic waves,* Phys. Rev. Lett. **106**, 047205 (2011).

[102] A. Borrielli, L. Marconi, F. Marin, F. Marino, B. Morana, G. Pandraud, A. Pontin, G. A. Prodi, P. M. Sarro, E. Serra, and M. Bonaldi, *Control of recoil losses in nanomechanical SiN membrane resonators,* Phys. Rev. B **94**, 121403 (2016).

[103] G. Dolfo and J. Vigué, *Damping of coupled harmonic oscillators,* European J. Phys **39**, 025005 (2018).

[104] B.-B. Li, D. Bulla, V. Prakash, S. Forstner, A. Dehghan-Manshadi, H. Rubinsztein-Dunlop, S. Foster, and W. P. Bowen, *Scalable high-sensitivity optomechanical magnetometers on a chip,* APL Photonics **3**, 120806 (2018).

[105] W. J. Westerveld, M. Mahmud-Ul-Hasan, R. Shnaiderman, V. Ntziachristos, X. Rottenberg, S. Severi, and V. Rochus, *Sensitive, small, broadband and scalable optomechanical ultrasound sensor in silicon photonics,* Nat. Photonics **15**, 341 (2021).

[106] D. H. Zanette, *Energy exchange between coupled mechanical oscillators: Linear regimes,* J. Phys. Commun. **2**, 095015 (2018).

[107] G. Luo, Z.-Z. Zhang, G.-W. Deng, H.-O. Li, G. Cao, M. Xiao, G.-C. Guo, L. Tian, and G.-P. Guo, *Strong indirect coupling between graphene-based mechanical resonators via a phonon cavity,* Nat Commun **9**, 383 (2018).

[108] Z.-Z. Zhang, X.-X. Song, G. Luo, Z.-J. Su, K.-L. Wang, G. Cao, H.-O. Li, M. Xiao, G.-C. Guo, L. Tian, G.-W. Deng, and G.-P. Guo, *Coherent phonon dynamics in spatially separated graphene mechanical resonators,* PNAS **117**, 5582 (2020).

[109] M. Šiškins, E. Sokolovskaya, M. Lee, S. Mañas-Valero, D. Davidovikj, H. S. J. van der Zant, and P. G. Steeneken, *Tunable strong coupling of mechanical reosnance between spatially separated $FePS_3$ nanodrums,* Nano Lett. **22**, 36 (2022).

[110] T. Faust, J. Rieger, M. J. Seitner, J. P. Kotthaus, and E. M. Weig, *Coherent control of a classical nanomechanical two-level system,* Nat. Phys. **9**, 485 (2013).

[111] L. G. Villanueva and S. Schmid, *Evidence of surface loss as ubiquitous limiting damping mechanism in SiN micro- and nanomechanical resonators,* Phys. Rev. Lett. **113**, 227201 (2014).

[112] K. Aubin, M. Zalalutdinov, T. Alan, R. B. Reichenbach, R. Rand, A. Zehnder, J. Parpia, and H. Craighead, *Limit cycle oscillations in CW-laser driven MEMS,* J Microelectromech S **13**, 1018 (2004).

[113] F. Yang, F. Rochau, J. S. Huber, A. Brieussel, G. Rastelli, E. M. Weig, and E. Scheer, *Spatial modulation of nonlinear flexural vibrations of membrane resonators,* Phys. Rev. Lett. **122**, 154301 (2019).

[114] F. Yang, F. Hellbach, F. Rochau, W. Belzig, E. M. Weig, G. Rastelli, and E. Scheer, *Persistent response in an ultrastrongly driven mechanical membrane resonator,* Phys. Rev. Lett. **127**, 014304 (2021).

[115] R. J. Dolleman, D. Davidovikj, H. S. J. van der Zant, and P. G. Steeneken, *Amplitude calibration of 2D mechanical resonators by nonlinear optical transduction,* Appl. Phys. Lett. **111**, 253104 (2017).

[116] S. T. Cundiff and J. Ye, *Colloquium: Femtosecond optical frequency combs,* Rev. Modern Phys. **75**, 325 (2003).

[117] T. Fortier and E. Baumann, *20 years of developsments in optical frequency comb technology and applications,* Commun Phys **2**, 153 (2019).

[118] A. J. Metcalf, T. Anderson, C. F. Bender, S. Blakeslee, W. Brand, D. R. Carlson, W. D. Cochran, S. A. Diddams, M. Endl, C. Fredrick, S. Halverston, D. D. Hickstein, F. Hearty, J. Jennings, S. Kanodia, K. F. Kaplan, E. Levi, E. Lubar, S. Mahadevan, A. Monson, J. P. Ninan, C. Nitroy, S. Osterman, S. B. Papp, F. Quinlan, L. Ramsey, P. Robertson, A. Roy, C. Schwab, S. Sigurdsson, K. Srinivasan, G. Stefansson, D. A. Sterner, R. Terrien, A. Wolszczan, J. T. Wright, and G. Ycas, *Stellar spectroscopy in the near-infrared with a laser frequency comb,* Optica **6**, 233 (2019).

[119] Boulder Atomic Clock Optical Network Collaboration, *Frequency ratio measurements at 18-digit accuracy using an optical clock network,* Nature **591**, 564 (2021).

[120] T. Rosenband, D. B. Hume, P. O. Schmidt, C. W. Chou, A. Brusch, L. Lorini, W. H. Oskay, R. E. Drullinger, T. M. Fortier, J. E. Stalnaker, S. A. Diddams, W. C. Swann, N. R. Newbury, W. M. Itano, D. M. Wineland, and J. C. Bergquist, *Frequency ratio of Al^+ and Hg^+ single-ion optical clocks; metrology at the 17th decimal place,* Science **319**, 1808 (2007).

[121] I. Mahboob, Q. Wilmart, K. Nishiguchi, A. Fujiwara, and H. Yamaguchi, *Tuneable electromechanical comb generation,* Appl. Phys. Lett. **100**, 113109 (2012).

[122] L. S. Cao, D. X. Qi, R. W. Peng, M. Wang, and P. Schmelcher, *Phononic frequency combs through nonlinear resonances,* Phys. Rev. Lett. **112**, 075505 (2014).

[123] I. S. Maksymov, B. Q. H. Nguyen, A. Pototsky, and S. A. Suslov, *Acoustic, phononic, Brillouin light scattering and Faraday wave based frequency combs: Physical foundations and applications,* Sensors **22**, 3921 (2022).

[124] M.-A. Miri, G. D'Aguanno, and A. Alù, *Optomechanical frequency combs,* New J. Phys. **20**, 043013 (2018).

[125] J. Zhang, B. Peng, S. Kim, F. Monifi, X. Jiang, Y. Li, P. Yu, L. Liu, A. Alù, and L. Yang, *Optomechanical dissipative solitons,* Nature **600**, 75 (2021).

[126] A. Erbe, H. Krömmer, A. Kraus, R. H. Blick, G. Corso, and K. Richter, *Mechanical mixing in nonlinear nanomechanical resonators,* Appl. Phys. Lett. **77**, 3102 (2000).

[127] I. Mahboob, R. Dupuy, K. Nishiguchi, A. Fujiwara, and H. Yamaguchi, *Hopf and period-doubling bifurcations in an electromechanical resonator,* Appl. Phys. Lett. **109**, 073101 (2016).

[128] M. J. Seitner, M. Abdi, A. Ridolfo, M. J. Hartmann, and E. M. Weig, *Parametric oscillation, frequency mixing, and injection locking of strongly coupled nanomechanical resonator modes,* Phys. Rev. Lett. **118**, 254301 (2017).

[129] A. Ganesan, C. Do, and A. Seshia, *Phononic frequency comb via intrinsic three-wave mixing,* Phys. Rev. Lett. **118**, 033903 (2017).

[130] D. A. Czaplewski, C. Chen, D. Lopez, O. Shoshani, A. M. Eriksson, S. Strachan, and S. M. Shaw, *Bifurcation generated mechanical frequency comb,* Phys. Rev. Lett. **121**, 244302 (2018).

[131] M. Park and A. Ansari, *Formation, evolution, and tuning of frequency combs in microelectromechanical resonators,* J Microelectromech S **28**, 429 (2019).

[132] M. Goryachev, S. Galliou, and M. E. Tobar, *Generation of ultralow power phononic combs,* Phys. Rev. Research **2**, 023035 (2020).

[133] R. Singh, A. Sarkar, C. Guria, R. J. T. Nicholl, S. Chakraborty, K. I. Bolotin, and S. Ghosh, *Giant tunable mechanical nonlinearity in graphene-silicon nitride hybrid resonator,* Nano Lett. **20**, 4659 (2020).

[134] A. Chiout, F. Correia, M.-Q. Zhao, A. T. C. Johnson, D. Pierucci, F. Oehler, A. Ouerghi, and J. Chaste, *Multi-order phononic frequency comb generation within a MoS_2 electromechanical resonators,* Appl. Phys. Lett. **119**, 173102 (2021).

[135] J. S. Ochs, D. K. J. Boneß, G. Rastelli, M. Seitner, W. Belzig, M. I. Dykman, and E. M. Weig, *Frequency comb from a single driven nonlinear nanomechanical mode,* (2022), arxiv preprint, 2207.04030 .

[136] X. Han, C.-L. Zou, W. Fu, M. Xu, Y. Xu, and H. X. Tang, *Superconducting cavity electromechanics: The realization of an acoustic frequency comb at microwave frequencies,* Phys. Rev. Lett. **129**, 107701 (2022).

[137] A. A. Batista and A. A. Lisboa de Souza, *Frequency-comb response of a parametrically driven Duffing oscillator to a small added ac excitation,* J Appl Phys **128**, 244901 (2020).

[138] A. Ganesan, C. Do, and A. Seshia, *Frequency transitions in phononic four-wave mixing,* Appl. Phys. Lett. **111**, 064101 (2017).

[139] A. Ganesan, C. Do, and A. Seshia, *Phononic frequency comb via three-mode parametric resonance,* Appl. Phys. Lett. **100**, 021906 (2018).

[140] A. Keşkekler, H. Arjmandi, P. G. Steeneken, and F. Alijani, *Symmetry-breaking induced frequency combs in graphene resonators,* Nano Letters **22**, 6048 (2022).

[141] H. Wu, Z. Qian, H. Zhang, X. Xu, B. Xue, and J. Zhai, *Precise underwater distance measurement by dual acoustic frequency combs,* Ann. Phys. **531**, 1900283 (2019).

[142] A. Ganesan and A. Seshia, *Resonance tracking in a micromechanical device using phononic frequency combs,* Sci. Rep. **9**, 9452 (2019).

[143] W. S. Wall, R. L. Kubena, Y.-K. Yook, J. Koehl, and R. J. Joyce, *Phase noise transfer in high-Q quartz phononic frequency combs,* in *2020 IEEE International Ultrasonics Symposium (IUS)* (2020).

[144] A. Aleman, S. Muralidhar, A. A. Awad, J. Åkerman, and D. Hanstorp, *Frequency comb enhanced Brillouin microscopy,* Opt Express **28**, 29540 (2020).

[145] S. Muralidhar, A. A. Awad, A. Alemán, R. Khymyn, M. Dvornik, D. Hanstorp, and J. Åkerman, *Sustained coherent spin wave emission using frequency combs,* Phys Rev B **101**, 224423 (2020).

[146] Y. Chu, P. Kharel, W. H. Renninger, L. D. Burkhart, L. Frunzio, P. T. Rakich, and R. J. Schoelkopf, *Quantum acoustics with superconducting qubits,* Science **358**, 199 (2017).

[147] J. Bochmann, A. Vainsencher, D. D. Awschalom, and A. N. Cleland, *Nanomechanical coupling between microwave and optical photons,* Nat. Phys. **9**, 712 (2013).

[148] L. R. Sletten, B. A. Morres, J. J. Viennot, and K. W. Lehnert, *Resolving phonon Fock states in a multimode cavity with a double-slit qubit,* Phys. Rev. X **9**, 021056 (2019).

[149] Z. Hu and H. J. Kimble, *Observation of a single atom in a magneto-optical trap,* Opt. Lett. **19**, 1888 (1994).

[150] M. Endres, H. Bernien, A. Keesling, H. Levine, E. R. Anschuetz, A. Krajenbrink, C. Senko, V. Vuletic, M. Greiner, and M. D. Lukin, *Atom-by-atom assembly of defect-free one-dimensional cold atom arrays,* Science **354**, 1024 (2016).

[151] K. Dholakia and T. Čižmar, *Shaping the future of manipulation,* Nat. Photonics **5**, 335 (2011).

[152] M. D. Wang, H. Yin, R. Landick, J. Gelles, and S. M. Block, *Stretching DNA with optical tweezers,* Biophys. J. **72**, 1335 (1997).

[153] A. Ashkin and J. M. Dziedzic, *Optical trapping and manipulation of single living cells using infra-red laser beams,* Ber. Bunsenges. Phys. Chem. **93**, 254 (1989).

[154] G. Guccione, M. Hosseini, S. Adlong, M. T. Johnsson, J. Hope, B. C. Buchler, and P. K. Lam, *Scattering-free optical levitation of a cavity mirror,* Phys. Rev. Lett. **111**, 183001 (2013).

[155] S. Bose, A. Mazumdar, G. W. Morley, H. Ulbricht, M. Toroš, M. Paternostro, A. A. Geraci, P. F. Barker, M. S. Kim, and G. Milburn, *Spin entanglement witness for quantum gravity,* Phys. Rev. Lett. **119**, 240401 (2017).

[156] U. Delić, M. Reisenbauer, K. Dare, D. Grass, V. Vuletić, N. Kiesel, and M. Aspelmeyer, *Cooling of a levitated nanoparticle to the motional quantum ground state,* Science **367**, 892 (2020).

[157] A. Ashkin, *Acceleration and trapping of particles by radiation pressure,* Phys. Rev. Lett. **24**, 156 (1970).

[158] P. Zemánek, A. Jonáš, L. Šrámek, and M. Liška, *Optical trapping of nanoparticles and microparticles by a Gaussian standing wave,* Opt. Lett. **24**, 1448 (1999).

[159] K.-K. Ni, R. Norte, D. J. Wilson, J. D. Hood, D. E. Chang, O. Painter, and H. J. Kimble, *Enhancement of mechanical Q factors by optical trapping,* Phys. Rev. Lett. **108**, 214302 (2012).

[160] L. Q. Zhou, G. Colston, M. J. Pearce, R. G. Prince, M. Myronov, D. R. Leadley, O. Trushkevych, and R. S. Edwards, *Non-linear vibrational response of Ge and SiC membranes,* Appl. Phys. Lett. **111**, 011904 (2017).

[161] Q. Yang, L. Xu, R. Huan, Z. Jiang, A. Ganesan, and X. Wei, *Measurement of comb finger and comb spacing stability in phononic frequency comb,* in *2021 IEEE 16th International Conference on Nano/Micro Engineered and Molecular Systems* (2021).

[162] X. Wang, Q. Yang, R. Huan, Z. Shi, W. Zhu, Z. Jiang, Z. Deng, and X. Wei, *Frequency comb in 1:3 internal resonance of coupled micromechanical resonators,* Applied Physics Letters **120**, 173506 (2022).

[163] G. Siegmund, *Sources of measurement error in laser Doppler vibrometers and proposal for unified specifications,* in *Eighth international conference on vibration measurements by laser techniques: Advances and applications* (2008).

[164] L. Yarovoi and G. Siegmund, *The effect of three-wave interference in laser Doppler vibrometry,* Meas. Sci. Technol. **15**, 2150 (2004).

[165] O. Dussarrat, D. Clark, and T. Moir, *New demodulation process to reduce cochannel interference for a laser vibrometer sensing system,* in *Third international conference on vibration measurements by laser techniques: Advances and applications* (1998).

[166] H. Sumali and M. Allen, *Apparent nonlinear effect of the microscope on the laser Doppler vibrometer,* in *Eighth international conference on vibration measurements by laser techniques: Advances and applications* (2008).

[167] A. Ashkin, J. M. Dziedzic, J. E. Bjorkholm, and S. Chu, *Observation of a single-beam gradient force optical trap for dielectric particles,* Opt. Lett. **11**, 288 (1986).

[168] H. A. Pohl, *The motion and precipitation of duspensoids in divergent electric fields,* J. Appl. Phys. **22**, 869 (1951).

[169] J. Steinlechner, C. Krüger, I. W. Martin, A. Bell, J. Hough, H. Kaufer, S. Rowan, R. Schnabel, and S. Steinlechner, *Optical absorption of silicon nitride membranes at 1064 nm and at 1550 nm,* Phys. Rev. D **96**, 022007 (2017).

[170] A. Frigg, A. Boes, G. Ren, I. Abdo, D.-Y. Choi, S. Gees, and A. Mitchell, *Low loss CMOS-compatible silicon nitride photonics utilizing reactive sputtered thin films,* Opt. Express **27**, 37795 (2019).

[171] A. Gorin, A. Jaouad, E. Grondin, V. Aimez, and P. Charette, *Fabrication of silicon nitride waveguides for visible-light using PECVD: a study of the effect of plasma frequency on optical properties,* Opt. Express **16**, 13509 (2008).

[172] M. T. Alam, M. P. Manoharan, M. A. Haque, C. Muratore, and A. Voevodin, *Influence of strain on thermal conductivity of silicon nitride thin films,* J Micromech Microeng **22**, 045001 (2012).

[173] T. Larsen, S. Schmid, L. G. Villanueva, and A. Boisen, *Photothermal analysis of individual nanoparticulate samples using micromechanical resonators,* ACS Nano **7**, 6188 (2013).

[174] C. Metzger, M. Ludwig, C. Neuenhahn, A. Ortlieb, I. Favero, K. Karrai, and F. Marquardt, *Self-induced oscillations in an optomechanical system driven by bolometric backaction,* Phys. Rev. Lett. **101**, 133903 (2008).

[175] R. Benguria and M. Kac, *Quantum Langevin equation,* Phys. Rev. Lett. **46**, 1 (1981).

[176] M. J. Bereyhi, A. Arabmoheghi, S. A. Fedorov, A. Beccari, G. Huang, T. J. Kippenberg, and N. J. Engelsen, *Perimeter modes of nanomechanical resonators exhibit quality factors exceeding* 10^9 *at room temperature,* Phys. Rev. X **12**, 021036 (2022).

[177] S. R.-K. Rodriguez, *Classical and quantum distinctions between weak and strong coupling,* European J. Phys **37**, 025802 (2016).

[178] B. H. Schneider, V. Singh, W. J. Venstra, H. B. Meerwaldt, and G. A. Steele, *Observation of decoherence in a carbon nanotube mechanical resonator,* Nat Commun **5**, 5819 (2014).

[179] A. Gloppe, P. Verlot, E. Dupont-Ferrier, A. Siria, P. Poncharal, G. Bachelier, P. Vincent, and O. Arcizet, *Bidimensional nano-optomechanics and topological backaction in a non-conservative radiation force field,* Nat. Nanotechnol. **9**, 920 (2014).

[180] L. Mercier de Lépinay, B. Pigeau, B. Besga, and O. Arcizet, *Eigenmode orthogonality breaking and anomalous dynamics in multimode nano-optomechanical systems under non-reciprocal coupling,* Nat Commun **9**, 1401 (2018).

[181] D. Hälg, T. Gisler, E. C. Langman, S. Misra, O. Zilberberg, A. Schliesser, C. Degen, and A. Eichler, *Strong parametric coupling between two ultra-coherent membrane modes,* Phys. Rev. Lett. **128**, 094301 (2022).

[182] G. La Gala, J. P. Mathew, P. Neveu, and E. Verhagen, *Nanomechanical design strategy for single-mode optomechanical measurement,* J. Phys. D: Appl. Phys. **55**, 225101 (2022).

[183] G. Heinrich, M. Ludwig, J. Qian, B. Kubala, and F. Marquardt, *Collective dynamics in optomechanical arrays,* Phys. Rev. Lett. **107**, 043603 (2011).

[184] C.-G. Liao, R.-X. Chen, H. Xie, M.-Y. He, and X.-M. Lin, *Quantum synchronization and correlations of two mechanical resonators in a dissipative optomechanical system,* Phys. Rev. A **99**, 033818 (2019).

[185] M. Zhang, G. S. Wiederhecker, S. Manipatruni, A. Barnard, P. McEuen, and M. Lipson, *Synchronization of micromechanical oscillators using light,* Phys. Rev. Lett. **109**, 233906 (2012).

[186] H. Xu, D. Mason, L. Jiang, and J. G. E. Harris, *Topological energy transfer in an optomechanical system with exceptional points,* Nature **537**, 80 (2016).

[187] K. Y. Fong, H.-K. Li, R. Zhao, S. Yang, Y. Wang, and X. Zhang, *Phonon heat transfer across a vacuum through quantum fluctuations,* Nature **576**, 243 (2019).

[188] M. J. Woolley and A. A. Clerk, *Two-mode squeezed states in cavity optomechanics via engineering of a single reservoir,* Phys. Rev. A **89**, 063805 (2014).

[189] Y. S. Patil, S. Chakram, L. Chang, and M. Vengalattore, *Thermomechanical two-mode squeezing in an ultrahigh-Q membrane resonator,* Phys. Rev. Lett. **115**, 017202 (2015).

[190] A. Pontin, M. Bonaldi, A. Borrielli, L. Marconi, F. Marino, G. Pandraud, G. A. Prodi, P. M. Sarro, E. Serra, and F. Marin, *Dynamical two-mode squeezing of thermal fluctuations in a cavity optomechanical system,* Phys. Rev. Lett. **116**, 103601 (2016).

[191] W. H. P. Nielsen, Y. Tsaturyan, C. B. Møller, E. S. Polzik, and A. Schliesser, *Multimode optomechanical system in the quantum regime,* PNAS **114**, 62 (2017).

[192] T. Caniard, P. Verlot, T. Briant, P.-F. Cohadon, and A. Heidmann, *Observation of back-action noise cancellation in interferometric and weak-force measurements,* Phys. Rev. Lett. **99**, 110801 (2007).

[193] M. Tsang and C. M. Caves, *Evading quantum mechanics: Engineering a classical subsystem within a quantum environment,* Phys. Rev. X **2**, 031016 (2012).

[194] L. Mercier de Lépinay, C. F. Ockeloen-Korppi, M. J. Woolley, and M. A. Sillanpää, *Quantummechanics-free subsystem with mechanical oscillators,* Science **372**, 625 (2021).

[195] J. Wiersig, *Enhancing the sensitivity of frequency and energy splitting detection by using exceptional points: Application to microcavity sensors for single-particle detection,* Physical Review Letters **112**, 203901 (2014).

[196] H.-K. Lau and A. A. Clerk, *Fundamental limits and non-reciprocal approaches in non-Hermitian quantum sensing,* Nat Commun **9**, 4320 (2018).

[197] J. P. Mathew, J. del Pino, and E. Verhagen, *Synthetic gauge fields for phonon transport in a nano-optomechanical system,* Nat. Nanotechnol. **15**, 198 (2020).

[198] J. del Pino, J. J. Slim, and E. Verhagen, *Non-Hermitian chiral phononics through optomechanically induced squeezing,* Nature **606**, 82 (2022).

[199] Y. S. S. Patil, J. Höller, P. A. Henry, C. Guria, Y. Zhang, L. Jiang, N. Kralj, N. Read, and J. G. E. Harris, *Measuring the know of non-Hermitian degeneracies and non-commuting braids,* Nature **607**, 271 (2022).

[200] S. H. Nitzan, V. Zega, M. Li, C. H. Ahn, A. Corigliano, T. W. Kenny, and D. A. Horsley, *Self-induced parametric amplification arising from nonlinear elastic coupling in a micromechanical resonating disk gyroscope,* Sci. Rep. **5**, 9036 (2015).

[201] M. Defoort, P. Taheri-Tehrani, S. H. Nitzan, and D. A. Horsley, *Impact of synchronization in micromechanical gyroscopes,* J. Vib. Acoust **139**, 040906 (2017).

[202] T. Antoni, K. Makles, R. Braive, T. Briant, P.-F. Cohadon, I. Sagnes, I. Robert-Philip, and A. Heidmann, *Nonlinear mechanics with suspended nanomembranes,* Europhys. Lett. **100**, 68005 (2012).

[203] C. Samanta, P. R. Yasasvi Gangavarapu, and A. K. Naik, *Nonlinear mode coupling an internal resonances in MoS_2 nanoelectromechanical system,* Appl. Phys. Lett. **107**, 173110 (2015).

[204] D. Antonio, D. H. Zanette, and D. López, *Frequency stabilization in nonlinear micromechanical resonators,* Nat Commun **3**, 806 (2012).

[205] A. Eichler, M. del Álamo Ruiz, J. A. Plaza, and A. Bachtold, *Strong coupling between mechanical modes in a nanotube resonator,* Phys. Rev. Lett. **109**, 025503 (2012).

[206] C. Chen, D. H. Zanette, D. A. Czaplewski, S. Shaw, and D. López, *Direct observation of coherent energy transfer in nonlinear micromechanical resonators,* Nat Commun **8**, 15523 (2017).

[207] A. Chandrashekar, P. Belardinelli, S. Lenci, U. Staufer, and F. Alijani, *Mode coupling in dynamic atomic force microscopy,* Phys. Rev. Appl. **15**, 024013 (2021).

[208] P. M. Polunin, Y. Yang, M. I. Dykman, T. W. Kenny, and S. W. Shaw, *Characterization of MEMS resonator nonlinearities using the ringdown response,* J Microelectromech S **25**, 297 (2016).

[209] J. Güttinger, A. Noury, P. Weber, A. M. Eriksson, C. Lagoin, J. Moser, C. Eichler, A. Wallraff, A. Isacsson, and A. Bachtold, *Energy-dependent path of dissipation in nanomechanical resonators,* Nat. Nanotechnol. **12**, 631 (2017).

[210] O. Shoshani, S. W. Shaw, and M. I. Dykman, *Anomalous decay of nanomechanical modes going through nonlinear resonance,* Sci. Rep. **7**, 18091 (2017).

[211] Y. Yan, X. Dong, L. Huang, K. Moskovtsev, and H. B. Chan, *Energy transfer into period-tripled states in coupled electromechanical modes at internal resonance,* Phys. Rev. X **12**, 031003 (2022).

[212] G. Anetsberger, R. Rivière, A. Schliesser, O. Arcizet, and T. J. Kippenberg, *Ultralow-dissipation optomechanical resonators on a chip,* Nat. Photonics **2**, 627 (2008).

[213] P. A. Truitt, J. B. Hertzberg, E. Altunkaya, and K. C. Schwab, *Linear and nonlinear coupling between transverse modes of a nanomechanical resonator,* J Appl Phys **114**, 114307 (2013).

[214] R. Lifshitz and M. C. Cross, *Reviews of nonlinear dynamics and complexity*, edited by H. G. Schuster (Wiley-VCH Verlag, 2008).

[215] L. E. Reichl, *A modern course in statistical physics*, 4th ed. (John Wiley & Sons Inc., 2016).

[216] Q. Lin, J. Rosenberg, D. Chang, R. Camacho, M. Eichenfield, K. J. Vahala, and O. Painter, *Coherent mixing of mechanical excitations in nano-optomechanical structures,* Nat. Photonics **4**, 236 (2010).

[217] F. Massel, S. U. Cho, J.-M. Pirkkalainen, P. J. Hakonen, T. T. Heikkilä, and M. A. Sillanpää, *Multimode circuit optomechanics near the quantum limit,* Nat. Commun. **3**, 987 (2012).

[218] A. B. Shkarin, N. E. Flowers-Jacobs, S. W. Hoch, A. D. Kashkanova, C. Deutsch, J. Reichel, and J. G. E. Harris, *Optically mediated hybridization between two mechanical modes,* Phys. Rev. Lett. **112**, 013602 (2014).

[219] C. F. Ockeloen-Korppi, M. F. Gely, E. Damskägg, M. Jenkins, G. A. Steele, and M. A. Sillanpää, *Sideband cooling of nearly degenerate micromechanical oscillators in a multimode optomechanical system,* Phys. Rev. A **99**, 023826 (2019).

[220] M. Bagheri, M. Poot, L. Fan, F. Marquardt, and H. X. Tang, *Photonic cavity synchronization of nanomechanical oscillators,* Phys. Rev. Lett. **111**, 213902 (2013).

[221] N. Spethmann, J. Kohler, S. Schreppler, L. Buchmann, and D. M. Stamper-Kurn, *Cavity-mediated coupling of mechanical oscillators limited by quantum back-action,* Nat. Phys. **12**, 27 (2016).

[222] I. Mahboob, H. Okamoto, K. Onomitsu, and H. Yamaguchi, *Two-mode thermal-noise squeezing in an electromechanical resonator,* Phys. Rev. Lett. **113**, 167203 (2014).

[223] C. F. Ockeloen-Korppi, E. Damskägg, J.-M. Pirkkalainen, M. Asjad, A. A. Clerk, F. Massel, M. J. Woolley, and M. A. Sillanpää, *Stabilized entanglement of massive mechanical oscillators,* Nature **556**, 478 (2018).

[224] D. C. Newsom, F. Luna, V. Fedoseev, W. Löffler, and D. Bouwmeester, *Optimal optomechanical coupling strength in multi-membrane systems,* Phys. Rev. A **101**, 033829 (2020).

[225] J. Li, I. M. Haghighi, N. Malossi, S. Zippilli, and D. Vitali, *Generation and detection of large and robust entanglement between two different mechanical resonators in cavity optomechanics,* New J. Phys. **17**, 103037 (2015).

[226] L. F. Buchmann and D. M. Stamper-Kurn, *Nondegenerate multimode optomechanics,* Phys. Rev. A **92**, 013851 (2015).

[227] T. Kipf and G. S. Agarwal, *Superradiance and collective gain in multimode optomechanics,* Phys. Rev. A **90**, 053808 (2014).

[228] H. Seok, L. F. Buchmann, S. Singh, and P. Meystre, *Optically mediated nonlinear quantum optomechanics,* Phys. Rev. A **86**, 063829 (2012).

[229] V. Fedoseev, F. Luna, W. Löffler, and D. Bouwmeester, *Stimulated Raman adiabatic passage in optomechanics,* Phys. Rev. Lett. **126**, 113601 (2021).

[230] S. Stassi, A. Chiado, G. Calafiore, G. Palmara, S. Cabrini, and C. Ricciardi, *Experimental evidence of Fano resonances in nanomechanical resonators,* Sci. Rep. **7**, 1065 (2017).

[231] J. M. Dobrindt and T. J. Kippenberg, *Theoretical analysis of mechanical displacement measurement using a multiple cavity mode transducer,* Phys. Rev. Lett. **104**, 033901 (2010).

[232] Y. Yanay, J. C. Sankey, and A. A. Clerk, *Quantum backaction and noise interference in asymmetric two-cavity optomechanical systems,* Phys. Rev. A **93**, 063809 (2016).

[233] A. M. Jayich, J. C. Sankey, B. M. Zwickl, C. Yang, J. D. Thompson, S. M. Girvin, A. A. Clerk, F. Marquardt, and J. G. E. Harris, *Dispersive optomechanics: a membrane inside a cavity,* New J. Phys. **10**, 095008 (2008).

[234] D. Boyanovsky and D. Jasnow, *Coherence of mechanical oscillators mediated by coupling to different baths,* Phys. Rev. A **96**, 012103 (2017).

[235] V. Giovannetti and D. Vitali, *Phase-noise measurement in a cavity with a movable mirror undergoing quantum Brownian motion,* Phys. Rev. A **63**, 023812 (2001).

[236] U. Fano, *Effects of configuration interaction on intensities and phase shifts,* Phys. Rev. **124**, 1866 (1961).

[237] S. Weis, R. Rivière, S. Deléglise, E. Gavartin, O. Arcizet, A. Schliesser, and T. J. Kippenberg, *Optomechanically induced transparency,* Science **330**, 1520 (2010).

[238] G. S. Agarwal and S. Huang, *Electromagnetically induced transparency in mechanical effects of light,* Phys. Rev. A **81**, 041803 (2010).

[239] R. A. Rodrigues, *Fano-like antiresonances in nanomechanical and optomechanical systems,* Phys. Rev. Lett. **102**, 067202 (2009).

[240] I. Wilson-Rae, N. Nooshi, W. Zwerger, and T. J. Kippenberg, *Theory of ground state cooling of a mechanical oscillator using dynamical backaction,* Phys. Rev. Lett. **99**, 093901 (2007).

[241] A. Xuereb, C. Genes, G. Pupillo, M. Paternostro, and A. Dantan, *Reconfigurable long-range phonon dynamics in optomechanical arrays,* Phys. Rev. Lett. **112**, 133604 (2014).

[242] P. C. Parks and V. Hahn, *Stability theory* (Springer Verlag, 1981).

[243] The LIGO scientific collaboration et al., *Advanced LIGO,* Class Quantum Gravity **32**, 074001 (2015).